



HAL
open science

Advanced control of microgrids for frequency and voltage stability: robust control co-design and real-time validation

Quang Linh Lam

► **To cite this version:**

Quang Linh Lam. Advanced control of microgrids for frequency and voltage stability: robust control co-design and real-time validation. Electric power. Université Grenoble Alpes, 2018. English. NNT : 2018GREAT002 . tel-01836292

HAL Id: tel-01836292

<https://theses.hal.science/tel-01836292>

Submitted on 12 Jul 2018

HAL is a multi-disciplinary open access archive for the deposit and dissemination of scientific research documents, whether they are published or not. The documents may come from teaching and research institutions in France or abroad, or from public or private research centers.

L'archive ouverte pluridisciplinaire **HAL**, est destinée au dépôt et à la diffusion de documents scientifiques de niveau recherche, publiés ou non, émanant des établissements d'enseignement et de recherche français ou étrangers, des laboratoires publics ou privés.

THÈSE

pour obtenir le grade de

DOCTEUR DE LA COMMUNAUTÉ
UNIVERSITÉ GRENOBLE ALPES

Spécialité : **Génie Électrique**

Arrêté ministériel : 25 mai 2016

Présentée par

Quang Linh LAM

Thèse dirigée par **Mme. Delphine RIU**

et co-encadrée par **Mme. Antoneta Iuliana BRATCU**

préparée au sein du **Laboratoire G2Elab**

et du **Laboratoire GIPSA-lab**

dans l'**École Doctorale EEATS**

Advanced control of microgrids for frequency and voltage stability : robust control co-design and real-time validation

Thèse soutenue publiquement le **17 janvier 2018**,
devant le jury composé de :

M. Xavier ROBOAM

Directeur de Recherche CNRS, Laboratoire LAPLACE, Président

Mme. Manuela SECHILARIU

Professeur des Universités, Université de Technologie de Compiègne,
Rapporteur

M. Rafael WISNIEWSKI

Professor, Aalborg University, Rapporteur

M. Olivier SENAME

Professeur des Universités, Grenoble INP, Examineur

M. Florian DÖRFLER

Assistant Professor, ETH Zürich, Examineur

Mme. Delphine RIU

Professeur des Universités, Grenoble INP, Directrice de thèse

Mme. Antoneta Iuliana BRATCU

Maître de Conférences, Grenoble INP, Co-encadrante de thèse



In loving memory of my grandparents

*This thesis is dedicated to
my beloved parents and my lovely little sister
for their endless love, unconditional support, and encouragement*

Acknowledgements

I would like to express my sincere gratitude to all the people who contributed to the work presented in this thesis.

First of all, I want to express my deep and sincere gratitude to my supervisor, Mme. Delphine RIU, for her support to work at G2Elab and for providing valuable guidance and encouragement throughout this research. Thank you for all the things you brought to this work and for your always interesting ideas and comments. Thank you for your ability of orienting me towards the correct direction in my research, for your discernment and vision to the analysis of my results. Moreover, I am very grateful to my co-supervisor, Mme. Antoneta Iuliana BRATCU, for the valuable discussion, her guidance, and her support to work at GIPSA-lab. Thank you for your energy and the time devoted to this work, always ready to help me. We have worked together since my master's thesis, February 2014, I would like to thank both of you for everything for this four years. I can overcome many difficulties and learned many things. I really enjoyed working with you, my supervisor and co-supervisor, thank you once again, I would always be grateful.

I would also like to thank M. Xavier ROBOAM for accepting to be the president of the committee, as well as Mme. Manuela SECHILARIU and M. Rafael WISNIEWSKI for accepting to serve as the reviewers of my thesis. I thank also M. Olivier SENAME and M. Florian DÖRFLER for accepting to take part in the committee. I wish to thank all the members of the committee for the energy devoted to the reading and correction of my thesis. And I am very grateful for their valuable discussions, suggestions, and comments.

Many thanks also go to M. Antoine LABONNE, M. Cédric BOUDINET, and M. Martin THOMAS for providing valuable assistance and advice on experimental setup issues as well as for instructing me many things about RT-LAB[®], dSPACE[®], and hardware. The real-time implementation of \mathcal{H}_∞ robust control, a cornerstone of this work, would not have been possible without their precious help.

Special thanks to M. Gérard MEUNIER and M. Nicolas RETIERE, who gave me the opportunity to come to France, to learn a new language, and to discover a new culture. Also, I express my thanks to M. Khac Nhan NGUYEN and M. Hieu NGUYEN HUU, who gave me the motivation to come to France and helped me with the application procedure of my master's program.

I would also like to thank all my friends, my colleagues, and the staff at G2Elab and GIPSA-lab for their friendship, useful discussions, encouraging supports, and help with administrative procedures and informatics service.

I also gratefully acknowledge the funding source from French Ministry for Higher Education and Research that made my thesis work possible.

My time at Grenoble was made memorable and enjoyable in large part due to the friends and groups that became a part of my life. I am grateful for time spent with labmates and friends, for memorable trips into the mountains, and for many other people and memories. Moreover, I would like to express my thanks to all my Vietnamese friends in France for their infinite friendship and assistances in numerous ways. My life in France could be hard without them. Thank you for everything. And I also thank my entire friends in Vietnam for their support, encouragement, and all warm welcome when I came back.

I cannot finish without revealing my thankfulness and gratefulness to all my families. My families (my parents, my little sister, my uncles and aunts) are my best back up team. Their encouragement makes me overcome all difficulties. I want to express my deepest gratitude to my beloved parents whose endless love, unconditional support, and guidance are with me in whatever I pursue. I also thank and appreciate my lovely little sister for her unconditional support and assistances. Thank you all from the bottom of my heart for everything. I love you all.

Finally, I would like to sincerely thank everything that brings me here, in France. It is an amazing, unforgettable, and valuable experience in my life.

Quang Linh LAM
Grenoble, France

Contents

Table of Acronyms	xxv
General introduction	1
1 Background	9
1.1 Introduction	9
1.2 Context of microgrids	9
1.2.1 Microgrids concept	9
1.2.2 Pico-, nano-, micro-, and minigrids	12
1.2.3 Microgrids operation and control	17
1.2.4 Energy storage in microgrids	21
1.2.5 Virtual synchronous generators	23
1.3 State-of-the-art on control strategies in microgrids	25
1.3.1 Grid-feeding control	27
1.3.2 Grid-forming control	27
1.4 State-of-the-art on classical and advanced control in microgrids	32
1.4.1 Classical approach with PI/PID control	32
1.4.2 Linear quadratic regulator	33
1.4.3 Sliding mode control	34
1.4.4 Model predictive control	35
1.4.5 Artificial-intelligence-based control	36
1.4.6 Adaptive control	39
1.4.7 Robust control	41
1.4.8 Comparative analysis of classical and advanced control techniques	44
1.5 Basics on \mathcal{H}_∞ control methodology	45

1.5.1	Singular values and \mathcal{H}_∞ norm	45
1.5.2	\mathcal{H}_∞ control approach	46
1.5.3	Robust stability and robust performance analysis	51
1.6	Case study presentation	55
1.7	Chapter conclusion	56
2	Robust control for primary frequency ancillary service in stand-alone microgrids	59
2.1	Introduction	59
2.2	Microgrid configuration	60
2.3	Proposed control methodology	61
2.4	Coordinated strategy in frequency control	62
2.5	Dynamic modeling of the microgrid	63
2.5.1	Diesel engine generator modeling	64
2.5.2	Microgrid modeling	66
2.5.3	Choice of energy storage technology	67
2.5.4	Energy storage system modeling	70
2.5.5	System modeling for \mathcal{H}_∞ control	79
2.6	Control design	80
2.6.1	Proposed cascaded two-level control structure	81
2.6.2	Classical PI-control-based low level	81
2.6.3	\mathcal{H}_∞ -control-based upper level	84
2.6.4	Systematic procedure for control design	89
2.6.5	Numerical simulation results	90
2.7	Robust performance analysis	95
2.7.1	Parametric uncertainties	96
2.7.2	Sensitivity analysis	97

2.7.3	Robustness analysis	100
2.8	Chapter conclusion	104
3	Voltage robust control in stand-alone microgrids	107
3.1	Introduction	107
3.2	Microgrid structure and dynamic specifications	109
3.2.1	System structure	109
3.2.2	Dynamic specifications for voltage control	109
3.3	Dynamic modeling of the microgrid	110
3.3.1	Topological modeling	110
3.3.2	Nonlinear averaged modeling	110
3.3.3	Equilibrium point computation	115
3.3.4	Linear averaged modeling	117
3.3.5	Per-unitized averaged modeling	119
3.3.6	System modeling for \mathcal{H}_∞ control	121
3.4	Open-loop system behavior	122
3.4.1	Without energy storage system	122
3.4.2	Whole system	128
3.5	Control design	134
3.5.1	Proposed cascaded two-level control structure	134
3.5.2	Current control level	135
3.5.3	\mathcal{H}_∞ control level	135
3.5.4	Numerical simulation results	145
3.6	Robust performance analysis	152
3.6.1	Parametric uncertainties	152
3.6.2	Sensitivity analysis	153
3.7	Chapter conclusion	164

4	Frequency robust control real-time validation using a rapid-prototyping test bench	165
4.1	Introduction	165
4.2	Implementation of a laboratory-scale prototype system	167
4.2.1	Description of the laboratory-scale prototype system	167
4.2.2	Correspondence with the physical elements	168
4.3	Frequency robust control real-time validation	173
4.3.1	Dynamic specifications	173
4.3.2	Equilibrium point computation	175
4.3.3	Control design	176
4.3.4	Experimental validation under small load step disturbances of $\pm 5\%$ of the load rated active power (± 150 W)	177
4.3.5	Experimental validation under more stressed conditions (large load active power step disturbances)	184
4.4	Chapter conclusion	191
	General conclusion and perspectives	193
	Résumé en français	197
	A Parameters of the studied microgrid for frequency and voltage control	203
	B Per-unit values for the studied microgrid	207
	C Park and inverse Park coordinates transformations	209
	D Parameters of the test bench for frequency control real-time validation	211
	E Some other experimental results for frequency robust control real-time validation	213
E.1	Experimental results under load step disturbances of $\pm 10\%$ of the load rated active power (± 300 W)	213

E.2 Experimental results under load step disturbances of $\pm 20\%$ of the load rated
active power (± 600 W) 215

Bibliography **234**

List of Figures

1.1	Sample smart grid [34].	10
1.2	Sample MG as a low voltage grid [2].	11
1.3	Sample MG as a low voltage feeder [2].	12
1.4	Sample MG as a low voltage house [2].	12
1.5	Dynamically decoupled and hierarchically interconnected structure of a novel electric power grid comprising AC and DC sub-grids [21].	14
1.6	Interoperability layers of the MG architecture model [132].	15
1.7	Physical structure of a smart electric power grid [132].	16
1.8	Machine-to-machine communication network architecture for the MG [132].	16
1.9	Hierarchical control structure of an MG [151].	19
1.10	Classification of power quality issues in MGs [157].	21
1.11	Utility applications of ESSs [193].	22
1.12	General structure and basic concept of a VSG [15].	24
1.13	Simplified MG structure with multiple VSG units [15], [3].	25
1.14	Classification of MG control strategies reported in the literature [189].	26
1.15	Classical control structure.	47
1.16	Classical control structure in the so-called P – K form.	47
1.17	General control configuration.	48
1.18	Control configuration in the so-called P – K form including weighting functions [180], [74].	50
1.19	Weighting function $W_{perf}(s)$ for the sensitivity function $S(s)$	50
1.20	Weighting function $W_u(s)$ for the complementary sensitivity function $KS(s)$	51
1.21	General control configuration of the perturbed system in the so-called N – Δ form.	54

1.22	Configurations for (a) robust performance analysis and (b) robust stability analysis.	55
1.23	Schematic diagram of the studied MG.	56
2.1	(a) Schematic diagram of the studied MG. (b) Simplified MG configuration for frequency stability analysis.	60
2.2	Proposed control methodology inspired from [173].	62
2.3	Performance specification on the MG frequency variation in response to a load step disturbance of $\pm 5\%$ of the load rated active power (± 60 kW) in the time domain.	63
2.4	(a) Classical speed control chain of a typical diesel engine generator [100]. (b) A simplified dynamic model inspired from [100].	64
2.5	Simplified dynamic model of the studied MG with the load self-regulation.	66
2.6	Ragone's plot: characteristics of energy storage devices [101].	67
2.7	Own frequency of energy storage devices.	68
2.8	Bode diagram of the system in (2.15) with only primary control ($K_p \neq 0$, $K_i = 0$), both primary and secondary control ($K_p \neq 0$, $K_i \neq 0$) without the dynamic part of the diesel generator ($T_{diesel} = 0$), both primary and secondary control with the dynamic part ($T_{diesel} \neq 0$).	69
2.9	Schematic diagram of the supercapacitor-based ESS.	71
2.10	Performance specification on the DC-bus voltage variation in response to a load step disturbance in the time domain.	71
2.11	Block diagram of the proposed global control structure.	81
2.12	(a) Block diagram for tracking the current reference variation ΔI_s^{ref} . (b) Block diagram for tracking the current reference variations ΔI_{rd}^{ref} and ΔI_{rq}^{ref}	82
2.13	Desired dynamic performance of the current control loops.	84
2.14	Control configuration in the so-called $\mathbf{P} - \mathbf{K}$ form, where \mathbf{P} denotes the plant together with the weighting functions and \mathbf{K} denotes the \mathcal{H}_∞ controller.	86
2.15	Translations of temporal norms into frequency-domain specifications.	87
2.16	Frequency-domain specifications on the supercapacitor output current reference variation ΔI_s^{ref} and the d -component of the inverter output current reference variation ΔI_{rd}^{ref}	88

2.17	Singular value plots of the sensitivity functions $S_1(s)$, $S_2(s)$; complementary sensitivity functions $KS_1(s)$, $KS_2(s)$; and corresponding templates.	90
2.18	(a) MG frequency time-domain response f_{grid} and (b) DC-bus voltage time-domain response V_{dc} under a small load step disturbance of + 5% of the load rated active power (+ 60 kW) with respect to the rated operating point.	91
2.19	Time-domain responses of (a) the supercapacitor output current I_s and (b) the d -component of the inverter output current I_{rd} under a small load step disturbance of + 5% of the load rated active power (+ 60 kW) with respect to the rated operating point.	92
2.20	Time-domain responses of the supercapacitor state of charge SoC_{sc} and voltage V_{sc} under a small load step disturbance of + 5% of the load rated active power (+ 60 kW) with respect to the rated operating point.	92
2.21	Active power variations of the sources and load under a small load step disturbance of + 5% of the load rated active power (+ 60 kW).	93
2.22	(a) MG frequency time-domain response f_{grid} and (b) DC-bus voltage time-domain response V_{dc} under a small load step disturbance of + 5% of the load rated active power (+ 60 kW) with respect to the rated operating point taking into account the secondary control of the diesel engine generator.	94
2.23	Time-domain responses of (a) the supercapacitor output current I_s and (b) the d -component of the inverter output current I_{rd} under a small load step disturbance of + 5% of the load rated active power (+ 60 kW) with respect to the rated operating point taking into account the secondary control of the diesel engine generator.	94
2.24	Time-domain responses of the supercapacitor state of charge SoC_{sc} and voltage V_{sc} under a small load step disturbance of + 5% of the load rated active power (+ 60 kW) with respect to the rated operating point taking into account the secondary control of the diesel engine generator.	95
2.25	Active power variations of the sources and load under a small load step disturbance of + 5% of the load rated active power (+ 60 kW) taking into account the secondary control of the diesel engine generator.	95
2.26	Schematic diagram of the supercapacitor.	96
2.27	Singular value plots of the sampled uncertain sensitivity functions $S_1(s)$, $S_2(s)$; complementary sensitivity functions $KS_1(s)$, $KS_2(s)$ obtained with 33.3% uncertainty in V_{sc_e} ; and corresponding templates.	97
2.28	(a) MG frequency time-domain response f_{grid} under a PV output active power step disturbance of - 60 kW taking into account the uncertainty in V_{sc_e} (or SoC_{sc_e}). (b) Temporal zoom in the time interval $t \in [9, 14]$ s.	98

2.29	(a) DC-bus voltage time-domain response V_{dc} under a PV output active power step disturbance of -60 kW taking into account the uncertainty in V_{sc_e} (or SoC_{sc_e}). (b) Temporal zoom in the time interval $t \in [9, 14]$ s.	98
2.30	(a) Time-domain response of the supercapacitor output current I_s under a PV output active power step disturbance of -60 kW taking into account the uncertainty in V_{sc_e} (or SoC_{sc_e}). (b) Temporal zoom in the time interval $t \in [9, 14]$ s.	99
2.31	(a) Time-domain response of the d -component of the inverter output current I_{rd} under a PV output active power step disturbance of -60 kW taking into account the uncertainty in V_{sc_e} (or SoC_{sc_e}). (b) Temporal zoom in the time interval $t \in [9, 14]$ s.	99
2.32	Configuration in the so-called $\mathbf{N} - \Delta$ form for robust performance analysis.	100
2.33	Robust performance μ -bounds plot for the uncertainty levels of 10%, 20%, 30%, 40%, 50%, 60%, and 69% in V_{sc_e}	101
2.34	Singular value plots of the sampled uncertain sensitivity functions $S_1(s)$, $S_2(s)$; complementary sensitivity functions $KS_1(s)$, $KS_2(s)$ obtained with 69% uncertainty in V_{sc_e} ; and corresponding templates.	102
2.35	(a) MG frequency time-domain response f_{grid} under small load step disturbances of $\pm 5\%$ of the load rated active power (± 60 kW) taking into account the uncertainty in V_{sc_e} (or SoC_{sc_e}). (b) Temporal zoom in the time interval $t \in [0, 5]$ s.	103
2.36	(a) DC-bus voltage time-domain response V_{dc} under small load step disturbances of $\pm 5\%$ of the load rated active power (± 60 kW) taking into account the uncertainty in V_{sc_e} (or SoC_{sc_e}). (b) Temporal zoom in the time interval $t \in [0, 5]$ s.	103
2.37	Time-domain responses of the supercapacitor output current I_s and the d -component of the inverter output current I_{rd} under small load step disturbances of $\pm 5\%$ of the load rated active power (± 60 kW) taking into account the uncertainty in V_{sc_e} (or SoC_{sc_e}).	104
3.1	Schematic diagram of the MG under consideration for voltage stability analysis.	108
3.2	Performance specification on the PCC line-to-line voltage magnitude variation in response to a load reactive power step disturbance in the time domain.	109
3.3	Values $\mathcal{Y}_{1,2} = \text{Im}(z_{1,2})/\text{Re}(z_{1,2}) $ of the left-half-plane complex conjugate zero pair $z_{1,2}$ of the open-loop sensitivity function $\Delta V_{PCCd}/(\Delta I_{loadd} - \Delta I_{PVd})$ or $\Delta V_{PCCq}/(\Delta I_{loadq} - \Delta I_{PVq})$	127

3.4	(a) Open-loop time-domain response of the PCC line-to-line voltage magnitude U_{PCC} under a small load step disturbance of + 5% of the load rated reactive power (+ 45 kVAr) with respect to the rated operating point of the studied MG without ESS. (b) Temporal zoom in the time interval $t \in [0.999, 1.01]$ s.	128
3.5	Values $\mathcal{Y}_{k,k+1} = \text{Im}(z_{k,k+1})/\text{Re}(z_{k,k+1}) $ of the left-half-plane complex conjugate zero pairs $z_{k,k+1}$ of the open-loop sensitivity function $\Delta V_{PCCd}/(\Delta I_{loadd} - \Delta I_{PVd})$ or $\Delta V_{PCCq}/(\Delta I_{loadq} - \Delta I_{PVq})$	131
3.6	Values $\mathcal{Y}_{k,k+1} = \text{Im}(z_{k,k+1})/\text{Re}(z_{k,k+1}) $ of the left-half-plane complex conjugate zero pairs $z_{k,k+1}$ of the open-loop sensitivity function $\Delta V_{PCCd}/(\Delta I_{loadq} - \Delta I_{PVq})$ or $\Delta V_{PCCq}/(\Delta I_{loadd} - \Delta I_{PVd})$	132
3.7	(a) Open-loop time-domain response of the PCC line-to-line voltage magnitude U_{PCC} under a small load step disturbance of + 5% of the load rated reactive power (+ 45 kVAr) with respect to the rated operating point of the studied whole MG. (b) Temporal zoom in the time interval $t \in [0.999, 1.01]$ s.	134
3.8	Block diagram of the proposed global control structure.	135
3.9	Control configuration in the so-called $\mathbf{P} - \mathbf{K}$ form, where \mathbf{P} denotes the plant together with the weighting functions and \mathbf{K} denotes the \mathcal{H}_∞ controller.	139
3.10	Representation of the dq -components of the PCC voltage V_{PCCd} and V_{PCCq}	140
3.11	Translations of temporal norms into frequency-domain specifications.	140
3.12	Frequency-domain specifications on the supercapacitor output current reference variation ΔI_s^{ref} and the dq -components of the inverter output current reference variation ΔI_{rd}^{ref} and ΔI_{rq}^{ref}	142
3.13	Singular value plots of the sensitivity functions $S_{11}(s)$, $S_{12}(s)$, $S_{21}(s)$, $S_{22}(s)$, $S_{31}(s)$, $S_{32}(s)$; complementary sensitivity functions $KS_{11}(s)$, $KS_{12}(s)$, $KS_{21}(s)$, $KS_{22}(s)$, $KS_{31}(s)$, $KS_{32}(s)$; and corresponding templates.	144
3.14	(a) Time-domain response of the PCC line-to-line voltage magnitude U_{PCC} under a small load step disturbance of + 5% of the load rated reactive power (+ 45 kVAr) with respect to the rated operating point. (b) Temporal zoom in the time interval $t \in [0.999, 1.01]$ s.	145
3.15	(a) Time-domain response of the d -component of the PCC voltage V_{PCCd} under a small load step disturbance of + 5% of the load rated reactive power (+ 45 kVAr) with respect to the rated operating point. (b) Temporal zoom in the time interval $t \in [0.999, 1.01]$ s.	146

3.16	(a) Time-domain response of the q -component of the PCC voltage V_{PCCq} under a small load step disturbance of + 5% of the load rated reactive power (+ 45 kVAr) with respect to the rated operating point. (b) Temporal zoom in the time interval $t \in [0.999, 1.01]$ s.	146
3.17	Time-domain responses of (a) the DC-bus voltage V_{dc} and (b) the supercapacitor output current I_s under a small load step disturbance of + 5% of the load rated reactive power (+ 45 kVAr) with respect to the rated operating point.	147
3.18	Time-domain responses of (a) the d -component I_{rd} and (b) the q -component I_{rq} of the inverter output current under a small load step disturbance of + 5% of the load rated reactive power (+ 45 kVAr) with respect to the rated operating point.	147
3.19	Time-domain responses of the supercapacitor state of charge SoC_{sc} and voltage V_{sc} under a small load step disturbance of + 5% of the load rated reactive power (+ 45 kVAr) with respect to the rated operating point.	148
3.20	(a) Active power variations of the sources and load under a small load step disturbance of + 5% of the load rated reactive power (+ 45 kVAr). (b) Temporal zoom in the time interval $t \in [0.999, 1.01]$ s.	148
3.21	(a) Reactive power variations of the sources and load under a small load step disturbance of + 5% of the load rated reactive power (+ 45 kVAr). (b) Temporal zoom in the time interval $t \in [0.999, 1.01]$ s.	149
3.22	(a) Time-domain response of the PCC line-to-line voltage magnitude U_{PCC} under a small load step disturbance of + 5% of the load rated reactive power (+ 45 kVAr) with respect to the rated operating point. (b) Temporal zoom in the time interval $t \in [0.999, 1.01]$ s.	150
3.23	(a) Time-domain response of the DC-bus voltage V_{dc} under a small load step disturbance of + 5% of the load rated reactive power (+ 45 kVAr) with respect to the rated operating point. (b) Temporal zoom in the time interval $t \in [0.9, 2]$ s.	150
3.24	(a) Time-domain response of the supercapacitor output current I_s under a small load step disturbance of + 5% of the load rated reactive power (+ 45 kVAr) with respect to the rated operating point. (b) Temporal zoom in the time interval $t \in [0.9, 2]$ s.	151
3.25	(a) Time-domain response of the d -component of the inverter output current I_{rd} under a small load step disturbance of + 5% of the load rated reactive power (+ 45 kVAr) with respect to the rated operating point. (b) Temporal zoom in the time interval $t \in [0.9, 2]$ s.	151

- 3.26 (a) Time-domain response of the q -component of the inverter output current I_{rq} under a small load step disturbance of + 5% of the load rated reactive power (+ 45 kVAr) with respect to the rated operating point. (b) Temporal zoom in the time interval $t \in [0.9, 2]$ s. 152
- 3.27 Singular value plots of the sampled uncertain sensitivity functions $S_{11}(s)$, $S_{12}(s)$, $S_{21}(s)$, $S_{22}(s)$, $S_{31}(s)$, $S_{32}(s)$; complementary sensitivity functions $KS_{11}(s)$, $KS_{12}(s)$, $KS_{21}(s)$, $KS_{22}(s)$, $KS_{31}(s)$, $KS_{32}(s)$ obtained with 33.3% uncertainty in V_{sc_e} and $l \in [1, 10]$ km; and corresponding templates. . . 153
- 3.28 (a) Time-domain response of the PCC line-to-line voltage magnitude U_{PCC} under small load step disturbances of $\pm 5\%$ of the load rated reactive power (± 45 kVAr) taking into account the uncertainty in V_{sc_e} (or SoC_{sc_e}). (b) Temporal zoom in the time interval $t \in [0.999, 1.01]$ s. 154
- 3.29 (a) Time-domain response of the d -component of the PCC voltage V_{PCCd} under small load step disturbances of $\pm 5\%$ of the load rated reactive power (± 45 kVAr) taking into account the uncertainty in V_{sc_e} (or SoC_{sc_e}). (b) Temporal zoom in the time interval $t \in [0.999, 1.01]$ s. 155
- 3.30 (a) Time-domain response of the q -component of the PCC voltage V_{PCCq} under small load step disturbances of $\pm 5\%$ of the load rated reactive power (± 45 kVAr) taking into account the uncertainty in V_{sc_e} (or SoC_{sc_e}). (b) Temporal zoom in the time interval $t \in [0.999, 1.01]$ s. 155
- 3.31 (a) Time-domain response of the DC-bus voltage V_{dc} under small load step disturbances of $\pm 5\%$ of the load rated reactive power (± 45 kVAr) taking into account the uncertainty in V_{sc_e} (or SoC_{sc_e}). (b) Temporal zoom in the time interval $t \in [0.9, 2]$ s. 156
- 3.32 (a) Time-domain response of the supercapacitor output current I_s under small load step disturbances of $\pm 5\%$ of the load rated reactive power (± 45 kVAr) taking into account the uncertainty in V_{sc_e} (or SoC_{sc_e}). (b) Temporal zoom in the time interval $t \in [0.9, 2]$ s. 156
- 3.33 (a) Time-domain response of the d -component of the inverter output current I_{rd} under small load step disturbances of $\pm 5\%$ of the load rated reactive power (± 45 kVAr) taking into account the uncertainty in V_{sc_e} (or SoC_{sc_e}). (b) Temporal zoom in the time interval $t \in [0.965, 1.35]$ s. 157
- 3.34 (a) Time-domain response of the q -component of the inverter output current I_{rq} under small load step disturbances of $\pm 5\%$ of the load rated reactive power (± 45 kVAr) taking into account the uncertainty in V_{sc_e} (or SoC_{sc_e}). (b) Temporal zoom in the time interval $t \in [0.965, 1.35]$ s. 157

- 3.35 (a) Time-domain response of the PCC line-to-line voltage magnitude U_{PCC} under small load step disturbances of $\pm 5\%$ of the load rated reactive power (± 45 kVAr) taking into account the uncertainty in l . (b) Temporal zoom in the time interval $t \in [0.999, 1.01]$ s. 158
- 3.36 (a) Time-domain response of the d -component of the PCC voltage V_{PCCd} under small load step disturbances of $\pm 5\%$ of the load rated reactive power (± 45 kVAr) taking into account the uncertainty in l . (b) Temporal zoom in the time interval $t \in [0.999, 1.01]$ s. 158
- 3.37 (a) Time-domain response of the q -component of the PCC voltage V_{PCCq} under small load step disturbances of $\pm 5\%$ of the load rated reactive power (± 45 kVAr) taking into account the uncertainty in l . (b) Temporal zoom in the time interval $t \in [0.999, 1.01]$ s. 159
- 3.38 (a) Time-domain response of the DC-bus voltage V_{dc} under small load step disturbances of $\pm 5\%$ of the load rated reactive power (± 45 kVAr) taking into account the uncertainty in l . (b) Temporal zoom in the time interval $t \in [0.9, 2]$ s. 159
- 3.39 (a) Time-domain response of the supercapacitor output current I_s under small load step disturbances of $\pm 5\%$ of the load rated reactive power (± 45 kVAr) taking into account the uncertainty in l . (b) Temporal zoom in the time interval $t \in [0.9, 2]$ s. 160
- 3.40 (a) Time-domain response of the d -component of the inverter output current I_{rd} under small load step disturbances of $\pm 5\%$ of the load rated reactive power (± 45 kVAr) taking into account the uncertainty in l . (b) Temporal zoom in the time interval $t \in [0.95, 1.5]$ s. 160
- 3.41 (a) Time-domain response of the q -component of the inverter output current I_{rq} under small load step disturbances of $\pm 5\%$ of the load rated reactive power (± 45 kVAr) taking into account the uncertainty in l . (b) Temporal zoom in the time interval $t \in [0.95, 1.5]$ s. 161
- 3.42 Time-domain responses of the supercapacitor state of charge SoC_{sc} and voltage V_{sc} under small load step disturbances of $\pm 5\%$ of the load rated reactive power (± 45 kVAr) taking into account the uncertainty in l 161
- 3.43 (a) Active power variation of the ESS step-up transformer output ΔP_t under small load step disturbances of $\pm 5\%$ of the load rated reactive power (± 45 kVAr) taking into account the uncertainty in l . (b) Temporal zoom in the time interval $t \in [0.965, 1.35]$ s. 162
- 3.44 (a) Active power variation of the diesel engine generator system output $\Delta P_g - (U_{PCC}^2 - U_{PCC_e}^2) / R_{l_p}$ under small load step disturbances of $\pm 5\%$ of the load rated reactive power (± 45 kVAr) taking into account the uncertainty in l . (b) Temporal zoom in the time interval $t \in [0.965, 1.35]$ s. 162

3.45	(a) Reactive power variation of the ESS step-up transformer output ΔQ_t under small load step disturbances of $\pm 5\%$ of the load rated reactive power (± 45 kVAr) taking into account the uncertainty in l . (b) Temporal zoom in the time interval $t \in [0.965, 1.35]$ s.	163
3.46	(a) Reactive power variation of the diesel engine generator system output $\Delta Q_g + (U_{PCC}^2 - U_{PCC_e}^2) C_l \omega_{grid}$ under small load step disturbances of $\pm 5\%$ of the load rated reactive power (± 45 kVAr) taking into account the uncertainty in l . (b) Temporal zoom in the time interval $t \in [0.965, 1.35]$ s.	163
4.1	Schematic diagram of the test bench for the stand-alone MG application based on the PHIL configuration.	168
4.2	Correspondence with the physical elements of the real supercapacitor-based ESS environment.	169
4.3	Structure of the RT-LAB [®] real-time digital simulator.	170
4.4	Correspondence with the physical elements for the emulation of the diesel-PV-load grid.	172
4.5	Performance specification on the MG frequency variation in response to a load step disturbance of $\pm 5\%$ of the load rated active power (± 150 W) in the time domain.	174
4.6	Performance specification on the DC-bus voltage variation in response to a load step disturbance in the time domain.	174
4.7	(a) MG frequency time-domain response f_{grid} under small load step disturbances of $\pm 5\%$ of the load rated active power (± 150 W) with respect to the rated operating point. (b) Temporal zoom in the time interval $t \in [62.25, 63.75]$ s.	178
4.8	(a) DC-bus voltage time-domain response V_{dc} under small load step disturbances of $\pm 5\%$ of the load rated active power (± 150 W) with respect to the rated operating point. (b) Temporal zoom in the time interval $t \in [62.25, 63.75]$ s.	178
4.9	(a) Experimental result for the time-domain response of the supercapacitor output current I_s under small load step disturbances of $\pm 5\%$ of the load rated active power (± 150 W) with respect to the rated operating point. (b) Temporal zoom in the time interval $t \in [62.25, 63.75]$ s.	179
4.10	(a) Experimental result for the time-domain response of the d -component of the inverter output current I_{rd} under small load step disturbances of $\pm 5\%$ of the load rated active power (± 150 W) with respect to the rated operating point. (b) Temporal zoom in the time interval $t \in [62, 65]$ s.	180

4.11	Experimental result for the time-domain response of the q -component of the inverter output current I_{rq} under small load step disturbances of $\pm 5\%$ of the load rated active power (± 150 W) with respect to the rated operating point.	180
4.12	Experimental results for the time-domain responses of the supercapacitor state of charge SoC_{sc} and voltage V_{sc} under small load step disturbances of $\pm 5\%$ of the load rated active power (± 150 W) with respect to the rated operating point.	181
4.13	Experimental results for the active power variations of the sources and load, (a) without ESS and (b) with ESS, under small load step disturbances of $\pm 5\%$ of the load rated active power (± 150 W) with respect to the rated operating point. (c) Temporal zoom for (b) in the time interval $t \in [62.25, 63.75]$ s. . . .	182
4.14	Experimental result for the time-domain response of the chopper duty cycle α_c under small load step disturbances of $\pm 5\%$ of the load rated active power (± 150 W) with respect to the rated operating point.	183
4.15	Experimental results for the time-domain responses of (a) the d -component β_d and (b) the q -component β_q of the inverter switching function under small load step disturbances of $\pm 5\%$ of the load rated active power (± 150 W) with respect to the rated operating point.	183
4.16	(a) Experimental result for the MG frequency time-domain response f_{grid} under load step disturbances of $\pm 10\%$ of the load rated active power (± 300 W) with respect to the rated operating point. (b) Temporal zoom in the time interval $t \in [65.4, 66.9]$ s.	186
4.17	(a) Experimental result for the DC-bus voltage time-domain response V_{dc} under load step disturbances of $\pm 10\%$ of the load rated active power (± 300 W) with respect to the rated operating point. (b) Temporal zoom in the time interval $t \in [65.4, 66.9]$ s.	186
4.18	(a) Experimental result for the MG frequency time-domain response f_{grid} under load step disturbances of $\pm 20\%$ of the load rated active power (± 600 W) with respect to the rated operating point. (b) Temporal zoom in the time interval $t \in [63.3, 64.8]$ s.	187
4.19	(a) Experimental result for the DC-bus voltage time-domain response V_{dc} under load step disturbances of $\pm 20\%$ of the load rated active power (± 600 W) with respect to the rated operating point. (b) Temporal zoom in the time interval $t \in [63.3, 64.8]$ s.	187
4.20	(a) Experimental result for the MG frequency time-domain response f_{grid} under load step disturbances of $\pm 30\%$ of the load rated active power (± 900 W) with respect to the rated operating point. (b) Temporal zoom in the time interval $t \in [63.4, 64.9]$ s.	188

4.21	(a) Experimental result for the DC-bus voltage time-domain response V_{dc} under load step disturbances of $\pm 30\%$ of the load rated active power (± 900 W) with respect to the rated operating point. (b) Temporal zoom in the time interval $t \in [63.4, 64.9]$ s.	188
4.22	(a) Experimental result for the time-domain response of the supercapacitor output current I_s under load step disturbances of $\pm 30\%$ of the load rated active power (± 900 W) with respect to the rated operating point. (b) Temporal zoom in the time interval $t \in [63.4, 64.9]$ s.	189
4.23	(a) Experimental result for the time-domain response of the d -component of the inverter output current I_{rd} under load step disturbances of $\pm 30\%$ of the load rated active power (± 900 W) with respect to the rated operating point. (b) Temporal zoom in the time interval $t \in [63, 66]$ s.	189
4.24	Experimental results for the time-domain responses of the supercapacitor state of charge SoC_{sc} and voltage V_{sc} under load step disturbances of $\pm 30\%$ of the load rated active power (± 900 W) with respect to the rated operating point.	190
4.25	(a) Experimental results for the active power variations of the sources and load under load step disturbances of $\pm 30\%$ of the load rated active power (± 900 W) with respect to the rated operating point. (b) Temporal zoom in the time interval $t \in [63.4, 64.9]$ s.	190
4.26	Block diagram of the novel global control structure for MG frequency and PCC voltage regulation.	195
E.1	(a) Experimental result for the time-domain response of the supercapacitor output current I_s under load step disturbances of $\pm 10\%$ of the load rated active power (± 300 W) with respect to the rated operating point. (b) Temporal zoom in the time interval $t \in [65.4, 66.9]$ s.	213
E.2	(a) Experimental result for the time-domain response of the d -component of the inverter output current I_{rd} under load step disturbances of $\pm 10\%$ of the load rated active power (± 300 W) with respect to the rated operating point. (b) Temporal zoom in the time interval $t \in [65, 68]$ s.	214
E.3	Experimental results for the time-domain responses of the supercapacitor state of charge SoC_{sc} and voltage V_{sc} under load step disturbances of $\pm 10\%$ of the load rated active power (± 300 W) with respect to the rated operating point.	214
E.4	(a) Experimental results for the active power variations of the sources and load under load step disturbances of $\pm 10\%$ of the load rated active power (± 300 W) with respect to the rated operating point. (b) Temporal zoom in the time interval $t \in [65.4, 66.9]$ s.	215

E.5	(a) Experimental result for the time-domain response of the supercapacitor output current I_s under load step disturbances of $\pm 20\%$ of the load rated active power (± 600 W) with respect to the rated operating point. (b) Temporal zoom in the time interval $t \in [63.3, 64.8]$ s.	215
E.6	(a) Experimental result for the time-domain response of the d -component of the inverter output current I_{rd} under load step disturbances of $\pm 20\%$ of the load rated active power (± 600 W) with respect to the rated operating point. (b) Temporal zoom in the time interval $t \in [63, 66]$ s.	216
E.7	Experimental results for the time-domain responses of the supercapacitor state of charge SoC_{sc} and voltage V_{sc} under load step disturbances of $\pm 20\%$ of the load rated active power (± 600 W) with respect to the rated operating point.	216
E.8	(a) Experimental results for the active power variations of the sources and load under load step disturbances of $\pm 20\%$ of the load rated active power (± 600 W) with respect to the rated operating point. (b) Temporal zoom in the time interval $t \in [63.3, 64.8]$ s.	217

List of Tables

1.1	Services at each level [132].	17
2.1	Topological model of the supercapacitor-based ESS.	73
2.2	Nonlinear averaged model of the supercapacitor-based ESS.	74
2.3	Steady-state real-unit values of the supercapacitor-based ESS.	76
3.1	Topological model of the studied MG.	111
3.2	Nonlinear averaged model of the studied MG.	112
3.3	Steady-state real-unit values of the studied MG.	117
3.4	Steady-state real-unit values of the studied MG without ESS.	123
3.5	Zeros of the open-loop sensitivity functions of the per-unitized linear system without ESS.	125
3.6	Relative deviations of parameters of the studied MG without ESS from their rated values.	127
3.7	Zeros of the open-loop sensitivity functions of the per-unitized linear whole system.	130
3.8	Relative deviations of parameters of the studied whole MG from their rated values.	133
3.9	Zeros of the open-loop transfer functions of the per-unitized linear system (3.114).137	
4.1	Steady-state real-unit values of the supercapacitor-based ESS.	176
4.2	Experimental results performed with load step disturbances from $\pm 5\%$ to $\pm 30\%$ of the load rated active power (from ± 150 W to ± 900 W), where σ means the overshoot and ε stands for the steady-state error.	185
A.1	Parameters of the studied MG for frequency control.	203
A.2	Parameters of the supercapacitor-based ESS for frequency and voltage control.	204
A.3	Parameters of the studied MG for voltage control.	205

A.4	Parameters of the diesel engine generator system for voltage control.	205
A.5	Parameters of the ESS step-up transformer for voltage control.	206
B.1	Per-unit values for the studied MG.	207
D.1	Parameters of the test bench for frequency control real-time validation. . . .	211
D.2	Parameters of the real supercapacitor-based ESS for frequency control real-time validation.	212

Table of Acronyms

MG	Microgrid
RES	Renewable Energy Source
DER	Distributed Energy Resource
ESS	Energy Storage System
PV	Photovoltaic
AC	Alternating Current
DC	Direct Current
LPV	Linear Parameter Varying
MIMO	Multiple Input Multiple Output
VSG	Virtual Synchronous Generator
PI/PID	Proportional Integral/Proportional Integral Derivative
PCC	Point of Common Coupling
PHIL/HIL	Power Hardware-In-the-Loop/Hardware-In-the-Loop
DG	Distributed Generation
SoC	State of Charge
LMI	Linear Matrix Inequalities
SISO	Single Input Single Output
PWM	Pulse-Width Modulation

General introduction

The architecture of electric power systems and their energy or power management are designed and adapted in realistic conditions to optimally provide electric power to consumers in all modes of production and consumption. Originally designed to supply electricity to consumers from nuclear, thermal, or hydraulic power plants, the architecture of classical electric power systems will undergo major changes in the future, including the arrival of numerous economic actors and low-power generation units (co-generation units, generators based on renewable or non-conventional energy sources) not interfaced with a supervisory position, leading to profound changes in the management of the current electric power systems including technical, environmental, and financial variables. An evolution towards new architectures well adapted to these recent modes of dispersed production has then to be imagined for future times. The definition of MGs, such as those already present in islands or isolated areas, could be a response to this development [105], [71].

MGs have two essential intrinsic characteristics which make them a major interest for the development of the electric power systems of the future:

- The proximity between local electricity production and different consumers leads to an immediate minimization of transportation losses;
- The distinctive autonomous operational capability of MGs has brought in higher reliability measures in supplying power demands when the utility grid is not available.

The future power grids will thus be multi-converter and multi-source systems, particularly with the massive insertion of RESs and storage devices interfaced with power-electronic converters, and the current trend favoring electricity as energy vector. This concerns especially MGs, building or eco-district networks, and future smart grids (at distribution level and even at transportation level). Electric power systems, integrating MGs, must therefore be partially or completely re-designed in order to integrate these new intermittent sources that could negatively affect quality of power supplied due to their very low short-circuit power. Moreover, the development of power-electronic interfaces can potentially induce unstable operation due to dynamic and harmonic interactions generated by the converters. Uncertainties associated with weather conditions or parametric sizing play also a major role in the lack of MGs reliability, which induces oversizing of different components within the MGs such as storage devices.

Research problems associated with MGs concern consequently the development of optimal control strategies allowing maximizing power quality, securing supply, managing intermittence and its impact on the system by using for instance storage devices, maximizing efficiency, performance, reliability, and costs associated with the system. The main difficulties result from the necessity to understand interactions and couplings between components within these systems, and then establish static, dynamic, and harmonic models that allow taking into

account the influence of weather conditions or load control strategies. In autonomous MGs, the stability and control issues are among the main challenges due to low inertia, uncertainties, and intermittent nature of DERs [151]. Maintaining frequency and voltage deviations within their predefined range is still critical in autonomous operation mode. High-frequency ESSs – *e.g.*, lithium-ion batteries, flywheels, or supercapacitors – have thus become necessary, leading to new grid configurations, for which more complex advanced control structures are needed for providing the MGs with desirable performance specifications in a wide range of operating conditions despite multiple constraints such as unexpected disturbances and model uncertainties. This kind of problem leads of course to some questions as follows:

- Therefore, which energy storage technology is suitable for frequency and voltage stability in a stand-alone MG taking into account the cut-off frequency of each storage technology (*i.e.*, trade-off between its available energy and power), its cost and lifespan, as well as the global cost of ownership ?
- Which advanced control technique is appropriate to handle multiple requirements in a systematic manner such as to guarantee stability and overall robust performance ?
- How to cast the specific engineering demands of MG operation into the control formalism ? More particularly, how to define the optimal specifications on grid performances in order to optimize the behavior of MGs ?
- How to take into account the impact of unexpected disturbances and model uncertainties in the controller synthesis ?

Hence, the objective of this thesis is to propose some solutions to these problems and particularly, define a systematic robust control design procedure for frequency and voltage stability in stand-alone MGs with a high PV penetration rate by making use of energy storage devices. It would also be important to validate this control approach with the help of an experimental bench.

This Ph.D. project, a joint work, received the financial support from the French Ministry for Higher Education and Research and was prepared within the Grenoble Electrical Engineering laboratory (G2Elab) and the Grenoble Images Speech Signal and Control Laboratory (GIPSA-lab), Grenoble Institute of Technology (Grenoble INP).

Some studies on robust control for various systems have already been conducted at the G2Elab and GIPSA-lab.

In the Ph.D. thesis of Sautreuil [173], a new methodology for the equipments design has been proposed, using robustness as an indicator of their “integration capability” in the system. The emphasis is placed on how a robust dynamic control can solve the subsystem integration problem at a minimum weight. This method is then applied to three AC/DC conversion structures for the generation system in future aircrafts (an auto transformer rectifier unit, a 6-phase diode rectifier unit, and a full-wave controlled rectifier), where the author establishes the links between standards, robustness, and mass.

Hernández-Torres has presented in his Ph.D. thesis [74] the design of several multi-variable robust control strategies for a hybrid power generator comprising a fuel cell and an auxiliary energy storage source. Different strategies are presented to control the hybrid boost power converter configuration for DC voltage applications. This control methodology is also adopted to AC islanded applications considering the additional control of a voltage-source inverter. Robustness analysis to parametric uncertainties by μ -analysis is also studied. In addition, for the air supply subsystem an LPV control approach based on gain-scheduling has been proposed. The LPV control is also considered to handle some given system uncertainties.

In the Ph.D. thesis of Mongkoltanatas [142], the use of energy storage to maintain the frequency stability in isolated MGs with high penetration rate of renewables is studied. The author has focused on appropriate sizing of energy storage and a comparison of different strategies for the primary frequency control participation of storage in isolated MGs with high PV penetration rate. An \mathcal{H}_∞ controller is also designed for the primary frequency control participation of the ESS.

Nwesaty has presented in his Ph.D. thesis [150] an LPV/ \mathcal{H}_∞ control design of on-board energy management systems for electric vehicles. A generic and not load-cycle-dependent power sharing strategy among three different kinds of current-controlled and parallel-operated sources – fuel cell, battery, and supercapacitor – based on a MIMO LPV/ \mathcal{H}_∞ controller is proposed with respect to source frequency characteristics. By means of a genetic algorithm whose optimization criterion expresses the frequency separation requirements, the parameters of weighting functions can be obtained. Moreover, a reduced-order LPV/ \mathcal{H}_∞ controller is also computed to deal with an embedded implementation with limited computational burden.

This work is then consistent with these previous Ph.D. theses, but focusing on voltage and primary frequency ancillary services and a real-time validation to prove the interest of such an advanced energy management system.

Outline of the thesis

This manuscript is organized in four chapters as follows.

Following this introduction, the first chapter, denoted “*Background*”, is devoted to introduce the topic of MGs operation and control. More specifically, an account of research in the context of MGs, including MGs concept, classification of MGs, MGs operation and control, energy storage in MGs, and applications of VSGs for MGs, is first provided. Then, an identification and a classification of most widely used control strategies in MGs, namely grid-forming, grid-feeding/following, and grid-supporting ones, are presented. Next, a state-of-the-art on classical and advanced control techniques applied to MGs, such as PI/PID control, linear quadratic regulator, sliding mode control, model predictive control, artificial intelligence-based control, adaptive control, and robust control, together with a comparative analysis amongst these control techniques, are introduced. Robust control, more precisely \mathcal{H}_∞ control, which is demonstrated to be more advantageous than other control techniques,

is utilized for frequency and voltage stability studies in our case study – a diesel-PV-storage hybrid power generation system operating in stand-alone mode – in the next chapters. Finally, some basics on \mathcal{H}_∞ control theory, as well as the methods available for control design and robustness analysis, are detailed.

The second chapter, entitled **“Robust control for primary frequency ancillary service in stand-alone microgrids”**, first presents frequency-control-oriented modeling and then proposes a systematic design of a multi-variable robust control structure for frequency stability in a diesel-PV-storage hybrid power generation system operating in stand-alone mode. The proposed control structure relies on a two-level architecture: classical PI-based current tracking controllers are placed on the low control level and receive references from an \mathcal{H}_∞ -control-based upper level. A comprehensive methodology that casts the specific engineering demands of MG operation into \mathcal{H}_∞ control formalism is detailed. It is also shown how closed-loop dynamic performance requirements must at their turn be taken into account in the initial MG setup and sizing, namely in appropriately choosing and rating the ESS. Next, a robust performance analysis of the synthesized \mathcal{H}_∞ controller in the presence of various load disturbances, PV output active power variations, and model uncertainties is carried out in order to determine the maximum parameter variation range for which the imposed closed-loop performances are respected for the considered operating point. Numerical simulations performed with MATLAB[®]/Simulink[®] show the effectiveness of the proposed frequency robust control strategy on a MVA-rated MG.

The third chapter, labelled **“Voltage robust control in stand-alone microgrids”**, first presents voltage-control-oriented modeling for the studied diesel-PV-supercapacitor hybrid power generation system operating in stand-alone mode. Next, the influence of system parameters on the dynamic behavior of open-loop system measured outputs is studied by means of an “analysis-of-zeros” method based on Monte Carlo simulation. We then focus on computing an \mathcal{H}_∞ -based multi-variable voltage controller so as to robustly force the voltage magnitude of the PCC to satisfy the required dynamic specifications. The same idea of cascaded two-level control structure – where this controller is placed on an upper control level and provides the references to current controllers placed on a lower level – is also adopted. Effectiveness of the proposed voltage robust control strategy and the “analysis-of-zeros” method is validated *via* MATLAB[®]/Simulink[®] closed-loop time-domain simulations. Finally, a sensitivity analysis of robust performance of the synthesized \mathcal{H}_∞ controller in the presence of various load disturbances and model uncertainties is studied based on MATLAB[®]/Simulink[®] time-domain simulations.

In the fourth chapter, named **“Frequency robust control real-time validation using a rapid-prototyping test bench”**, a rapid-prototyping test bench composed of a real supercapacitor-based ESS and an emulated diesel-PV-load grid, is implemented for the experimental validation of the proposed frequency robust control strategy in stand-alone MGs under realistic operating conditions. The tests are executed on real-time digital simulators, namely RT-LAB[®] and dSPACE[®]. We first set up a PHIL configuration in which the constitutive elements of the software and material architectures of the test bench, as well as the control architecture, are arranged and implemented. Next, for the system under test,

some preliminary steps needed for experimental validation, *e.g.*, definition of dynamic specifications, equilibrium point computation, control design, are realized. Finally, a series of experiments under various test scenarios are performed to show the validity and effectiveness of the proposed frequency robust control approach.

The manuscript ends with a general conclusion gathering the most pertinent results, then outlining some future research work.

Contribution of the thesis

This thesis provides an effective application of multi-variable robust control for a diesel-PV-storage hybrid power generation system operating in stand-alone mode or any remote MGs. The methodology involved in the control strategy aims to provide a systematic approach, where control design is easy to conduct. An emphasis is put on \mathcal{H}_∞ control. More precisely, the main contributions are as follows.

Robust control for primary frequency ancillary service

- We first present frequency-control-oriented modeling and then propose a systematic design of a cascaded two-level robust control structure for frequency stability in a diesel-PV-storage hybrid power generation system operating in stand-alone mode;
- We develop a comprehensive methodology in which the specific engineering demands of MG operation are cast into \mathcal{H}_∞ control formalism;
- We perform a robust performance analysis of the synthesized \mathcal{H}_∞ controller in the presence of various disturbances and model uncertainties;
- We present an experimental validation of the proposed frequency robust control strategy in stand-alone MGs on a rapid-prototyping PHIL test bench.

Voltage robust control

- We propose voltage-control-oriented modeling for a diesel-PV-supercapacitor hybrid power generation system operating in stand-alone mode;
- We propose an “analysis-of-zeros” method based on Monte Carlo simulation for the open-loop system;
- We develop a hierarchical two-level robust control strategy for voltage stability in stand-alone MGs to satisfy the required dynamic performance specifications;
- We perform a sensitivity analysis of robust performance of the synthesized \mathcal{H}_∞ controller in the presence of various disturbances and model uncertainties.

Methodology

- We develop a complete co-design method for ESSs;
- We develop a robust control approach on complex MGs.

List of publications during the thesis

The following is a list of publications that have been written during the development of this thesis. Some other still unpublished results proposed and described in this manuscript will be considered for future submission to peer-reviewed journals and conferences.

International journal papers

- Q. L. Lam, A. I. Bratcu, C. Boudinet, M. Thomas, A. Labonne, and D. Riu, “Primary frequency \mathcal{H}_∞ control in stand-alone microgrids with storage units : a robustness analysis confirmed by real-time experiments” (submitted to *Control Eng. Pract.*).
- Q. L. Lam, A. I. Bratcu, C. Boudinet, M. Thomas, A. Labonne, and D. Riu, “Power hardware-in-the-loop validation for frequency robust control in stand-alone microgrids with storage units” (in preparation for submission to *IEEE Trans. Sustain. Energy*).

International conference papers with proceedings

- Q. L. Lam, A. I. Bratcu, and D. Riu, “Voltage regulation in stand-alone microgrids with storage units : a multi-variable \mathcal{H}_∞ control approach,” In *CIREN Workshop*, Jun. 2018 (accepted).
- Q. L. Lam, A. I. Bratcu, and D. Riu, “Robustness analysis of primary frequency \mathcal{H}_∞ control in stand-alone microgrids with storage units,” In *Proc. IFAC Workshop Control Transmiss. Distrib. Smart Grids (CTDSG)*, pp. 123–128, Oct. 2016.
- Q. L. Lam, A. I. Bratcu, and D. Riu, “Systematic multi-variable \mathcal{H}_∞ control design for primary frequency regulation in stand-alone microgrids with high penetration of renewable energy sources,” In *Proc. Europ. Control Conf. (ECC)*, pp. 1794–1799, Jun. 2016.
- Q. L. Lam, A. I. Bratcu, D. Riu, and J. Mongkoltanatas, “Multi-variable \mathcal{H}_∞ robust control applied to primary frequency regulation in microgrids with large integration of photovoltaic energy source,” In *Proc. IEEE Int. Conf. Ind. Technol. (ICIT)*, pp. 2921–2928, Mar. 2015.

National conference papers with proceedings

- Q. L. Lam, A. I. Bratcu, and D. Riu, “[Frequency robust control in stand-alone microgrids with PV sources : design and sensitivity analysis](#),” In *Proc. Sympo. Génie Elect. (SGE)*, Jun. 2016.

Talks

- Q. L. Lam, A. I. Bratcu, and D. Riu, “[Robust primary frequency control in stand-alone microgrids with high penetration of renewable energy : synthesis and robustness analysis](#),” In *MOSAR – GdR MACS Workgroup Meeting*, Mar. 2016, Nantes.

Background

1.1 Introduction

In this chapter, a background to the topic of MGs operation and control is presented, together with some fundamentals of robust control theory, which are needed for our case study. More specifically, Section 1.2 is devoted to the context of MGs. In Section 1.3, a state-of-the-art on control strategies in MGs is introduced. The next section gives a state-of-the-art on classical and advanced control techniques in MGs. Basics on \mathcal{H}_∞ control methodology are provided in Section 1.5. The case study taken into account all along the manuscript is presented in Section 1.6. Some concluding remarks are drawn in Section 1.7.

1.2 Context of microgrids

This section provides an account of research in areas related to MGs, including MGs concept, classification of MGs, MGs operation and control, energy storage in MGs, and applications of VSGs for MGs.

1.2.1 Microgrids concept

Modern society depends critically on an uninterrupted and reliable supply of electricity. Countries without adequate reserves of fossil fuels are facing growing concerns for primary energy availability. Moreover, security, reliability, and quality of supply are increasingly being threatened due to the aging infrastructure of current electricity transmission and distribution networks. Hence, it becomes mandatory to re-design electricity grids taking into account the new roles and challenges. Considerable investment will be required to develop and renew these infrastructures, while the most efficient way to achieve this is by incorporating innovative solutions, technologies, and grid architectures [2], [34]. The evolution of electricity grids can be referred to through notion of **smart grids** that can intelligently integrate the actions of all users connected to them – generators, consumers and those that suppose both roles (*i.e.*, prosumers) – in order to efficiently deliver sustainable, economic, and secure electricity supplies [2], [34]. A smart grid integrates innovative products and services together with self-monitoring, pervasive control, two-way communication, and self-healing technologies [79],

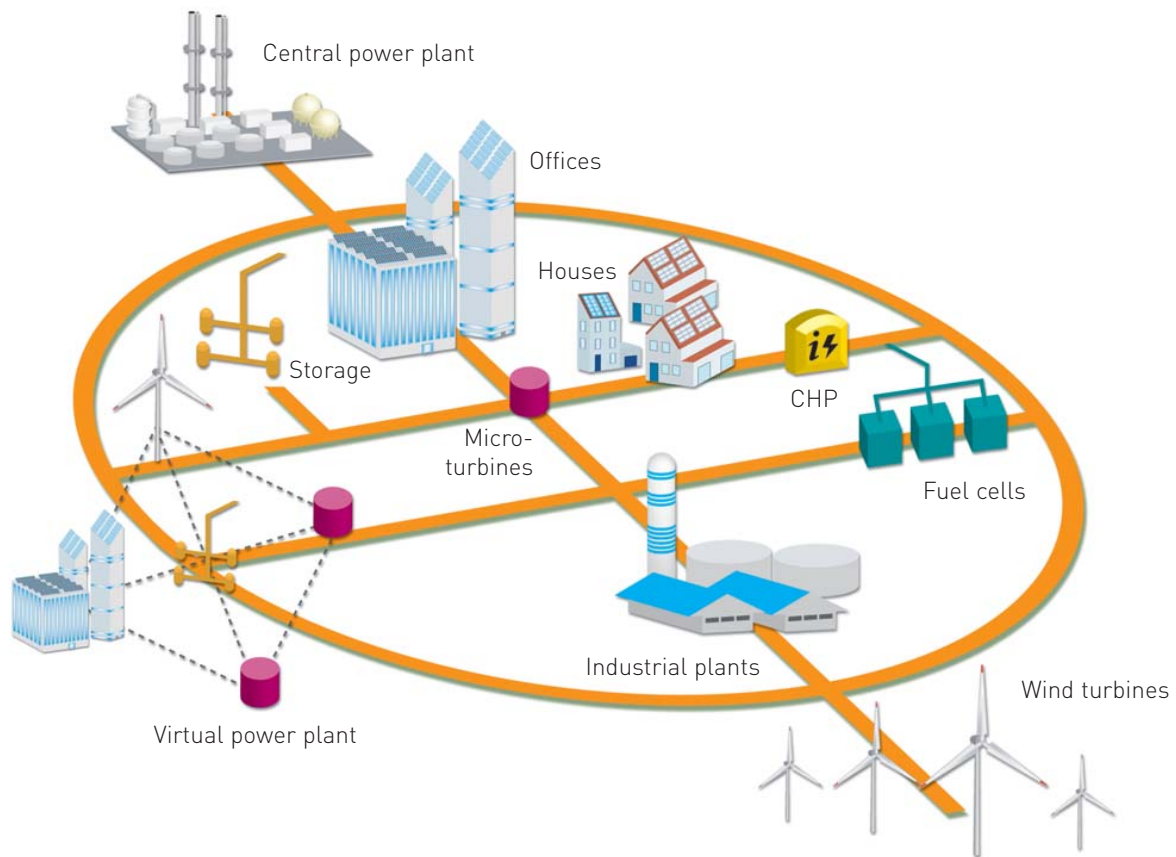


Figure 1.1 – Sample smart grid [34].

[50]. A typical example of future smart grids is illustrated in Figure 1.1, where a percentage of the electricity generated by DG, RESs, demand response, demand-side management, and ESSs will substitute for large conventional plants [34]. At the transmission level, it is worth noting that power systems have always been “smart”. The biggest changes are happening at the distribution level that needs to become “smarter” in order to facilitate access to DG based on RESs [159], [122], improve flexibility of suppliers and consumers [128], enable local energy demand management and smart metering [49], and adopt technologies already deployed in transmission grids [108]. To sum up, distribution grids are being transformed from **passive** to **active networks**, which eases the integration of distributed generators, demand-side integration, and energy storage technologies, and also creates opportunities for novel types of equipment and services, all of which would need to comply with common protocols and standards [2].

One of the promising, novel smart grid concepts in achieving the aforementioned goals is to employ a system approach which views local generation and associated loads as a subsystem, namely an MG [2], [105], [71]. A definition of MGs has been given as follows [72]:

“MGs comprise low voltage distribution systems with DERs (microturbines, fuel

cells, PV, etc.) together with storage devices (flywheels, energy capacitors, and batteries). Such systems can be operated in a non-autonomous way, if interconnected to the grid, or in an autonomous way, if disconnected from the main grid. The operation of micro-sources in the network can provide distinct benefits to the overall system performance, if managed and coordinated efficiently.”

Three key messages which characterize MGs can be yielded from this definition, namely as [2]:

- 1 MG is an integration platform for supply-side (micro-generation) and demand-side resources (storage units and flexible loads) co-located in a local distribution grid. Thus, aggregator models that disregard physical locations of generators and loads (such as virtual power plants with cross-regional setups [161], [149]) are not MGs. Furthermore, both supply-side and demand-side resources should simultaneously be contained in an MG;
- 2 An MG should be capable of dealing with both normal state (grid-connected) and emergency state (islanded) operations except for those built on physical islands;
- 3 The difference between an MG and a passive grid penetrated by micro-sources lies mainly in terms of management and coordination of available resources:
 - An MG operator is more than an aggregator of small generators, or a network service provider, or a load controller, or an emission regulator – it performs all

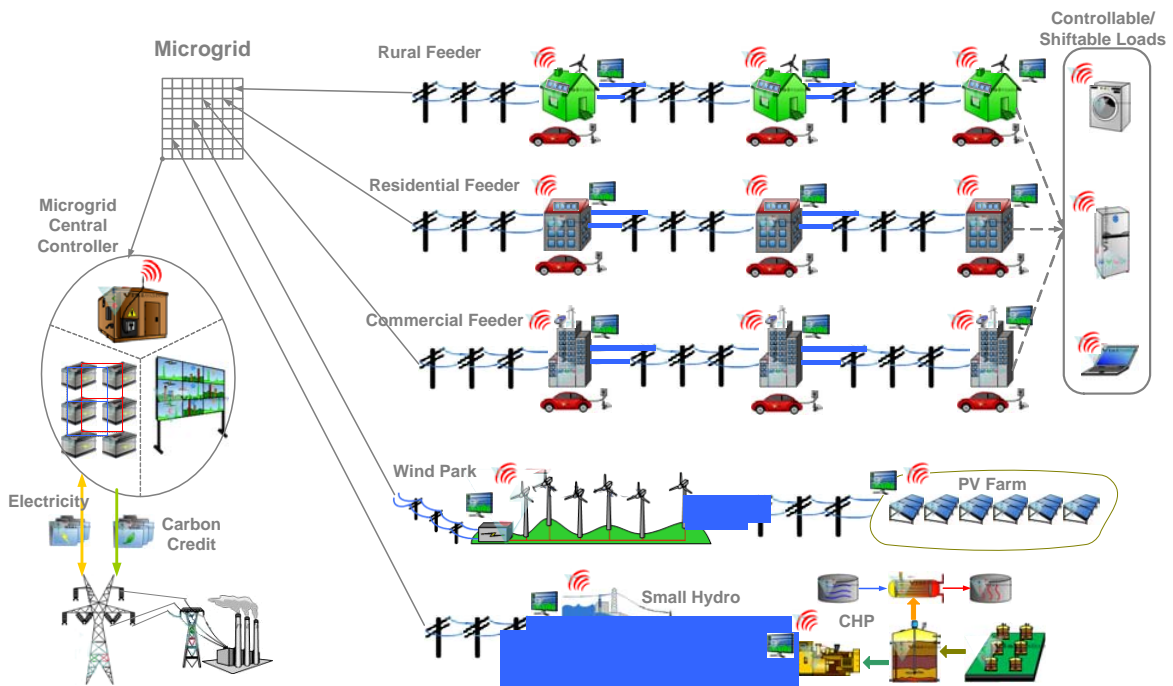


Figure 1.2 – Sample MG as a low voltage grid [2].



Figure 1.3 – Sample MG as a low voltage feeder [2].

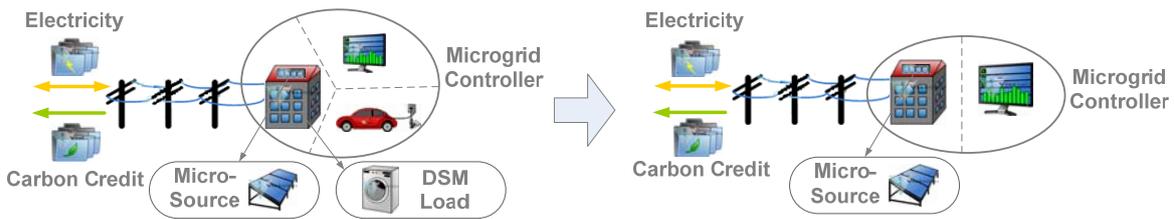


Figure 1.4 – Sample MG as a low voltage house [2].

these functionalities and serves multiple economic, technical, and environmental aims (*e.g.*, enhanced reliability, improved power quality, reduced carbon footprint, and lower costs of investment and energy supply);

- One major benefit of the MG concept over other “intelligent” solutions lies in its capability of coping with conflicting interests of different stakeholders so as to obtain a globally optimal operation decision for all players involved.

An MG could appear in a wide variety of scales – examples for MGs as a low voltage grid, a low voltage feeder, or a low voltage house are shown in Figure 1.2, Figure 1.3, and Figure 1.4 respectively [2]. As an MG grows in scale, it will be likely equipped with more balancing capacities and feature better controllability due to reduction of intermittency from both load side and renewable energy resources side. Nevertheless, in general the maximum capacity of an MG is limited to several MW (*e.g.*, European scale) in terms of peak load demand, above which multi-microgrid concepts are applied by dividing the aggregated units into interconnected but separated MGs [200].

1.2.2 Pico-, nano-, micro-, and minigrids

“Local grids”, current denoted nano-, micro-, and minigrids, is a topic of increasing interest. However, the lack of clarity of the key terms hinders the development towards delivering good policy and creating needed technology such as interoperability standards [25]. A review on pico-, nano-, micro-, and minigrid concepts along with their main features and functionalities is hereafter presented.

Several recommendations on definition of the terms “pico-, nano-, micro-, and minigrid” have been found in the literature as follows:

- **Picogrid:** adapted from [54], a picogrid is defined as “an individual device with its own internal battery for operation when external sources are not available or not preferred, and managed use of the battery”. [162] considers a picogrid as a set of “dumb” appliances and loads without the ability of power consumption self-monitoring, power pattern self-management, and communication with higher management systems. A network of electric devices in a home or building sometimes including some distributed energy sources like electric vehicles or solar cells can be regarded as a picogrid in [195], whereas [21] views an electrical system in a plug-in hybrid electric vehicle as a picogrid. [82] considers a picogrid as a desktop level network with ultra-low power demands such as smartphones, tablet PCs, sensor networks, USB 2.0/3.0 devices, *etc.* In summary, the key property of a picogrid can be inferred as being **singularity**;
- **Nanogrid:** the recommended definition of a nanogrid as “a single domain of power, single physical layer of power distribution, reliability, quality, price, and administration” can be found in [147]. [98] proposes a smart nanogrid for a domestic electrical system composed of multiple power generating sources, energy storage units, an in-house power distribution system, and a variety of appliances operating at below 50 V DC. A novel multi-tenant cloud-based nanogrid for self-sustainable smart buildings including various RESs, storage units, and various appliances is presented in [99]. In [82], a nanogrid is defined as an occupied-zone distribution network serving low power demands such as LED lighting, desktop hubs, thin film PV on windows, *etc.* [24] regards a nanogrid as a small isolated DC power system that utilizes distributed RESs together with storage units to feed continuous power to small local loads. In short, the main attribute of a nanogrid is **simplicity**;
- **Microgrid:** the MG concept has already been defined in [105], [72], [71] in Subsection 1.2.1 where the focus is on the ability to island from an utility grid (to operate independently). A DC MG that integrates a wind turbine generator, a battery-based ESS, DC loads, and a grid-connected converter system and can operate in both grid-tied and in islanded modes is detailed in [199]. [86] proposes an MG applied for residential houses where all houses have a co-generation system such as gas engine or fuel cell and the power are shared among the houses. [82] considers an MG as a building-wide distribution network that serves high powered loads/sources such as servers, large-scale root PV, fuel systems, *etc.* In a word, the major characteristic of an MG is **capability**;
- **Minigrid:** A minigrid is like a traditional utility grid (an electricity distribution system with one entity that provides power to customers connected to it) but with limited scope of geography and capacity [148]. In [186], a minigrid is viewed as an isolated, small-scale distribution network typically operating below 11 kV that supplies power to a localized group of customers and generates electricity from small generators, potentially coupled with ESSs. A minigrid in [80] is broadly considered as a local producer network that utilizes DERs and manages local electricity supply and demand. It can be deduced that minigrids represent some formal characterizations of MGs. Furthermore,

the term “minigrd” is often used interchangeably with the term “microgrid”. In [80], minigrds are defined like those with an installed capacity lower than 50 MW, whereas MGs are marked out by power capacities below 1 MW. Hence, minigrds are generally understood to be larger than MGs, although there is no firm and consistent definition of the separating line between them. Moreover, minigrds are split into micro-, nano-, and picogrds, although the relationship and size differences between the three kinds of systems do not correspond to their mathematical equivalents. A common attribute of pico-, nano-, micro-, and minigrds is that in many cases they are semi-autonomous and can operate in islanded mode of operation, but are also often connected to larger grids.

A typical example of a conceptual system structured as a dynamically decoupled and hierarchically interconnected hybrid mix of AC and DC architectures composed of pico-, nano-, and microgrids is illustrated in Figure 1.5 [21].

A novel classification of MGs complying with their interoperability layers (functional layers) inspired by the division of the smart grid architecture model defined by the European Committee in [25] is reviewed in [132]. The functional layers (*i.e.*, infrastructure, communication, intelligence, and business models) are separated into different levels (*i.e.*, pico-, nano-, and microgrid) in compliance with their functionalities within the MG concept (Figure 1.6).

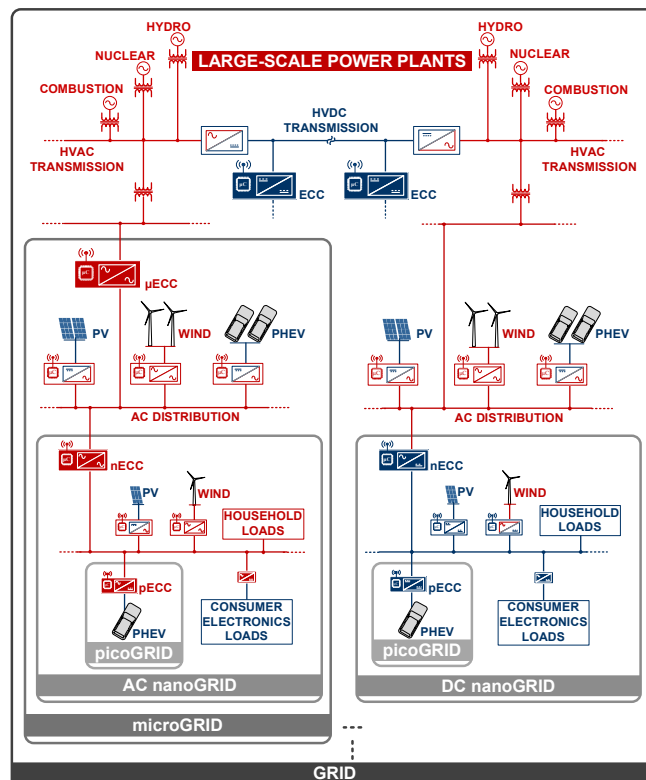


Figure 1.5 – Dynamically decoupled and hierarchically interconnected structure of a novel electric power grid comprising AC and DC sub-grids [21].

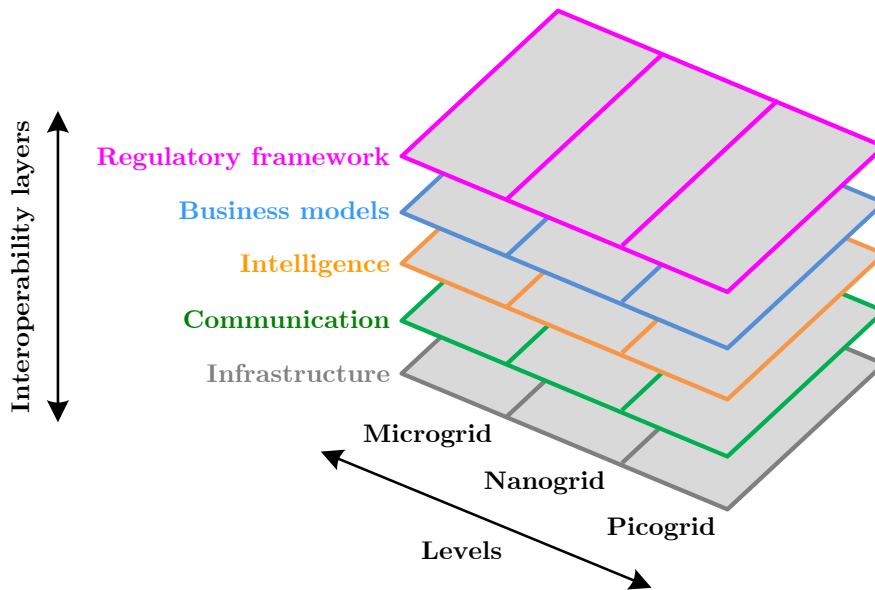


Figure 1.6 – Interoperability layers of the MG architecture model [132].

“Infrastructure” layer

This layer contains all physical elements that constitute an MG (or smart grid in a wider sense): DGs (*e.g.*, PV systems, wind turbine generators), storage units (*e.g.*, batteries, electric vehicles), power-electronic systems, and loads. The physical structure of a smart electric power grid is shown in Figure 1.7 [132], where picogrids can bundle together to form a nanogrid and a set of multiple nanogrids can form an MG.

“Communication” layer

In order to properly carry out functions of the physical layer, all the data and information representing its status is sent to the intelligence layer by means of the communication layer. In the literature, different levels of communication networks used for smart grids can be found. The same concepts could also be applied to MGs schemes. Hence, the organization of the communication protocols can be divided into several area networks such as wide-area network (WAN), field-area network (FAN), neighborhood-area network (NAN), building-area network (BAN), industrial-area network (IAN), and home-area network (HAN) [65], [53], [146], [5].

Figure 1.8 shows how all these different area networks used in the smart grid concept fit into the MG conceptual model. The most commonly-used communication protocols at each of these levels are described as follows. The BAN and the HAN are considered as the lowest levels of the communication architecture. The communications inside each building (*i.e.*, nanogrid) are managed by the BAN being responsible for collecting the power consumption data of each apartment (*i.e.*, picogrid) and the power production data within the building, whereas the

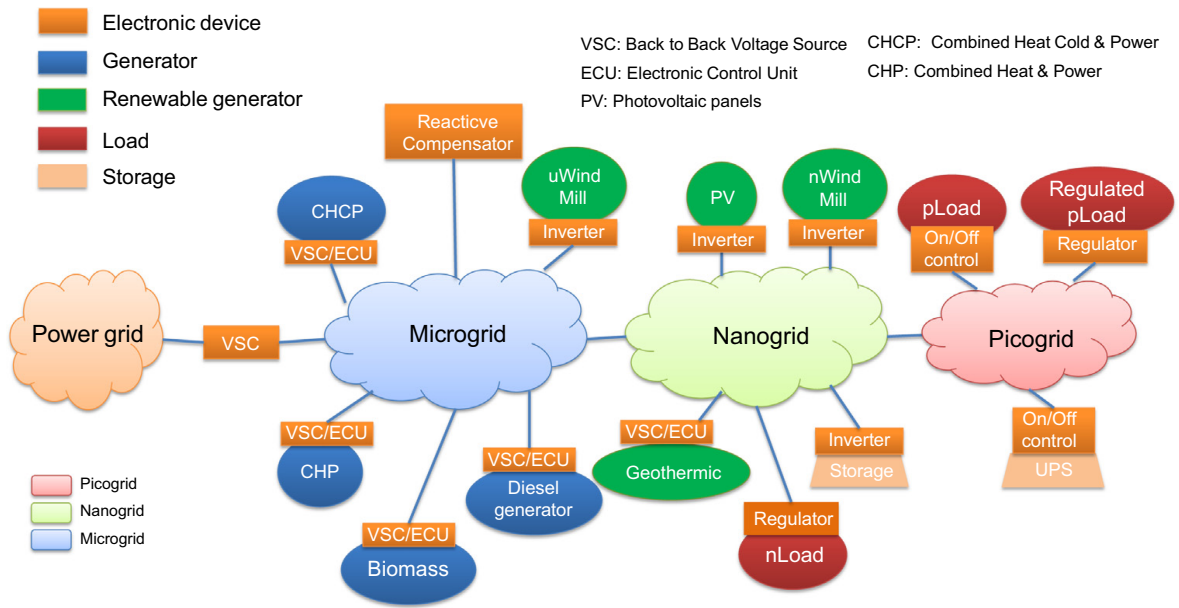


Figure 1.7 – Physical structure of a smart electric power grid [132].

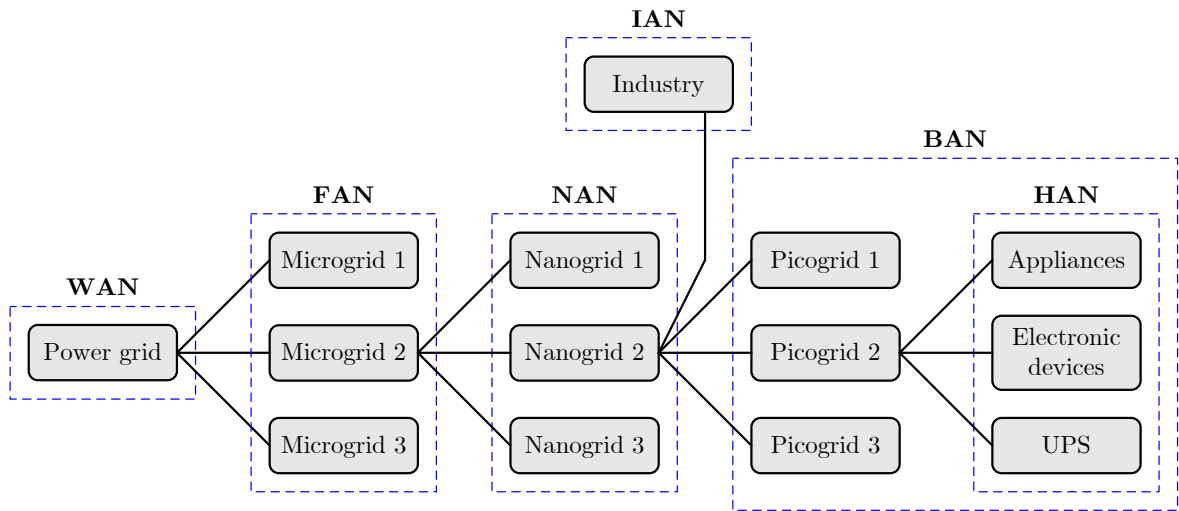


Figure 1.8 – Machine-to-machine communication network architecture for the MG [132].

HAN is in charge of gathering the consumption data and controlling the smart appliances within each apartment. Inside a nanogrid, the industry-related communications could be done with an IAN. At upper levels, a NAN and a FAN could be used for the communications inside an MG and between the substations and the MG respectively. Finally, the consumption and production data of each MG are transferred to a gateway from the smart meters, then the gateway sends the message to the WAN – the highest communication level inside a power grid.

Table 1.1 – Services at each level [132].

Level	Size	Resources			Services
		DER	ESS	Loads	
Picogrid	House			✓	Load management, energy efficiency, demand response
Nanogrid	Building	✓	✓	✓	DG and load management, energy efficiency
Microgrid	Neighborhood	✓	✓	✓	DG and load management, energy trading, resiliency, aggregation

“Intelligence” layer

This layer is composed of all the control and decision-making systems that process the information coming from the elements located on the physical layer (DGs, ESSs, power-electronic systems, and loads). The connection with actuators, sensors, and metering systems located in the physical layer is realized by means of the communication layer. Each sub-grid (*i.e.*, pico-, nano-, and microgrid) has its own major roles which is shortly indicated in Table 1.1 [132].

“Business models” layer

The business layer represents the business view on the information exchange related to MGs. The types of business models which may be deployed for different elements in an MG are tackled by this layer. A detailed literature review on the business models layer can be found in [132].

1.2.3 Microgrids operation and control

The MG modes of operation can be categorized into grid-connected, islanded, and transition from islanded to grid-connected and *vice versa*. In the grid-connected mode, ancillary services can be provided by trading activity between the MG and the main grid. In the islanded mode of operation instead, the active and reactive power generated within the MG should be in balance with the local load demand. Islanding, *i.e.*, disconnection of the MG from the main grid, can be either intentional (*e.g.*, scheduled maintenance, degraded power quality of the host grid that can harm MG operation, economic reason) or unintentional (*e.g.*, faults, other unscheduled events). Use of MGs can actively handle both of these situations. Furthermore, MGs can operate permanently in stand-alone mode, namely isolated MGs. This is the case of remote sites where an interconnection with the main grid is not possible due to either technical and/or economic constraints [151].

Protection and control challenges

In order to ensure reliable operation of MGs and fully exploit the potential benefits of DGs, a number of operational challenges need to be solved in the design of protection schemes and control systems. Some of these challenges emerge from invalid assumptions typically applied to conventional distribution systems, whereas others are caused by stability issues previously occurred only at a transmission system level. The most relevant challenges in MG protection and control comprise [151]:

- Requirement of bidirectional operation of electronically-interfaced DG units;
- Stability issues due to interaction of DG control systems and transition between the grid-connected and islanded modes of operation;
- Three-phase balanced conditions, primarily inductive transmission lines, and constant-power loads are no longer valid in MG modeling;
- Low-inertia characteristic of power-electronic-interfaced DG units;
- High degree of parametric and topological uncertainties (*e.g.*, stochastic (unpredictable) nature of RESs, load profile uncertainty).

Stability issues and problems related to low inertia and uncertainties due to the presence of RESs are among the main control challenges. Indeed, the low inertia in the system can result in severe frequency deviations in stand-alone operation if a proper control mechanism is not implemented [151]. For instance, consequent to an outage of a production group where its rated power is approximately equal to 17 % the rated power of the system, a frequency drop of more than 1 Hz/s was observed in the MG of Guadeloupe island, as stated in the Ph.D. thesis of Delille [41].

Reliable and economical operation

Proper control and management of MGs is a required prior condition for continued stable and economically efficient operation [91], [105], [71] while overcoming the aforementioned challenges. In particular, the desired features of the MG control structure include [18], [151]:

- Frequency and voltage regulation for grid-connected and islanded modes of operation;
- Proper load sharing and DG coordination;
- Demand-side management;
- MG resynchronization with the host grid and adapted control may then be associated to manage this state change;
- Power flow control between the MG and the main grid;

- Proper handling of transients and restoration of desired conditions while switching between modes of operation;
- Economic dispatch, *i.e.*, optimizing the MG operating cost.

These requirements are of different importances and time constants, therefore a hierarchical control structure is required to deal with each task at a different control hierarchy level [64], [18], [151]. The MG hierarchical control structure, depicted in Figure 1.9, is typically composed of three broad layers, namely primary, secondary, and tertiary controls as inspired from classical power grids. First, the primary control, at the lowest level with fastest response, is designed to stabilize the voltage and frequency of the MG subsequent to the islanding process when switching from the grid-connected mode, provide plug-and-play capability for DGs and properly share the active and reactive power among them without any communication links if possible, as well as alleviate circulating currents that can result in overcurrent phenomenon in the power-electronic devices and destroy the DC-link capacitor [90], [89], [145], [133], [64], [18], [151]. The primary control provides the setpoints for the voltage and current control loops of DGs which are commonly referred to as zero-level control, *i.e.*, power sharing using droop control for instance. Next, the secondary control is designed to have slower dynamics response (typically seconds to minutes sampling time) than that of the primary control, which justifies the decoupled dynamics of the primary and secondary control loops and facilitates

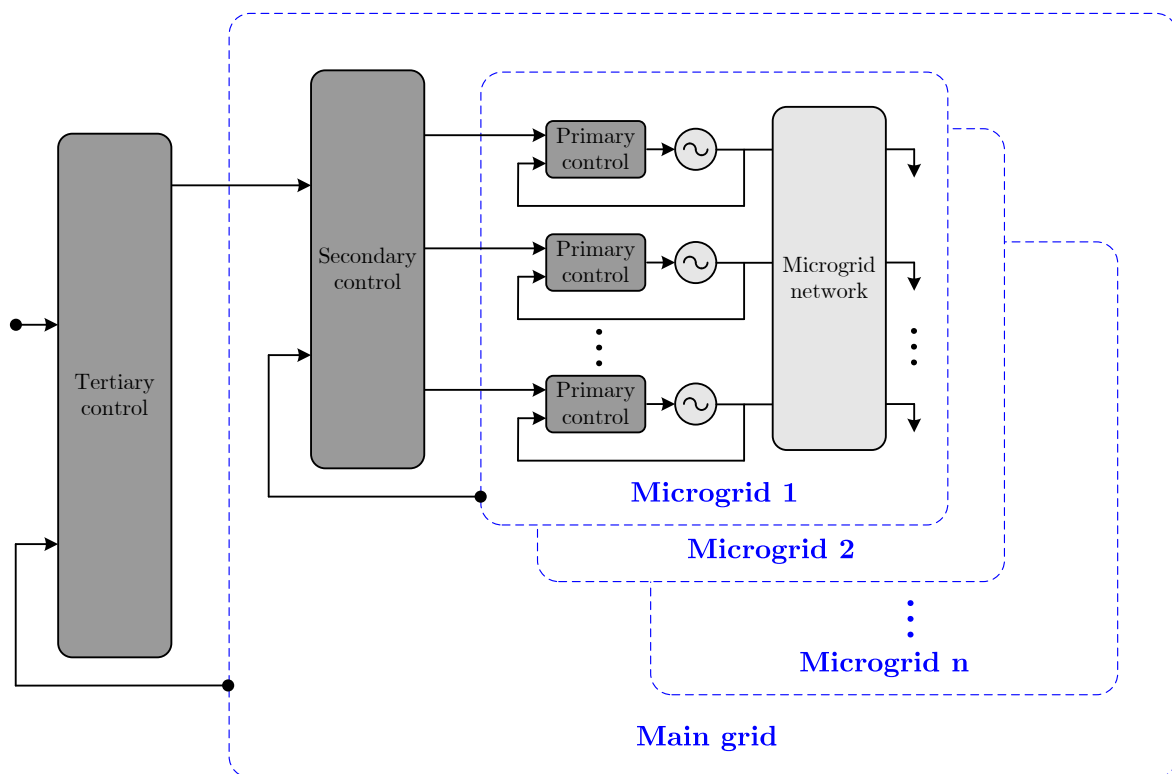


Figure 1.9 – Hierarchical control structure of an MG [151].

their individual designs [131]. The secondary control gives the setpoints to the primary control and compensates for the voltage and frequency deviations caused by the primary control [18], [151]. Ultimately, at the highest level with slowest timescale (minutes to hours sampling time), the tertiary control manages the power flow between the MG and the main grid and facilitates an economically optimal operation [133], [64], [18], [151].

General operating requirements

In the grid-connected mode of operation, the MG frequency and the voltage at the PCC are dominantly imposed by the utility grid. In this case, each DG unit should act as a controllable current source, which exchanges the real and reactive power with the main grid using the current-mode control strategy. Reactive power injection by a DG unit can be employed for power factor correction, reactive power supply, or voltage control at the corresponding point of connection [151]. In this mode, the voltage regulation or control participation of DG units in the neighborhood of the PCC may not be allowed in order to avoid interaction with the same functionality provided by the host grid [78].

In the stand-alone mode of operation, the MG operates as a single, independent entity. This mode of operation is considerably more challenging than the grid-connected mode, as the critical demand-supply equilibrium necessitates the implementation of accurate load sharing mechanisms among DG units to balance sudden active power mismatches [151]. The MG voltage and frequency are no longer supported by the main grid, and the current-mode control strategy used in the grid-connected mode cannot ensure the sustainable operation of the islanded MG. It is the collaborative responsibility of the DG units to regulate the MG voltage and frequency – an objective that can be attained most effectively and conveniently if the DG units act as controllable voltage sources (voltage-mode control strategy) [111]. Thus, subsequent to an islanding event, the islanding must be detected as fast as possible [11], and an appropriate voltage-mode control strategy must be adopted to regulate the MG voltage and frequency and to manage/share the real and reactive power among the DG units.

Power quality

In recent years, the growing application of voltage sensitive loads, including a large number of various electronic loads and LEDs, results in a considerable increase in electricity consumers' needs for higher power quality. The term “power quality” in electrical networks refers to maintaining the waveforms of the voltage and current close to the pure sinusoidal ones at the rated magnitude and frequency [26]. Utilities are always searching for efficient ways of improving power quality issues by handling prevailing concerns arisen from voltage and harmonics. MGs provide a quick and efficient answer for dealing with power quality demands by allowing local control of the current and voltage of sources, especially with ESSs [158]. The quality of electric power supply should comprise three major parts, as illustrated in Figure 1.10 [157], where the power quality means the continuity of supply and voltage quality.

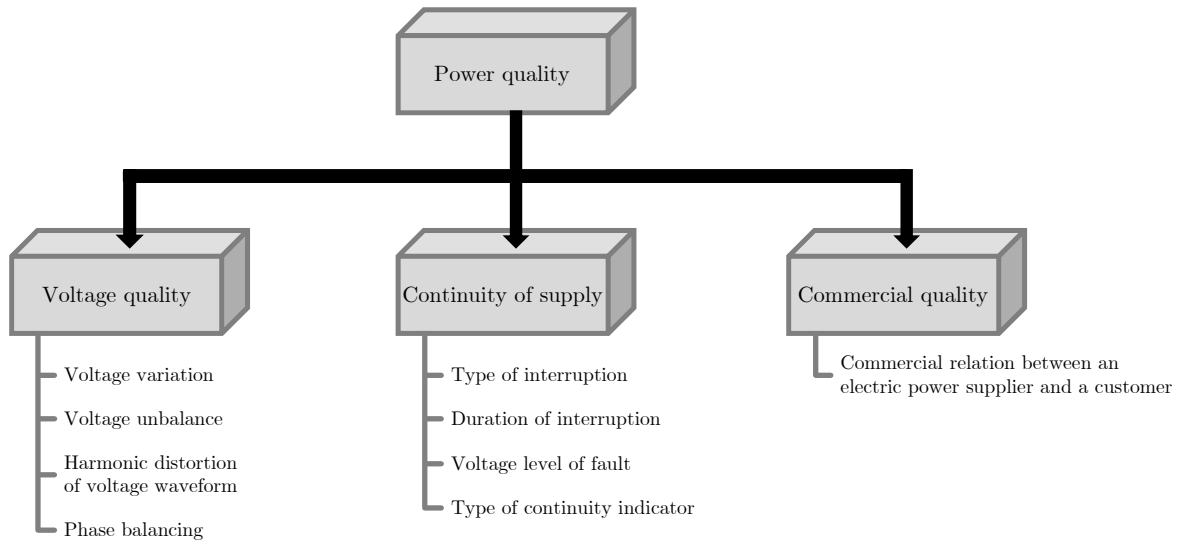


Figure 1.10 – Classification of power quality issues in MGs [157].

Power quality characteristics and requirements are normally separated into two broad categories, namely steady-state characteristics and disturbances, respectively. Steady-state characteristics refer to the requirements for the normal voltage provided from the power system and the respective responsibilities of the supply system, end users, and equipment in preserving the required quality of the voltage. Voltage and frequency deviation, voltage and current unbalance, voltage and current harmonics, and flicker are regarded as the steady-state power quality quantities. Disturbances, on the other hand, are events that occur randomly but can impact the equipment performance. Thus, different methods of describing performance and coordination requirements are needed. Disturbances comprise voltage and current transients, voltage sags/swells, and interruptions. Interruptions that last more than one minute (sometimes five minutes) are usually referred to as outages and are involved in reliability statistics. Short interruptions are categorized with power quality variations [192].

In this thesis framework, we are mainly interested in frequency and voltage stability in stand-alone MGs with a high intermittent PV penetration rate.

1.2.4 Energy storage in microgrids

Due to recent developments and advances in energy storage and power electronics converters, the use of energy storage technologies are increasingly becoming a feasible solution for modern power applications. “Electrical energy storage refers to a process of converting electrical energy from a power network into a form that can be stored for converting back to electrical energy when needed” [12], [28], [193]. The choice of an ESS for a specific application is dependent on the application power and energy ratings, response time, weight, volume, and operating temperature [193].

Energy storage technologies

ESSs installed within an electricity system are divided into a number of fairly well defined categories, mainly [28]:

- Chemical energy storage: electrochemical (conventional and flow-cell batteries), chemical (fuel-cell/electrolyser systems, metal-air batteries), and thermochemical (solar hydrogen, solar metal, solar chemical heat pipe);
- Mechanical energy storage: kinetic or electromechanical (flywheels) and potential (pumped hydroelectric and compressed air systems);
- Electrical energy storage: electrostatic (capacitors, supercapacitors) and electromagnetic (principally superconducting magnetic energy storage);
- Thermal energy storage: low temperature (aquiferous cold and cryogenic energy storage) and high temperature (sensible and latent heat systems).

Applications of energy storage

ESSs can enhance the performance of several applications. According to green energy trend, they are particularly suitable for transport and utility-scale applications [193]. Figure 1.11 shows the duration requirement versus power operational range for various utility applications. In this case, time and power ranges change from tens of minutes to hours and from megawatts to gigawatts respectively [193]. The impact of ESSs on the utility grid is becoming increasingly important as a solution to stability problems. ESSs have main applications in RES penetration increasing, load leveling, frequency regulation, transmission line capability improvement, voltage support, and power quality and reliability enhancement [165], [193].

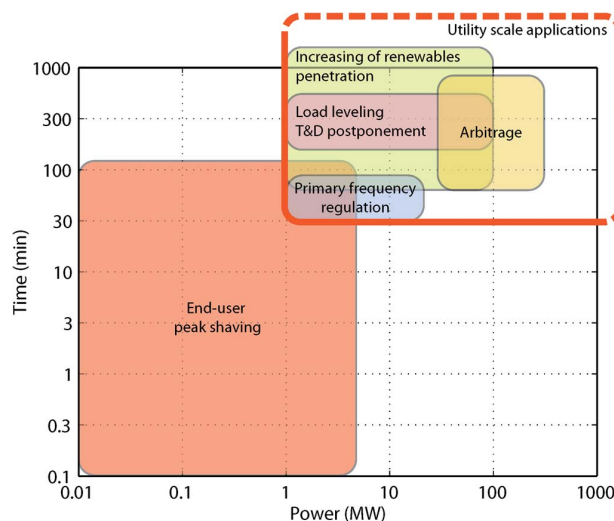


Figure 1.11 – Utility applications of ESSs [193].

In the context of the distribution network and customer interface, the key applications for ESSs include integration of renewables into the utility distribution system, voltage regulation, peak shaving/demand management, distribution capacity deferrals, and quality of supply/power quality [12]. Among them, the two most principal applications of ESSs are power quality for MGs with renewables and in service with renewables. For MGs without renewable energy impact, ESSs can maintain the voltage and frequency stability after the transition from the grid-connected mode to the islanded mode [97]. For MGs with renewables, ESSs are regarded as a mean to increase the penetration of renewables while enhancing the system reliability [13], [193]. In MGs where RESs are a pillar, without storage units, the generation of RESs cannot enhance the system reliability and has to be replaced by other means of generation. A storage unit can provide a functionality similar to that of the inertia of a synchronous generator by absorbing temporary mismatches between power generated and consumed, especially in a low-inertia converter-dominated MG. Thus, the system stabilization can be enhanced by providing voltage/frequency control, for example, based on a droop scheme [151].

1.2.5 Virtual synchronous generators

Compared to conventional power plants, in which synchronous generators dominate, DG units have either considerably smaller or no rotational mass and damping property and thus, can affect the grid dynamic performance and stability. Some negative consequences such as voltage increase due to reverse power from PV generations, excessive supplies and congestions of electricity in the grid due to full generation by the DG units, power fluctuations due to intermittent nature of RESs, and degradation of frequency regulation, especially in islanded MGs, can arise from the mentioned issues [15], [3].

Basic concepts

In order to stabilize such a grid, an additional inertia should virtually be provided. Use of short-term energy storage together with a power-electronic inverter/converter and a proper control mechanism can create a virtual inertia for DG units. This concept has been reported in the literature as VSG [181], [178], [116], [117] or virtual synchronous machine [37], [103]. The same concept under the title of synchronverter was presented in [206], [207], [144]. This design is expected to mimic the behavior of a real synchronous generator, displaying the amount of inertia and damping property. Therefore, power sharing among DG units in future grids without compromising the system stability may be enabled based on the virtual inertia concept.

The idea of the VSG lies in duplicating the dynamic properties of a real synchronous generator for the electronically-interfaced DG units, in order to make use of the benefits of a synchronous generator in stability improvement such as adjustable active and reactive power, dependency of the grid frequency on the rotor speed, and the rotating mass and damping windings effect, as well as stable operation with a high parallelism level [29]. Furthermore,

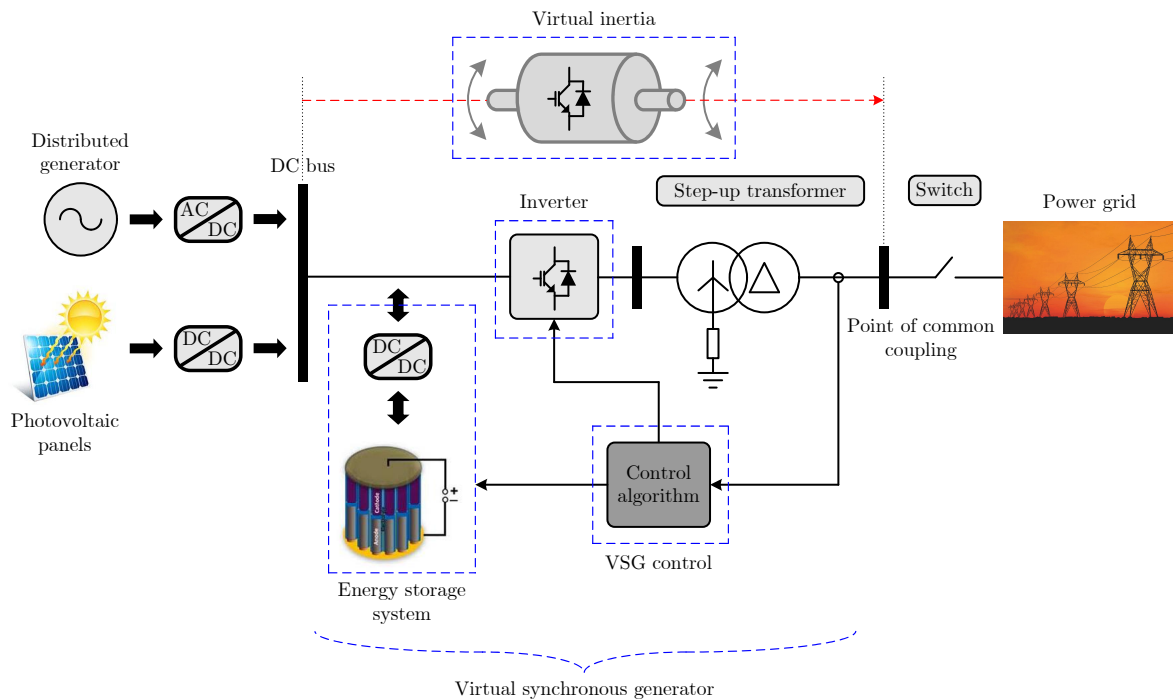


Figure 1.12 – General structure and basic concept of a VSG [15].

the rule of the VSG can be applied either to a single DG, or to a group of DGs.

A VSG comprises energy storage, an inverter, and a control mechanism as illustrated in Figure 1.12. In this structure, the VSG acts as an interface between the DC bus and the power grid and represents the DC source to the grid as a synchronous generator from the inertia and damping property point of view. Indeed, the virtual inertia is emulated in the system by means of the inverter active power control which is in inverse proportion to the rotor speed. Apart from high-frequency noise caused by the inverter switching, from the grid point of view there is no difference between the electrical appearance of an electromechanical synchronous generator and an electrical VSG [30]. In the VSG control block shown in Figure 1.12, in general, a dynamic equation similar to the swing equation of a synchronous generator is inserted in order to determine the output power of a VSG unit based on the rate of the grid frequency change $d\Delta f_{grid}/dt$ and the frequency deviation Δf_{grid} [15], [3].

Applications for microgrids

The VSG systems can be employed as effective control units to compensate for the lack of inertia and lead to the control of active and reactive power, as well as the MG voltage and frequency. Figure 1.13 presents a simplified MG structure with multiple VSG units. The VSGs can be connected between a DC bus/source and an AC bus, anywhere in the MG. These systems are going to be more crucial to overcome fluctuations arisen in the MG due to

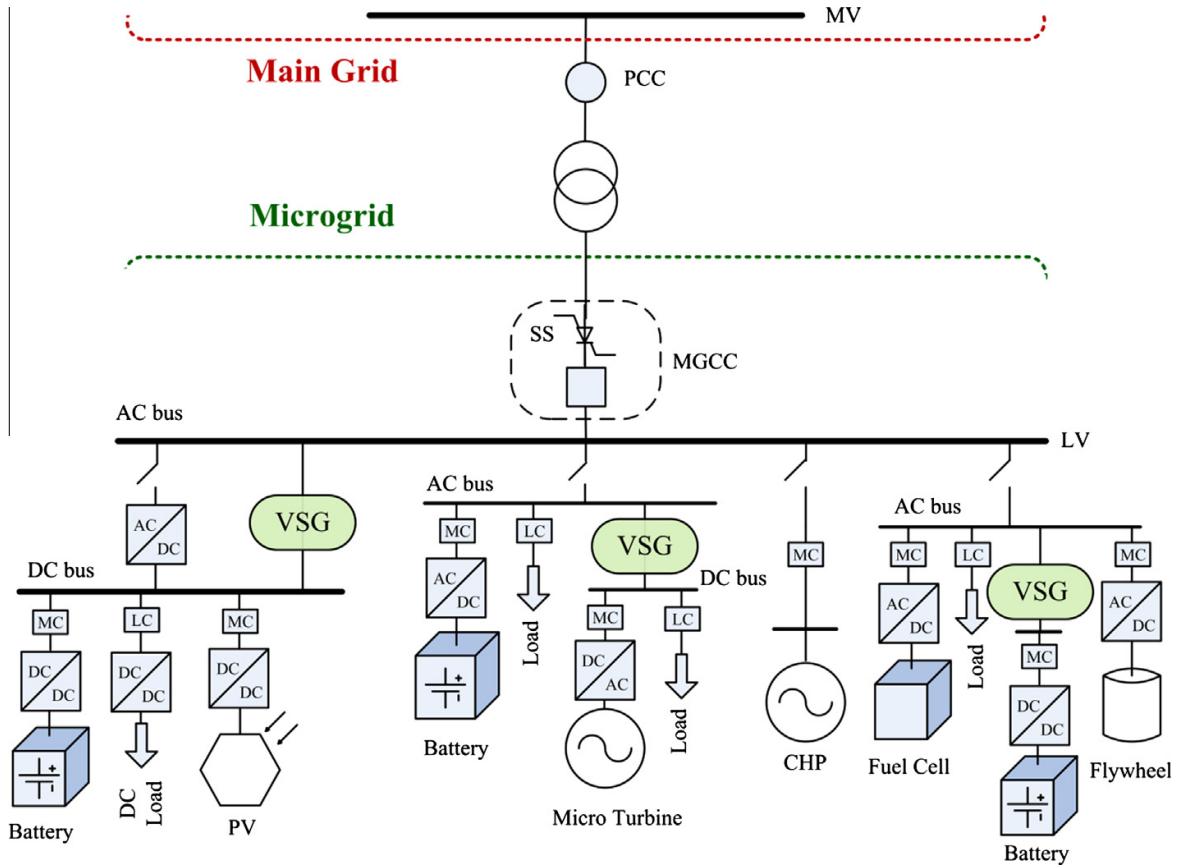


Figure 1.13 – Simplified MG structure with multiple VSG units [15], [3].

large integration of low-inertia power-electronic-interfaced DG units [15], [3].

MGs are considered as complex structures of low short-circuit power with the integration of numerous technical and numerical components, as well as variability sources. Therefore, it is compulsory to implement sophisticated control strategies for this kind of system.

1.3 State-of-the-art on control strategies in microgrids

The identification and classification of most commonly used control strategies in MGs are not simple as they depend mainly on the characteristics of the MG. In the literature, control strategies based on a hierarchical structure, as shown in Figure 1.9, have been adopted by most authors. Based on the studies reported in the literature, the classification of the most pertinent control strategies at each hierarchical control level can be observed in Figure 1.14 [189]. In this thesis framework, a literature review of the primary control level is hereafter presented, where its main ideas are detailed in [189].

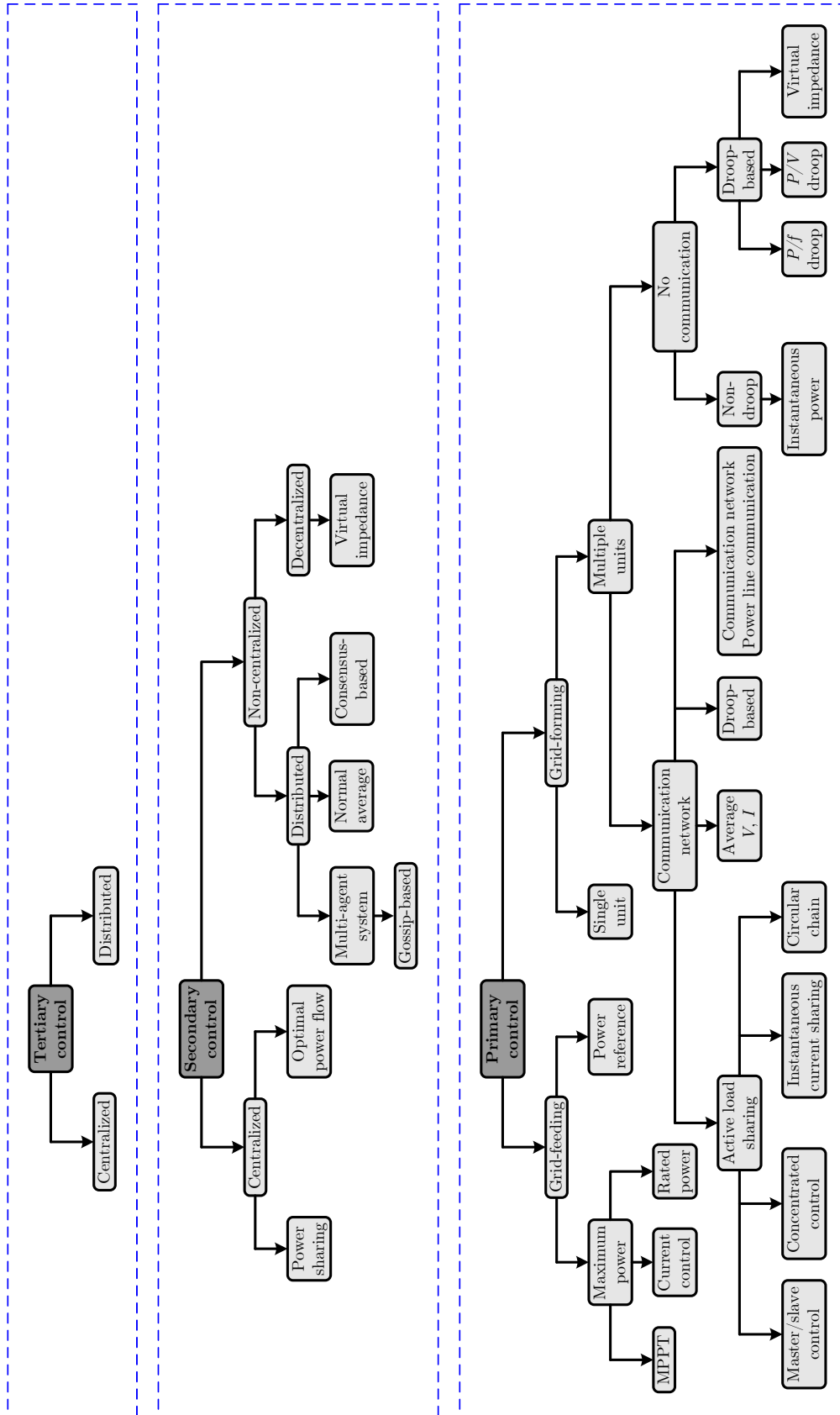


Figure 1.14 – Classification of MG control strategies reported in the literature [189].

In the literature, primary control levels are usually classified into two or three classes according to their role. Three strategies can be carried out, namely grid-forming, grid-feeding/following, and grid-supporting ones, as stated in [22], [166]; whereas other studies in [155], [190] simplify this classification by reducing the number of primary control strategies to grid-forming and grid-feeding ones. Since the grid-supporting strategies contribute to the grid voltage regulation, they are put in the grid-forming category.

1.3.1 Grid-feeding control

When operating in grid-connected mode, the MG voltage and frequency are set by the host grid. In this case, DG units usually operate in current-controlled mode to extract as much power as possible from DERs, *e.g.*, maximum power point tracking (MPPT) for wind or solar generation, diesel/biomass generation at rated power, *etc.* [190]. Aside from that, this kind of control can act at a non-optimal point outside the maximum power range – when the references of active and reactive power are established by upper control levels with the aim of optimizing the power sharing strategy of the network [166]. These strategies can be applied to both AC- and DC-based units; the key difference is the synchronization process of the AC-based ones to the AC side of the MG [189].

In this context, a review of some of the most widely used grid-feeding control strategies for DG units, together with the main grid synchronization methods in the case of AC-based DG units such as zero crossing, filtering of grid voltages, and phase-locked loop techniques, are presented in the work of Blaabjerg *et al.* [20]. Usually, these strategies consist mainly of two nested loops, namely a fast-dynamic inner current loop and an outer voltage one [20]. Following this work, a classification of primary control strategies where the most broadly used grid-feeding techniques are distinguished, *e.g.*, dq synchronous reference frame, $\alpha\beta$ stationary reference frame, and abc three-phase reference frame, has recently been discussed in the work of Palizban *et al.* [155].

In a similar manner, some of the most pertinent control techniques for the connection of devices to AC grids are reviewed in the work of Rocabert *et al.* [166] and Rodriguez *et al.* [168]. These strategies could be applied on the AC side of the hybrid MG or in both AC and DC networks after some adaptations [189].

1.3.2 Grid-forming control

When an MG operate in stand-alone mode, DG units and ESSs must be responsible for ensuring voltage and frequency stability of the AC and DC networks of the MG, which thus requires an optimal active and reactive power control in order to provide adequate power sharing among devices. This theme has previously been reported in the work of Guerrero *et al.* [62] applied for distributed uninterruptible power supply systems.

Depending on the requirements, some or all the DG units will operate in parallel to

control the MG voltage [190], *i.e.*, in grid-forming mode, while the remainder acts in grid-feeding mode. This control strategy has been implemented within two major configurations as follows [190]:

Single grid-forming unit

In this configuration, one of the converter-interfaced DG units operates in grid-forming mode and its reference is set to provide a certain voltage and frequency, while all other units are current-controlled to absorb as much power as possible from DERs, *i.e.*, in grid-feeding mode [190].

Multiple grid-forming units

More than one converter-interfaced DG unit act in grid-forming mode in this strategy, which therefore requires a synchronization process so as to guarantee voltage and frequency stability for both the AC and DC MG networks while simultaneously fulfilling a power sharing demand.

Approaches under this group can be separated depending on whether interface converters are interconnected by a communication network or not, as stated in [156], [191], [93], [18]. An exhaustive review of grid-forming control strategies for multiple grid-forming converter-interfaced DG units has been given in the work of Vandoorn *et al.* where the classification mentioned above is presented [191].

- **Communication network between devices**

These strategies are usually based on active load sharing, among which one can cite use of master/slave control, concentrated control, instantaneous current sharing, or circular chain approaches [155], [191]. One of the major drawbacks of these techniques is that the communication network can turn out to be extremely sophisticated in highly extended MGs, which may lead to failures in the control strategy if any part of the communication network works incorrectly. Furthermore, plug-and-play capability for DG units is not guaranteed, so the integration of upcoming devices into the existing network could be a challenge [189].

In this context, a primary control strategy for a hybrid AC/DC MG composed of a PV panel, a doubly-fed induction generator-based wind turbine, an ESS, and an AC and DC load is studied in the work of Liu *et al.* [118]. A dual-loop control consisting of an outer voltage loop and an inner current loop is utilized for the DG and ESS devices, as well as for the interface converter, along with some information exchanged between these control schemes, so as to achieve good stability and power sharing demand under various load and resource conditions.

Another application can be found in the work of Bidram *et al.* [19], where the authors introduce a two-layer, multiobjective control framework for AC islanded MGs based on the droop control technique. Inverter-interfaced DG units can operate either as

voltage-controlled voltage source inverters supplying voltage and frequency support (in first control layer) or as current-controlled voltage source inverters regulating active and reactive power generated (in second control layer). These controllers are implemented by means of two communication networks with one-way communication links, where each DG unit requires its own information and the information exchanged with the neighboring systems, however, use of a central controller for the MG management is not essential.

Other studies have been conducted where communication between DG units and ESSs is required but no communication network is used [189]. These solutions are implemented based on the communication between the power lines of the MG, namely power line communication or power line signaling. An application of this strategy has been reported in the work of Dragičević *et al.* [44]. Here the authors propose a method for coordination of an autonomous MG composed of several sources based on power line signaling, where signals of different frequencies are sent *via* the power line in order to synchronize the converters connected to the grid. Even if no additional communication network is needed in this control strategy, it has the drawback of polluting the voltage and frequency due to the circulation of the control signals *via* the MG. Furthermore, the range of frequencies where the signals can be injected is decreased when the number of devices already connected is high, which makes the integration of new generation or storage units into the MG a more challenging task.

In spite of some advantages – such as providing adequate power sharing, MG stability improvement – primary control strategies based on a communication network are not very commonly used in the literature. A more broadly used solution is to use an autonomous primary control associated with a centralized or distributed secondary control, which is explained more in detail in [189].

- **No communication network**

- *Droop-based control*

Without use of a communication network, droop-based control is regarded as one of the most studied strategies in the literature [23], [127], [203], [64], [96], [140], [27], [63], [106], [121], [120], [160], [176], [42], [45], [59], [123], [124], [129], [169], [205], [48], [68], [77], [198]. Over the last decade, this topic has attracted an extensive amount of interest from researchers due to its benefits compared to other control strategies such as plug-and-play capability, power sharing, less faults due to the lack of a communication network, easy implementation, *etc.* Depending on the active and reactive power demand, droop control aims at varying the voltage amplitude and frequency references in order to ensure the power sharing among devices. In the conventional utility grid, this strategy is broadly employed so as to achieve the power sharing among synchronous generators. In islanded or grid-connected mode of MG operation, this strategy is also adopted for ESSs in order to achieve optimal current sharing. Furthermore, droop control can be integrated in DG units to perform an optimal power sharing in islanded mode, whereas in grid-connected mode the MPPT regulation can be obtained by means of this strategy [64].

In this context, several droop-based primary control strategies for AC and DC MG configurations, which are appropriately implemented in hybrid MGs, have been proposed in the work of Guerrero *et al.* [64]. Here the authors state that, apart from some advantages over other approaches, conventional droop control strategies also show some limitations, for instance, no capability for nonlinear load sharing, power sharing being influenced by the output impedance of DG units and the line impedances, load-dependent frequency variation, and intrinsic trade-off between frequency and voltage regulation and active and reactive power sharing accuracy in islanded mode of operation. These problems can be tackled by the use of a hierarchical control comprising three levels – namely primary, secondary, and tertiary control – where the secondary level can compensate for voltage and frequency deviations [64].

In a similar way, an exhaustive comparative analysis of various droop-based control methods for AC MGs along with their most potential advantages and drawbacks have been reported in the work of Bidram and Davoudi [18].

Based on droop control, a slightly different solution can also be presented in the work of Gu *et al.* [61]. In the proposed technique, the droop curves have been adapted depending on the three distinct modes of MG operation, namely utility-, storage-, and generation-dominating mode, so that a certain device operates in each case. The switching between the operation modes is determined based on the MG voltage levels. Here the authors state that a fully mode-adaptive decentralized control can be achieved as the devices adjust their operating mode autonomously. It should be noted that each droop-based method has its own benefits and shortcomings. Thus, it is not possible to find out an optimal solution that can deal with all kind of applications, and their feasibility has to be investigated in detail depending on each case.

In the aforementioned studies, droop-based control is independently applied to AC or DC MGs. However, with slight adaptations, it can be performed in hybrid MGs. Under this category, Loh *et al.* have proposed in [121] a droop control scheme so as to guarantee proportional power sharing in an autonomous hybrid MG by the use of interlinking converters. In this strategy, a normalization process of the AC frequency and DC voltage is deployed in order to manage the power flow among all sources distributed throughout both sides of the MG.

Another interesting approach has been introduced in the work of Eghtedarpour and Farjah [47], where the authors consider the power flow control and management issues amongst multiple sources dispersed throughout both AC and DC MGs. A decentralized control strategy based on the two-stage modified droop method by measuring the AC MG frequency and the DC MG voltage is adopted for the control of the interface converter that is located between the AC and DC MGs. Using this droop method, the interlinking AC/DC converter is able to achieve power sharing under different modes of MG operation.

– *Virtual impedance*

The virtual-impedance-based control concept has increasingly been introduced in the literature as an extra characteristic of droop-based techniques [168], [196]. In

general, these virtual impedances are mainly embedded as an additional degree of freedom for active stabilization and disturbance rejection, or are used as a command reference generator to provide ancillary services to the MG.

In this context, a novel real-time voltage and frequency compensation strategy for mitigating the fluctuations in a PV-based AC MG is presented in the work of Shi *et al.* [177]. Here the authors perform voltage regulation using an adaptive virtual impedance loop while the frequency is regulated by means of an adaptive virtual frequency-impedance loop. In Yu *et al.* [202] and in Savaghebi *et al.* [174], a virtual impedance scheme has been proposed to improve the power-balance accuracy among converter-interfaced DG units. Furthermore, a virtual inductance realization scheme is carried out in the work of Li and Kao [112] so as to effectively prevent the coupling between the real and reactive power of converters. Here the authors state that, based on the predominantly inductive impedance, the proposed algorithm can considerably improve the reactive power control and sharing accuracy.

In [96] Kim *et al.* or in [205] Zhang *et al.* have conducted a study on an ancillary service provided by the adaptive virtual impedance so as to avoid the power flow circulation among converters connected in parallel. The latter work, for instance, proposes the interconnection of six three-stage solid-state transformer converters operated in parallel, and an adaptive virtual impedance is utilized for the suppression of circulating currents among them.

Gu *et al.* have introduced in [60] another interesting frequency-coordinating virtual impedance concept for an autonomous DC MG. Here the proposed technique is applied to the coordinating regulation of a hybrid ESS comprising batteries and supercapacitors. Depending on whether the storage unit is battery- or supercapacitor-based, the virtual impedance is adapted so the response time scale of their converters corresponds to their power capabilities. In this case, the virtual impedance dynamics of the supercapacitors will be faster than the one of the batteries.

– *Non-droop-based control*

Other strategies, namely non-droop-based control, where no communication network is used, have been reported in the literature aside from droop-based techniques. For instance, Ovalle *et al.* propose in [152] a decentralized control strategy in voltage-source-converter-dominated MGs based on the instantaneous power theory. Here the authors state that the power sharing objective among devices can be obtained without any communication links, barely with local measurements.

Another interesting control strategy applied to the voltage-source-converter-based DC-voltage power port in hybrid AC/DC multi-terminal MGs has been proposed in the work of Davari and Mohamed [39]. Here a robust multi-objective controller with a simple fixed-parameter low-order structure has been synthesized, which ensures great tracking performance, robust disturbance rejection, and robust stability against operating point or parameter variations.

As it can be noted, a large number of control strategies without communication network are based on droop control techniques. Nevertheless, as mentioned above, additional

modifications should be taken in droop techniques so as to guarantee a reliable and efficient management of the MG.

In some cases hybrid control approaches are also employed, although they are not as widely used as the aforementioned strategies [191]. Yu *et al.* have proposed in [202] a hybrid control structure for a distributed AC MG comprising parallel-connected inverter-interfaced DG units, where a communication-based and autonomous control strategy are combined. In this case, for such DG inverter blocks that are physically apart, the autonomous control is applied based on the modified wireless droop control technique. On the other hand, inside each inverter block, the parallel inverters which are near each other are controlled with a dynamic power distribution scheme. Here the authors state that this proposed strategy guarantees balanced power sharing while simultaneously increasing MG efficiency.

1.4 State-of-the-art on classical and advanced control in microgrids

Generally, a variety of conventional control techniques have been employed in the application of MGs such as PI/PID, sliding mode, linear quadratic with fixed parameters for a given operating point. In this case, a proper performance in steady state can be obtained with the prescribed values of the control system parameters. Nevertheless, these methods have limited possibility to ensure satisfactory trade-off among dynamic performances when the operating conditions vary significantly. As a result, the control parameters need to be retuned for the current case [125].

The stability and control issues of autonomous MGs are among the main challenges due to low inertia, uncertainties, and intermittent nature of DERs [151]. One critical control task in autonomous operation mode is the regulation of the network voltage and frequency. High-frequency ESSs – *e.g.*, lithium-ion batteries, flywheels, or supercapacitors – have thus become necessary for reliable and robust operation enhancement of autonomous MGs, leading to new grid configurations, for which more complex advanced control structures are needed for providing the MGs with desirable performance specifications in a wide range of operating conditions despite multiple constraints such as unexpected disturbances and model uncertainties. This section presents a review on classical and advanced control techniques which are applied to MGs. A comparative analysis among these control techniques is then shortly discussed.

1.4.1 Classical approach with PI/PID control

The PI/PID controller has widely been used in the industrial field and power systems for decades due to their simple structure. It is a robust, reliable controller and offers quasi-optimal performance of the control system with adequate tuning of gains [125]. In the literature, there are several strategies which have been employed to tune the PID gains, among which one can

cite use of Ziegler and Nichols, Cohen Coon, Chien, Hrones and Reswick, fine tuned, and rule of thumb methods [94], [125]. Nevertheless, the PI/PID tuning methods have limited capability of optimally tuning the PID gains for nonlinear and complex systems. Within this framework, the PID performance significantly depends on the suitable values of the PID parameters [125]. In order to overcome this disadvantage, Khooban *et al.* have successfully developed in [94] an intelligent online fuzzy tuning approach which is used to optimally select parameters of a PI/PID controller. In the work of Zhang *et al.* [204], a static synchronous series compensator with or without a battery-based ESS has been used to ensure power flow control, improve transient stability, and damp power oscillation in stand-alone grid. Under voltage and frequency fluctuations, classical PI controllers for the static synchronous series compensator and ESS systems are implemented to regulate power flow in the network.

1.4.2 Linear quadratic regulator

The idea of the linear quadratic regulator aims at minimizing/maximizing the utility cost function to compute the optimal control policy. One of the main challenging issues with the linear quadratic regulation is the appropriate selection of the weighted matrices “**Q**” and “**R**” required by the Riccati equation to ensure the proper response [125]. The linear quadratic regulator has been used in many engineering problems related to MGs.

In this context, Mishra *et al.* have applied in [136] a biogeography-based optimization technique to come up with the best “**Q**” and “**R**” matrices such that the MG frequency excursion consequent to a disturbance is minimized. A Kalman estimator has been used to estimate the states which may not be measurable in the practical system. These estimated states together with other measured states are employed by the linear quadratic regulator to generate the desired control signal. Here the authors state that the proposed approach improves the MG frequency response. Moreover, it is shown that the life span of the battery increases and its capacity decreases due to the participation of the wind energy conversion system in frequency control.

In the work of Shahnia *et al.* [175], a decentralized power sharing algorithm based on droop control for parallel converter-interfaced DG units in the system of multiple interconnected autonomous MGs has been introduced. A cascaded primary control structure is developed, where the inner control loop is in charge of appropriate switchings in the converter such that a proper tracking of the desired references in the DG converter output is obtained. This loop receives the references from the outer one and is based on the local current and voltage measurements in the DG converter output. In addition, a closed-loop optimal linear robust controller, namely linear quadratic regulator based on suitably tuned state feedback, is utilized in this inner loop to prevent instability and weak dynamic performance of the DG unit when autonomous MGs are interconnected. The outer control loop is responsible for proper output power control of the DG unit in the MG. This loop generates the proper references for the inner one and is different for the grid-connected and autonomous modes of operation. Here the authors state that the proposed method prevents any undesired voltage, power and frequency variations in the network.

Another systematic approach can be found in the work of Das *et al.* [38], where the authors have proposed the design of a linear-quadratic-regulator-based bumpless transfer controller so as to obtain seamless transition between the grid-connected and the islanded modes of MG operation. In the grid-connected mode, the inverter-interfaced DG units are current-controlled to provide constant active and reactive power, whereas they are regarded as voltage-controlled sources in the islanded mode. Severe voltage and frequency transients can arise during the transition between the two modes of operation. By optimally decreasing an error measure based on the linear quadratic regulator theory, the proposed bumpless compensator minimizes the error between the outputs of two controllers when the transition happens. It has been stated that the proposed resynchronizing and islanding compensators have considerably reduced the voltage and frequency transients during the mode transitions for a wide range of operating conditions.

1.4.3 Sliding mode control

Sliding mode control has exhaustively been studied for nonlinear robust control to guarantee stability subject to parameter constraints. The sliding mode control can suffer from the chattering problem once it is applicable for variable-structure problems. Generally, the sliding mode control has a number of disadvantages, *e.g.*, unacceptable transient and non-zero steady-state error. Nevertheless, the chattering can be dealt with through an adequate design of the feedforward controller and sliding surface [125].

In this context, Mishra *et al.* have applied in [137] a multiple control loop structure for a PV-diesel MG operating both in the grid-connected and isolated modes. Here three PI-control-based setpoint loops have been built so as to generate the required reference values for the second-order-sliding-mode-control-based main PV control loop. In this control scheme, the MG frequency is regulated by the DG unit, whereas the inverter of the PV system is responsible for the PCC voltage regulation. However, the authors note that one of the major limitations of this control scheme is that it cannot incorporate the changes in the system.

In the work of Rezaei *et al.* [164], a robust control scheme for an islanded multi-bus MG comprising multiple inverter-based DG units has been introduced. A master/slave control structure is adopted, where an adaptive-sliding-mode-based voltage controller is computed to robustly force the voltage magnitude and frequency of the master unit to track the predefined trajectories, while the output active and reactive power of the slave units are regulated by a direct power controller based on the adaptive input–output feedback linearization control method. In addition, the computational burden is also taken into account in the control design. Here the authors state that the proposed control method is well robust and stable against various disturbances, *e.g.*, MG black-start, harmonic and unbalanced load energization, and sudden accidental outage of slave units, as well as MG parameters uncertainties.

Another similar approach can be found in the work of Cucuzzella *et al.* [36], where high-order sliding mode control strategies have been proposed for an MG including several voltage-sourced-converter-interfaced DG units. More particularly, a second-order sliding mode control

algorithm is used for both the grid-connected and islanded modes of operation, while a third-order sliding mode algorithm is designed only for the islanded mode, so as to ensure, also in this case, chattering alleviation. *Via* the proposed sliding mode control laws, the authors state that the controlled MG system displays appreciable stability properties and guarantees closed-loop performance in the presence of load variations, nonlinearities, and inevitable modeling uncertainties. Following this work, the same sliding mode control strategy is adopted in [35], but in this case the dynamics of the interconnecting distribution lines are taken into account.

1.4.4 Model predictive control

Model-predictive-based control techniques are improved to predict the reference signals. A key feature of these schemes is that they minimize the tracking error [125].

In this context, Pahasa *et al.* have introduced in [154] a multiple model predictive control for plug-in hybrid electric vehicles bidirectional charging/discharging and *SoC* control for MG frequency stabilization, while simultaneously ensuring the desired *SoC*. Based on the plant model, past manipulate, and system control signals, the future control signals can be computed *via* a quadratic programming optimization. It has been stated that the multiple model predictive control is able to decrease the frequency variation, produce the desired *SoC*, and being robust subject to the system parameter uncertainties, compared with the PID and model predictive controllers. Similarly, the authors have proposed in [153] coordinated control of wind turbine blade pitch angle and plug-in hybrid electric vehicles for stabilizing the MG frequency using model predictive control. The simulation results performed in this study show that the proposed coordinated control reduces the MG frequency fluctuation and the number of plug-in hybrid electric vehicles, while being robust subject to the system parameters variation over the PID controller.

Wang *et al.* have presented in [197] an estimator-based voltage predictive control strategy for AC islanded MGs. For each DG unit, the proposed control strategy comprises a network voltage estimator serving to achieve network voltages response with no communication link and a voltage-predictive controller used to implement offset-free voltage control for a given bus. *Via* small-signal analysis, the proposed control approach is demonstrated to be able to perform offset-free voltage control without any communication links and robust to parametric uncertainties such as line parameters perturbation, load parameters variation, different disturbance locations, *LC* filters perturbation, output impedances perturbation, and DG units fault.

In the work of Minchala-Avila *et al.* [134], an optimal predictive control scheme applied to an islanded MG has been presented. A nonlinear model predictive control algorithm is employed for processing a data set comprising the batteries *SoC*, the DERs active power generation, and the predicted load. Under this approach, the balance between the power produced by the DERs and the load demand is ensured, while simultaneously keeping the voltage magnitude within the admissible maximum variation margin.

Another application can be found in the work of Tavakoli *et al.* [185], where the authors

propose a decentralized control strategy of multiple inverter-based DG units based on a combination of a voltage controller using model predictive control and a fast current controller applying discrete-time sliding mode control for restricting the inverter currents under overload conditions. Here the authors state that the proposed control strategy ensures robust stability and obtains desired performance, *e.g.*, fast transient recovery and zero steady-state tracking in voltage and current under short-circuit conditions, load transients, and unbalanced loads.

Liang *et al.* have proposed in [115] a nonlinear model predictive controller for operating coordination of two kinds of controllable resources represented by diesel generators and the battery-based ESS in an islanded MG so as to coordinately perform a frequency control and voltage regulations. Consequent to the fast variations due to renewable outputs, the proposed model predictive controller has the ability to effectively regulate the MG frequency and voltage. Moreover, by setting suitable values to the weighting factors of the objective functions, multiple operating objectives with different priorities can be obtained by this controller.

Another interesting solution has been presented in the work of Babqi *et al.* [7], where a control strategy is proposed for an MG composed of multiple voltage-sourced-inverter-interfaced DG units operating in both grid-connected and islanded modes. In the grid-connected mode, the power flow between each DG unit and the utility grid is managed by means of direct power model predictive control, whereas voltage model predictive control, as the primary control, and droop control, as the secondary control, are used to control the output voltage of each DG unit and the MG frequency in the islanded mode. Moreover, the proposed control approach is able to achieve a smooth transition while switching from the grid-connected to islanded mode and *vice versa*.

1.4.5 Artificial-intelligence-based control

In the literature, a variety of heuristic algorithms have been applied to improve the control and optimization for MGs and DG units, among which one can cite use of particle swarm optimization, fuzzy logic, neural network, and genetic algorithm. Thus, intelligent and evaluation techniques are effectively applied in both the grid-connected and islanded modes of MG operation [125]. Traditionally, trial and error strategy has given adequate droop performance in forms of few different DGs. Several powerful techniques have been proposed in the literature to optimally tune the values of controller parameters, for example, differential evolution algorithm [57], bacterial foraging optimization technique [135], colonial competitive algorithm using game theory [172], online cuckoo search technique [163]. A brief review on particle swarm optimization, fuzzy logic, and neural network is hereafter presented.

Particle swarm optimization

The particle swarm optimization has attracted a lot of research effort for a while due to its contribution in optimizing uncertain parameters for huge optimization issues [125].

In this context, Bevrani *et al.* have proposed in [17] an online intelligent approach by combining the fuzzy logic and the particle swarm optimization techniques to optimally tune the PI-based frequency controllers in AC MGs. Compared to the pure fuzzy PI and the Ziegler-Nichols PI control design methods, the proposed intelligent control synthesis achieves stability and better performance, and is robust against environmental and dynamical changes, *e.g.*, damping coefficient, inertia constant, droop constant, turbine time constant, generator time constant, flywheel-based ESS time constant, and battery-based ESS time constant.

As the operating conditions vary significantly due to sudden mode changes and variations in bus voltages and system frequency, MGs can endure performance degradation. In this context, in order to stably coordinate multiple inverter-interfaced DG units and to robustly control individual interface inverters subject to voltage and frequency disturbances, Chung *et al.* have presented in [33] controller design and optimization methods. Droop-control ideas are employed as system-level multiple DG units coordination controllers, while device-level inverter controllers are designed based on \mathcal{L}_∞ control theory. Moreover, use of particle swarm optimization algorithms yields optimal control parameters.

Using particle swarm optimization, Hassan *et al.* have introduced in [70] an optimal design of MGs in autonomous and grid-connected modes of operation. The particle swarm optimization technique is used to search for the optimal settings of the optimized parameters of PI controllers, filter, and power sharing coefficients. The proposed particle-swarm-optimization-based approach is demonstrated to be able to satisfy system performance under various disturbances, being robust with respect to its initial guess, and able to avoid trapping into local minima.

Fuzzy logic

Fuzzy logic control is exhaustively used in various challenge fields. Fuzzy logic control is regarded as one of the leading intelligent tools for addressing distributed power optimization problems. Critical developments of fuzzy logic control functions have mainly been carried out so as to provide more capability to deal with issues of expert systems [125].

In this context, a generalized droop control scheme for simultaneous voltage and frequency regulation in islanded MGs is proposed in the work of Bevrani *et al.* [16]. In order to propose a model-free based generalized droop control, a strategy based on adaptive neuro-fuzzy inference system is then developed. Here the authors state that the proposed intelligent control structure successfully tracks the generalized droop control dynamic behavior and displays desired performance and response in the presence of various load change scenarios.

Kamel *et al.* have proposed in [88] three control strategies to smooth the output power of the wind generation during the islanded mode of MG operation. First, a fuzzy logic pitch angle controller is developed, which can partially smooth the wind power fluctuations. Second, the ultracapacitor-based ESS controller is designed to completely suppress the fluctuations of the frequency, voltage, and active and reactive power caused by the wind power fluctuations inside the MG system. Then, storage batteries are used to sustain the MG in the islanding

mode. Here the authors state that the proposed controllers such as fuzzy logic, ultracapacitor-based ESS ensure better performance compared to the conventional PI controller. Moreover, the performance of the ultracapacitor-based ESS controller is shown to be better than that of the fuzzy logic controller, whereas conversely the cost of the fuzzy logic controller is much lower than that of the ultracapacitor-based ESS controller.

Khorramabadi *et al.* have introduced in [95] a critic-based self-tuning PI structure for active and reactive power control of voltage source converters in MGs. In order to deal with limited possibility of conventional PI controllers in the presence of power changes, disturbances, and high DG penetrations, an online tuning algorithm based on a fuzzy critic (*i.e.*, neuro-dynamic programming) for tuning the PI parameters is proposed. Here the authors state that the critic-based self-tuning PI controller has considerably enhanced the MG performance in terms of convergence time, power oscillations, and tracking error especially in case of higher DG penetrations, compared to the conventional PI controller.

Neural network

The idea of neural network is essentially coming from human brain. Neural networks have been applied in a wide range of research fields. A neural network may be effectively employed to identify, control, and optimize the system parameters in offline/online or real-time applications [125].

In this context, in the work of Mohamed *et al.* [139], based on neural network identification and deadbeat current regulation, an adaptive discrete-time grid-voltage sensorless interfacing scheme for DG inverters operating in the grid-connected mode has been proposed. First, the interfacing parameters and the grid voltage vector are simultaneously estimated online by a neural-network-based estimation unit of low computational demand. Second, use of a delay compensation method yields a deadbeat current controller of high bandwidth attribute. Third, a grid-voltage sensorless average-power control loop is implemented *via* the use of the estimated grid voltage, which ensures high power quality injection. Here the authors state that the proposed grid-voltage sensorless interfacing scheme is intrinsically self-tuning and ensures optimum performance with no constraint condition and *a priori* knowledge of the system.

Based on a radial basis function neural network incorporating particle swarm optimization, Kerdphol *et al.* have proposed in [92] an optimum online intelligent management method of both active and reactive power of a battery-based ESS so as to prevent the stand-alone MG from instability and system collapse. The battery-based ESS is centrally controlled by the radial-basis-function-neural-network-based controller, while particle swarm optimization is employed to compute the optimized active and reactive power during every change in the load/generation, so the effect of the MG frequency, voltage, and reference power regulation can be monitored. Here the authors state that the results predicted with the proposed radial basis function neural network model only slightly differ from the target results based on particle swarm optimization. Moreover, compared with the multilayer perceptron neural

network model, the radial basis function neural network model presents superior performance in terms of error efficiency and positional accuracy.

1.4.6 Adaptive control

Adaptive control techniques have widely been studied and attracted a lot of research effort over decades. Adaptive control strategies are mainly being employed to deal with parametric uncertainties and disturbances. Beyond any doubt, adaptive control strategies can effectively ensure sustained stability, robustness convergence, and tracking of the system dynamics. It should be noted that the operating conditions of the system may change. Consequently, the controller performance in the plant might not be optimal. In order to overcome such challenges, crucial adaptive solutions are exhaustively used to search for quasi-optimal operation conditions [125]. This work presents a couple of the most remarkable topics of adaptive control in MGs, namely adaptive PI/PID control, adaptive droop control, adaptive sliding mode control, and reinforcement learning.

Adaptive PI/PID control

PI/PID control with fixed gains has widely been used in various control problems. Nevertheless, when the operating conditions change due to external disturbances or uncertainties, the PID gains need to be automatically retuned to tackle these problems. A variety of evaluation algorithms have exhaustively been applied to adjust the PID gains, which enables online and self tuning of the PID parameters over the maximum operating points [125]. For example, neural network – a powerful tool – is trained in order to identify the PID parameters over a wide range of operating conditions. In the work of Mahmoud *et al.* [126], the output voltage and frequency regulation of stand-alone MGs are handled by the use of a neural-network-based distributed secondary control.

Adaptive droop control

Adaptive droop control has been a topic of increasing interest for enhancing stability, reliability, power quality, and robustness performance in MGs operation subject to disturbances. In this context, Mohamed *et al.* have proposed in [138] an adaptive decentralized droop-based control scheme for preserving power sharing stability of paralleled inverters in DG MGs. The proposed power sharing strategy is based on the combination of the static droop characteristics and an adaptive transient droop function, which yields a two-degree-of-freedom tunable controller. Active damping of power oscillations at various operating conditions can be guaranteed due to the adaptive nature of the proposed controller. Therefore, stable and robust power sharing performance is fulfilled in the paralleled inverter system.

In the work of Kim *et al.* [96], a mode adaptive droop control scheme with virtual impedances for an inverter-based flexible AC MG has been presented. In order to improve

the power loop dynamics, in the islanded mode of MG operation droop control associated with a derivative controller is utilized, while a combination of droop control and an integral controller is adopted in the grid-connected mode to properly control the power factor at the PCC. The proposed control is demonstrated to be able to work seamlessly in full mode of operation without control switching and improve power sharing performance.

Another application can be found in the work of He *et al.* [73], where an adaptive hybrid voltage and current controlled method is proposed to enhance power quality in electronically interfaced DG systems. When the MG suffers from frequency deviations, the proposed approach can enhance DG unit steady-state power control accuracy. Moreover, under varying MG frequency conditions, the DG unit also attains superior harmonic compensation performance *via* the proposed adaptive method.

Adaptive sliding mode control

Su *et al.* have proved in [182] a considerable enhancement in stability, reliability, dynamic response, and robustness performance of stand-alone MGs *via* the use of a centralized stabilizer control system, namely adaptive robust total sliding mode control. MGs are beneficial from this kind of reliable and effective control to deal with the issues that might occur due to uncertainties and disturbances.

In the work of Liu *et al.* [119], a control scheme for a three-phase four-wire inverter operating in both the grid-connected and islanded modes is proposed. In the grid-connected mode, the inverter is controlled by an inner adaptive sliding-mode-control-based current loop and an outer constant power control loop, which effectively rejects grid voltage disturbances and parameter uncertainties, meanwhile generating constant currents to the grid. In the islanded mode, the inverter is controlled *via* an inner adaptive sliding-mode-control-based voltage loop, an immediate virtual resistive output impedance loop, and an outer power sharing control loop, which ensures the parallel operation of the MG inverters with robust performance and power sharing accuracy. During the transition, the proposed control scheme guarantees dynamic characteristics and disturbance rejection performance.

Chen *et al.* have proposed in [31] an adaptive sliding mode voltage control strategy to improve disturbance rejection performance for parallel-operated inverters in islanded MGs. External disturbances and internal perturbation can be observed by the proper design of adaptive algorithms, which makes the control system obtain global robustness. By properly designing an adaptive algorithm of the switching gain, the undesirable chattering of the control input signal can significantly be reduced. The proposed control scheme is demonstrated to be able to effectively reduce the total harmonic distortion, chattering, and steady-state error of the inverter output voltage, as well as to enhance dynamic performance and disturbance rejection capability of the inverter control system.

In the work of Kalla *et al.* [87], an adaptive sliding mode control strategy for a stand-alone single-phase hydro-wind-PV-battery hybrid power generation system is proposed. An adaptive sliding mode control algorithm is utilized to estimate the reference source current,

which serves for single-phase voltage-source converter control, MG voltage and frequency regulation, and current harmonics mitigation. Here the authors state that the proposed control strategy can regulate the MG voltage and frequency in response to a sudden change in loads and under intermittent penetration of renewable energy.

Reinforcement learning

In the literature, the reinforcement learning methodology has been introduced in terms of actor-critic networks to control of stand-alone MGs [125]. In the work of Abouheaf *et al.* [1], reinforcement learning based on a value iteration algorithm is utilized to tackle load fluctuations. Reinforcement learning is effectively used to decrease electricity prices by improving the management process of the electric power in the grid-connected mode of agents operation and performed to regulate voltages and frequency in the operation of islanded agents. Thus, reinforcement learning has the capability to determine the optimal policy decisions and the best objective function for system performance improvement, as stated in the work of Li *et al.* [107].

The reinforcement learning algorithm based on machine learning is proposed to obtain customer goals for the battery scheduling, as stated in the work of Kuznetsova *et al.* [102]. This algorithm has considerably increased the utilization rate of the battery during peak load demand. The reinforcement learning mechanism predicts available wind power to take good decision for the optimal battery scheduling.

1.4.7 Robust control

\mathcal{H}_∞ robust control theory applied to frequency and voltage regulation in MGs has attracted the attention of many researchers for several reasons. First, many control objectives such as disturbance attenuation, robust stabilization of uncertain systems, or shaping of the open-loop response can be handled by \mathcal{H}_∞ and μ -synthesis techniques [32]. Then, the solution found is optimal with respect to a defined criterion, which means that if no solution to the control objectives is found, then no solution exists. Next, there is a link between the imposed dynamic performance and the control design, which means that the control objectives can be fulfilled if the design of the control system is properly implemented. Finally, sensitivity and robustness analysis to model uncertainties can possibly be associated with \mathcal{H}_∞ and μ -synthesis controls.

Generally speaking, the \mathcal{H}_∞ control problem has widely been used to synthesize the \mathcal{H}_∞ controller so as to ensure system stability and performance in the presence of model uncertainties and external disturbances using LMI methods. LMI is a powerful tool that is used to directly search for a feasible and optimal solution. More particularly, the vital goal of \mathcal{H}_∞ control is to reduce the impacts of the uncertainties and the disturbances. In addition, it is an effective strategy for transient characteristic enhancement against the uncertainties [125].

Some studies on frequency robust control for various MGs have already been conducted in

the literature. For example, in the work of Goya *et al.* [58], based on droop characteristics, \mathcal{H}_∞ control theory is applied to frequency control in isolated MGs composed of diesel generators, wind turbine generators, battery-based ESSs, and loads. A control system is designed to enable parallel operation without communication between these units and to achieve active load sharing demand. \mathcal{H}_∞ -based droop controllers are used for the battery-based ESSs. The diesel generator is also controlled *via* an \mathcal{H}_∞ controller. Here the proposed \mathcal{H}_∞ -based droop control system achieves better transient response compared to the conventional droop control systems. In addition, use of the \mathcal{H}_∞ -based droop control system ensures robust stability against the measurement noise. In this study, system trade-offs are optimized, however, the controllers robustness to model uncertainties is not analyzed.

Similarly, Singh *et al.* have presented in [179] \mathcal{H}_∞ control with loop shaping through genetic algorithm and particle swarm optimization and \mathcal{H}_∞ -based droop control for improving frequency deviation in isolated hybrid generation systems composed of DG units, ESSs, and loads. Only the controller sensitivity to system parameter uncertainties is analyzed in this study. The performance of the particle-swarm-optimization-based \mathcal{H}_∞ controller is demonstrated to be more robust against system parameter uncertainties, random wind input, and load change compared with the other controllers.

Another \mathcal{H}_∞ approach based on decentralized static output feedback for coordination of storage and generation in power system frequency control can be found in the work of Zhu *et al.* [209]. *Via* frequency-dependent weighting functions introduced in the \mathcal{H}_∞ control configuration, a so-called frequency separation objective is fulfilled, where low-frequency components of the RES and load variations are compensated by the conventional generators, while the ESSs are responsible for balancing high-frequency components in the RES and load variations. The involved \mathcal{H}_∞ problem is solved by use of an improved iterative linear matrix inequality algorithm.

In a similar way, an \mathcal{H}_∞ -based frequency robust control approach for coordination of a wind turbine generator and a battery-based ESS in a small power system has been introduced in the work of Howlader *et al.* [76]. The \mathcal{H}_∞ controllers are designed for the pitch angle system of the wind turbine generator and the output power command system of the battery-based ESS. Here the authors state that the proposed method can alleviate the wind turbine blades stress, decrease the frequency deviation, and reduce the size of the battery-based ESS. However, these studies do not analyze the controllers robustness subject to model uncertainties.

Han *et al.* have proposed in [69] a robust control strategy for reducing system frequency deviation due to load and RESs fluctuations in an MG with attached storage. A D - K -iteration-based μ -synthesis control approach is used to cope with system uncertainties such as load transients, wind turbine generation output fluctuations, model uncertainties, and measurement noise/errors. Here the authors state that the MG frequency deviation can be considerably reduced while at the same time minimizing the size of storage. In addition, compared with conventional PID control, this approach is demonstrated to be much more robust and has better performance.

Another interesting application can be found in the work of Bevrani *et al.* [14], where the focus is on \mathcal{H}_∞ and μ -synthesis (via D - K iteration) robust control techniques for improving secondary frequency control performance in an islanded MG. Uncertainties in the MG model are here included in the control synthesis procedure. In the \mathcal{H}_∞ control approach, the parametric perturbation is modeled as the unstructured uncertainty, while the structured uncertainty is used in the μ -synthesis method. The proposed controllers are shown to be able to properly balance the power generation and load and to effectively regulate the MG frequency. In addition, the μ -synthesis controller ensures better performance compared to the \mathcal{H}_∞ controller.

With regard to voltage robust control in MGs, several studies on this topic have been reported in the literature. For example, Li *et al.* have presented in [113] a robust control scheme for an MG with a power-factor correction capacitor connected at the PCC. An integrated control strategy composed of an outer \mathcal{H}_∞ voltage controller, an inner filter inductor current feedback controller, and a virtual resistance compensator is presented. By properly selecting the weighting functions, the synthesized \mathcal{H}_∞ controller designed for stable control of the DG interfacing voltage-source inverter can effectively produce desired performance and explicitly specify the degree of robustness against effective shunt filter capacitance variations.

Kahrobaeian *et al.* have introduced in [85] a robust system-oriented control approach for voltage performance improvement and suppression of typical interaction dynamics in DG converter-based MGs. The proposed control scheme uses a robust \mathcal{H}_∞ voltage controller which is designed under an extended model comprising different converter-MG interactions imposed on the output voltage, *e.g.*, MG impedance variation, local load interactions, uncertainties in the AC-side filter parameters. Unlike conventional droop controllers, the proposed strategy generates a two-degree-of-freedom controller, leading to stable and smooth power sharing performance over a wide range of loading conditions. Similarly, the authors have presented in [83] a direct single-loop μ -synthesis voltage control scheme for suppression of multiple resonances caused by power-factor correction capacitors and residential capacitive loads in DG MGs. Compared to the conventional \mathcal{H}_∞ multi-loop controller, the proposed μ -synthesis single-loop controller, with reduced sensor requirement and no additional passive or active damping mechanism, can ensure robust stability and robust performance of the MG subject to parameter uncertainties and uncertain resonant peaks due to the connection of the power-factor correction capacitors.

Another interesting approach can be found in the work of Li *et al.* [114], where a novel cascaded-loop strategy for control of a grid-forming inverter has been proposed. Even if a precise model for the inverter system is not required, the proposed method can tackle uncertainties and LC filter resonance without any passive or active damping techniques. It comprises a sliding-mode-control-based inner current loop and a mixed- $\mathcal{H}_2/\mathcal{H}_\infty$ -control-based outer voltage loop, which provides the benefits of constant switching frequency, low total harmonic distortion, robustness against parameters variations, and fast transient response. Moreover, the proposed control strategy is demonstrated to be able to ensure better transient and steady performance compared to the conventional PI-based nested-loop control method.

Other voltage robust control strategies have also been conducted in the literature, for

example, robust two-degree-of-freedom feedback-feedforward control scheme for islanded operation of an MG in the work of Babazadeh *et al.* [6], robust multi-objective control based on μ -synthesis approach applied to the voltage-source-converter-based DC-voltage power port in hybrid AC/DC multi-terminal MGs in the work of Davari *et al.* [39], \mathcal{H}_∞ -loop-shaping-based robust control design for current sharing improvement in an islanded MG composed of parallel-connected inverter-interfaced DG units in the work of Taher *et al.* [183], \mathcal{H}_∞ -based robust control for autonomous operation of an MG comprising electronically coupled DG units under unbalanced and nonlinear load conditions in the work of Hamzeh *et al.* [67], reactive power compensation and voltage stability of a PV-wind-diesel hybrid power generation system with robust control based on \mathcal{H}_∞ loop shaping through genetic algorithm and particle swarm optimization and μ -synthesis in the work of Mohanty *et al.* [141], voltage control strategy based on feedforward compensation and internal model robust feedback control applied to autonomous operation of three/single-phase hybrid multi-microgrid in the work of Wang *et al.* [194], decentralized robust control strategies for plug-and-play voltage stabilization in islanded inverter-interfaced MGs and in islanded DC MGs in the work of Sadabadi *et al.*, [171] and [170] respectively.

Another similar work for utilizing \mathcal{H}_∞ robust control is presented in [110]. Mixed $\mathcal{H}_2/\mathcal{H}_\infty$ control schemes can be found in [9] and [10]. More works on μ -synthesis robust control methods are introduced in [84], [66], [109], and [184]. \mathcal{H}_∞ robust control for power sharing in both grid-connected and islanded modes of MG operation is given in [75] and [55].

1.4.8 Comparative analysis of classical and advanced control techniques

Some of the main advantages and drawbacks of the classical and advanced control techniques are now resumed and illustrated with the recent state-of-the-art. The main ideas presented below are detailed in [125]. The PI/PID control can provide good performance with simple structure, widely applicable in industrial process systems, and has only three parameters to optimize. Nevertheless, the PI/PID controller with fixed gains cannot deal with control challenges due to fast change of operating points and/or complex systems. In addition, it is difficult to tackle MIMO and large-scale systems. The linear quadratic regulator is more beneficial (stable and robust) than the PI/PID control, in which an optimal solution can be yielded in terms of weighted matrices. However, it has some disadvantages, *e.g.*, all the system states need to be measurable, constraints and disturbances in the system cannot be tackled, it is quite difficult to find an analytical solution to the Ricatti equation. The sliding mode control is more advantageous than the linear quadratic regulator since it is robust against disturbances and model uncertainties. The sliding mode controller is a nonlinear one with low computational burden. However, its major shortcoming is the chattering phenomenon due to the discontinuous terms and sometimes it exhibits unacceptable performance in terms of unmatched uncertainties and load variations. The model predictive control is fast computing, widely used especially in industrial plants, straightforward applicable to large and multi-variable processes, and can predict system dynamic behavior over a finite horizon. It has the advantage over the linear quadratic regulator since it can deal with state and control constraints, non-minimum phase behavior, interaction among variables, and system complex-

ity. However, the greatest drawback of the model predictive control is that it needs to identify the process model correctly. Moreover, it cannot tackle unknown parameters due to its strong dependence on the model and performance analysis is quite difficult as well. Heuristic algorithms, namely particle swarm optimization, fuzzy logic, and neural network have extensively been used to tune parameters and learn behavior of dynamic systems. Nevertheless, their main shortcoming is that they search for the quasi-optimal solution only and cannot sustain the optimal solution. Generally, particle swarm optimization has some advantages, *e.g.*, ability to solve nonlinear, non-differentiable, and multi-modal function optimization, simplicity and ease of implementation, effectiveness by means of adjustable parameters. However, it has various parameters to tune with slow convergence rate and produces quasi-optimal solutions only. In terms of fuzzy logic and neural network, they have the ability to handle nonlinear and fast-varying systems, and are also effective with small-scale systems. Conversely, various parameters need to be tuned, inducing large sensitivity to the distribution of the memberships, difficulties in analyzing and tuning large-scale systems, and long-time training period are amongst their major drawbacks.

In spite of some drawbacks such as enough mathematical understanding requirement, being probably impractical for large-scale systems, robust control has various advantages over the above mentioned control techniques. Indeed, it is very useful to deal with MIMO models for which many control objectives can simultaneously be fulfilled. Then, *via* an optimization algorithm, an optimal solution can be yielded with respect to a defined criterion. In addition, the desirable dynamic performance imposed can be linked with the control design procedure *via* the so-called weighting functions. Moreover, robust control can tackle model uncertainties and minimize the impact of disturbances on the control system. Robust control is also applicable for cross-coupling among communication paths and communication constraints. Due to its benefits, robust control, more particularly \mathcal{H}_∞ control, will be used for frequency and voltage stability problems of stand-alone MGs in this thesis framework.

1.5 Basics on \mathcal{H}_∞ control methodology

In this section, a general presentation of the robust and optimal control theory used in this thesis is proposed. Some basic definitions and principles of the \mathcal{H}_∞ robust control theory are introduced. Then, the mixed sensitivity methodology is presented. Next, some introductory principles on defining the desired performance specifications are given. We also discuss the methods available for control design and robustness analysis.

1.5.1 Singular values and \mathcal{H}_∞ norm

Before the presentation of the \mathcal{H}_∞ control synthesis approach, some basic definitions are introduced for better understanding the mathematical indications of the control procedure. These definitions are outlined in detail in the classic books by Zhou *et al.* [208], Duc and Font [46], Skogestad and Postlethwaite [180].

Singular values of a transfer matrix

Let $\mathbf{G}(s)$ be the transfer matrix between an input vector $\mathbf{u}(t)$ and an output vector $\mathbf{y}(t)$, of dimension m and p respectively, of a linear time-invariant system. For a mono-variable system, the gain of the system at the pulsation ω is defined by the modulus $|\mathbf{G}(j\omega)|$. In the multi-variable case, the notion of singular values is used. These singular values correspond to the square roots of the eigenvalues of $\mathbf{G}(j\omega)$ multiplied by its transconjugate as follows [46]

$$\sigma_i(\mathbf{G}(j\omega)) = \sqrt{\lambda_i(\mathbf{G}(j\omega)\mathbf{G}(-j\omega)^T)} = \sqrt{\lambda_i(\mathbf{G}(-j\omega)^T\mathbf{G}(j\omega))}, \quad i = 1, \min(m, p). \quad (1.1)$$

The singular values are positive or null real numbers. We then denote $\bar{\sigma}(\mathbf{G})$ as the highest singular value and $\underline{\sigma}(\mathbf{G})$ the smallest. The singular values $\sigma_i(\mathbf{G}(j\omega))$ constitute a generalization of the notion of gain to multi-variable systems. For a multi-variable system, the gain at a given frequency is between the lower and upper singular value [46].

\mathcal{H}_∞ norm of a linear time-invariant system

A linear time-invariant system can be described by the following state-space representation

$$\begin{cases} \dot{\mathbf{x}}(t) = \mathbf{A}\mathbf{x}(t) + \mathbf{B}\mathbf{u}(t) \\ \mathbf{y}(t) = \mathbf{C}\mathbf{x}(t) + \mathbf{D}\mathbf{u}(t) \end{cases} \quad (1.2)$$

The transfer matrix of this system is then given by

$$\mathbf{G}(s) = \mathbf{C}(s\mathbf{I} - \mathbf{A})^{-1}\mathbf{B} + \mathbf{D}. \quad (1.3)$$

For every matrix $\mathbf{G}(s)$ in \mathcal{RH}_∞ (the set of transfer matrices $\mathbf{G}(s)$ corresponding to a stable system), the \mathcal{H}_∞ norm, denoted as $\|\mathbf{G}(s)\|_\infty$, is defined as follows [46]

$$\|\mathbf{G}(s)\|_\infty = \sup_{\omega \in \mathcal{R}} \bar{\sigma}(\mathbf{G}(j\omega)). \quad (1.4)$$

$\|\mathbf{G}(s)\|_\infty$ is the highest value of the system gain over the studied frequency range. This value should be minimized in order to improve the stability of the system. The minimization of this norm will result in minimizing the energy of the system in the vicinity of an unstable pole [208], [46], [180].

1.5.2 \mathcal{H}_∞ control approach

The basic principles of the \mathcal{H}_∞ robust control theory together with the mixed-sensitivity problem, the definition of the desired performance specifications, and the methods used for control design are hereafter presented.

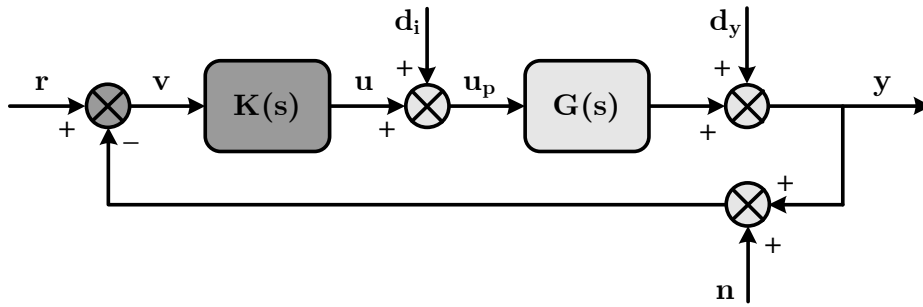


Figure 1.15 – Classical control structure.

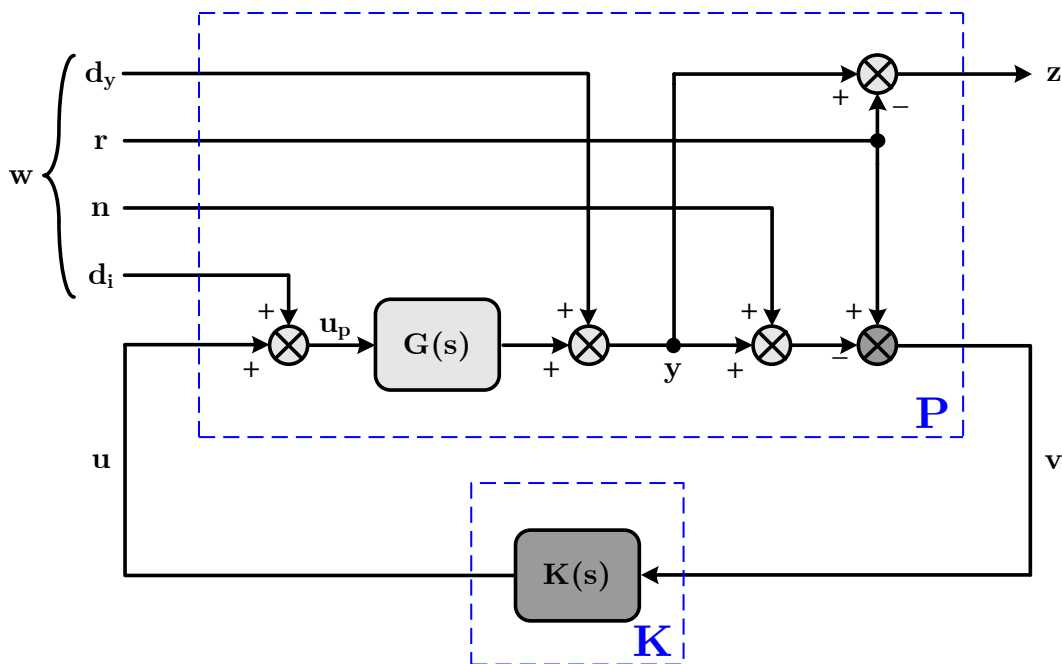


Figure 1.16 – Classical control structure in the so-called **P** – **K** form.

General control configuration

The control problem of any system can be reduced to the classical control scheme as shown in Figure 1.15, where $\mathbf{K}(s)$ denotes the controller to be synthesized, $\mathbf{G}(s)$ the controlled plant described by its transfer matrix, \mathbf{r} the references, \mathbf{u} the control signals, \mathbf{d}_i and \mathbf{d}_y the input and output disturbances respectively, and \mathbf{n} the measurement noises. Subsequently, the measurement noises and the input disturbances are considered to be equal to zero, *i.e.*, $\mathbf{n} = 0$ and $\mathbf{d}_i = 0$. This scheme can be redesigned in a **P** – **K** form as illustrated in Figure 1.16.

Based on the classical control structure, the general control configuration can be deduced as shown in Figure 1.17. In its simplest form, the \mathcal{H}_∞ problem is a disturbance rejection

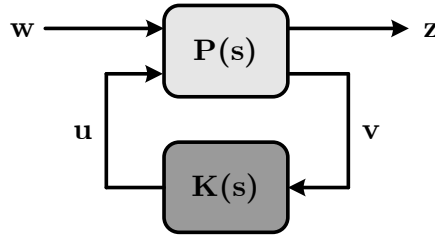


Figure 1.17 – General control configuration.

issue. It consists in minimizing the effects of the inputs \mathbf{w} on the “error” signals \mathbf{z} of a system [208], [46], [180]. In order to achieve this objective, the measured signals \mathbf{v} and the control signals \mathbf{u} are required. The system in Figure 1.17 can be written in the following form

$$\begin{bmatrix} \mathbf{z} \\ \mathbf{v} \end{bmatrix} = \mathbf{P}(s) \begin{bmatrix} \mathbf{w} \\ \mathbf{u} \end{bmatrix} = \begin{bmatrix} \mathbf{P}_{11}(s) & \mathbf{P}_{12}(s) \\ \mathbf{P}_{21}(s) & \mathbf{P}_{22}(s) \end{bmatrix} \begin{bmatrix} \mathbf{w} \\ \mathbf{u} \end{bmatrix}, \quad (1.5)$$

$$\mathbf{u} = \mathbf{K}(s) \mathbf{v}. \quad (1.6)$$

Let us note that the closed-loop transfer from \mathbf{w} to \mathbf{z} is computed by the linear fractional transformation as follows [208], [46], [180]

$$\mathbf{F}_1(\mathbf{P}, \mathbf{K}) = \mathbf{P}_{11} + \mathbf{P}_{12} \mathbf{K} (\mathbf{I} - \mathbf{P}_{22} \mathbf{K})^{-1} \mathbf{P}_{21}. \quad (1.7)$$

The \mathcal{H}_∞ optimal control problem then consists in finding a stabilizing controller \mathbf{K} which minimizes the following term [208], [46], [180]

$$\|\mathbf{F}_1(\mathbf{P}, \mathbf{K})(s)\|_\infty = \max_{\omega} \bar{\sigma}(\mathbf{F}_1(\mathbf{P}, \mathbf{K})(j\omega)). \quad (1.8)$$

For the majority of applications, it is not necessary to obtain an optimal controller for the \mathcal{H}_∞ problem and it is often easier (numerically) to solve a sub-optimal problem. Let γ_{min} be the minimum value of $\|\mathbf{F}_1(\mathbf{P}, \mathbf{K})(s)\|_\infty$ which can be reachable. Let $\gamma > \gamma_{min}$, the sub-optimal problem consists in finding a stabilizing controller \mathbf{K} such as [208], [46], [180]

$$\|\mathbf{F}_1(\mathbf{P}, \mathbf{K})(s)\|_\infty < \gamma. \quad (1.9)$$

Let us note that by reducing γ little by little, we can approach the optimal solution.

Mixed-sensitivity problem

Here we discuss the definition of required performances for the control problem. Let us take again the classical control structure in Figure 1.15 for a SISO system, where the controller has only one degree of freedom. Thus, we can write

$$y = \underbrace{\frac{G(s)K(s)}{1+G(s)K(s)}}_{T(s)} r + \underbrace{\frac{1}{1+G(s)K(s)}}_{S(s)} d_y - \underbrace{\frac{G(s)K(s)}{1+G(s)K(s)}}_{T(s)} n + \frac{G(s)}{1+G(s)K(s)} d_i. \quad (1.10)$$

The S transfer is called the sensitivity function of the system, and the T transfer the complementary sensitivity function. Note that we have the equality $S + T = I$. Therefore, we must minimize S for the output disturbance rejection d_y , and minimize T for the insensitivity to the measurement noise n . However, this objective cannot simultaneously be fulfilled (*i.e.*, on the same frequency domain) since $S + T = I$, thus trade-offs must be formalized in the control problem, namely S/T mixed synthesis [208], [180], [173]. For the disturbance rejection problems, the KS transfer is also often of considerable importance. This transfer describes the behavior of the control signal u following an output disturbance d_y . It is important to include the KS transfer in the control problem to limit the demand on amplitude and bandwidth. The amplitude limitation may allow avoiding possible destruction of the actuator. The bandwidth limitation, on the other hand, can be used to impose a practical implementation constraint to the controller (indeed, it is not possible to design an infinitely fast actuator). In summary, the limitation on KS therefore limits the control energy used [180], [173]. This constitutes a S/KS mixed synthesis.

In order to formalize the required performances for each of the S and KS transfers, we will use frequency weights, namely $W_{perf}(s)$ for S and $W_u(s)$ for KS . We will explain how to choose these transfers in the sequel. The \mathcal{H}_∞ problem consists in minimizing [208], [46], [180]

$$\|F_l(P, K)(s)\|_\infty = \left\| \frac{W_{perf}S}{W_uKS} \right\|_\infty < \gamma. \quad (1.11)$$

Performance specifications

The desired performance specifications are introduced in the form of some weighting functions (frequency filters) on the sensitivity transfer characteristics [208], [46], [180]. The system \mathbf{P} in (1.5) then comprises the original open-loop system and the specified weighting functions. Here we consider the output disturbance d_y as the only disturbance of the system. This structure is depicted in more details in Figure 1.18, which corresponds (if $G_d = 0$) to the S/KS mixed-sensitivity problem. Nevertheless, these results can easily be extended to the general case [74].

The functions with robustness and performance requirements are expressed by the following structure [208], [46], [180], [74]

- Weighting function on the sensitivity function $S(s) = 1/(1 + G(s)K(s))$ (Figure 1.19)

$$\frac{1}{W_{perf}(s)} = \frac{s + \omega_b A_\varepsilon}{s/M_s + \omega_b}. \quad (1.12)$$

The function $1/W_{perf}(s)$ can be representative of the time-domain response specifications, where the high-frequency gain M_s has an impact on the system overshoot and module margin, the low-frequency gain A_ε can allow steady-state error limitation, and the cut-off frequency ω_b is representative of the response time.

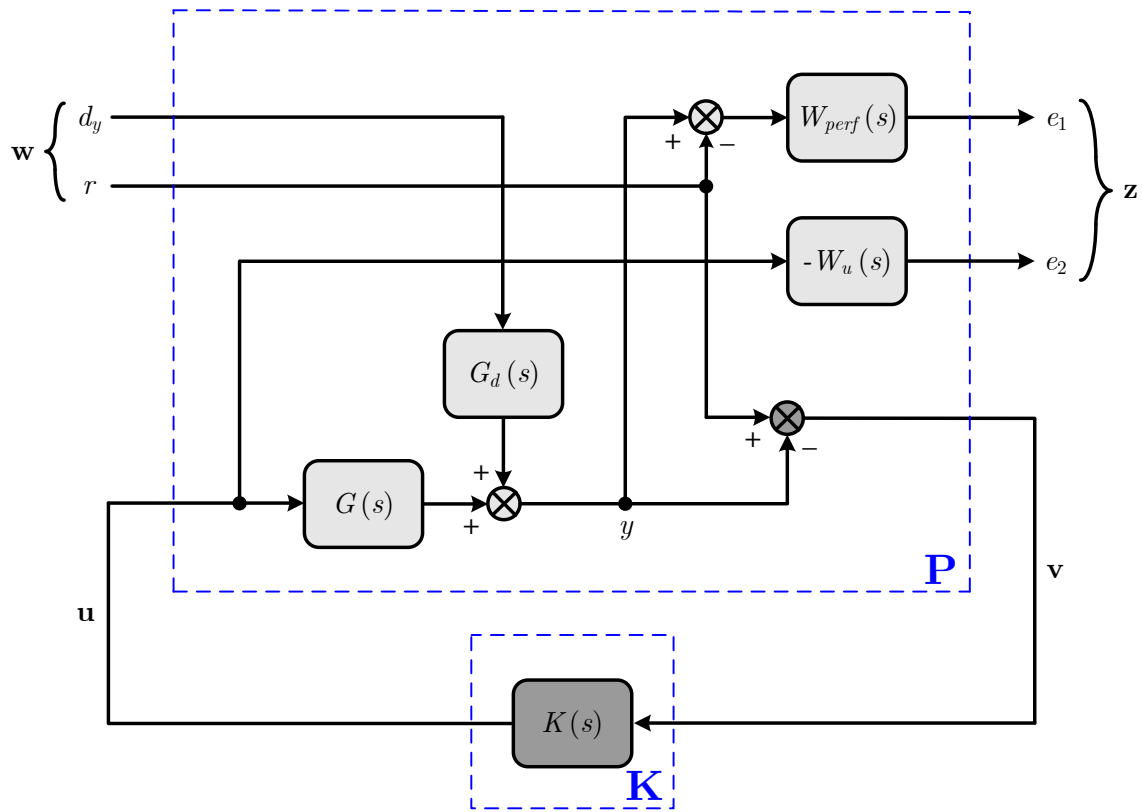


Figure 1.18 – Control configuration in the so-called **P** – **K** form including weighting functions [180], [74].

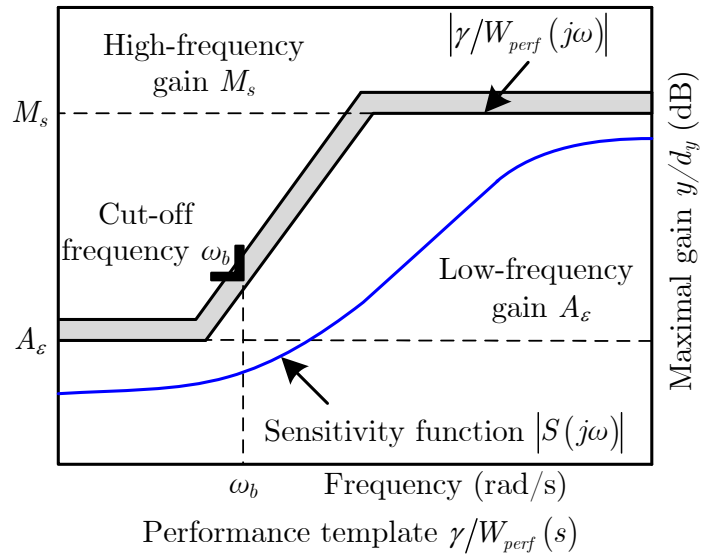


Figure 1.19 – Weighting function $W_{perf}(s)$ for the sensitivity function $S(s)$.

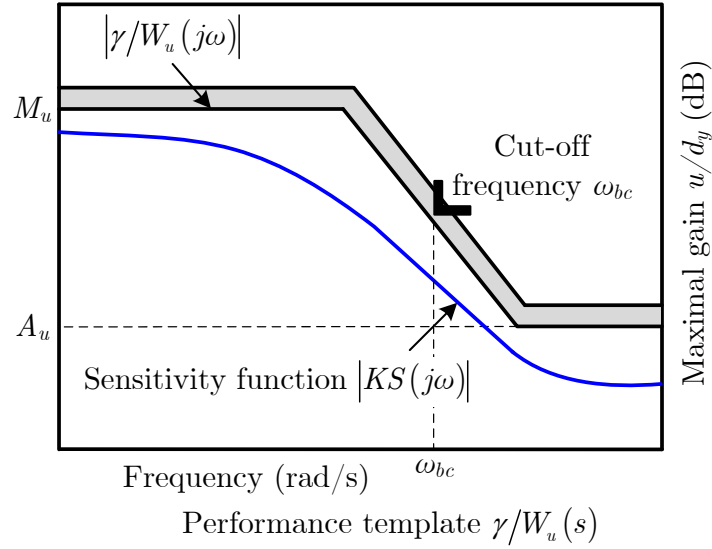


Figure 1.20 – Weighting function $W_u(s)$ for the complementary sensitivity function $KS(s)$.

- Weighting function on the complementary sensitivity function $KS(s) = K(s) / (1 + G(s)K(s))$ (Figure 1.20)

$$\frac{1}{W_u(s)} = \frac{A_u s + \omega_{bc}}{s + \omega_{bc}/M_u}. \quad (1.13)$$

For this weighting function M_u is chosen to match the system behavior at low frequencies and is normally utilized to include some limitation on the control input (for limitations on system actuators, for instance). In this case, ω_{bc} has an impact on the system robustness and can accordingly be chosen for ensuring good robust performance.

Numerical solution of the \mathcal{H}_∞ problem by the Riccati and LMI methods

The numerical solution of the \mathcal{H}_∞ problem by the Riccati equations utilizes the Glover-Doyle algorithm. This algorithm was implemented in the 1980s [56], [43] and is considered as the basis of \mathcal{H}_∞ synthesis applications. The controller synthesis by the LMI method is more recent than that using the Riccati equations. LMI is regarded as a very powerful tool in robust control optimization theory. LMI is a mathematical formulation that allows to solve a convex optimization problem [32]. The optimal control design for MIMO systems with multi-objective performances is the key interest of this methodology. Conversely, the order of the controller may be high even if some order reduction methods are possible and proven.

1.5.3 Robust stability and robust performance analysis

In this thesis framework, analysis of closed-loop systems is based on both time and frequency responses. Nevertheless, robustness is a key attribute of the proposed \mathcal{H}_∞ control methodol-

ogy. A control system is said to be robust if it is insensitive to a model subject to uncertainties. These uncertainties on the model/plant could be representative of the unknown or neglected (unmodeled) dynamics of the system. The objective of the robustness analysis is to determine whether the controller ensures both stability conditions and desired performances or not for a system subject to modeling uncertainties. An exhaustive review on robustness analysis, for both SISO and MIMO systems, can be identified in the work of Zhou *et al.* [208] and Skogestad and Postlethwaite [180].

Uncertainties modeling

Uncertainties are assumed to be bounded in norm around their nominal values and can be classified into two main categories, namely structured and unstructured uncertainties. The unstructured uncertainties are used to represent the different dynamics of the real system which are neglected in the theoretical (mathematical) model or the misunderstandings of the model in high frequencies. The structured uncertainties are regarded as parametric uncertainties which have impact on low frequency performance [208], [46], [180].

The parametric uncertainties are modeled assuming that each uncertain parameter x varies between upper and lower margins [208], [180], *i.e.*, $x = x_{nom} (1 + p_x \delta_x)$, where x_{nom} is the nominal value of the parameter and p_x the relative uncertainty on x . In this case, δ_x is a real or scalar perturbation, with $|\delta_x| \leq 1$. The dynamics uncertainties can be defined in the frequency domain. They are then characterized by a complex perturbation Δ which is normalized in such a way that $\|\Delta(s)\|_\infty \leq 1$ [208], [46], [180].

Once the uncertainties of the system are identified, they can be put into the following diagonal matrix form [208], [46], [180]

$$\mathbf{\Delta}(s) = \text{diag} \{ \delta_1 I_{r_1} \quad \cdots \quad \delta_i I_{r_i} \quad \cdots \quad \delta_r I_{r_r} \quad \Delta_1(s) \quad \cdots \quad \Delta_j(s) \quad \cdots \quad \Delta_q(s) \}, \quad (1.14)$$

where $\delta_i \in \mathcal{R}$, $i = \overline{1, r}$, and $\Delta_j \in \mathcal{RH}_\infty$, $j = \overline{1, q}$. In addition, the following normalization conditions are generally adopted

$$(\delta_i \in]-1, +1[; \|\Delta_j(s)\|_\infty \leq 1) \Leftrightarrow (\|\mathbf{\Delta}(s)\|_\infty \leq 1). \quad (1.15)$$

The matrix $\mathbf{\Delta}(s)$ thus comprises r real blocks, namely “repeated scalars” (the scalar δ_i being repeated r_i times so as to account for the corresponding uncertainty), related to the parametric uncertainties and q full complex blocks (of dimension r_j) representing the neglected dynamics uncertainties.

μ -Analysis

The robustness analysis in the presence of model uncertainties is implemented using μ -analysis. Some theoretical fundamentals on this technique are discussed in detail in [208] and [180]. Many practical problems are also solved by this approach, for example, in [39],

[83], [84], [66], [69], [104], [109], [14], [141], and [184]. We now define the structured singular value μ .

- **Structured singular value μ**

The structured singular value is normally denoted as μ . The obtention of this value represents an analysis tool that allows to estimate the stability margins of a multi-variable system subject to uncertainties. Nevertheless, the perturbation matrix is now expressed using the structured form, *i.e.*, $\Delta(\mathbf{s}) = \text{diag} \{ \Delta_{\mathbf{f}}(\mathbf{s}) \quad \Delta_{\mathbf{s}}(\mathbf{s}) \}$, a block-diagonal matrix which is made up of [208], [180]:

- 1 n fictive uncertainties, related to frequency weights representative of performances: $\Delta_{\mathbf{f}}(\mathbf{s}) = \text{diag} \{ \Delta_{f_1}(s) \quad \Delta_{f_2}(s) \quad \cdots \quad \Delta_{f_n}(s) \}$, with $\|\Delta_{f_i}(s)\|_\infty \leq 1$, $i = \overline{1, n}$;
- 2 r real blocks, linked with parametric uncertainties. Each parametric uncertainty is repeated $r_{n+1}, r_{n+2}, \dots, r_{n+r}$ times: $\text{diag} \{ \delta_{n+1} I_{r_{n+1}} \quad \delta_{n+2} I_{r_{n+2}} \quad \cdots \quad \delta_{n+r} I_{r_{n+r}} \}$, with $|\delta_i| \leq 1$, $i = \overline{n+1, n+r}$;
- 3 q full complex blocks, associated with neglected dynamics uncertainties: $\text{diag} \{ \Delta_{n+r+1}(s) \quad \Delta_{n+r+2}(s) \quad \cdots \quad \Delta_{n+r+q}(s) \}$, with $\|\Delta_i(s)\|_\infty \leq 1$, $i = \overline{n+r+1, n+r+q}$.

The general control configuration for the system perturbed by uncertainties is depicted in Figure 1.21. The different configurations for the robust performance and robust stability analysis are presented in Figure 1.22(a) and Figure 1.22(b) respectively. For the robust performance and robust stability analysis, it is essential to consider the $\mathbf{N} - \Delta$ and $\mathbf{M} - \Delta_{\mathbf{s}}$ structures respectively. The matrices $\mathbf{N}(\mathbf{s})$ and $\mathbf{M}(\mathbf{s}) = \mathbf{N}_{11}(\mathbf{s})$ are computed using the linear fractional transformation [208], [46], [180].

In the general case, the structured singular value $\mu(\mathbf{M})$, defined for the $\mathbf{M} - \Delta_{\mathbf{s}}$ structure, is expressed as follows [208], [46], [180]

$$\mu_{\Delta_{\mathbf{s}}}(\mathbf{M}(j\omega)) = \left(\min_{\Delta_i \in \Delta_{\mathbf{s}}} \{ \bar{\sigma}(\Delta_i) \mid \det(I - \mathbf{M}\Delta_i) = 0 \} \right)^{-1}, \quad i = \overline{1, r+q}. \quad (1.16)$$

In practice, due to numerical solution issues, the computation of μ is carried out by approximating its value between an upper and a lower bound. Using the Nyquist theorem, it can be demonstrated that the stability limit is attained at $\det(I - \mathbf{M}(\mathbf{s})\Delta(\mathbf{s})) = 0$. The value $\mu_{\Delta_{\mathbf{s}}}(\mathbf{M}(j\omega))^{-1}$ appears as the measure of the smallest perturbation $\Delta_i \in \Delta_{\mathbf{s}}$ that drives the system to the unstable region. This value thus represents a certain “distance” of the system from instability [208], [46], [180], [74].

- **μ -Conditions for robust stability and robust performance**

According to the different closed-loop configurations shown in Figure 1.22, μ -conditions for robust stability and robust performance are summarized as follows [208], [46], [180]:

- 1 Nominal stability $\Leftrightarrow \mathbf{N}$ is internally stable;
- 2 Nominal performance $\Leftrightarrow \forall \omega, \mu_{\Delta_{\mathbf{f}}}(\mathbf{N}_{22}(j\omega)) \leq 1$ and nominal stability;

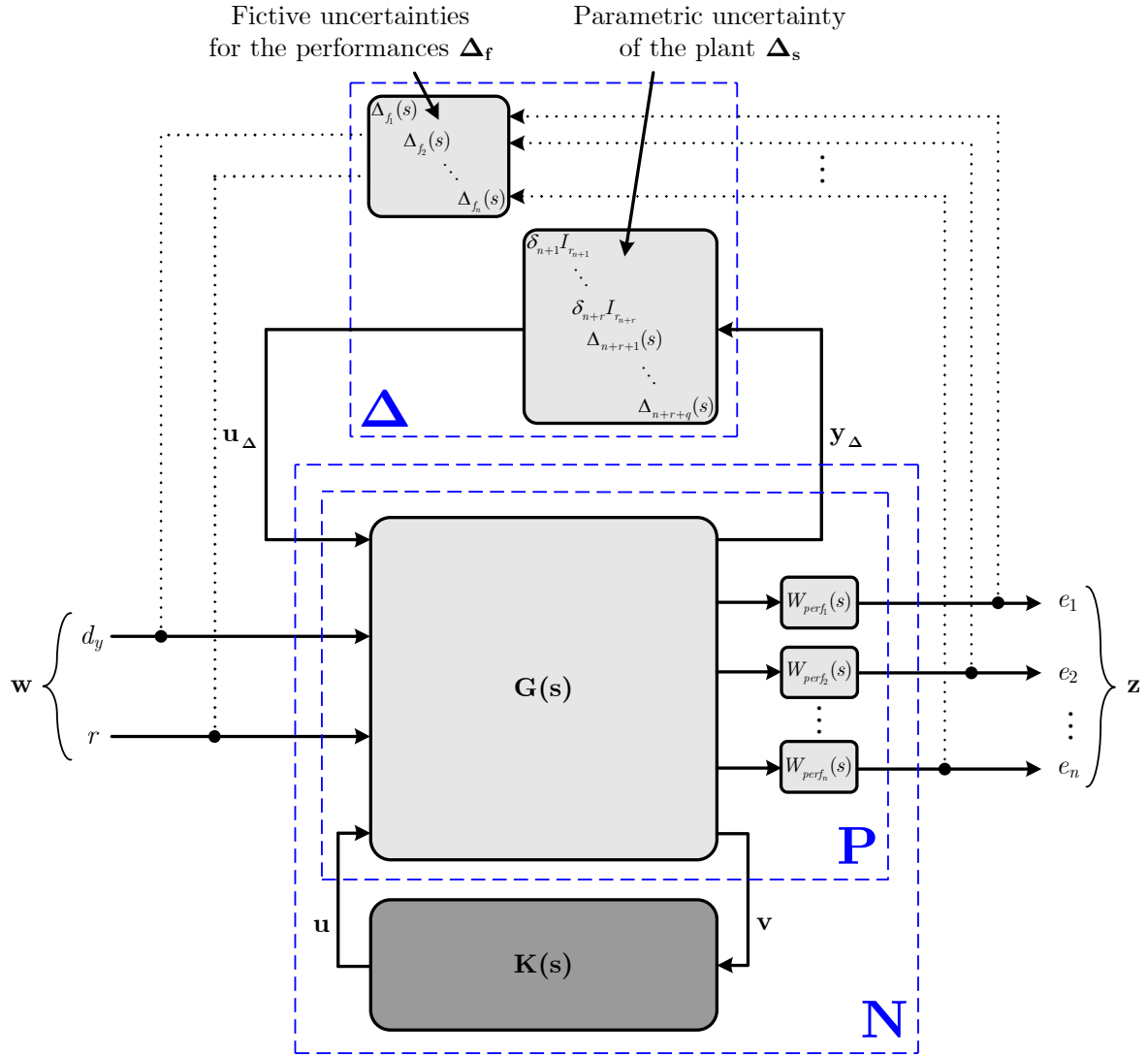


Figure 1.21 – General control configuration of the perturbed system in the so-called $N - \Delta$ form.

3 Robust stability $\Leftrightarrow \forall \omega, \mu_{\Delta_s}(\mathbf{N}_{11}(j\omega)) \leq 1$ and nominal stability;

4 Robust performance $\Leftrightarrow \forall \omega, \mu_{\Delta}(\mathbf{N}(j\omega)) \leq 1$ and nominal stability;

where

$$\mathbf{N}(s) = \begin{bmatrix} \mathbf{N}_{11}(s) & \mathbf{N}_{12}(s) \\ \mathbf{N}_{21}(s) & \mathbf{N}_{22}(s) \end{bmatrix}. \quad (1.17)$$

The values of μ depend on the problem considered since the definition and modeling of uncertainties are different. In the case of robust stability, the following interpretation is precise. If the computed value of μ at a given frequency is different from 1, then

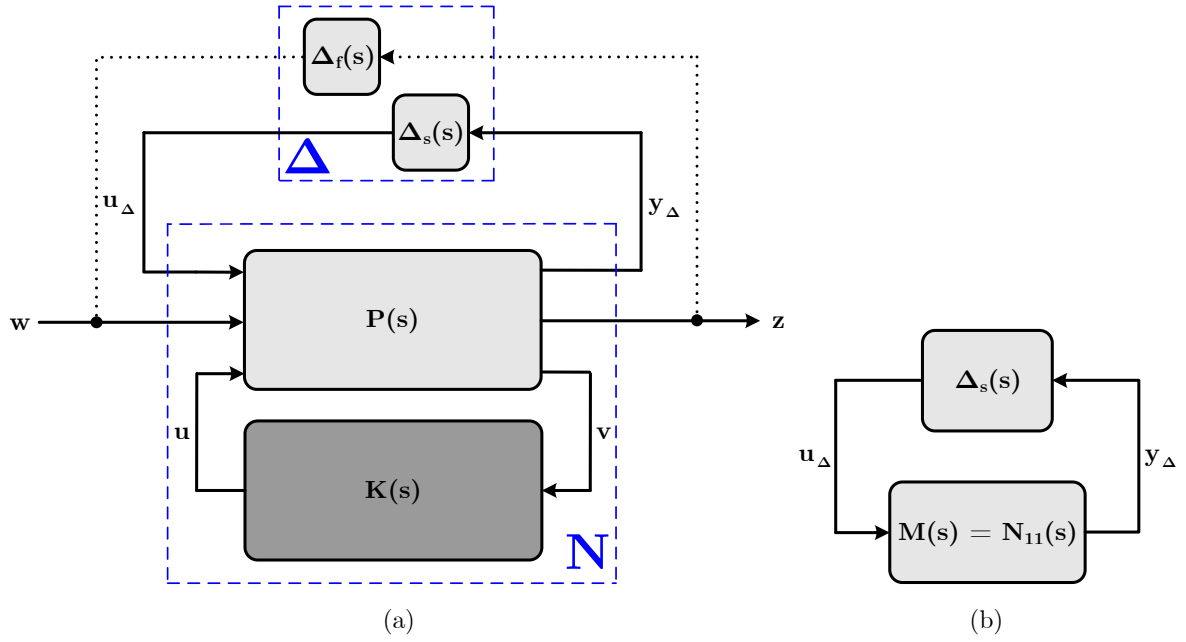


Figure 1.22 – Configurations for (a) robust performance analysis and (b) robust stability analysis.

at this frequency the closed-loop system remains stable with uncertainties of $1/\mu$ times larger than the uncertainty level used to compute μ [208], [46], [180]. If the value of μ is plotted over some frequency range, the effect of uncertainty on the stability and performance of the closed-loop system can be evaluated. This constitutes the concept of μ -analysis [74].

1.6 Case study presentation

In this thesis, our work focuses on the frequency and voltage stability problems of stand-alone MGs with high penetration of decentralized, renewable, and intermittent energy production. The MG configuration under consideration is depicted in Figure 1.23. Power sources within the considered MG – a diesel engine generator as a classical source, a PV unit as a renewable source, and an energy storage unit – are connected in parallel to a PCC and feed an aggregated static load. The diesel generator is connected to the PCC *via* a three-phase step-up transformer and a transmission line. The PV panel bank is connected to the PCC through a power-electronic conversion system including a PWM-controlled one-quadrant chopper and a PWM-controlled three-phase inverter, and a three-phase step-up transformer, which only allows unidirectional power flow, whereas the ESS is connected to the PCC by means of a three-phase step-up transformer and allows bidirectional power flow. A three-phase step-down transformer connects the aggregated load to the PCC. The choice of an appropriate ESS for frequency and voltage control participation will be detailed further in Subsection 2.5.3. The

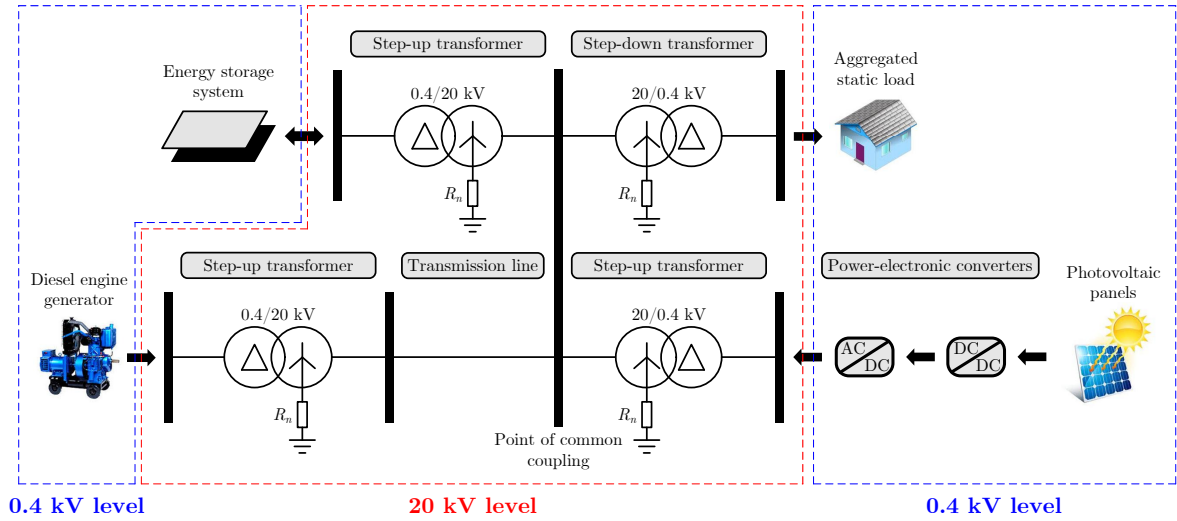


Figure 1.23 – Schematic diagram of the studied MG.

parameters of the studied MG are given in Appendix A.

The diesel-PV-supercapacitor hybrid power generation system presented above is only a simplified example of stand-alone MGs deduced from the Ph.D. thesis of Delille [41]. However, it can be considered as a sufficiently representative structure of such MGs. In the sequel, the general control methodology will be applied on this example.

1.7 Chapter conclusion

In this chapter, we have first provided an introduction to the topic of MGs operation and control. More particularly, we have introduced the concept and classification of MGs. A glimpse has been presented on MGs operation and control, use of energy storage in MGs, and applications of virtual synchronous generators for MGs. Then, a brief review has been given on control strategies applied in MGs, namely grid-feeding/following and grid-forming. Next, we have presented a state-of-the-art on classical and advanced control techniques in MGs, including PI/PID control, linear quadratic regulator, sliding mode control, model predictive control, artificial-intelligence-based control, adaptive control, and robust control, together with a comparative analysis between these control techniques. Robust control has been demonstrated to be more advantageous than other advanced control techniques in tackling MIMO models for which may control objectives can simultaneously be achieved, yielding an optimal solution with respect to a defined criterion *via* an optimization algorithm, linking the desirable dynamic performance with the control design procedure *via* the so-called weighting functions, as well as handling model uncertainties and disturbance rejection objectives. Moreover, these control problems need to be addressed in our study. As a result, due to its advantages, robust control, more specifically \mathcal{H}_∞ control, will be employed for frequency and voltage stability

problems in stand-alone MGs in the next chapters. Finally, we have presented the \mathcal{H}_∞ control methodology which plays a very important role for our study in this thesis framework, including some basic definitions and principles of the \mathcal{H}_∞ control approach, as well as the methods available for control design and robustness analysis.

Robust control for primary frequency ancillary service in stand-alone microgrids

2.1 Introduction

In this chapter, our work focuses on the frequency stability problem of stand-alone MGs with high penetration of decentralized, renewable, and intermittent energy production. In [69] it is shown that relatively small storage units can significantly reduce frequency deviation, provided that saturation conditions are avoided, by dynamically coordinating storage with other generation sources. First, we propose a systematic design procedure of a centralized, multi-variable \mathcal{H}_∞ robust controller for frequency regulation in a diesel-PV-storage hybrid power generation system operating in stand-alone mode. This controller is placed on an upper control level and provides the references to current controllers placed on a lower level. It is also shown how closed-loop operation demands must at their turn be taken into account in the initial MG setup and sizing, namely in appropriately choosing and rating the ESS. Second, a robust performance analysis of the synthesized \mathcal{H}_∞ controller in the presence of load transients, PV output active power variations, and model uncertainties is conducted in order to come back over the design of the MG allowing to increase dynamic performances.

The remainder of this chapter is structured as follows. Section 2.2 introduces the studied MG setup. Section 2.3 is devoted to the proposed control methodology. Section 2.4 presents the coordinated strategy in frequency control. In Section 2.5, choice of energy storage technology and dynamic modeling of the MG for \mathcal{H}_∞ control are provided. The detailed process of designing the \mathcal{H}_∞ controller, along with some closed-loop time-domain simulations performed in the rated operating point, are described in Section 2.6. Section 2.7 details the robust performance analysis of the synthesized \mathcal{H}_∞ controller when the supercapacitor voltage V_{sc} – which is an image of its SoC_{sc} – is considered a time-variant parameter in the simulation model; the controller robustness to the uncertainty in the steady-state value of V_{sc} is then demonstrated through a series of closed-loop time-domain simulations. Some concluding remarks are drawn in Section 2.8.

2.2 Microgrid configuration

A brief description of the considered MG configuration has been given in Section 1.6. In order to ease frequency stability analysis, the simplified MG configuration derived from the studied MG structure, as shown in Figure 2.1(b), has been used. Its equivalent inertia constant H

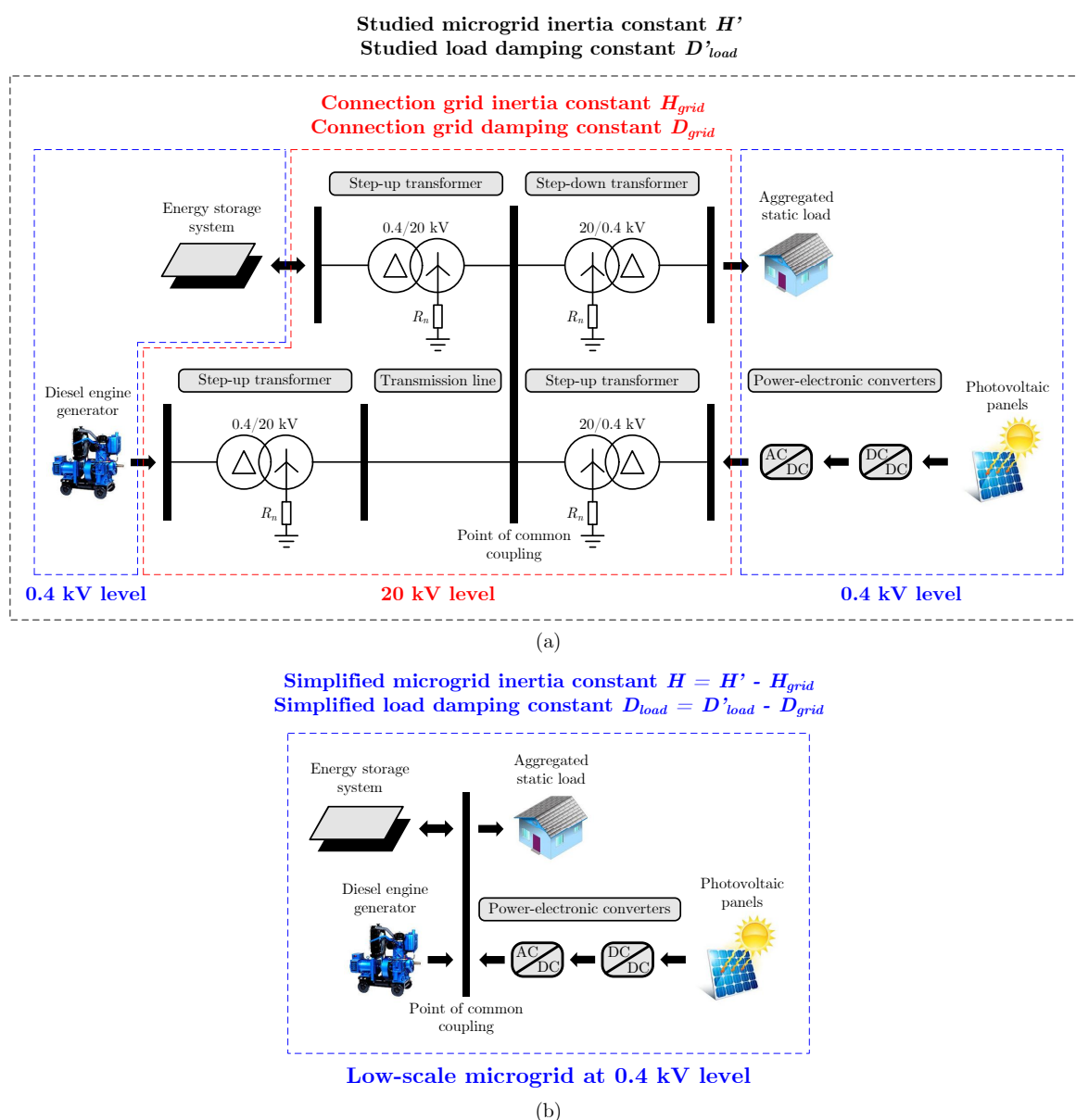


Figure 2.1 – (a) Schematic diagram of the studied MG. (b) Simplified MG configuration for frequency stability analysis.

and load damping constant D_{load} can thus be expressed as follows

$$H = H' - H_{grid}, \quad (2.1)$$

$$D_{load} = D'_{load} - D_{grid}, \quad (2.2)$$

where H' and H_{grid} are the studied MG equivalent inertia constant and the connection grid inertia constant respectively, D'_{load} and D_{grid} the studied load damping constant and the connection grid damping constant respectively. It should be noted here that the low voltage level of 0.4 kV will be used for frequency stability analysis.

2.3 Proposed control methodology

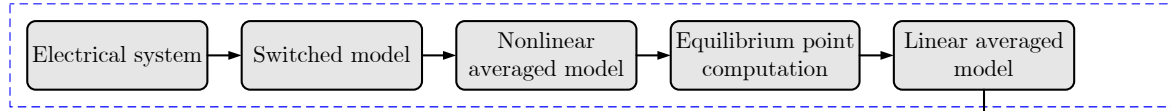
A generalized methodology based on \mathcal{H}_∞ control taking into account robustness for control design is proposed in this work. Then, it allows reducing the time spent for the design process as the optimal controller is found for the defined dynamic specifications (performances and robustness). This methodology is resumed in Figure 2.2 and can be divided into four steps which are detailed below [173]:

- 1 First, performances and robustness levels are specified by the designer according to standards and control objectives expressed in terms of required steady-state and dynamic performance according to system limitations and natural time response;
- 2 Afterwards, dynamic equations and equivalent averaged models of power-electronic converters are used to describe the behavior of the electrical system. By linearizing these equations for a given steady-state point – generally, such point characterizes rated values of interest variables (like frequency and DC-link voltages) – a linear state-space model can then be obtained. The open-loop system validation can be achieved using the topological model or real system tests;
- 3 In order to respect performances, a control architecture is then designed for the considered steady-state point with nominal values of any parameters using \mathcal{H}_∞ control. Control objectives are introduced using weighting functions over particular closed-loop transfer functions [180]. An extended model including these weighting functions is then obtained. An optimal controller can now be computed using control tools in the MATLAB[®] software environment. A multi-variable \mathcal{H}_∞ controller is classically obtained, which ensures that all desired control objectives are satisfied. If such a controller cannot be obtained in a first step, choice of weighting functions should be reviewed. Then, the controller design is resumed with the new weighting functions. For the validation of control design, closed-loop time-domain simulations using the averaged or topological models are convenient;
- 4 Finally, a robustness analysis, where uncertainties models could be introduced to consider parametric uncertainties or unmodeled dynamics, is carried out to assess the desired \mathcal{H}_∞ controller robustness. If this is not satisfied, the control objectives must be modified and Step 3 is re-conducted.

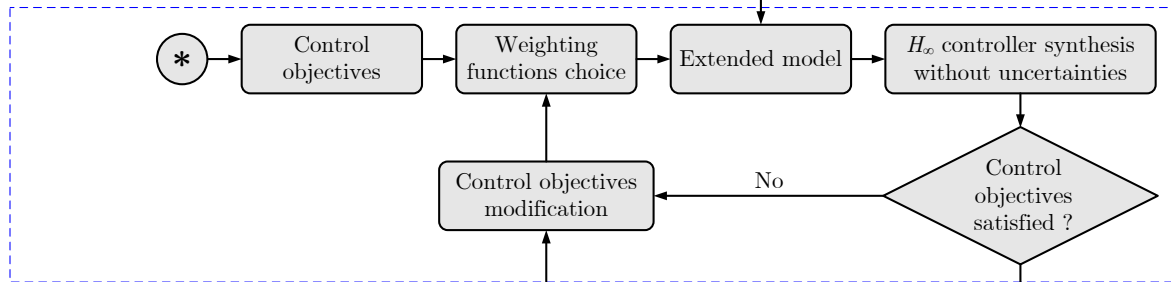
① Dynamic specifications



② Dynamic modeling



③ Control design



④ Robustness analysis

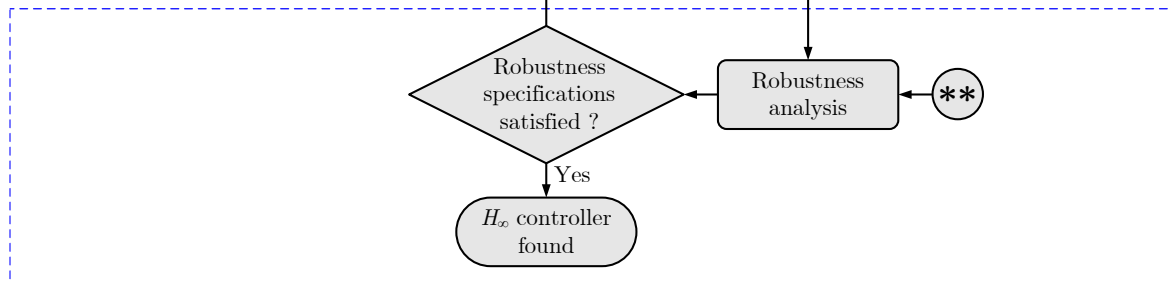


Figure 2.2 – Proposed control methodology inspired from [173].

As a general approach, closed-loop time-domain simulations performed with MATLAB[®]/Simulink[®] using the topological and averaged modeling methodology will be used in this thesis framework to test the validation for the desired controller performance and robustness.

2.4 Coordinated strategy in frequency control

In stand-alone MGs with high penetration of PV energy sources, the frequency is risky to be unstable or its variations can be considerable and unacceptable [40]. ESSs can then be used to maintain the stability and/or improve the transient response of the frequency by injecting or absorbing active power within instants in case of disturbances. In the studied MG, the proposed coordinated strategy supposes the participation of both the ESS and the

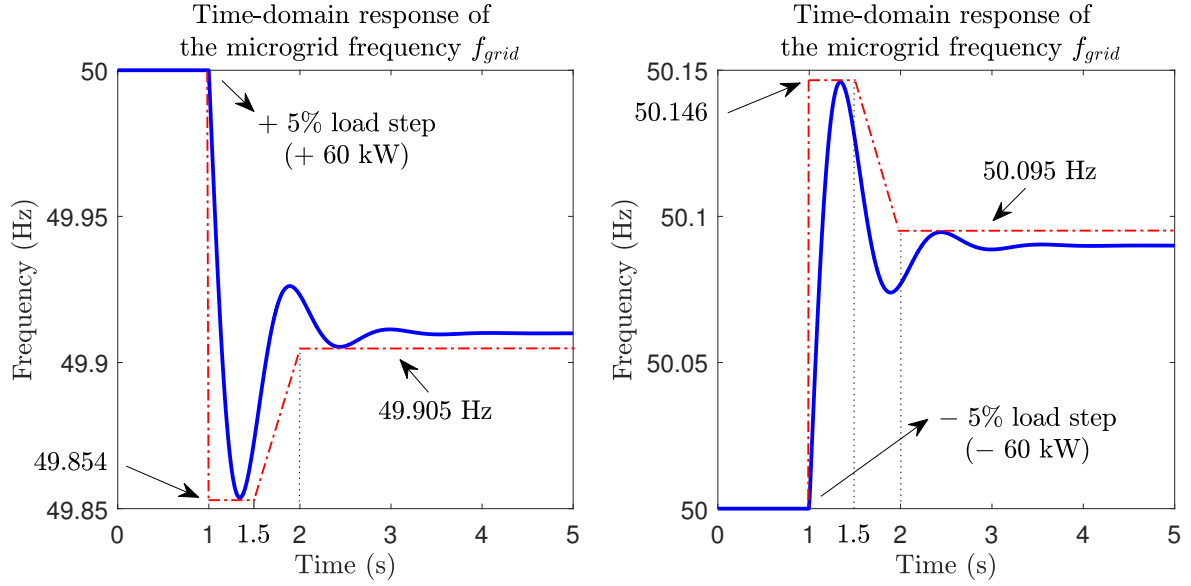


Figure 2.3 – Performance specification on the MG frequency variation in response to a load step disturbance of $\pm 5\%$ of the load rated active power (± 60 kW) in the time domain.

diesel engine generator in primary frequency control. The role of the ESS is to guarantee faster recovery of the MG frequency f_{grid} consequent to a load or PV output active power variation, *i.e.*, to improve its dynamic performances (overshoot, response time, steady-state error). A template for the frequency deviation in response to a load step disturbance of $\pm 5\%$ of the load rated active power (± 60 kW) is shown in Figure 2.3; it is defined based on its time-domain response in the case where only the diesel generator participates in primary control.

2.5 Dynamic modeling of the microgrid

This section presents frequency-control-oriented modeling of the considered MG, which is able to represent the approximated dynamics of the real system. First, the simplified model of each subsystem – the diesel engine generator, the PV unit, the aggregated load, and the ESS – is provided. Then, by aggregating these models, a frequency-control-oriented model of the whole system can be obtained. Let us note that PV system modeling is not addressed in this thesis framework.

It is often more convenient to work with per-unit models of power systems [100], [201]. In particular, when it comes about designing control structures, per-unit models of power systems are generally better conditioned, especially when it is about high-order, possibly multi-scale systems [100], [201]. Moreover, use of a per-unit system can improve numerical stability of automatic computation methods. Therefore, in this work, the dynamic model of the studied MG is converted from real unit into per unit in order to serve the control design procedure which is detailed in the next section.

2.5.1 Diesel engine generator modeling

The diesel engine generator model consists of four sub-models: the diesel engine, the synchronous generator, the coupling shaft, and the speed governor, which are presented in Figure 2.4(a) [100].

The speed governor is turned to frequency control. The P - f droop characteristic is applied for primary frequency control of the diesel generator as shown in (2.3), where ΔP_{diesel}^{ref} denotes the mechanical power reference variation, $\Delta f_{grid}^{est} \approx \Delta f_{grid}$ the MG frequency deviation, and s_{diesel} the droop value. Besides, primary and secondary frequency control by a PI controller is represented in (2.4). The proportional gain of this controller corresponds to primary control, with $K_p = 1/s_{diesel}$. The integral gain, K_i , corresponds to secondary control and is the inverse

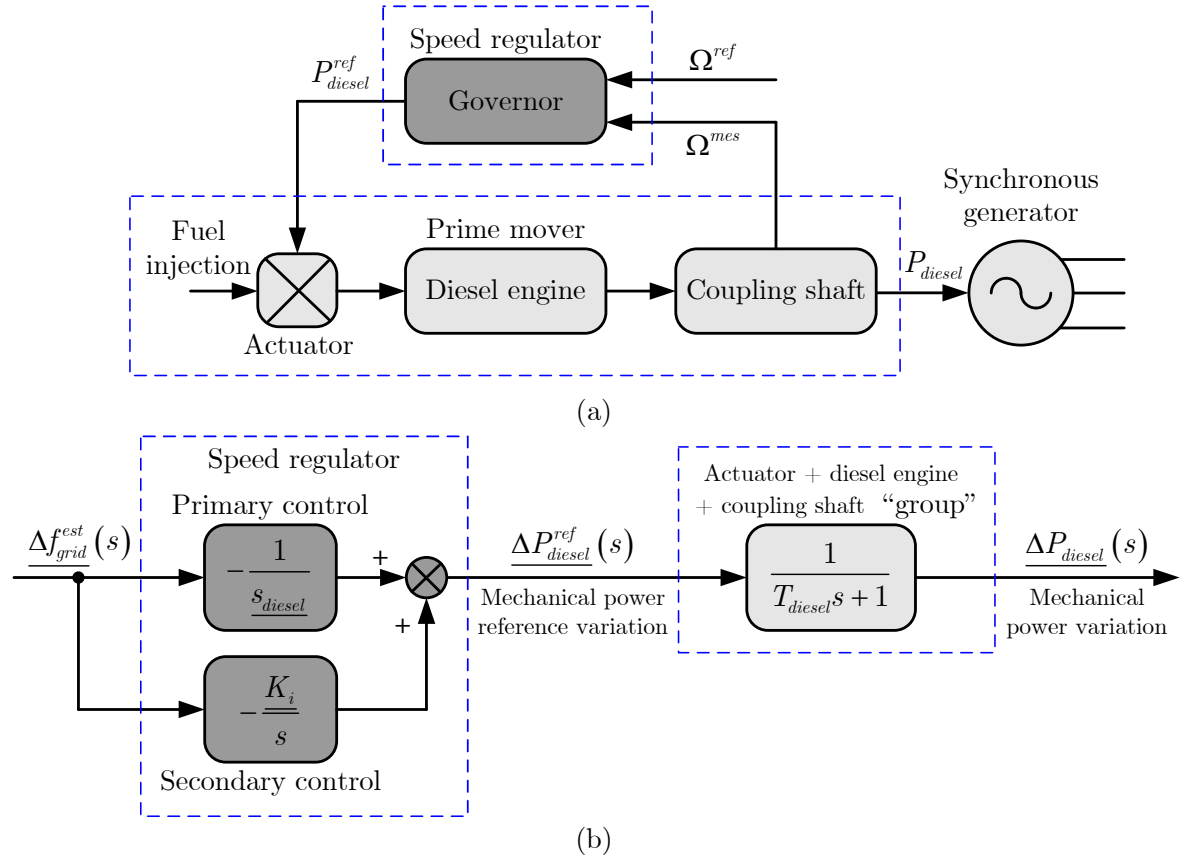


Figure 2.4 – (a) Classical speed control chain of a typical diesel engine generator [100]. (b) A simplified dynamic model inspired from [100].

of the response time of secondary control [100].

$$\Delta P_{diesel}^{ref}(s) = -\frac{1}{s_{diesel}} \Delta f_{grid}(s). \quad (2.3)$$

$$\Delta P_{diesel}^{ref}(s) = -\left(K_p + \frac{K_i}{s}\right) \Delta f_{grid}(s). \quad (2.4)$$

The dynamic behavior of the diesel engine can be modeled using different ways and degrees of complexity (*e.g.*, use of stabilization or not, type of field excitation, *etc.*). In this thesis framework, the {actuator + diesel engine + coupling shaft} system is represented, for small variations only, by a first-order transfer function as shown in (2.5) and considered to be largely sufficient for frequency stability analysis [142].

$$\Delta P_{diesel}(s) = \frac{1}{T_{diesel}s + 1} \Delta P_{diesel}^{ref}(s), \quad (2.5)$$

where ΔP_{diesel} denotes the mechanical power variation of the diesel generator and T_{diesel} its time constant.

Substituting (2.4) into (2.5) gives

$$\Delta P_{diesel}(s) = -\frac{1}{T_{diesel}s + 1} \left(K_p + \frac{K_i}{s}\right) \Delta f_{grid}(s). \quad (2.6)$$

The time derivative of the mechanical power variation of the diesel generator for only primary control participation (*i.e.*, $K_p \neq 0$, $K_i = 0$) can be obtained by applying the inverse Laplace transform to (2.6)

$$\frac{d\Delta P_{diesel}}{dt} = -\frac{1}{T_{diesel}} \Delta P_{diesel} - \frac{1}{T_{diesel}s_{diesel}} \Delta f_{grid}. \quad (2.7)$$

In per-unit values, this time derivative can be expressed as follows

$$\frac{d\underline{\Delta P_{diesel}}}{dt} = -\frac{1}{T_{diesel}} \underline{\Delta P_{diesel}} - \frac{1}{T_{diesel}s_{diesel}} \underline{\Delta f_{grid}}, \quad (2.8)$$

where the underline denotes per-unitized values, $\underline{\Delta P_{diesel}} = \Delta P_{diesel}/S_b$, $\underline{s_{diesel}} = s_{diesel}S_b/f_b$, and $\underline{\Delta f_{grid}} = \Delta f_{grid}/f_b$, with S_b is the MG power base unit and f_b the MG frequency base unit.

Applying the Laplace transform to (2.8) gives

$$\underline{\Delta P_{diesel}}(s) = -\frac{1}{T_{diesel}s + 1} \frac{1}{\underline{s_{diesel}}} \underline{\Delta f_{grid}}(s). \quad (2.9)$$

If secondary control is also taken into account (*i.e.*, $K_i \neq 0$), one has

$$\underline{\Delta P_{diesel}}(s) = -\frac{1}{T_{diesel}s + 1} \left(K_p + \frac{K_i}{s}\right) \underline{\Delta f_{grid}}(s), \quad (2.10)$$

where $\underline{K_i} = K_i f_b/S_b$.

As a result, the block diagram of the simplified dynamic model of the diesel generator around an equilibrium point for frequency control is given in Figure 2.4(b). Its parameter values are presented in Appendix A.

2.5.2 Microgrid modeling

In any power system, the active power generation must constantly match the demand. Disturbances in this balance are compensated for by the kinetic energy of the rotating generators and motors connected to the grid, and by the self-regulating effect of the load, resulting in a variation in the system frequency f_{grid} from its setpoint value f_{gride} . Based on results in [100] and [41], the time derivative of the system frequency can be estimated as follows

$$\frac{df_{grid}}{dt} = \frac{1}{2H} \frac{f_{gride}^2}{f_{grid}} (P_s + P_{diesel} + P_{PV} - P_{load}) - \frac{D_{load}}{2H} f_{gride}^2, \quad (2.11)$$

where P_s is the output active power of the energy storage device, P_{diesel} the active power of the diesel engine generator, P_{PV} the output active power of the PV energy source, P_{load} the load active power, H the equivalent inertia constant of the system which represents the kinetic energy stored in the rotating masses of the synchronous area, and D_{load} the damping constant representing the load self-regulation.

Under small-signal conditions, the time derivative of the system frequency deviation Δf_{grid} can be deduced from (2.11)

$$\frac{d\Delta f_{grid}}{dt} = \frac{1}{2H} f_{gride} (\Delta P_s + \Delta P_{diesel} + \Delta P_{PV} - \Delta P_{load}) - \frac{D_{load}}{2H} f_{gride} \Delta f_{grid}, \quad (2.12)$$

where ΔP_s is the output active power variation of the energy storage device, ΔP_{diesel} the active power variation of the diesel generator, ΔP_{PV} the output active power variation of the PV energy source, and ΔP_{load} the load active power variation. In per-unit values, this time derivative can be written as follows

$$\frac{d\underline{\Delta f_{grid}}}{dt} = \frac{1}{2\underline{H}} (\underline{\Delta P_s} + \underline{\Delta P_{diesel}} + \underline{\Delta P_{PV}} - \underline{\Delta P_{load}}) - \frac{\underline{D_{load}}}{2\underline{H}} \underline{\Delta f_{grid}}, \quad (2.13)$$

where the underline denotes per-unitized values, $f_b = f_{grid}^{ref}$, $\underline{\Delta P_s} = \Delta P_s/S_b$, $\underline{\Delta P_{PV}} = \Delta P_{PV}/S_b$, $\underline{\Delta P_{load}} = \Delta P_{load}/S_b$, $\underline{H} = H/S_b$, and $\underline{D_{load}} = D_{load}f_b/S_b$.

By applying the Laplace transform to (2.13), one has

$$\underline{\Delta f_{grid}}(s) = \frac{1}{2\underline{H}s + \underline{D_{load}}} [\underline{\Delta P_s}(s) + \underline{\Delta P_{diesel}}(s) + \underline{\Delta P_{PV}}(s) - \underline{\Delta P_{load}}(s)]. \quad (2.14)$$

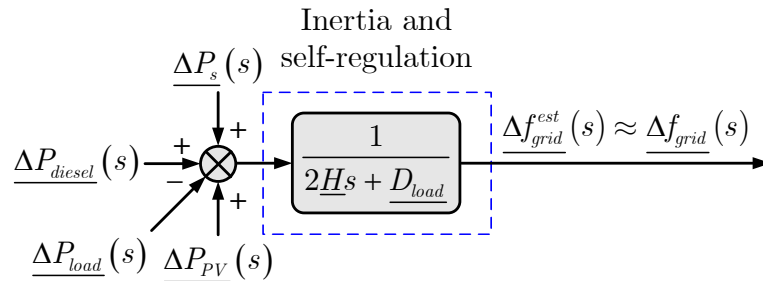


Figure 2.5 – Simplified dynamic model of the studied MG with the load self-regulation.

Consequently, the simplified dynamic model of the power system with the load self-regulation around an equilibrium state for frequency control is presented in Figure 2.5. Its parameter values are presented in Appendix A.

2.5.3 Choice of energy storage technology

There are two main groups of energy storage devices, identified with respect to their power or energy supply ability [187]:

- 1 Sources with high power density which are able to supply high power for a short period of time with fast dynamic characteristics (electrochemical double-layer capacitors, ultracapacitors, electrolytic capacitors, and flywheels belong to this class of sources);
- 2 Sources with high energy density, able to provide power over long periods of time with slow dynamic characteristics (fuel cells and long-time batteries are typical examples of such type of sources).

This classification is illustrated by Ragone's plot in Figure 2.6 [101].

The choice of energy storage technology depends on desired services. The own frequency f_p (Hz) of each technology of a storage device is determined by $f_p = \rho_p / \rho_e$, where ρ_p (W/kg) and ρ_e (Wh/kg) are the power density and the energy density of the storage device respectively. The own frequency of storage devices, deduced from Ragone's plot, is shown in Figure 2.7. It corresponds ideally to the solicitation frequency of a given storage technology.

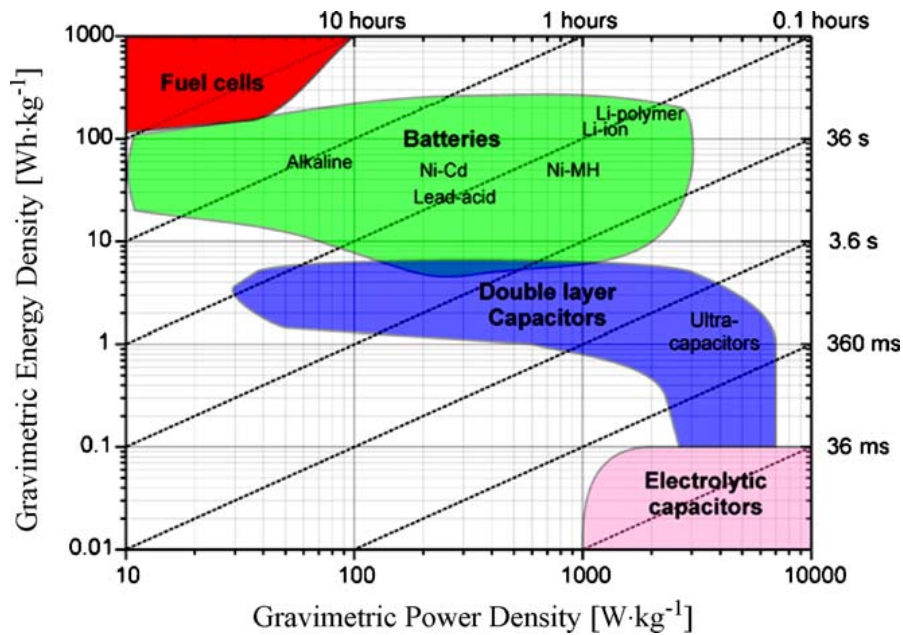


Figure 2.6 – Ragone's plot: characteristics of energy storage devices [101].

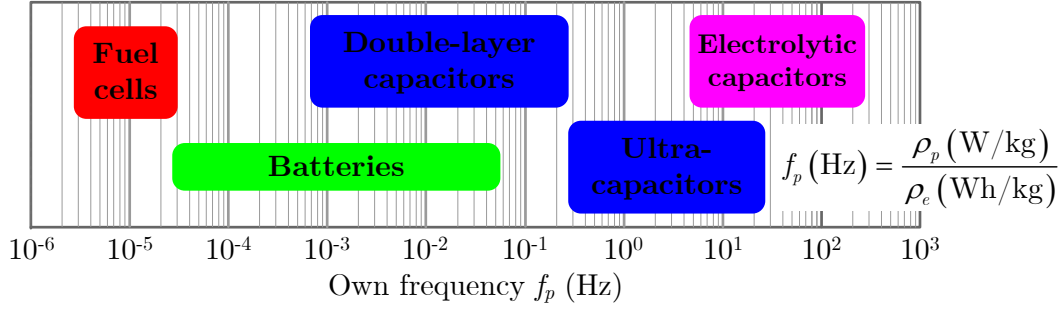


Figure 2.7 – Own frequency of energy storage devices.

The choice of storage devices for primary frequency control is based on analyzing the transfer function between the MG frequency deviation $\Delta f_{grid}(s)$ and the active power variation $\Delta P_{diff}(s) = \Delta P_{PV}(s) - \Delta P_{load}(s)$ in the frequency domain. The most critical situation of the frequency variation – the largest frequency deviation consequent to an active power variation – is first studied, then a suitable interval around a critical frequency will be defined for the storage device participation. Without storage device (*i.e.*, $\Delta P_s(s) = 0$), this transfer function is yielded by substituting (2.10) into (2.14) [142]

$$\frac{\Delta f_{grid}(s)}{\Delta P_{diff}(s)} = \frac{(T_{diesel}s + 1)s}{2HT_{diesel}s^3 + (2H + T_{diesel}D_{load})s^2 + (D_{load} + K_p)s + K_i}, \quad (2.15)$$

where its zeros and poles, computed with MG parameter values from Appendix A, are $z_1 = 0$, $z_2 = -4.55$, $p_{1,2} = -2.21 \pm 5.7j$, and $p_3 = -0.12$ respectively. If the secondary control of the diesel engine generator is not considered (*i.e.*, $K_i = 0$), then the transfer function in (2.15) has the form [142]

$$\begin{aligned} \frac{\Delta f_{grid}(s)}{\Delta P_{diff}(s)} &= \frac{(T_{diesel}s + 1)s_{diesel}}{2HT_{diesel}s_{diesel}s^2 + (2H + T_{diesel}D_{load})s_{diesel}s + D_{load}s_{diesel} + 1} \\ &= \frac{1}{D_{load}s_{diesel} + 1} \frac{(T_{diesel}s + 1)s_{diesel}}{\frac{2HT_{diesel}s_{diesel}}{D_{load}s_{diesel} + 1}s^2 + \frac{(2H + T_{diesel}D_{load})s_{diesel}}{D_{load}s_{diesel} + 1}s + 1}, \end{aligned} \quad (2.16)$$

where its zero and poles are $z_1 = -4.55$ and $p_{1,2} = -2.27 \pm 5.72j$ respectively. Therefore, the initial system without storage device is stable since all real parts of its poles are negative.

The Bode diagrams of the transfer functions in (2.15) and (2.16) are shown in Figure 2.8. The system with only primary control can be assumed as a low-pass filter. High-frequency power fluctuations are then filtered by the MG equivalent inertia. The DC gain of the transfer function is constant and equal to the droop value s_{diesel} . Low-frequency power variations are damped by secondary control [142].

The management strategy of the storage device presented here can be adapted to the system to which it is connected. In this situation, the role of DGs inside the system is to participate in either primary or secondary control or both depending on desired services.

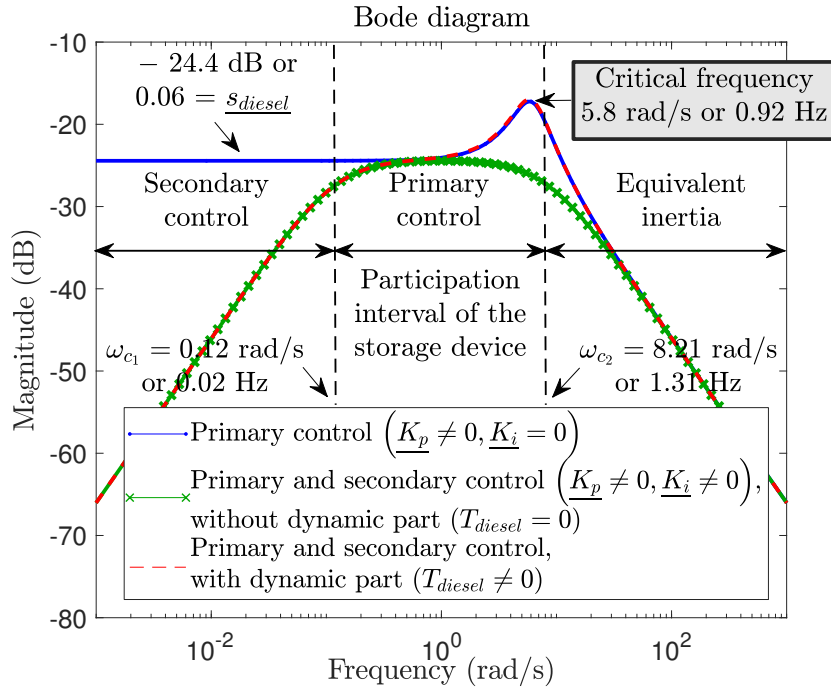


Figure 2.8 – Bode diagram of the system in (2.15) with only primary control ($\underline{K}_p \neq 0, \underline{K}_i = 0$), both primary and secondary control ($\underline{K}_p \neq 0, \underline{K}_i \neq 0$) without the dynamic part of the diesel generator ($T_{diesel} = 0$), both primary and secondary control with the dynamic part ($T_{diesel} \neq 0$).

Critical frequency

A particular frequency, namely critical (or resonant) frequency f_{cr} , around which power fluctuations $\Delta P_{diff}(s)$ can cause very large frequency variations $\Delta f_{grid}(s)$, can be here deduced from the modulus of the poles of the system in (2.15) or (2.16). Values of this modulus with and without secondary control are 6.11 and 6.15 respectively. It has been assumed that the critical frequencies of these two different systems are quasi-identical. Hence, the system with only primary control in (2.16) is used to define the critical frequency because of its lower order [142]. This system corresponds to a second-order one with a zero $z_1 = -1/T_{diesel}$, the corner frequency $\omega_n = \sqrt{(D_{load}s_{diesel} + 1) / (2HT_{diesel}s_{diesel})}$, and the damping ratio $\zeta = (2H + T_{diesel}D_{load})s_{diesel} / (2\sqrt{(D_{load}s_{diesel} + 1)2HT_{diesel}s_{diesel}})$. By numerical application with MG parameter values, one obtains $\omega_n = 6.15$ rad/s and $\zeta = 0.37$. Since $0 < \zeta < 1/\sqrt{2}$, the critical frequency can be computed as $\omega_{cr} = \omega_n \sqrt{1 - 2\zeta^2}$. By numerical application, one has $\omega_{cr} = 5.25$ rad/s or $f_{cr} = 0.84$ Hz. These values are approximately equal to the estimated ones shown in Figure 2.8.

It is important to know the critical frequency value depending on whether the storage device is considered in secondary control participation or not. Indeed, if the storage device is used for primary control participation only, a suitable interval around this critical frequency

value need to be determined to limit the storage device bandwidth. However, if both the primary and secondary control of the storage device are simultaneously taken into account, a larger bandwidth is required for its participation, then the definition of this critical frequency value is no longer useful.

As analyzed from the Bode diagrams in Figure 2.8, use of a storage device in a medium-frequency interval around the defined critical frequency to limit MG frequency variations is thus suitable.

Adopted storage technology

Definition of cut-off frequencies to separate frequency intervals of storage device participation bandwidth is useful, as it is further used for choosing an appropriate storage technology. In order to compute these cut-off frequencies, the diesel generator dynamics is first neglected (*i.e.*, $T_{diesel} = 0$) to simplify the transfer function (2.15) as follows [142]

$$\frac{\Delta f_{grid}(s)}{\Delta P_{diff}(s)} = \frac{s/K_i}{\frac{2H}{K_i}s^2 + \frac{D_{load} + K_p}{K_i}s + 1}, \quad (2.17)$$

which corresponds to a second-order system with a zero at the origin, the corner frequency $\omega_n = \sqrt{K_i/2H}$, and the damping ratio $\zeta = (D_{load} + K_p) / (2\sqrt{2HK_i})$. The magnitude of this transfer function is illustrated in Figure 2.8. For the considered MG, ζ is equal to 4.17 and $A_F = (D_{load} + K_p)^2 - 8HK_i = 261.78 > 0$, therefore, two cut-off frequencies denoted $\omega_{c_{1,2}}$ can be computed as

$$\omega_{c_{1,2}} = \frac{1}{4H} \left| - (D_{load} + K_p) \pm \sqrt{(D_{load} + K_p)^2 - 8HK_i} \right|. \quad (2.18)$$

Substituting MG parameter values into (2.18) gives the low cut-off frequency $\omega_{c_1} = 0.12$ rad/s (or $f_{c_1} = 0.02$ Hz) and the high cut-off frequency $\omega_{c_2} = 8.21$ rad/s (or $f_{c_2} = 1.31$ Hz). As analyzed in Figure 2.8, the dynamic part affects the medium-frequency region corresponding to primary control and it hardly affects the cut-off frequencies [142]. Hence, the frequency interval $f_c \in [0.02, 1.31]$ Hz is chosen for the primary control participation of the storage device. According to Ragone's plot [101], one can see that **supercapacitor storage technology** with its own frequency $f_p \in [0.00069, 27.78]$ Hz corresponds best to the identified frequency interval and is consequently selected for primary control participation.

2.5.4 Energy storage system modeling

Figure 2.9 shows the schematic diagram of the supercapacitor-based ESS that has been designed, modeled, simulated, and then tested using real-time simulation. The supercapacitor

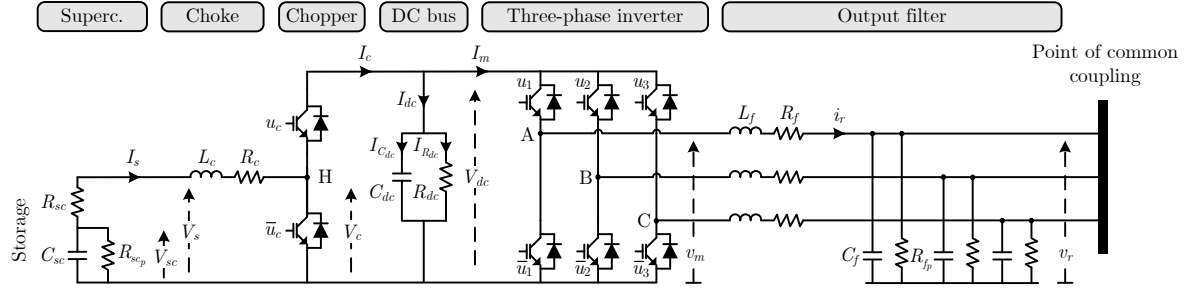


Figure 2.9 – Schematic diagram of the supercapacitor-based ESS.

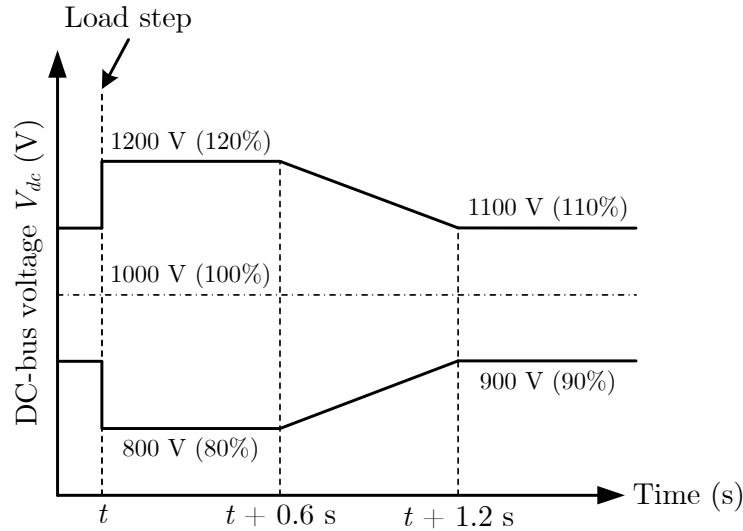


Figure 2.10 – Performance specification on the DC-bus voltage variation in response to a load step disturbance in the time domain.

power source is connected to the PCC by means of a power-electronic conversion system including a PWM-controlled two-quadrant chopper and a PWM-controlled three-phase voltage-source inverter which allows bidirectional power flow. An output filter allowing to limit the injection of current harmonics, is represented here in its simplest form (first-order filter), which is a fundamental-frequency approximation of the more complex structures used in practice (in particular $LC(L)$ filters [4] or [81]).

Another control objective which must be taken into account is to regulate the DC-bus voltage V_{dc} at a reference value V_{dc}^{ref} that has been here chosen as 1000 V. However, we notice that – contrary to the frequency variation case where stiff grid codes must be met – there are no strict requirements to impose to this voltage variation. A performance specification on the DC-bus voltage variation, relied on the one proposed recently in [173] and [74], is shown in Figure 2.10; this specification is defined for any load step value and then it is not possible to translate it exactly into small-signal specifications. Nevertheless, by imposing suitable small-signal performances, large-signal standards can be guaranteed [173], [74].

Several approaches can be employed to model power-electronic-based devices, among

which one can cite use of either topological (switched) models or nonlinear averaged models [130]. Other representations can be deduced from these models, for example, linear averaged models and sampled-data models [130]. In this thesis framework, in order to obtain a desired control-oriented model for the ESS, averaged modeling is used. The averaged model can be linear or nonlinear depending on the dynamics of the chopper and inverter, and derived from the topological model of the ESS.

Topological modeling

The topological model with ideal switches considers that the switching function of the chopper is defined as $u_c \in \{0, 1\}$. The three-phase inverter is controlled *via* three switching functions u_1, u_2 , and u_3 taking values in the discrete set $\{0, 1\}$. The states $u_c = 1, u_k = 1$ with $k = \overline{1, 3}$ indicate closed switch positions, at this time the complementary signals will be $\overline{u_c} = 0, \overline{u_k} = 0$ indicating open positions.

The dynamic equations describing the physical behavior of each element of the ESS using the variables shown in Figure 2.9 are given in Table 2.1, where the state variables of the topological model are: the supercapacitor voltage V_{sc} , the supercapacitor output current I_s , the DC-bus voltage V_{dc} , and the inverter output currents i_{r123} .

Nonlinear averaged modeling

The classical nonlinear averaged models of the supercapacitor, choke, and DC bus are deduced from (2.19), (2.20), and (2.23), (2.24) respectively by replacing the state variables X by their sliding averages $\langle X \rangle_0$ during a switching period $T_{PWM} = 1/f_{PWM}$, where f_{PWM} is the PWM switching frequency. The nonlinear classical averaged model of the chopper can be obtained by the substitution of u_c in (2.21) and (2.22) by its PWM duty cycle $\alpha_c = \langle u_c \rangle_0$, which varies continuously between zero and unity.

Let us remark here that classical averaged modeling is restricted to DC converters only and not useful for converters having one or multiple AC stages (zero average value of certain variables). Therefore, in order to represent the behavior of converters containing AC stages, generalized averaged models, where averages of higher-order harmonics can be handled, are hereafter used [8].

If only the first-order harmonic of the AC variables $\langle x \rangle_1$ and the average of the DC variables $\langle X \rangle_0$ are of interest, the generalized averaged models in the three-phase reference frame applied to the three-phase inverter and output filter are obtained by averaging (2.25), (2.26), and (2.27) respectively.

As a result, the nonlinear averaged model of the ESS is presented in Table 2.2. Note here that the first-order sliding harmonics of the signals $u_k, k = \overline{1, 3}$, represent the control inputs denoted by $\beta_k, k = \overline{1, 3}$, respectively. Also, note here that the system $\{\beta_k\}_{k=\overline{1, 3}}$ is a three-phase system, therefore $\sum_{k=1}^3 \beta_k = \sum_{k=1}^3 \langle u_k \rangle_1 = 0$.

Table 2.1 – Topological model of the supercapacitor-based ESS.

Element	Dynamic equation
Supercapacitor	$\frac{dV_{sc}}{dt} = -\frac{1}{C_{sc}}I_s - \frac{1}{R_{scp}C_{sc}}V_{sc}. \quad (2.19)$
Choke	$\frac{dI_s}{dt} = \frac{1}{L_c}V_{sc} - \frac{R_{sc} + R_c}{L_c}I_s - \frac{1}{L_c}V_c. \quad (2.20)$
Chopper	$V_c = u_c V_{dc}, \quad (2.21)$
	$I_c = u_c I_s. \quad (2.22)$
DC bus	$\frac{dV_{dc}}{dt} = \frac{1}{C_{dc}}I_{dc} - \frac{1}{R_{dc}C_{dc}}V_{dc}, \quad (2.23)$
	$I_{dc} = I_c - I_m. \quad (2.24)$
Three-phase inverter	$\begin{bmatrix} v_{m1} \\ v_{m2} \\ v_{m3} \end{bmatrix} = \frac{1}{3} \begin{bmatrix} 2u_1 - u_2 - u_3 \\ -u_1 + 2u_2 - u_3 \\ -u_1 - u_2 + 2u_3 \end{bmatrix} V_{dc}, \quad (2.25)$
	$I_m = \begin{bmatrix} u_1 & u_2 & u_3 \end{bmatrix} \begin{bmatrix} i_{r1} \\ i_{r2} \\ i_{r3} \end{bmatrix}. \quad (2.26)$
Output filter	$\begin{bmatrix} \frac{di_{r1}}{dt} \\ \frac{di_{r2}}{dt} \\ \frac{di_{r3}}{dt} \end{bmatrix} = \frac{1}{L_f} \begin{bmatrix} v_{m1} \\ v_{m2} \\ v_{m3} \end{bmatrix} - \frac{R_f}{L_f} \begin{bmatrix} i_{r1} \\ i_{r2} \\ i_{r3} \end{bmatrix} - \frac{1}{L_f} \begin{bmatrix} v_{r1} \\ v_{r2} \\ v_{r3} \end{bmatrix}. \quad (2.27)$

Applying the Park coordinates transformation (presented in Appendix C) to (2.34), (2.35), and (2.36), after some algebraic calculus, the generalized averaged models of the three-phase inverter and output filter in the dq reference frame can thus be obtained in (2.37), (2.38), and (2.39) respectively. Note here that β_d and β_q are the direct and quadrature components of the inverter switching functions $\{\beta_k\}_{k=1,3}$, respectively.

From the equations in Table 2.2 and by notation $X = \langle X \rangle_0$ from now on (for the sake of simplicity), after some simple algebra, the nonlinear averaged model of the ESS is finally

Table 2.2 – Nonlinear averaged model of the supercapacitor-based ESS.

Element	Dynamic equation
Supercapacitor	$\frac{d\langle V_{sc}\rangle_0}{dt} = -\frac{1}{C_{sc}}\langle I_s\rangle_0 - \frac{1}{R_{sc_p}C_{sc}}\langle V_{sc}\rangle_0. \quad (2.28)$
Choke	$\frac{d\langle I_s\rangle_0}{dt} = \frac{1}{L_c}\langle V_{sc}\rangle_0 - \frac{R_{sc} + R_c}{L_c}\langle I_s\rangle_0 - \frac{1}{L_c}\langle V_c\rangle_0. \quad (2.29)$
Chopper	$\langle V_c\rangle_0 = \alpha_c \langle V_{dc}\rangle_0, \quad (2.30)$
	$\langle I_c\rangle_0 = \alpha_c \langle I_s\rangle_0. \quad (2.31)$
DC bus	$\frac{d\langle V_{dc}\rangle_0}{dt} = \frac{1}{C_{dc}}\langle I_{dc}\rangle_0 - \frac{1}{R_{dc}C_{dc}}\langle V_{dc}\rangle_0, \quad (2.32)$
	$\langle I_{dc}\rangle_0 = \langle I_c\rangle_0 - \langle I_m\rangle_0. \quad (2.33)$
Three-phase reference frame	
Three-phase inverter	$\begin{bmatrix} \langle v_{m1}\rangle_1 \\ \langle v_{m2}\rangle_1 \\ \langle v_{m3}\rangle_1 \end{bmatrix} = \frac{1}{3} \begin{bmatrix} 2\beta_1 - \beta_2 - \beta_3 \\ -\beta_1 + 2\beta_2 - \beta_3 \\ -\beta_1 - \beta_2 + 2\beta_3 \end{bmatrix} \langle V_{dc}\rangle_0, \quad (2.34)$
	$\begin{aligned} \langle I_m\rangle_0 &= \sum_{k=1}^3 \langle u_k i_{rk}\rangle_0 \\ &= 2 \sum_{k=1}^3 [\text{Re}(\beta_k) \text{Re}(\langle i_{rk}\rangle_1) + \text{Im}(\beta_k) \text{Im}(\langle i_{rk}\rangle_1)]. \end{aligned} \quad (2.35)$
Output filter	$\begin{aligned} \begin{bmatrix} \frac{d\langle i_{r1}\rangle_1}{dt} \\ \frac{d\langle i_{r2}\rangle_1}{dt} \\ \frac{d\langle i_{r3}\rangle_1}{dt} \end{bmatrix} &= \frac{1}{L_f} \begin{bmatrix} \langle v_{m1}\rangle_1 \\ \langle v_{m2}\rangle_1 \\ \langle v_{m3}\rangle_1 \end{bmatrix} - \frac{R_f}{L_f} \begin{bmatrix} \langle i_{r1}\rangle_1 \\ \langle i_{r2}\rangle_1 \\ \langle i_{r3}\rangle_1 \end{bmatrix} - \frac{1}{L_f} \begin{bmatrix} \langle v_{r1}\rangle_1 \\ \langle v_{r2}\rangle_1 \\ \langle v_{r3}\rangle_1 \end{bmatrix} \\ &\quad - \begin{bmatrix} j\omega_{grid} \langle i_{r1}\rangle_1 \\ j\omega_{grid} \langle i_{r2}\rangle_1 \\ j\omega_{grid} \langle i_{r3}\rangle_1 \end{bmatrix}. \end{aligned} \quad (2.36)$
dq reference frame	
Three-phase inverter	$\begin{bmatrix} V_{md} \\ V_{mq} \end{bmatrix} = \begin{bmatrix} \beta_d \\ \beta_q \end{bmatrix} \langle V_{dc}\rangle_0, \quad (2.37)$
	$\langle I_m\rangle_0 = \begin{bmatrix} \beta_d & \beta_q \end{bmatrix} \begin{bmatrix} I_{rd} \\ I_{rq} \end{bmatrix}. \quad (2.38)$
Output filter	$\begin{bmatrix} \frac{dI_{rd}}{dt} \\ \frac{dI_{rq}}{dt} \end{bmatrix} = \frac{1}{L_f} \begin{bmatrix} V_{md} \\ V_{mq} \end{bmatrix} - \frac{R_f}{L_f} \begin{bmatrix} I_{rd} \\ I_{rq} \end{bmatrix} - \frac{1}{L_f} \begin{bmatrix} V_{rd} \\ V_{rq} \end{bmatrix} + \begin{bmatrix} \omega_{grid} I_{rq} \\ -\omega_{grid} I_{rd} \end{bmatrix}. \quad (2.39)$

rewritten as follows

$$\frac{dV_{sc}}{dt} = -\frac{1}{C_{sc}}I_s - \frac{1}{R_{scp}C_{sc}}V_{sc}, \quad (2.40)$$

$$\frac{dI_s}{dt} = \frac{1}{L_c}V_{sc} - \frac{R_{sc} + R_c}{L_c}I_s - \frac{1}{L_c}\alpha_c V_{dc}, \quad (2.41)$$

$$\frac{dV_{dc}}{dt} = \frac{1}{C_{dc}}\alpha_c I_s - \frac{1}{C_{dc}}(\beta_d I_{rd} + \beta_q I_{rq}) - \frac{1}{R_{dc}C_{dc}}V_{dc}, \quad (2.42)$$

$$\frac{dI_{rd}}{dt} = \frac{1}{L_f}\beta_d V_{dc} - \frac{R_f}{L_f}I_{rd} - \frac{1}{L_f}V_{rd} + \omega_{grid}I_{rq}, \quad (2.43)$$

$$\frac{dI_{rq}}{dt} = \frac{1}{L_f}\beta_q V_{dc} - \frac{R_f}{L_f}I_{rq} - \frac{1}{L_f}V_{rq} - \omega_{grid}I_{rd}, \quad (2.44)$$

where the state variables are: V_{sc} , I_s , V_{dc} , the direct and quadrature components of the inverter output current I_{rd} and I_{rq} respectively. V_{rd} and V_{rq} are the direct and quadrature components of the PCC voltage respectively. ω_{grid} is the MG pulsation.

Finally, the power of the ESS can be computed by the following equations

$$P_s = V_s I_s = (V_{sc} - R_{sc} I_s) I_s = V_{sc} I_s - R_{sc} I_s^2, \quad (2.45)$$

$$P_r = V_{rd} I_{rd} + V_{rq} I_{rq}, \quad (2.46)$$

$$Q_r = V_{rq} I_{rd} - V_{rd} I_{rq}, \quad (2.47)$$

where P_s is the supercapacitor output active power, P_r and Q_r are the output active and reactive power of the three-phase inverter respectively.

Equilibrium point computation

In order to compute an equilibrium state of the ESS (indicated by the subscript e), several initial conditions are first given as follows:

- 1] The supercapacitor voltage V_{sc} – which is an image of its state of charge SoC_{sc} – is considered to be initially known, *i.e.*, $V_{sc} = V_{sc_e}$ (or $SoC_{sc} = SoC_{sc_e}$);
- 2] The DC-bus voltage V_{dc} is assumed to be initially equal to its setpoint value, *i.e.*, $V_{dc} = V_{dc_e} = V_{dc}^{ref}$;
- 3] Without loss of generality, the dq reference frame is chosen to be synchronized with the PCC phase voltage vector $v_{r1} = \sqrt{2}V_r \cos(\omega_{grid}t)$. According to the inverse Park coordinates transformation one has $v_{r1} = \sqrt{\frac{2}{3}}[V_{rd} \cos(\omega_{grid}t) - V_{rq} \sin(\omega_{grid}t)]$, therefore one deduces $V_{rd} = \sqrt{3}V_r = U_r$ and $V_{rq} = 0$. Moreover, the PCC line-to-line voltage magnitude U_r is supposed to be well regulated at its reference value, *i.e.*, $U_r = U_{r_e} = U_r^{ref}$, thus one obtains $V_{rd} = V_{rd_e} = U_r^{ref}$ and $V_{rq} = V_{rq_e} = 0$;
- 4] The output reactive power of the three-phase inverter Q_r is assumed to be initially equal to zero, *i.e.*, $Q_r = Q_{r_e} = V_{rq_e} I_{rd_e} - V_{rd_e} I_{rq_e} = 0$, therefore one deduces $I_{rq_e} = 0$.

The steady-state point can be found by imposing all the derivative terms dX/dt in (2.40) – (2.44) to be equal to zero as follows

$$\left(\frac{dV_{sc}}{dt}\right)_e = 0 \Rightarrow -\frac{1}{C_{sc}}I_{s_e} - \frac{1}{R_{sc_p}C_{sc}}V_{sc_e} = 0, \quad (2.48)$$

$$\left(\frac{dI_s}{dt}\right)_e = 0 \Rightarrow \frac{1}{L_c}V_{sc_e} - \frac{R_{sc} + R_c}{L_c}I_{s_e} - \frac{1}{L_c}\alpha_{c_e}V_{dc_e} = 0, \quad (2.49)$$

$$\left(\frac{dV_{dc}}{dt}\right)_e = 0 \Rightarrow \frac{1}{C_{dc}}\alpha_{c_e}I_{s_e} - \frac{1}{C_{dc}}(\beta_{d_e}I_{rd_e} + \beta_{q_e}I_{rq_e}) - \frac{1}{R_{dc}C_{dc}}V_{dc_e} = 0, \quad (2.50)$$

$$\left(\frac{dI_{rd}}{dt}\right)_e = 0 \Rightarrow \frac{1}{L_f}\beta_{d_e}V_{dc_e} - \frac{R_f}{L_f}I_{rd_e} - \frac{1}{L_f}V_{rd_e} + \omega_{grid_e}I_{rq_e} = 0, \quad (2.51)$$

$$\left(\frac{dI_{rq}}{dt}\right)_e = 0 \Rightarrow \frac{1}{L_f}\beta_{q_e}V_{dc_e} - \frac{R_f}{L_f}I_{rq_e} - \frac{1}{L_f}V_{rq_e} - \omega_{grid_e}I_{rd_e} = 0. \quad (2.52)$$

Solving the nonlinear equation system (2.48) – (2.52) by some simple algebraic calculus and taking into account the aforementioned initial conditions gives

$$I_{s_e} = -\frac{V_{sc_e}}{R_{sc_p}}, \quad \alpha_{c_e} = \frac{V_{sc_e} - (R_{sc} + R_c)I_{s_e}}{V_{dc_e}},$$

$$I_{rd_e} = \frac{-R_{dc}V_{rd_e} \pm \sqrt{(R_{dc}V_{rd_e})^2 - 4R_{dc}R_f(V_{dc_e}^2 - R_{dc}\alpha_{c_e}I_{s_e}V_{dc_e})}}{2R_{dc}R_f},$$

$$\beta_{d_e} = \frac{V_{rd_e} + R_fI_{rd_e}}{V_{dc_e}}, \quad \beta_{q_e} = \frac{L_f\omega_{grid_e}I_{rd_e}}{V_{dc_e}}.$$

From (2.45) and (2.46), one also has $P_{s_e} = V_{sc_e}I_{s_e} - R_{sc}I_{s_e}^2$ and $P_{r_e} = V_{rd_e}I_{rd_e} + V_{rq_e}I_{rq_e}$. By numerical application with MG parameter values, the steady-state operating point of the ESS is finally given in Table 2.3. Note that the value V_{sc_e} chosen for \mathcal{H}_∞ control design corresponds here to the midrange between the minimum and maximum supercapacitor voltages. In this case, $V_{sc_e} = 585$ V, where 390 V ($SoC_{sc} = 25\%$) is taken as the minimum value and 780 V ($SoC_{sc} = 100\%$) is the maximum value of V_{sc} .

Table 2.3 – Steady-state real-unit values of the supercapacitor-based ESS.

Variable	V_{sc_e}	V_{dc_e}	V_{rd_e}	V_{rq_e}	I_{s_e}
Value	585 V	1000 V	400 V	0 V	-2.53 A
Variable	I_{rd_e}	I_{rq_e}	α_{c_e}	β_{d_e}	β_{q_e}
Value	-18.68 A	0 A	0.585	0.4	-0.0027
Variable	P_{s_e}	P_{r_e}	Q_{r_e}	f_{grid_e}	ω_{grid_e}
Value	-1.48 kW	-7.47 kW	0 kVAr	50 Hz	100π rad/s

Linear averaged modeling

By linearizing the nonlinear averaged model of the ESS (2.40) – (2.44) around the given equilibrium point, supposing that the direct and quadrature components of the PCC voltage V_{rd} and V_{rq} respectively remain constant (*i.e.*, $\Delta V_{rd} = 0$ and $\Delta V_{rq} = 0$), the linear averaged model can be obtained as follows

$$\frac{d\Delta V_{sc}}{dt} = -\frac{1}{C_{sc}}\Delta I_s - \frac{1}{R_{scp}C_{sc}}\Delta V_{sc}, \quad (2.53)$$

$$\frac{d\Delta I_s}{dt} = \frac{1}{L_c}\Delta V_{sc} - \frac{R_{sc} + R_c}{L_c}\Delta I_s - \frac{1}{L_c}\alpha_{ce}\Delta V_{dc} - \frac{1}{L_c}V_{dc_e}\Delta\alpha_c, \quad (2.54)$$

$$\begin{aligned} \frac{d\Delta V_{dc}}{dt} = & \frac{1}{C_{dc}}\alpha_{ce}\Delta I_s + \frac{1}{C_{dc}}I_{se}\Delta\alpha_c - \frac{1}{C_{dc}}(\beta_{de}\Delta I_{rd} + I_{rde}\Delta\beta_d + \beta_{qe}\Delta I_{rq} + I_{rqe}\Delta\beta_q) \\ & - \frac{1}{R_{dc}C_{dc}}\Delta V_{dc}, \end{aligned} \quad (2.55)$$

$$\frac{d\Delta I_{rd}}{dt} = \frac{1}{L_f}\beta_{de}\Delta V_{dc} + \frac{1}{L_f}V_{dc_e}\Delta\beta_d - \frac{R_f}{L_f}\Delta I_{rd} + \omega_{grid_e}\Delta I_{rq} + I_{rqe}\Delta\omega_{grid}, \quad (2.56)$$

$$\frac{d\Delta I_{rq}}{dt} = \frac{1}{L_f}\beta_{qe}\Delta V_{dc} + \frac{1}{L_f}V_{dc_e}\Delta\beta_q - \frac{R_f}{L_f}\Delta I_{rq} - \omega_{grid_e}\Delta I_{rd} - I_{rde}\Delta\omega_{grid}, \quad (2.57)$$

where the prefix Δ denotes a linearized variable $\Delta X = X - X_e$. The state variables are: the supercapacitor voltage variation ΔV_{sc} , the supercapacitor output current variation ΔI_s , the DC-bus voltage variation ΔV_{dc} , the direct and quadrature components of the inverter output current variation ΔI_{rd} and ΔI_{rq} respectively. $\Delta\alpha_c$ is the PWM duty cycle variation of the chopper, $\Delta\beta_d$ and $\Delta\beta_q$ are the direct and quadrature components of the inverter switching function variations $\{\Delta\beta_k\}_{k=\overline{1,3}}$, respectively. $\Delta\omega_{grid}$ is the MG pulsation variation.

Similarly, the power variations of the ESS can be linearized from (2.45) – (2.47) as follows

$$\Delta P_s = (V_{sc_e} - 2R_{sc}I_{se})\Delta I_s + I_{se}\Delta V_{sc}, \quad (2.58)$$

$$\Delta P_r = V_{rde}\Delta I_{rd} + V_{rqe}\Delta I_{rq}, \quad (2.59)$$

$$\Delta Q_r = V_{rqe}\Delta I_{rd} - V_{rde}\Delta I_{rq}, \quad (2.60)$$

where ΔP_s is the output active power variation of the supercapacitor, ΔP_r and ΔQ_r are the output active and reactive power variations of the three-phase inverter, respectively.

Per-unitized averaged modeling

For the considered ESS, the base values for AC-side quantities are first selected as in Appendix B. The DC-side base values are then determined as in Appendix B based on those of the AC side. Let us note a per-unitized value by the underline \underline{X} , then the nonlinear averaged model, derived from the real-unit nonlinear equation system (2.40) – (2.44), can be described

by the following per-unitized set of equations

$$\frac{1}{\omega_b} \frac{dV_{sc}}{dt} = -\frac{1}{C_{sc}} I_s - \frac{1}{R_{sc_p} C_{sc}} V_{sc}, \quad (2.61)$$

$$\frac{1}{\omega_b} \frac{dI_s}{dt} = \frac{1}{L_c} V_{sc} - \frac{R_{sc} + R_c}{L_c} I_s - \frac{1}{L_c} \alpha_c V_{dc}, \quad (2.62)$$

$$\frac{1}{\omega_b} \frac{dV_{dc}}{dt} = \frac{1}{C_{dc}} \alpha_c I_s - \frac{1}{C_{dc}} (\beta_d I_{rd} + \beta_q I_{rq}) - \frac{1}{R_{dc} C_{dc}} V_{dc}, \quad (2.63)$$

$$\frac{1}{\omega_b} \frac{dI_{rd}}{dt} = \frac{1}{L_f} \beta_d V_{dc} - \frac{R_f}{L_f} I_{rd} - \frac{1}{L_f} V_{rd} + \omega_{grid} I_{rq}, \quad (2.64)$$

$$\frac{1}{\omega_b} \frac{dI_{rq}}{dt} = \frac{1}{L_f} \beta_q V_{dc} - \frac{R_f}{L_f} I_{rq} - \frac{1}{L_f} V_{rq} - \omega_{grid} I_{rd}, \quad (2.65)$$

where the state variables are: V_{sc} , I_s , V_{dc} , I_{rd} , and I_{rq} . It should be noted that, based on the foregoing per-unit system, we do not express the modulating signals α_c , β_d , and β_q in per-unit terms. The reason is that the absolute values of the modulating signals are already between zero and unity. The equation system (2.61) – (2.65) indicates that each derivative term of an original equation is premultiplied by the factor $1/\omega_b$ in the corresponding per-unit counterpart.

By per-unitizing (2.45) – (2.47), the power of the ESS can be computed as follows

$$P_s = V_s I_s = (V_{sc} - R_{sc} I_s) I_s = V_{sc} I_s - R_{sc} I_s^2, \quad (2.66)$$

$$P_r = V_{rd} I_{rd} + V_{rq} I_{rq}, \quad (2.67)$$

$$Q_r = V_{rq} I_{rd} - V_{rd} I_{rq}. \quad (2.68)$$

The per-unitized steady-state point can easily be found either by solving the nonlinear equation system $(d\mathbf{X}/dt)_e = 0$ deduced from (2.61) – (2.65) or by per-unitizing the real-unit equilibrium one which has been computed above

$$\begin{aligned} \underline{I}_{s_e} &= -\frac{V_{sc_e}}{R_{sc_p}}, \quad \alpha_{c_e} = \frac{V_{sc_e} - (R_{sc} + R_c) \underline{I}_{s_e}}{V_{dc_e}}, \\ \underline{I}_{rd_e} &= \frac{-R_{dc} V_{rd_e} \pm \sqrt{(R_{dc} V_{rd_e})^2 - 4R_{dc} R_f (V_{dc_e}^2 - R_{dc} \alpha_{c_e} \underline{I}_{s_e} V_{dc_e})}}{2R_{dc} R_f}, \\ \beta_{d_e} &= \frac{V_{rd_e} + R_f \underline{I}_{rd_e}}{V_{dc_e}}, \quad \beta_{q_e} = \frac{L_f \omega_{grid_e} \underline{I}_{rd_e}}{V_{dc_e}}. \end{aligned}$$

By linearizing the nonlinear averaged model of the ESS (2.61) – (2.65) around the given equilibrium point supposing that the direct and quadrature components of the PCC voltage, V_{rd} and V_{rq} respectively, remain constant (*i.e.*, $\Delta V_{rd} = 0$ and $\Delta V_{rq} = 0$), or by per-unitizing the real-unit linear equation system (2.53) – (2.57), the linear averaged model can be expressed

by the following per-unitized set of equations

$$\frac{1}{\omega_b} \frac{d\Delta V_{sc}}{dt} = -\frac{1}{C_{sc}} \Delta I_s - \frac{1}{R_{sc_p} C_{sc}} \Delta V_{sc}, \quad (2.69)$$

$$\frac{1}{\omega_b} \frac{d\Delta I_s}{dt} = \frac{1}{L_c} \Delta V_{sc} - \frac{R_{sc} + R_c}{L_c} \Delta I_s - \frac{1}{L_c} \alpha_{c_e} \Delta V_{dc} - \frac{1}{L_c} V_{dc_e} \Delta \alpha_c, \quad (2.70)$$

$$\begin{aligned} \frac{1}{\omega_b} \frac{d\Delta V_{dc}}{dt} &= \frac{1}{C_{dc}} \alpha_{c_e} \Delta I_s + \frac{1}{C_{dc}} I_{s_e} \Delta \alpha_c \\ &\quad - \frac{1}{C_{dc}} \left(\beta_{d_e} \Delta I_{rd} + I_{rd_e} \Delta \beta_d + \beta_{q_e} \Delta I_{rq} + I_{rq_e} \Delta \beta_q \right) - \frac{1}{R_{dc} C_{dc}} \Delta V_{dc}, \end{aligned} \quad (2.71)$$

$$\frac{1}{\omega_b} \frac{d\Delta I_{rd}}{dt} = \frac{1}{L_f} \beta_{d_e} \Delta V_{dc} + \frac{1}{L_f} V_{dc_e} \Delta \beta_d - \frac{R_f}{L_f} \Delta I_{rd} + \omega_{grid_e} \Delta I_{rq} + I_{rq_e} \Delta \omega_{grid}, \quad (2.72)$$

$$\frac{1}{\omega_b} \frac{d\Delta I_{rq}}{dt} = \frac{1}{L_f} \beta_{q_e} \Delta V_{dc} + \frac{1}{L_f} V_{dc_e} \Delta \beta_q - \frac{R_f}{L_f} \Delta I_{rq} - \omega_{grid_e} \Delta I_{rd} - I_{rd_e} \Delta \omega_{grid}, \quad (2.73)$$

where the state variables are: ΔV_{sc} , ΔI_s , ΔV_{dc} , ΔI_{rd} , and ΔI_{rq} .

By linearizing (2.66) – (2.68) or by per-unitizing (2.58) – (2.60), the per-unitized power variations of the ESS can be deduced as follows

$$\Delta P_s = \left(V_{sc_e} - 2R_{sc} I_{s_e} \right) \Delta I_s + I_{s_e} \Delta V_{sc}, \quad (2.74)$$

$$\Delta P_r = V_{rd_e} \Delta I_{rd} + V_{rq_e} \Delta I_{rq}, \quad (2.75)$$

$$\Delta Q_r = V_{rq_e} \Delta I_{rd} - V_{rd_e} \Delta I_{rq}. \quad (2.76)$$

2.5.5 System modeling for \mathcal{H}_∞ control

By aggregating the state equations (2.69) – (2.73), (2.8) and (2.13), the per-unitized linear averaged model of the whole system around the precomputed equilibrium point can finally be obtained as follows (with the output active power variation of the supercapacitor ΔP_s in

(2.13) which participates in frequency control being replaced by (2.74))

$$\frac{d\Delta V_{sc}}{dt} = -\frac{\omega_b}{C_{sc}}\Delta I_s - \frac{\omega_b}{R_{scp}C_{sc}}\Delta V_{sc}, \quad (2.77)$$

$$\begin{aligned} \frac{d\Delta V_{dc}}{dt} &= \frac{\omega_b}{C_{dc}}\alpha_{ce}\Delta I_s + \frac{\omega_b}{C_{dc}}I_{se}\Delta\alpha_c \\ &\quad - \frac{\omega_b}{C_{dc}}\left(\beta_{de}\Delta I_{rd} + I_{rde}\Delta\beta_d + \beta_{qe}\Delta I_{rq} + I_{rqe}\Delta\beta_q\right) - \frac{\omega_b}{R_{dc}C_{dc}}\Delta V_{dc}, \end{aligned} \quad (2.78)$$

$$\frac{d\Delta P_{diesel}}{dt} = -\frac{1}{T_{diesel}}\Delta P_{diesel} - \frac{1}{T_{diesel}S_{diesel}}\Delta f_{grid}, \quad (2.79)$$

$$\begin{aligned} \frac{d\Delta f_{grid}}{dt} &= \frac{1}{2H}\left[\left(V_{sc_e} - 2R_{sc}I_{s_e}\right)\Delta I_s + I_{s_e}\Delta V_{sc} + \Delta P_{diesel} + \Delta P_{PV} - \Delta P_{load}\right] \\ &\quad - \frac{D_{load}}{2H}\Delta f_{grid}, \end{aligned} \quad (2.80)$$

$$\frac{1}{\omega_b}\frac{d\Delta I_s}{dt} = \frac{1}{L_c}\Delta V_{sc} - \frac{R_{sc} + R_c}{L_c}\Delta I_s - \frac{1}{L_c}\alpha_{ce}\Delta V_{dc} - \frac{1}{L_c}V_{dc_e}\Delta\alpha_c, \quad (2.81)$$

$$\frac{1}{\omega_b}\frac{d\Delta I_{rd}}{dt} = \frac{1}{L_f}\beta_{de}\Delta V_{dc} + \frac{1}{L_f}V_{dc_e}\Delta\beta_d - \frac{R_f}{L_f}\Delta I_{rd} + \omega_{grid_e}\Delta I_{rq} + I_{rqe}\Delta\omega_{grid}, \quad (2.82)$$

$$\frac{1}{\omega_b}\frac{d\Delta I_{rq}}{dt} = \frac{1}{L_f}\beta_{qe}\Delta V_{dc} + \frac{1}{L_f}V_{dc_e}\Delta\beta_q - \frac{R_f}{L_f}\Delta I_{rq} - \omega_{grid_e}\Delta I_{rd} - I_{rde}\Delta\omega_{grid}, \quad (2.83)$$

where the state variables are: ΔV_{sc} , ΔV_{dc} , ΔP_{diesel} , Δf_{grid} , ΔI_s , ΔI_{rd} , and ΔI_{rq} . The external disturbance applied to the system is the active power variation $\Delta P_{load} - \Delta P_{PV}$. Without loss of generality, ΔP_{PV} may always be included in the aggregated load. It should be noted that this averaged model takes into consideration only the primary control of the diesel engine generator.

In the next section, control design will be presented based on this linear averaged model.

2.6 Control design

This section details a robust control design approach used to achieve the aforementioned control objectives in Section 2.4 and Section 2.5. Here the basic idea is to consider the current variations ΔI_s , ΔI_{rd} , and ΔI_{rq} in (2.81) – (2.83) as control inputs for the linear system (2.77) – (2.80), which should result from the disturbance rejection requirement $\Delta P_{load} - \Delta P_{PV}$. In particular, as the quadrature current I_{rq} does not participate to frequency control, its variation is set to 0, *i.e.*, $\Delta I_{rq} = 0$, hence only two control inputs are effectively used: ΔI_s and ΔI_{rd} . Therefore, a hierarchical control strategy consisting of two levels is adopted in this work, where the outer control loop deals with output regulation imposing low-frequency dynamics (*e.g.*, ΔV_{sc} , ΔV_{dc} , ΔP_{diesel} , Δf_{grid}) and the inner loop concerns current reference tracking of high-frequency dynamics (*e.g.*, ΔI_s , ΔI_{rd} , ΔI_{rq}). This allows the output circuit regulation, meanwhile preserving the internal variables within specified safety limits [8]. Moreover, in

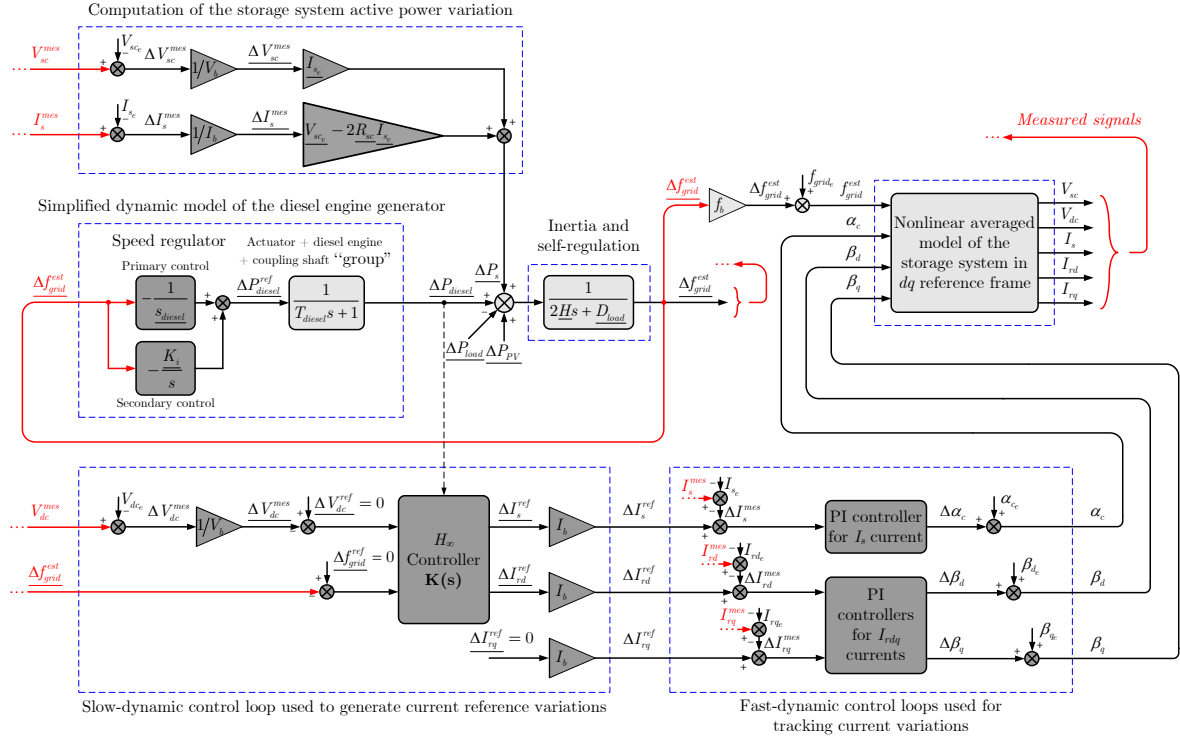


Figure 2.11 – Block diagram of the proposed global control structure.

this way, the \mathcal{H}_∞ upper-level controller computes current references to track by the PI low-level controllers, such that load disturbances to be rejected in an optimal manner, while all dynamic performance and constraints are met. MATLAB[®]/Simulink[®] closed-loop time-domain simulations are performed and discussed to show the effectiveness of the proposed robust control strategy. In addition, this frequency robust control strategy will experimentally be validated on a dedicated rapid-prototyping test bench in Chapter 4.

2.6.1 Proposed cascaded two-level control structure

As can be seen in most energy management systems and according to control objectives, it is preferred – from the application point of view – to consider power sources acting as current sources [150]. Therefore, a cascaded two-level control structure – where classical PI-based current tracking controllers are placed on the low control level and receive references from an \mathcal{H}_∞ -control-based upper level – is hereafter developed. The proposed global control structure is illustrated in Figure 2.11.

2.6.2 Classical PI-control-based low level

The current variations ΔI_s , ΔI_{rd} , and ΔI_{rq} must be controlled and prevented from exceeding admissible limits. All current control loops have fast closed-loop dynamics compared to the

\mathcal{H}_∞ control loop, therefore, they are grouped together.

ΔI_{rq} (or ΔI_{rdq}) in (2.57) appears as a high-frequency perturbation; the same applies for ΔI_{rd} (or ΔI_{rdq}) in (2.56). Their reciprocal influence is significantly reduced by the $d - q$ decoupling structure, as shown in Figure 2.12. ΔV_{dc} (or ΔV_{dc}) and $\Delta \omega_{grid}$ (or $\Delta \omega_{grid}$) in (2.54), (2.56), and (2.57) are regarded as low-frequency perturbations that are rejected by the upper-level control. The supercapacitor voltage V_{sc} is regarded as a time-invariant parameter in the PI controller synthesis, *i.e.*, $\Delta V_{sc} = 0$ (or $\Delta V_{sc} = 0$). Hence, transfer functions relating the current variations with the duty ratio variations (inner plants) can be computed straightforwardly from (2.54), (2.56), and (2.57)

$$G_{I_s - \alpha_c}(s) = \frac{\Delta I_s(s)}{\Delta \alpha_c(s)} = \frac{K_s}{T_s s + 1}, \quad (2.84)$$

$$G_{I_{rdq} - \beta_{dq}}(s) = \frac{\Delta I_{rd}(s)}{\Delta \beta_d(s)} = \frac{\Delta I_{rq}(s)}{\Delta \beta_q(s)} = \frac{K_{rdq}}{T_{rdq} s + 1}, \quad (2.85)$$

where $K_s = -V_{dc_e} / (R_{sc} + R_c)$, $T_s = L_c / (R_{sc} + R_c)$, $K_{rdq} = V_{dc_e} / R_f$, and $T_{rdq} = L_f / R_f$. By numerical application with MG parameter values, one obtains $K_s = -5.2 \times 10^4$ A, $T_s = 114$ ms, $K_{rdq} = 2.1 \times 10^5$ A, and $T_{rdq} = 96$ ms.

Because the inner plants are of first order, PI controllers of the form $G_{PI}(s) = K_p \left(1 + \frac{1}{T_i s}\right)$ are effectively used to ensure both the zero steady-state error and the desired closed-loop bandwidth. Current reference variations ΔI_s^{ref} and ΔI_{rd}^{ref} are generated by the outer \mathcal{H}_∞ control loop, whereas $\Delta I_{rq}^{ref} = 0$ (the output reactive power reference variation

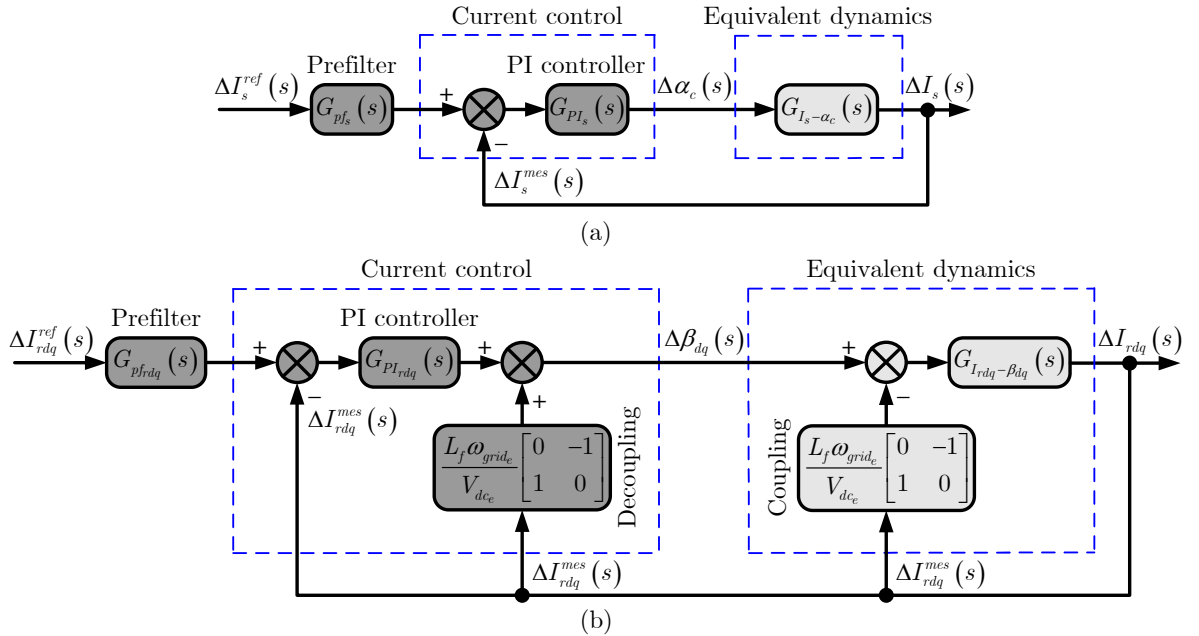


Figure 2.12 – (a) Block diagram for tracking the current reference variation ΔI_s^{ref} . (b) Block diagram for tracking the current reference variations ΔI_{rd}^{ref} and ΔI_{rq}^{ref} .

ΔQ_r^{ref} of the three-phase inverter is assumed to be equal to 0, therefore from (2.60) one has $\Delta I_{rq}^{ref} = -\Delta Q_r^{ref}/V_{rde} = 0$). The control structures are shown in Figure 2.12(a) and Figure 2.12(b). The closed-loop transfer functions of the inner control loops turn out to be

$$G_s(s) = \frac{\Delta I_s(s)}{\Delta I_s^{ref}(s)} = \frac{T_{i_s}s + 1}{\frac{T_{i_s}T_s}{K_{p_s}K_s}s^2 + T_{i_s}\left(1 + \frac{1}{K_{p_s}K_s}\right)s + 1}, \quad (2.86)$$

$$G_{rdq}(s) = \frac{\Delta I_{rd}(s)}{\Delta I_{rd}^{ref}(s)} = \frac{\Delta I_{rq}(s)}{\Delta I_{rq}^{ref}(s)} = \frac{T_{i_{rdq}}s + 1}{\frac{T_{i_{rdq}}T_{rdq}}{K_{p_{rdq}}K_{rdq}}s^2 + T_{i_{rdq}}\left(1 + \frac{1}{K_{p_{rdq}}K_{rdq}}\right)s + 1}. \quad (2.87)$$

Let the inner closed-loop dynamic performance be described by the bandwidth $1/T_0$ and the damping coefficient ζ_0 , the PI controller parameters can be computed *via* identification as follows

$$T_{i_s} = 2\zeta_{0_s}T_{0_s} - \frac{T_{0_s}^2}{T_s}, \quad K_{p_s} = \frac{1}{K_s} \left(\frac{2\zeta_{0_s}T_s}{T_{0_s}} - 1 \right), \quad (2.88)$$

$$T_{i_{rdq}} = 2\zeta_{0_{rdq}}T_{0_{rdq}} - \frac{T_{0_{rdq}}^2}{T_{rdq}}, \quad K_{p_{rdq}} = \frac{1}{K_{rdq}} \left(\frac{2\zeta_{0_{rdq}}T_{rdq}}{T_{0_{rdq}}} - 1 \right). \quad (2.89)$$

As the closed-loop high bandwidth is a basic requirement for converter control, parameter/model variations may reduce the stability phase margin to dangerously low levels [143]. Therefore, a “strongly” tuned controller may easily lead to instabilities in certain operating regimes. For these reasons, the designer may sometimes sacrifice performance for the sake of robustness [8]. In practice, the closed-loop dynamic performance can usually be imposed within an interval as follows

$$xT_{PWM_c} \leq T_{0_s} \leq \frac{T_s}{y}, \quad (2.90)$$

$$xT_{PWM_i} \leq T_{0_{rdq}} \leq \frac{T_{rdq}}{y}, \quad (2.91)$$

where $1/T_{PWM_c}$ and $1/T_{PWM_i}$ are the PWM switching frequency of the chopper and three-phase inverter, respectively, $1/T_{0_s}$ and $1/T_{0_{rdq}}$ are the bandwidths of the two types of current control loops, respectively, $1/T_s$ and $1/T_{rdq}$ are the bandwidths of the original current plants, respectively. $x_{min} = 5$ is imposed, which means that the closed-loop maximum bandwidth is chosen to be five times smaller than the PWM switching frequency, whereas imposing $y_{min} = 5$ indicates that the minimum value of the closed-loop bandwidth is five times larger than the original current plant bandwidth. The desired dynamic performance of the current control loops is illustrated in Figure 2.13.

In our case study, we impose the closed-loop dynamics ten times faster than the original current plants, *i.e.*, $T_{0_s} = T_s/10 = 11.4$ ms, $T_{0_{rdq}} = T_{rdq}/10 = 9.6$ ms and the damping ratios $\zeta_{0_s} = \zeta_{0_{rdq}} = 0.8$. Substituting these values into (2.88) and (2.89) yields $T_{i_s} = 17.1$ ms, $K_{p_s} = -2.9 \times 10^{-4}$ A⁻¹, $T_{i_{rdq}} = 14.4$ ms, and $K_{p_{rdq}} = 7.2 \times 10^{-5}$ A⁻¹. Additionally, prefilters $G_{pfs}(s) = 1/(T_{i_s}s + 1)$ and $G_{pfrdq}(s) = 1/(T_{i_{rdq}}s + 1)$ have been inserted to cancel the inner closed-loop zeros.

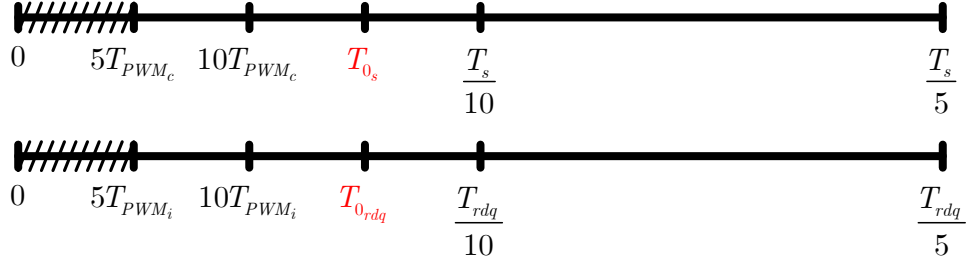


Figure 2.13 – Desired dynamic performance of the current control loops.

2.6.3 \mathcal{H}_∞ -control-based upper level

Linear state-space representation

The current variations ΔI_s and ΔI_{rd} are controlled by the very-fast-dynamic control loops tracking the current reference variations generated by the \mathcal{H}_∞ controller; therefore, the outer \mathcal{H}_∞ plant “sees” $\Delta I_s \equiv \Delta I_s^{ref}$ and $\Delta I_{rd} \equiv \Delta I_{rd}^{ref}$. The supercapacitor voltage V_{sc} is regarded in a first place as a time-invariant parameter in the \mathcal{H}_∞ controller synthesis, *i.e.*, $\underline{\Delta V_{sc}} = 0$ (its dynamic equation $\underline{\Delta \dot{V}_{sc}} = f(\underline{\Delta V_{sc}}, \underline{\Delta I_s})$ in (2.77) being neglected). Thus, the linear system (2.78) – (2.80) can be represented in the state-space form as follows (with the terms $\frac{\omega_b}{C_{dc}} \underline{I_{se}} \Delta \alpha_c$, $\frac{\omega_b}{C_{dc}} \underline{I_{rde}} \Delta \beta_d$, and $\frac{\omega_b}{C_{dc}} \underline{I_{rqe}} \Delta \beta_q$ in (2.78) being neglected in the outer \mathcal{H}_∞ control loop design, $\underline{\Delta I_{rq}} \equiv \underline{\Delta I_{rq}^{ref}} = 0$)

$$\begin{cases} \underline{\Delta \dot{\mathbf{x}}} = \mathbf{A} \underline{\Delta \mathbf{x}} + \mathbf{B}_1 \underline{\Delta \mathbf{u}} + \mathbf{B}_2 \underline{\Delta \mathbf{w}} \\ \underline{\Delta \mathbf{y}} = \mathbf{C} \underline{\Delta \mathbf{x}} + \mathbf{D}_1 \underline{\Delta \mathbf{u}} + \mathbf{D}_2 \underline{\Delta \mathbf{w}} \end{cases}, \quad (2.92)$$

where $\underline{\Delta \mathbf{x}} = [\underline{\Delta V_{dc}} \quad \underline{\Delta P_{diesel}} \quad \underline{\Delta f_{grid}}]^T$ is the state vector, $\underline{\Delta \mathbf{u}} = [\underline{\Delta I_s^{ref}} \quad \underline{\Delta I_{rd}^{ref}}]^T$ the control input vector, $\underline{\Delta \mathbf{w}} = \underline{\Delta P_{load}} - \underline{\Delta P_{PV}}$ the disturbance input, and $\underline{\Delta \mathbf{y}} = [\underline{\Delta V_{dc}} \quad \underline{\Delta f_{grid}}]^T$ the measured output vector. Matrices \mathbf{A} , \mathbf{B}_1 , \mathbf{B}_2 , \mathbf{C} , \mathbf{D}_1 , and \mathbf{D}_2 in (2.92) are given as follows

$$\mathbf{A} = \begin{bmatrix} -\frac{\omega_b}{R_{dc} C_{dc}} & 0 & 0 \\ 0 & -\frac{1}{T_{diesel}} & -\frac{1}{T_{diesel} s_{diesel}} \\ 0 & \frac{1}{2H} & -\frac{D_{load}}{2H} \end{bmatrix}, \quad \mathbf{B}_1 = \begin{bmatrix} \frac{\omega_b}{C_{dc}} \alpha_{ce} & -\frac{\omega_b}{C_{dc}} \beta_{de} \\ 0 & 0 \\ \frac{1}{2H} (V_{sc_e} - 2R_{sc} I_{se}) & 0 \end{bmatrix}, \quad (2.93)$$

$$\mathbf{B}_2 = \begin{bmatrix} 0 \\ 0 \\ -\frac{1}{2H} \end{bmatrix}, \quad \mathbf{C} = \begin{bmatrix} 1 & 0 & 0 \\ 0 & 0 & 1 \end{bmatrix}, \quad \mathbf{D}_1 = \begin{bmatrix} 0 & 0 \\ 0 & 0 \end{bmatrix}, \quad \mathbf{D}_2 = \begin{bmatrix} 0 \\ 0 \end{bmatrix}.$$

Analysis of system structural properties

An analysis of important structural properties: stability, controllability, and observability of the linear system (2.92), which play a prominent role in the understanding of its behavior, is investigated. Stability, from a geometric point of view, is related to the properties of system trajectories around an equilibrium point. Controllability is another geometric property of the system, describing the ability to “drive” the system states to arbitrary values through the control input. Its dual notion of observability describes the ability to infer the system states given output measurements in an interval [188].

The structural properties of the linear system (2.92) are analyzed based on its matrices \mathbf{A} , \mathbf{B}_1 , and \mathbf{C} . With MG parameter values, eigenvalues of the matrix \mathbf{A} are equal to $p_{1,2} = -2.27 \pm 5.72j$ and $p_3 = -0.03$. All eigenvalues have negative real parts, so the system is stable for small variations around the steady-state operating point. Next, the controllability condition can be checked by using the MATLAB[®] function “`ctrb`”. The controllability matrix $\mathbf{Q}_c = \text{ctrb}(\mathbf{A}, \mathbf{B}_1)$ has the rank of 3 which is equal to the rank of the matrix \mathbf{A} , therefore, the system is said to be completely controllable. Finally, the MATLAB[®] function “`obsv`” can be used to evaluate the observability condition. The rank of the observability matrix $\mathbf{Q}_o = \text{obsv}(\mathbf{A}, \mathbf{C})$ is equal to the rank of the matrix \mathbf{A} , *i.e.*, 3, so the system is well observable.

Control configuration in the P – K form

Multi-variable \mathcal{H}_∞ control design for the linear system (2.92), which is cast into the formalism in Figure 2.14, is afforded by the general control configuration in [180]. The approach considered here is a “small-signal” one that allows using the linear state-space model of the system. In this case, focus is on rejecting disturbance due to the load and output PV active power variation. Moreover, it is assumed that the measurement noise is relatively insignificant. Tracking is not an issue and therefore the S/KS mixed-sensitivity optimization in the standard regulation form must typically be solved [180]. It is important to include KS as a mechanism for limiting the size and bandwidth of the \mathcal{H}_∞ controller, and hence the control energy used. The key of this design method is the appropriate definition of frequency weights $W_{perf}(s)$ to formalize the disturbance rejection objectives (performance specifications) and frequency weights $W_u(s)$ to translate the constraints imposed to the control inputs.

The generalized plant \mathbf{P} has three inputs, namely, the active power variation $\underline{\Delta P}_{load} - \underline{\Delta P}_{PV}$ acting as a disturbance input $\underline{\Delta \mathbf{w}}$ and the current reference variations $\underline{\Delta I}_s^{ref}$, $\underline{\Delta I}_{rd}^{ref}$, which are the control inputs $\underline{\Delta \mathbf{u}}$. The measured output vector $\underline{\Delta \mathbf{y}}$ is composed of the DC-bus voltage variation $\underline{\Delta V}_{dc}$ and the MG frequency variation $\underline{\Delta f}_{grid}$. The desired performances are expressed in the form of weighting functions on the chosen performance outputs. $\underline{\Delta V}_{dc}$, $\underline{\Delta f}_{grid}$, as well as $\underline{\Delta I}_s^{ref}$, $\underline{\Delta I}_{rd}^{ref}$, are chosen as performance outputs. Its vector is noted $\underline{\Delta \mathbf{z}}$ in Figure 2.14.

The S/KS mixed-sensitivity optimization of the \mathcal{H}_∞ control problem consists in designing

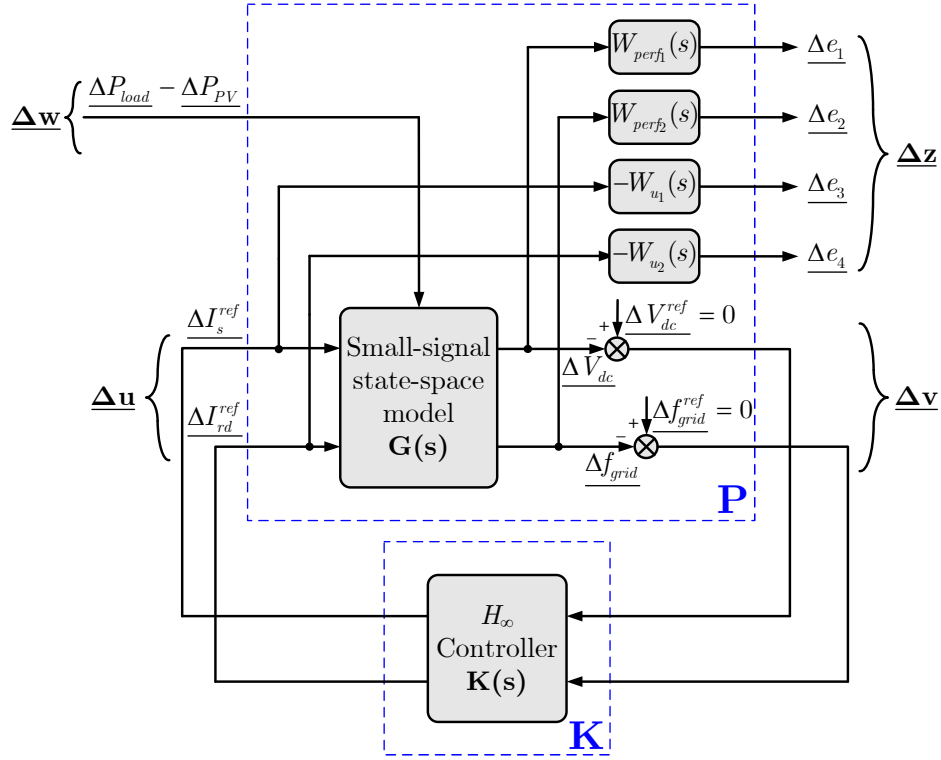


Figure 2.14 – Control configuration in the so-called $\mathbf{P} - \mathbf{K}$ form, where \mathbf{P} denotes the plant together with the weighting functions and \mathbf{K} denotes the \mathcal{H}_∞ controller.

a stabilizing controller which minimizes the norm $\left\| \begin{matrix} W_{perf} S \\ W_u K S \end{matrix} \right\|_\infty$.

Weighting functions selection

Linear time-invariant weighting functions selection is the key to cope with the performance requirements. The DC-bus voltage variation ΔV_{dc} and the MG frequency variation Δf_{grid} are bounded by first-order weighting functions $W_{perf}(s)$ of the following form [180]

$$\frac{1}{W_{perf}(s)} = \frac{s + \omega_b A_\varepsilon}{s/M_s + \omega_b}. \quad (2.94)$$

The function $1/W_{perf}(s)$ can be representative of time-domain response specifications, where the high-frequency gain M_s has an influence on the system overshoot, whereas the cut-off frequency ω_b tunes the desired response time and the low-frequency gain A_ε allows limiting the steady-state error [74]. That ensures equivalences between desired time-domain performances and frequency-domain specifications, as shown in Figure 2.15.

The first weighting function $W_{perf_1}(s)$ is designed such that to ensure a bandwidth for ΔV_{dc} forty times smaller than the ΔI_{rd} (or ΔI_{rd}) inner closed-loop one, *i.e.*, $\omega_{b_1} = 1/(40T_{0_{rdq}}) = 2.61$ rad/s (or a response time of approximately $t_{r_1} \approx 1.2$ s). $M_{s_1} =$

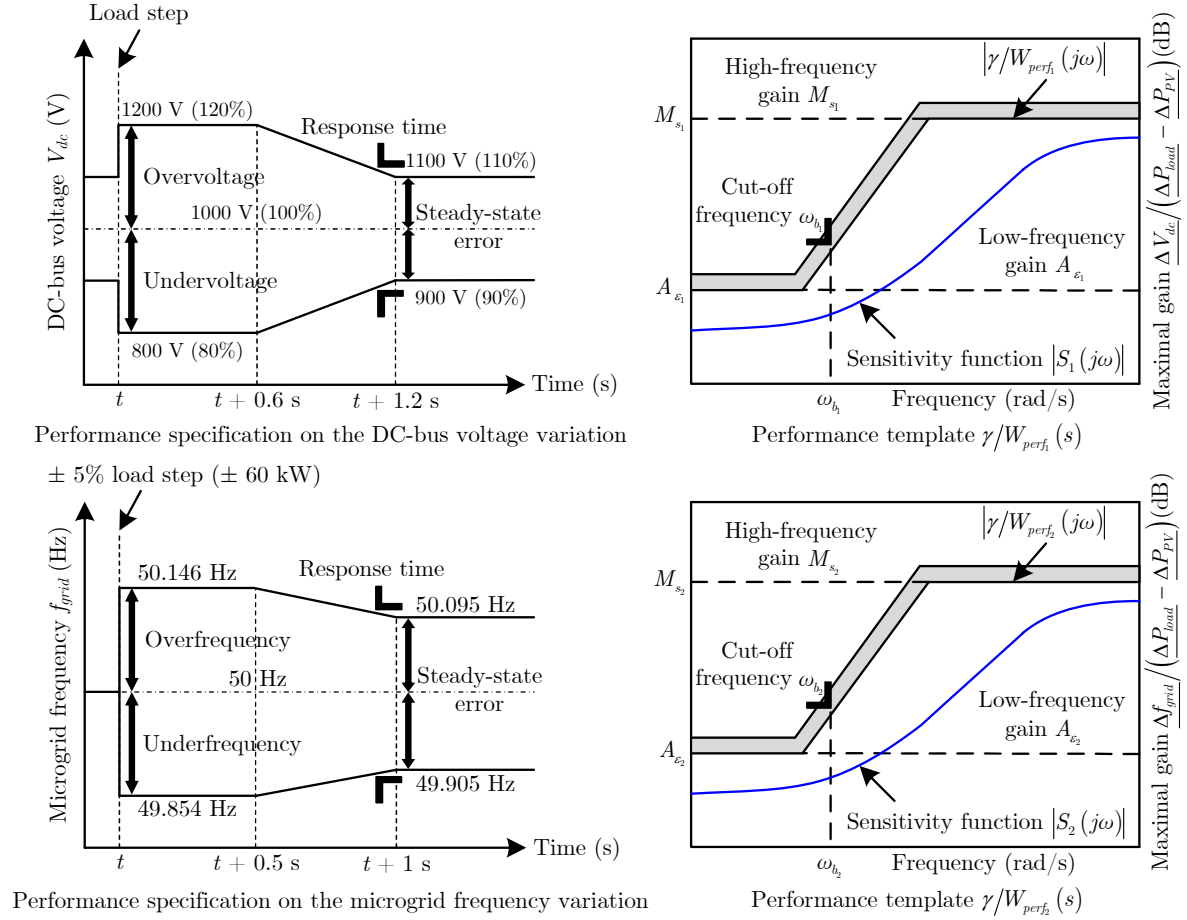


Figure 2.15 – Translations of temporal norms into frequency-domain specifications.

$(0.02V_{dc_e}) / (0.05P_{load_e}) = 1.667$ is chosen to limit the DC-bus voltage overshoot at 2% of its rated value V_{dc_e} (*i.e.*, 20 V) in response to a load step of 5% of the load rated active power P_{load_e} (*i.e.*, 60 kW). Similarly, one imposes $A_{\varepsilon_1} = (0.01V_{dc_e}) / (0.05P_{load_e}) = 0.833$ to ensure a desired steady-state error being less than or equal to 1% of V_{dc_e} (*i.e.*, 10 V).

The parameters of the second weighting function $W_{perf_2}(s)$ designed for Δf_{grid} are chosen to improve the transient response of the MG frequency compared to its performance specification in Figure 2.3. $\omega_{b_2} = 2\omega_{b_1} = 1 / (20T_{0_{rdq}}) = 5.22$ rad/s is chosen to ensure a response time of approximately $t_{r_2} \approx 0.6$ s. Imposing $M_{s_2} = [(50.12 - 50) / f_b] / (0.05P_{load_e}) = 0.08$ allows limiting the frequency overshoot at 0.12 Hz in response to a load step of 5% of P_{load_e} (*i.e.*, 60 kW). $A_{\varepsilon_2} = [(50.06 - 50) / f_b] / (0.05P_{load_e}) = 0.04$ is chosen to ensure a desired steady-state error being less than or equal to 0.06 Hz.

As analyzed in Subsection 2.5.3, the frequency interval $f_c \in [0.02, 1.31]$ Hz (or $\omega_c \in [0.12, 8.21]$ rad/s) was selected for the primary frequency control participation of the energy storage device. Moreover, the active power injection or absorption of the ESS is controlled

via I_s . Thus, the supercapacitor output current reference variation $\underline{\Delta I_s^{ref}}$ is bounded by a band-pass weighting function $W_{u_1}(s)$ written as follows

$$\frac{1}{W_{u_1}(s)} = A_{u_1} \frac{\left(\frac{M_{u_1}}{\omega_{bc11}}s + 1\right) \left(\frac{A_{u_1}}{\omega_{bc12}}s + 1\right)}{\left(\frac{A_{u_1}}{\omega_{bc11}}s + 1\right) \left(\frac{M_{u_1}}{\omega_{bc12}}s + 1\right)}, \quad \frac{\omega_{bc11}}{A_{u_1}} < \frac{\omega_{bc12}}{M_{u_1}}. \quad (2.95)$$

The frequency-domain specification on this current reference variation is presented in Figure 2.16. $M_{u_1} = \left(\frac{I_{smax} - I_{se}}{0.05P_{load_e}}\right) = 9.6$ is chosen to prevent the supercapacitor output current reference from exceeding its admissible limit I_{smax} consequent to a load step of 5% of P_{load_e} (i.e., 60 kW). A small value of $A_{u_1} = 0.1M_{u_1} = 0.96$ is imposed. In our case study, the own frequency of the selected supercapacitor technology is $f_p = 0.48$ Hz (or $\omega_p = 3.04$ rad/s), therefore, one chooses $\omega_{bc11}/A_{u_1} = 3.04$ rad/s resulting in $\omega_{bc11} = 2.92$ rad/s. Additionally, $\omega_{bc12}/M_{u_1} = 60$ rad/s is chosen, which leads to $\omega_{bc12} = 576.12$ rad/s.

The DC-bus voltage is regulated via I_{rd} . The direct component of the inverter output current reference variation $\underline{\Delta I_{rd}^{ref}}$ is bounded by the following first-order weighting function [180]

$$\frac{1}{W_{u_2}(s)} = \frac{A_{u_2}s + \omega_{bc2}}{s + \omega_{bc2}/M_{u_2}}. \quad (2.96)$$

The frequency-domain specification on this current reference variation is given in Figure 2.16. $M_{u_2} = \left(\frac{I_{rdmax} - I_{rd_e}}{0.05P_{load_e}}\right) = 8.46$ is imposed to limit the current reference below its maximum value I_{rdmax} consequent to a load step of 5% of P_{load_e} (i.e., 60 kW). A small value of $A_{u_2} = 0.1M_{u_2} = 0.846$ is chosen. $\omega_{bc2} = 1/(100T_{PWM_i}) = 40$ rad/s, where $T_{PWM_i} = 1/f_{PWM_i}$, is chosen to impose a bandwidth one hundred times smaller than the PWM switching frequency of the three-phase inverter f_{PWM_i} .

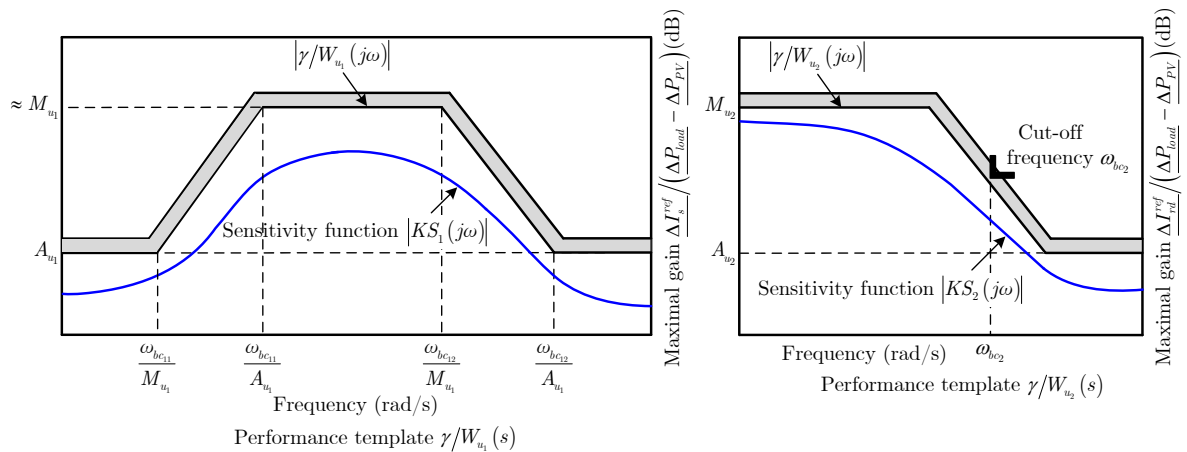


Figure 2.16 – Frequency-domain specifications on the supercapacitor output current reference variation $\underline{\Delta I_s^{ref}}$ and the d -component of the inverter output current reference variation $\underline{\Delta I_{rd}^{ref}}$.

\mathcal{H}_∞ controller synthesis

According to the system modeling and the selected weighting functions, a full-order \mathcal{H}_∞ controller is designed using the MATLAB[®] software environment and especially the robust control toolbox. The obtained result corresponds to the minimization of the norm

$$\left\| \begin{matrix} W_{perf} S \\ W_u K S \end{matrix} \right\|_\infty < \gamma. \quad (2.97)$$

Design procedure may yield unstable controllers. In this case, the value γ_{min} must be slightly increased to relax the constraint on the control and result in stable controllers. The LMI algorithm under the MATLAB[®] software environment yields a solution after one iteration for a multi-variable full-order \mathcal{H}_∞ controller which has 8 states with a conditioning value of $\gamma = 1301.27$ and an \mathcal{H}_∞ norm = 3.48. This optimization quality allows the designed \mathcal{H}_∞ controller to guarantee stable and robust performance in case of a load step of 5% of P_{load_e} (*i.e.*, 60 kW) in the system, which is demonstrated in the sequel.

For the studied system shown in Figure 2.14, sensitivity functions $S_1(s)$, $S_2(s)$ and complementary sensitivity functions $KS_1(s)$, $KS_2(s)$ are defined as follows

$$S_1(s) = \frac{\Delta V_{dc}}{\Delta P_{load} - \Delta P_{PV}}, \quad S_2(s) = \frac{\Delta f_{grid}}{\Delta P_{load} - \Delta P_{PV}}. \quad (2.98)$$

$$KS_1(s) = \frac{\Delta I_s^{ref}}{\Delta P_{load} - \Delta P_{PV}}, \quad KS_2(s) = \frac{\Delta I_{rd}^{ref}}{\Delta P_{load} - \Delta P_{PV}}. \quad (2.99)$$

The singular value plots of the sensitivity functions $S(s)$, complementary sensitivity functions $KS(s)$, and corresponding templates of the closed-loop system are shown in Figure 2.17. The results show how the shaping of \mathcal{H}_∞ performance is straightforward for the full-order \mathcal{H}_∞ controller using the weighting functions templates. One can see that the imposed control performance weights are well respected since the sensitivity functions are placed below the corresponding templates regardless of the frequency value.

2.6.4 Systematic procedure for control design

In summary, the systematic procedure for control design can be described as follows

- 1] Analyze the transfer function between the MG frequency deviation Δf_{grid} and the active power variation $\Delta P_{load} - \Delta P_{PV}$ in the frequency domain, then compute a suitable frequency interval for the storage device participation in frequency control and choose the storage technology the most appropriate to this frequency interval;
- 2] System modeling and casting of the specific engineering demands of MG operation into the \mathcal{H}_∞ control formalism;
- 3] Select weighting functions according to control objectives and control input constraints;

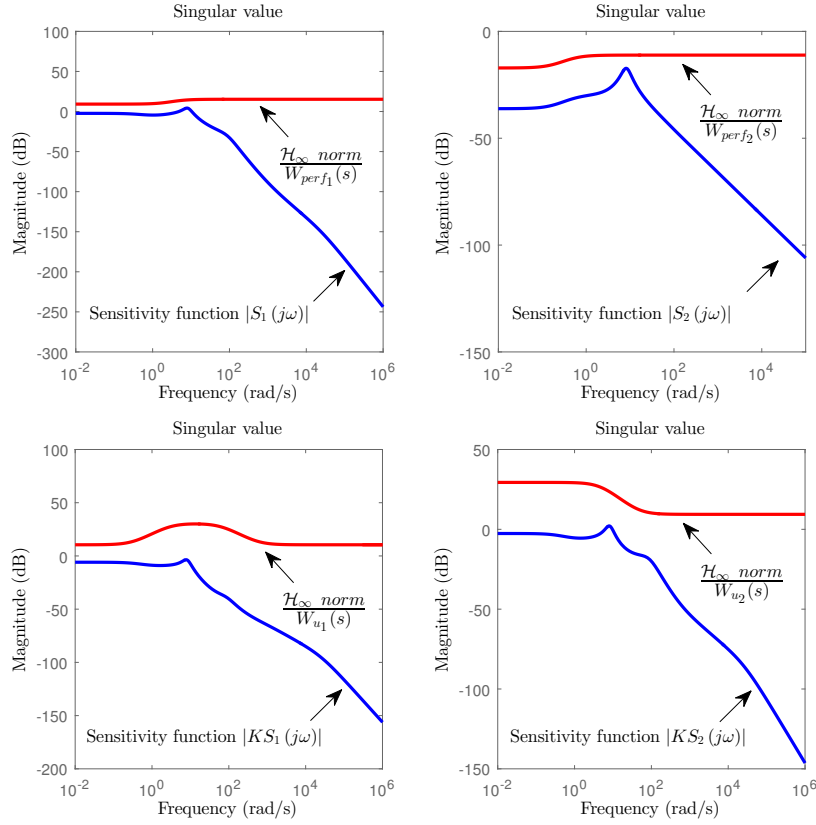


Figure 2.17 – Singular value plots of the sensitivity functions $S_1(s)$, $S_2(s)$; complementary sensitivity functions $KS_1(s)$, $KS_2(s)$; and corresponding templates.

- 4] Design an \mathcal{H}_∞ controller and perform numerical simulations to verify if the control objectives are satisfied or not. If not, go to Step 3.

2.6.5 Numerical simulation results

In order to validate the effectiveness of the proposed control approach, MATLAB[®]/Simulink[®] closed-loop time-domain simulations are performed on the topological model, as well as the nonlinear and linear averaged models. The topological model refers here to the complete model of the ESS considering the ideal PWM switching functions of the chopper and of the three-phase inverter as control inputs. Without loss of generality, a load step change of + 5% of the load rated active power P_{load_e} (*i.e.*, + 60 kW) at $t = 1$ s is applied as a perturbation. The supercapacitor voltage V_{sc} , initially considered as a time-invariant parameter in the \mathcal{H}_∞ controller synthesis to ensure a prerequisite for the robust performance analysis of this controller in the sequel (*i.e.*, V_{sc} must be considered as a parametric uncertainty), is regarded now as a time-variant one, *i.e.*, $\Delta V_{sc} \neq 0$ (its dynamic equation $\dot{V}_{sc} = f(V_{sc}, I_s)$ being taken into account in the simulation models) in order to make the physical representativeness of these models closer to the reality.

Model validation and effectiveness of the proposed robust control strategy

The comparison of topological and averaged modeling for the time-domain responses of the MG frequency f_{grid} and DC-bus voltage V_{dc} is presented in Figure 2.18(a) and Figure 2.18(b) respectively. The results show a good concordance of these models in the sense that the averaged model approximates very well the converter's low-frequency behavior, the one generally used for control purposes. Therefore, the averaged models themselves are validated when compared to the topological model results. From Figure 2.18(a) it can be observed that the MG frequency desired time-domain performances are successfully achieved with respect to the choice of the weighting function $W_{perf_2}(s)$. Compared with the case in which only the diesel engine generator participates in primary frequency control, the storage device participation has considerably improved the dynamic performances (*i.e.*, lower overshoot, faster response time, smaller steady-state error) of the frequency. The system is also always stable. Figure 2.18(b) shows that the DC-bus voltage desired time-domain performances corresponding to the tuning of the weighting function $W_{perf_1}(s)$ are satisfied. Hence, the synthesized \mathcal{H}_∞ controller ensures the desired performance specifications.

Figure 2.19(a) and Figure 2.19(b) respectively compare the time-domain responses of the supercapacitor output current I_s and the direct component of the inverter output current I_{rd} obtained with both topological and averaged models. Despite oscillations observed in the topological model, the results show a good agreement between these models. Therefore, the averaged models precisely represent the dynamics of the ESS. Moreover, one can see that the admissible limit is guaranteed for both of these currents, which means that their dynamic performances are satisfied.

Without loss of generality and for the sake of simplicity, the nonlinear averaged model will from now on be used for time-domain simulation.

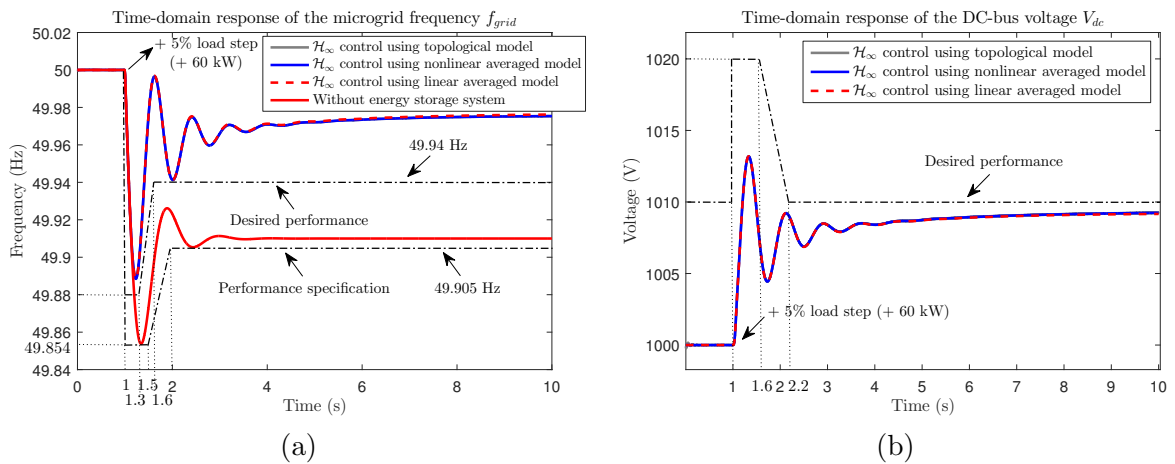


Figure 2.18 – (a) MG frequency time-domain response f_{grid} and (b) DC-bus voltage time-domain response V_{dc} under a small load step disturbance of +5% of the load rated active power (+60 kW) with respect to the rated operating point.

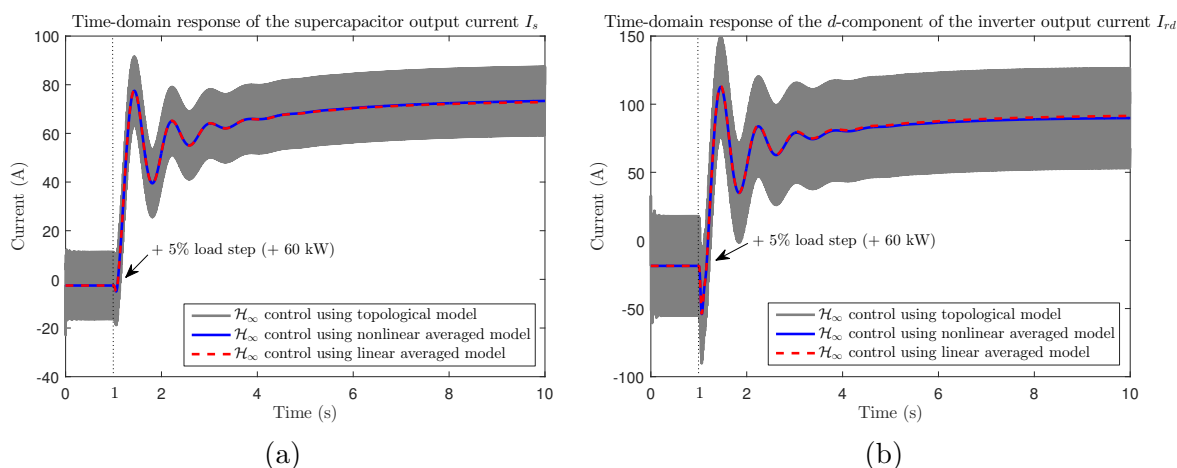


Figure 2.19 – Time-domain responses of (a) the supercapacitor output current I_s and (b) the d -component of the inverter output current I_{rd} under a small load step disturbance of + 5% of the load rated active power (+ 60 kW) with respect to the rated operating point.

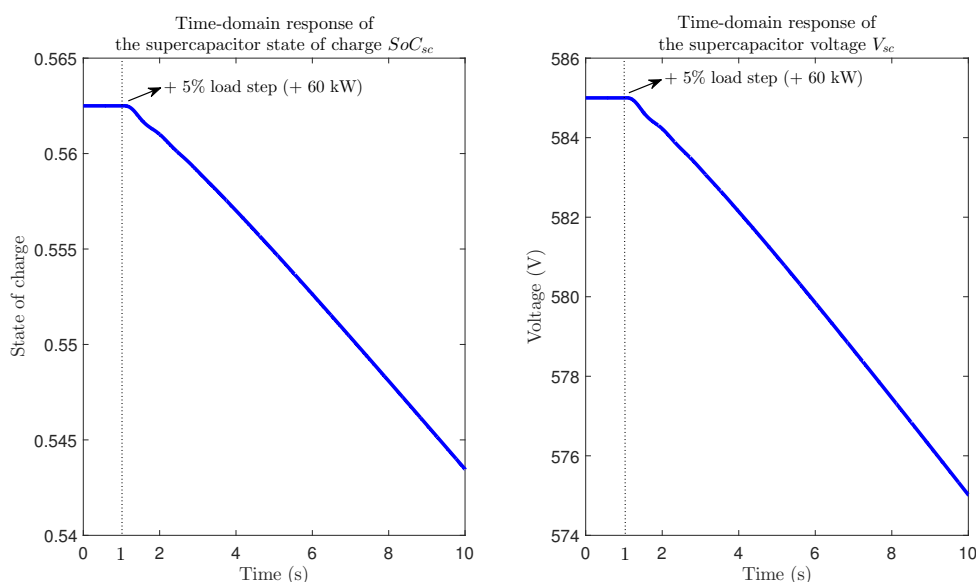


Figure 2.20 – Time-domain responses of the supercapacitor state of charge SoC_{sc} and voltage V_{sc} under a small load step disturbance of + 5% of the load rated active power (+ 60 kW) with respect to the rated operating point.

Figure 2.20 illustrates the time-domain responses of the supercapacitor state of charge SoC_{sc} and voltage V_{sc} . These values tend to decrease linearly and quite slowly, which means that the supercapacitor is in discharging mode.

The ESS participation in primary frequency control has reduced the active power variation of the diesel generator and slowed down its transient response, as shown in Figure 2.21. From the time-domain response of the power variation of the energy storage device, its sizing can be defined from the maximum active power variation of the load or PV source. Then, an

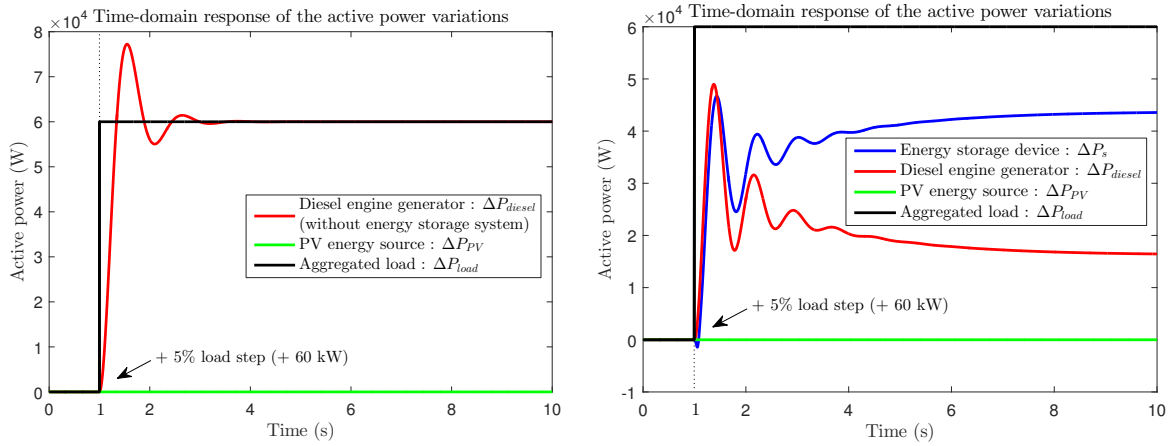


Figure 2.21 – Active power variations of the sources and load under a small load step disturbance of + 5% of the load rated active power (+ 60 kW).

important peak of power provided by the storage device is needed if a small variation of the transient frequency is required. A compromise between the MG admissible frequency variation and the rated power of the storage device is necessary. As the MG frequency variation with the ESS by \mathcal{H}_∞ control is fixed by the definition of the weighting function $W_{perf_2}(s)$, the desired performance specification should be relaxed in order to increase the MG admissible frequency variation, resulting in power and energy reduction used by the storage device, which has impact on the energy storage cost. For instance, the desired steady-state value of the MG frequency can be increased from 0.06 Hz to 0.09 Hz (nearer to that of the MG frequency time-domain response without ESS) to reduce the power supplied by the storage device. The desired performance of the MG frequency variation focuses on primary frequency control only. Therefore, the ESS does not participate in secondary frequency control. The diesel generator will bring the MG frequency back to 50 Hz after 15 seconds of disturbance. If the ESS is used to participate in secondary frequency control, the weighting function of the MG frequency variation $W_{perf_2}(s)$ should be redesigned with a small steady-state value of the MG frequency variation (small A_{e_2}). However, in this case, a high energy density of the storage device should be required and induces a rise in the investment cost [142].

Impact of the secondary control of the diesel engine generator

The impact of the secondary control of the diesel generator on the system response is also analyzed. Secondary control is turned on after 15 seconds of disturbance with some values of \underline{K}_i . As can be seen from Figure 2.22(a), the secondary control participation of the diesel generator brings the MG frequency back to its rated value of 50 Hz. Frequency error canceling depends on how secondary control is tuned, *i.e.*, the value of \underline{K}_i . Let us remark here that the error cancellation is obtained more rapidly in the system without ESS. The ESS is brought back to the initial steady-state operating point as shown in Figure 2.22(b), Figure 2.23(a), Figure 2.23(b), and Figure 2.25 respectively, except that the supercapacitor state of charge

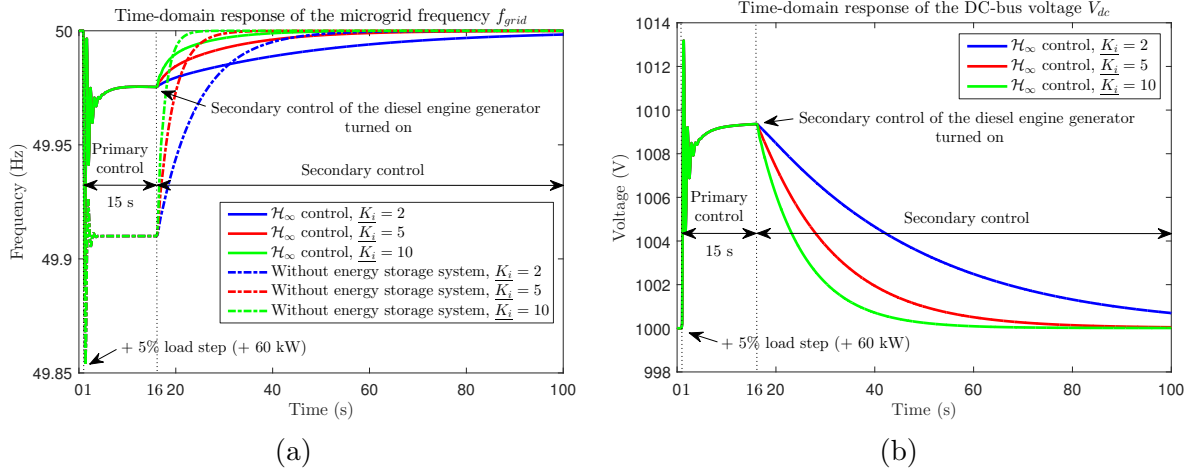


Figure 2.22 – (a) MG frequency time-domain response f_{grid} and (b) DC-bus voltage time-domain response V_{dc} under a small load step disturbance of + 5% of the load rated active power (+ 60 kW) with respect to the rated operating point taking into account the secondary control of the diesel engine generator.

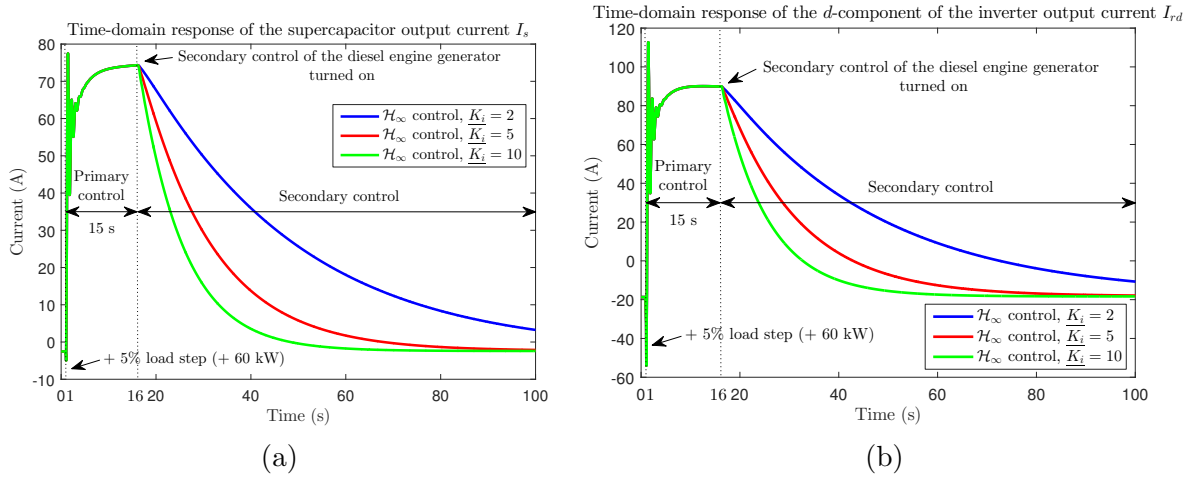


Figure 2.23 – Time-domain responses of (a) the supercapacitor output current I_s and (b) the d -component of the inverter output current I_{rd} under a small load step disturbance of + 5% of the load rated active power (+ 60 kW) with respect to the rated operating point taking into account the secondary control of the diesel engine generator.

and voltage shown in Figure 2.24 are decreased due to its participation in frequency control. The system trajectory depends also on the tuning of secondary control. In steady-state operation, the load active power variation is totally compensated by only the diesel generator, as illustrated in Figure 2.25.

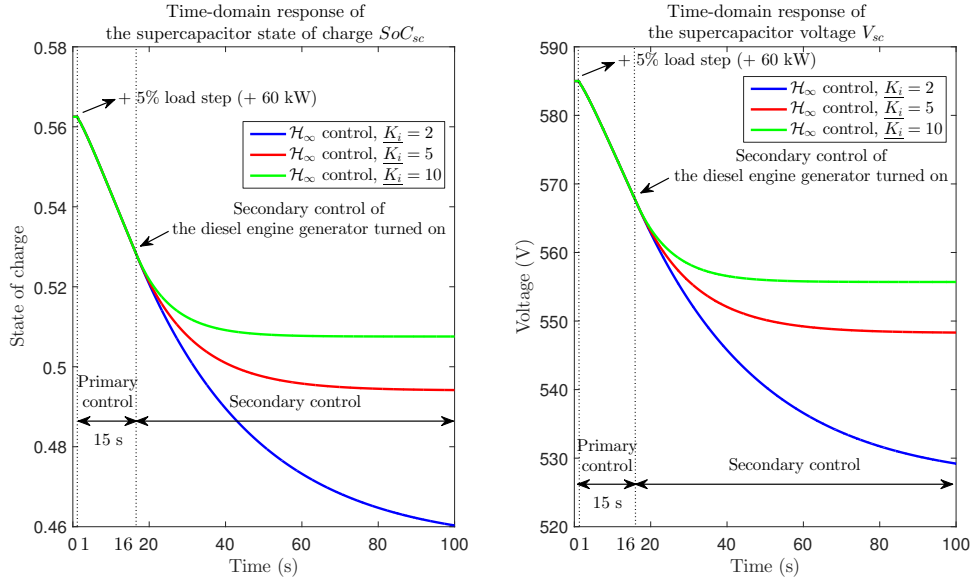


Figure 2.24 – Time-domain responses of the supercapacitor state of charge SoC_{sc} and voltage V_{sc} under a small load step disturbance of + 5% of the load rated active power (+ 60 kW) with respect to the rated operating point taking into account the secondary control of the diesel engine generator.

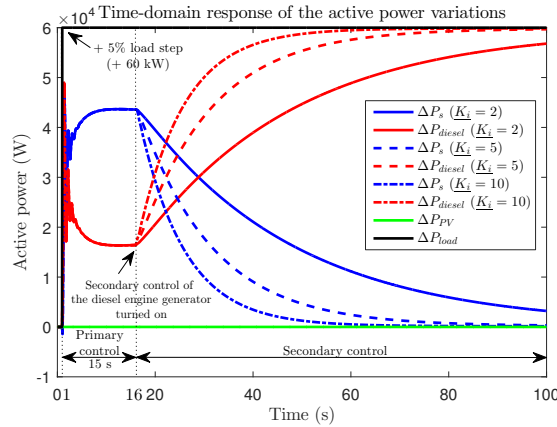


Figure 2.25 – Active power variations of the sources and load under a small load step disturbance of + 5% of the load rated active power (+ 60 kW) taking into account the secondary control of the diesel engine generator.

2.7 Robust performance analysis

The studied diesel-PV-supercapacitor hybrid power generation system can be subject to numerous uncertainty sources. These uncertainties could be associated first with the parameters of the system. They could also represent the different dynamics of the real system which are neglected (unmodeled) in the theoretical (mathematical) model or the misunderstandings of the model in high frequencies. Variations of the operating point (*e.g.*, variability of the PV

system output power, ESS capacity, *etc.*) could also be regarded as uncertainty sources.

In this section, a robust performance analysis of the \mathcal{H}_∞ controller, which was synthesized in the previous section while the system parameters are fixed at their rated values, is detailed. More particularly, the parametric uncertainty in the steady-state value of the supercapacitor state of charge SoC_{sc_e} (or supercapacitor voltage V_{sc_e}) is first considered. Then, a sensitivity analysis and robustness analysis by μ -analysis are carried out in order to determine the maximum variation range of the value SoC_{sc_e} (or V_{sc_e}) for which the imposed closed-loop performances are respected. Some MATLAB[®]/Simulink[®] closed-loop time-domain simulations are finally presented to validate the controller robustness and performance in the presence of various load and PV output disturbances, as well as the uncertainty in SoC_{sc_e} .

2.7.1 Parametric uncertainties

Parametric uncertainties belonging to the class of structured uncertainties are here considered. In the case of the studied hybrid system, these uncertainties could be associated first with the parameters of the ESS (capacitor C_{sc} , series resistor R_{sc} , and parallel resistor R_{sc_p} of the supercapacitor; inductor L_c and resistor R_c of the choke; capacitor C_{dc} and resistor R_{dc} of the DC bus; inductor L_f , capacitor C_f , and resistor R_f of the output filter) but could also be representative of the variation in the steady-state value of the supercapacitor state of charge SoC_{sc_e} (or supercapacitor voltage V_{sc_e}), which leads to changes in the steady-state operating point of the system. They could also represent changes in the MG equivalent inertia constant H and load damping constant D_{load} . In addition, the time constant T_{diesel} , droop value s_{diesel} , and secondary control gain K_i of the diesel engine generator could also be regarded as parametric uncertainties.

For the sensitivity and robustness analysis which are hereafter presented, only the uncertainty in SoC_{sc_e} (or V_{sc_e}) is taken into account. SoC_{sc} estimation is very important in determining the best operating strategy of the ESS. SoC_{sc} is approximated as the ratio between the stored energy W_{sc}^* shown in Figure 2.26 and the maximum storable energy $W_{sc_{max}}^*$ as follows (with the internal resistances R_{sc} and R_{sc_p} being neglected)

$$SoC_{sc} = \frac{W_{sc}^*}{W_{sc_{max}}^*} = \frac{\frac{1}{2}C_{sc}V_{sc}^2}{\frac{1}{2}C_{sc}V_{sc_{max}}^2} = \left(\frac{V_{sc}}{V_{sc_{max}}}\right)^2, \quad (2.100)$$

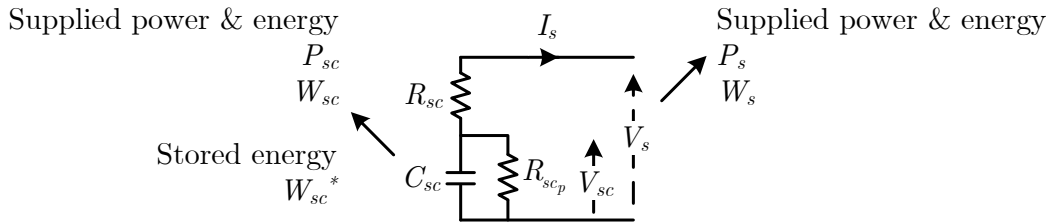


Figure 2.26 – Schematic diagram of the supercapacitor.

where $V_{sc_{max}} = 780$ V is the maximum possible supercapacitor voltage. In practice, SoC_{sc} is maintained within the admissible range of $[25, 100]$ % to ensure reliable, efficient, and safe operation of the supercapacitor and prolong its lifespan. The limited variation range, corroborated with (2.100), indicates that the V_{sc} value must be controlled between 390 V and 780 V. The midrange between these two values, *i.e.*, $V_{sc} = 585$ V, is a convenient choice for designing the nominal \mathcal{H}_∞ controller whose robustness is further assessed.

2.7.2 Sensitivity analysis

In this subsection, the sensitivity analysis of robust performance of the \mathcal{H}_∞ controller is considered to answer the question whether the closed-loop system remains robust or not (from a performance point of view) to a given parametric uncertainty level in the steady-state value of the supercapacitor voltage V_{sc_e} around its design value, 585 V.

The sampled uncertain sensitivity functions $S(s)$, complementary sensitivity functions $KS(s)$ obtained with 33.3% uncertainty in V_{sc_e} around its design value, 585 V (*i.e.*, $SoC_{sc_e} \in [25, 100]$ % or $V_{sc_e} \in [390, 780]$ V) and corresponding templates of the closed-loop system performed with the \mathcal{H}_∞ norm = 3.48 are presented in Figure 2.27. It can be observed that,

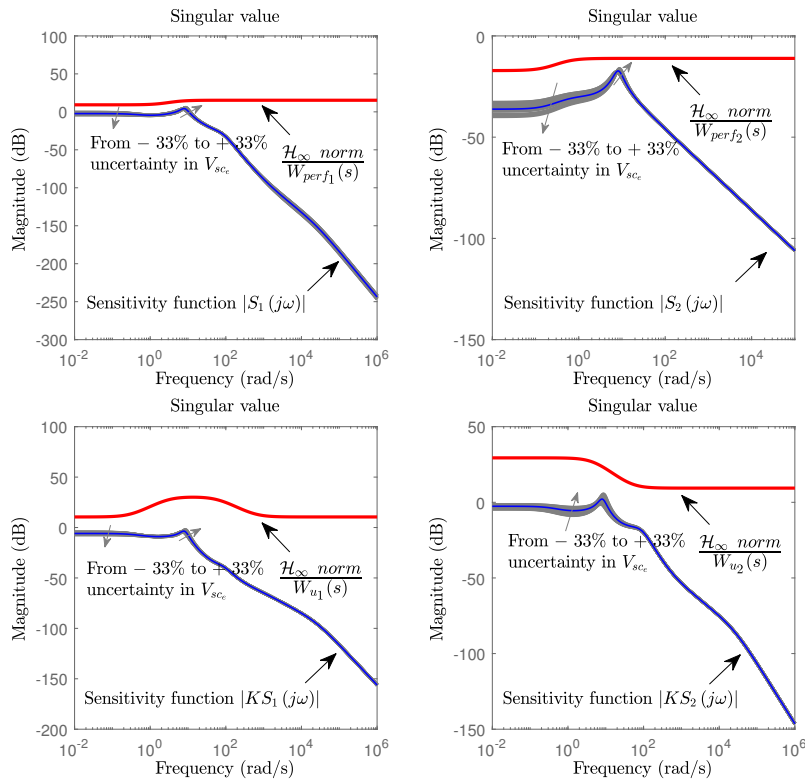


Figure 2.27 – Singular value plots of the sampled uncertain sensitivity functions $S_1(s)$, $S_2(s)$; complementary sensitivity functions $KS_1(s)$, $KS_2(s)$ obtained with 33.3% uncertainty in V_{sc_e} ; and corresponding templates.

irrespective of the parametric uncertainty in V_{sc_e} , these functions are well located below the corresponding weights, which means that the imposed overshoot performance specifications are guaranteed.

Without loss of generality, MATLAB[®]/Simulink[®] closed-loop time-domain simulations using the nonlinear averaged model are carried out with a PV output active power step disturbance of -60 kW at $t = 10$ s. The supercapacitor voltage V_{sc} appears as a time-variant parameter (*i.e.*, $\Delta V_{sc} \neq 0$) in the simulation model. The initial value of SoC_{sc} is varied between 25% and 100% in simulation. As predicted by analyzing the sampled uncertain sensitivity functions $S(s)$, complementary sensitivity functions $KS(s)$, and corresponding templates in Figure 2.27, as well as seen in Figure 2.28 and Figure 2.29, the imposed closed-

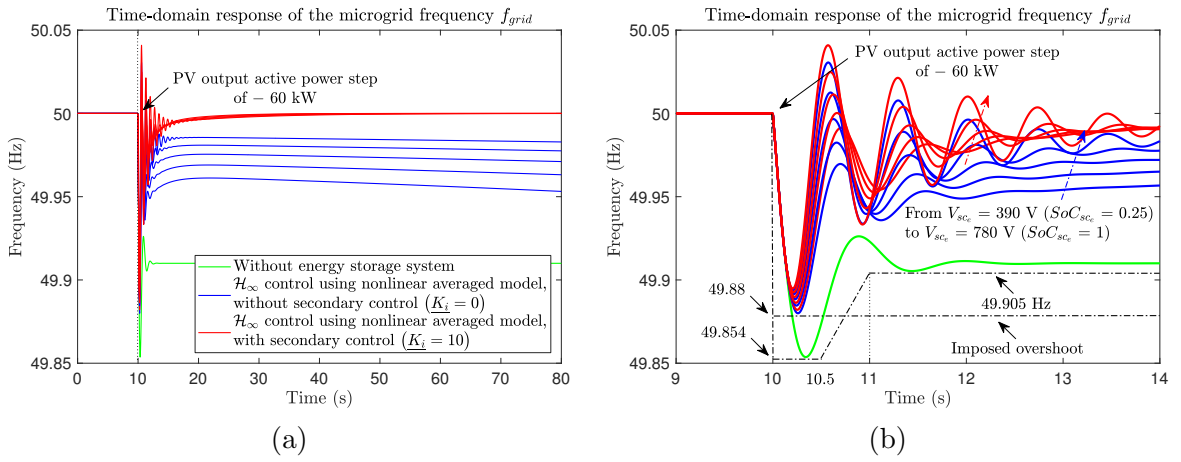


Figure 2.28 – (a) MG frequency time-domain response f_{grid} under a PV output active power step disturbance of -60 kW taking into account the uncertainty in V_{sc_e} (or SoC_{sc_e}). (b) Temporal zoom in the time interval $t \in [9, 14]$ s.

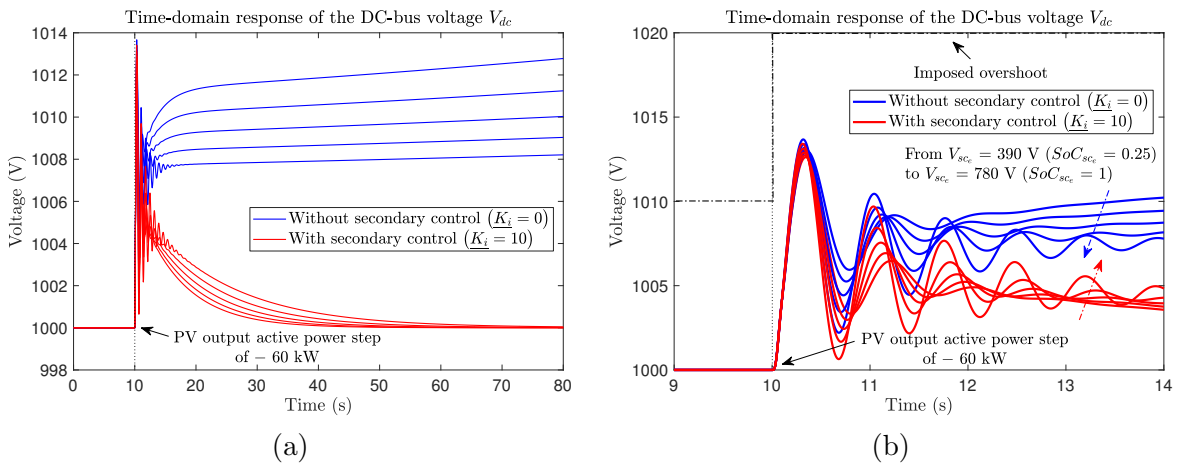


Figure 2.29 – (a) DC-bus voltage time-domain response V_{dc} under a PV output active power step disturbance of -60 kW taking into account the uncertainty in V_{sc_e} (or SoC_{sc_e}). (b) Temporal zoom in the time interval $t \in [9, 14]$ s.

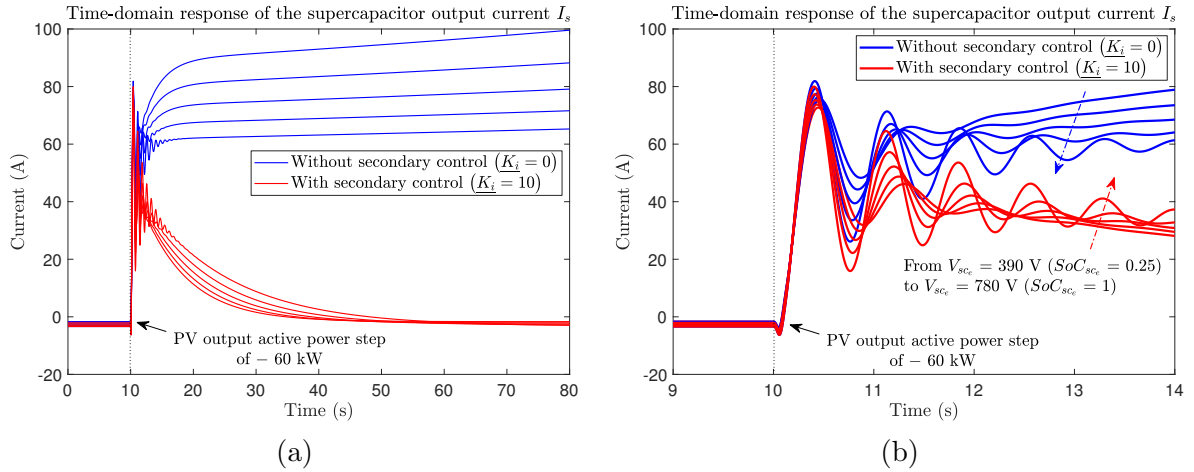


Figure 2.30 – (a) Time-domain response of the supercapacitor output current I_s under a PV output active power step disturbance of -60 kW taking into account the uncertainty in V_{sc_e} (or SoC_{sc_e}). (b) Temporal zoom in the time interval $t \in [9, 14]$ s.

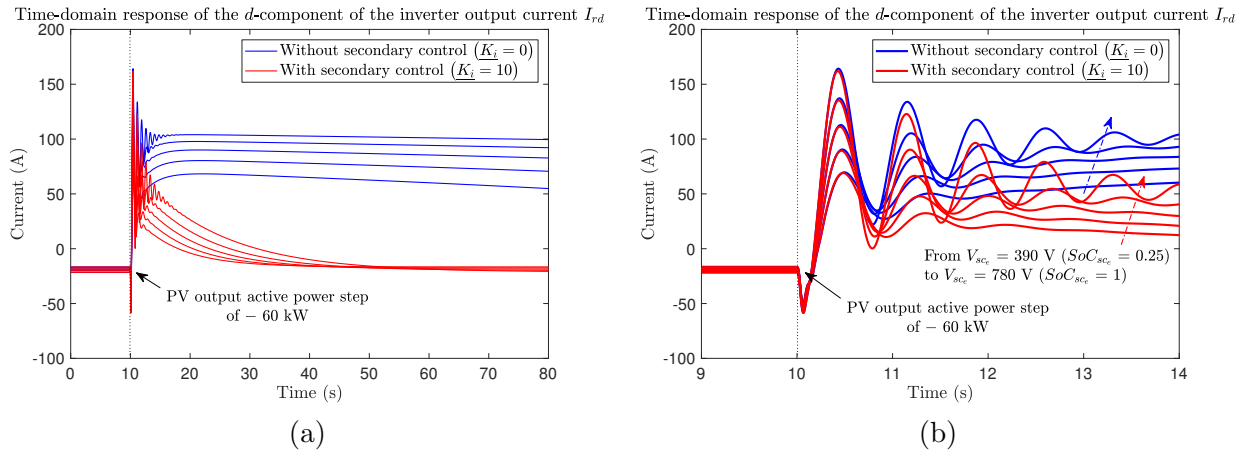


Figure 2.31 – (a) Time-domain response of the d -component of the inverter output current I_{rd} under a PV output active power step disturbance of -60 kW taking into account the uncertainty in V_{sc_e} (or SoC_{sc_e}). (b) Temporal zoom in the time interval $t \in [9, 14]$ s.

loop overshoot performances of the MG frequency f_{grid} and the DC-bus voltage V_{dc} are preserved regardless of the initial value of SoC_{sc} . Frequency error canceling depends on how secondary, PI, control, is tuned. Hence, the synthesized \mathcal{H}_∞ controller is robust in performance to $SoC_{sc_e} \in [25, 100]\%$ (or $V_{sc_e} \in [390, 780]$ V). The time-domain responses of the supercapacitor output current I_s and the direct component of the inverter output current I_{rd} taking into account the uncertainty in V_{sc_e} are given in Figure 2.30 and Figure 2.31, respectively. It can be observed that the admissible limit is ensured for both of these currents, which means that their dynamic performances are fulfilled.

The above mentioned sensitivity analysis is considered as just an illustrative example for assessing robust performance of the designed \mathcal{H}_∞ controller subject to a given parametric

value of the supercapacitor voltage V_{sc_e} around its design value, 585 V.

In the \mathcal{H}_∞ control framework, the extended general control configuration in the so-called $\mathbf{N} - \mathbf{\Delta}$ form for robust performance analysis is considered in Figure 2.32 (see [180] for more details). Since μ -analysis will be carried out for the closed-loop system, $\mathbf{N}(s)$ should be defined as the connection of the plant together with the weighting functions and the previously synthesized \mathcal{H}_∞ controller. The linear time-invariant uncertain matrix is $\mathbf{\Delta}(s) = \text{diag}\{\mathbf{\Delta}_f(s) \ \mathbf{\Delta}_s(s)\}$, where $\mathbf{\Delta}_f(s)$ is the fictive full block complex uncertain matrix representing the \mathcal{H}_∞ norm specifications and $\mathbf{\Delta}_s(s)$ the block diagonal real uncertain matrix which represents the parametric uncertainty in V_{sc_e} .

Let us remark that the robust performance analysis is quite conservative and needs a tight definition of the weighting functions that do represent the performance objectives to be fulfilled by the uncertain closed-loop system. Hence, it is essential to distinguish the weighting functions used for the nominal design from the ones used for the robust performance analysis. Here all the weighting functions of the uncertain closed-loop system $W_{perf_{CL}}(s)$ and $W_{u_{CL}}(s)$ are taken into account in the robust performance test, where they have been modified by the coefficient “ \mathcal{H}_∞ norm” compared to the nominal weights, *i.e.*, $W_{perf_{CL}}(s) = W_{perf}(s) / \mathcal{H}_\infty \text{ norm}$ and $W_{u_{CL}}(s) = W_u(s) / \mathcal{H}_\infty \text{ norm}$, as illustrated in Figure 2.32.

μ -Analysis result

Let us remark that the structured singular value μ cannot be explicitly determined, so that the method consists in computing an upper bound and a lower bound, as close as possible to μ .

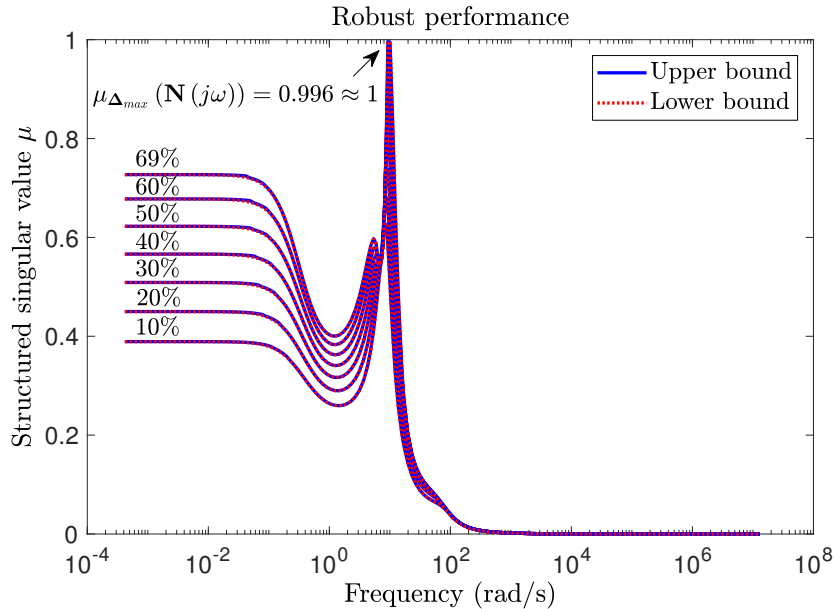


Figure 2.33 – Robust performance μ -bounds plot for the uncertainty levels of 10%, 20%, 30%, 40%, 50%, 60%, and 69% in V_{sc_e} .

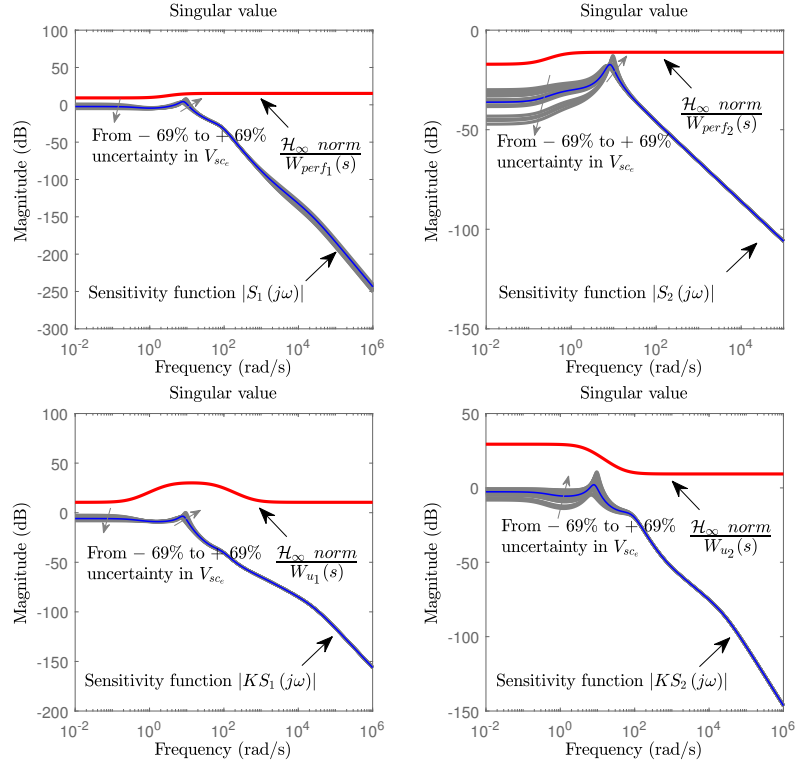


Figure 2.34 – Singular value plots of the sampled uncertain sensitivity functions $S_1(s)$, $S_2(s)$; complementary sensitivity functions $KS_1(s)$, $KS_2(s)$ obtained with 69% uncertainty in V_{sc_e} ; and corresponding templates.

In μ -analysis, V_{sc_e} appears as a parametric uncertainty in the matrix \mathbf{B}_1 of (2.93). The robust performance μ -bounds plot for several uncertainty levels in V_{sc_e} is shown in Figure 2.33. It can be observed that the closed-loop system remains robust in performance up to 69% uncertainty in V_{sc_e} around its design value, 585 V, which corresponds to $\mu_{\Delta_{max}}(\mathbf{N}(j\omega)) = 0.996 \approx 1$. This variation range corresponds theoretically to [181, 989] V, knowing that SoC_{sc} cannot exceed 100%, *i.e.*, 780 V.

The singular value plots of the sampled uncertain sensitivity functions $S(s)$, complementary sensitivity functions $KS(s)$ obtained with 69% uncertainty in V_{sc_e} , and corresponding templates of the closed-loop system are presented in Figure 2.34. The results show how the shaping of \mathcal{H}_∞ performance is straightforward for the full-order \mathcal{H}_∞ controller using the template weights. Irrespective of the parametric uncertainty in V_{sc_e} , one can see that the imposed overshoot performance weights are well respected since the sensitivity functions are placed below the corresponding templates regardless of the frequency value.

Numerical simulation results

Without loss of generality, MATLAB[®]/Simulink[®] closed-loop time-domain simulations using the nonlinear averaged model are carried out with load steps of + 5% of the load rated

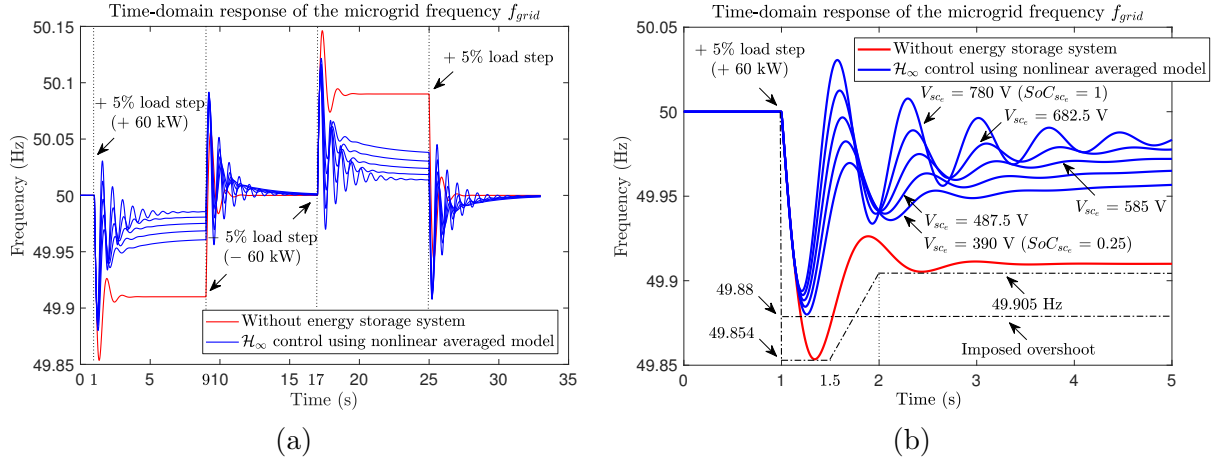


Figure 2.35 – (a) MG frequency time-domain response f_{grid} under small load step disturbances of $\pm 5\%$ of the load rated active power (± 60 kW) taking into account the uncertainty in V_{sc_e} (or SoC_{sc_e}). (b) Temporal zoom in the time interval $t \in [0, 5]$ s.

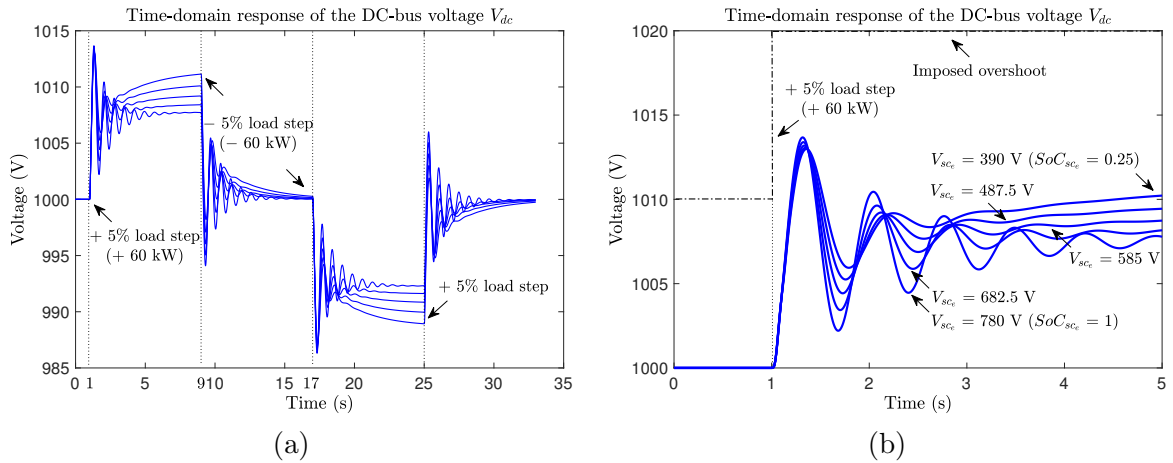


Figure 2.36 – (a) DC-bus voltage time-domain response V_{dc} under small load step disturbances of $\pm 5\%$ of the load rated active power (± 60 kW) taking into account the uncertainty in V_{sc_e} (or SoC_{sc_e}). (b) Temporal zoom in the time interval $t \in [0, 5]$ s.

active power P_{load_e} (*i.e.*, $+ 60$ kW) at $t = 1$ s, $- 5\%$ at $t = 9$ s, $- 5\%$ at $t = 17$ s, and $+ 5\%$ at $t = 25$ s. The supercapacitor voltage V_{sc} appears as a time-variant parameter (*i.e.*, $\Delta V_{sc} \neq 0$) in the simulation model. The initial value of SoC_{sc} is varied between 25% and 100% in simulation. As predicted by the robustness analysis, as well as seen in Figure 2.35 and Figure 2.36, the imposed closed-loop overshoot performances of the MG frequency f_{grid} and the DC-bus voltage V_{dc} are preserved regardless of the initial value of SoC_{sc} . Frequency error canceling depends on how secondary, PI, control, is tuned. Hence, the synthesized \mathcal{H}_∞ controller is robust in performance to $SoC_{sc_e} \in [25, 100]\%$ (or $V_{sc_e} \in [390, 780]$ V). The time-domain responses of the supercapacitor output current I_s and the direct component of the inverter output current I_{rd} taking into account the uncertainty in V_{sc_e} are given in Figure 2.37. It can be observed that the admissible limit is guaranteed for both of these currents, which

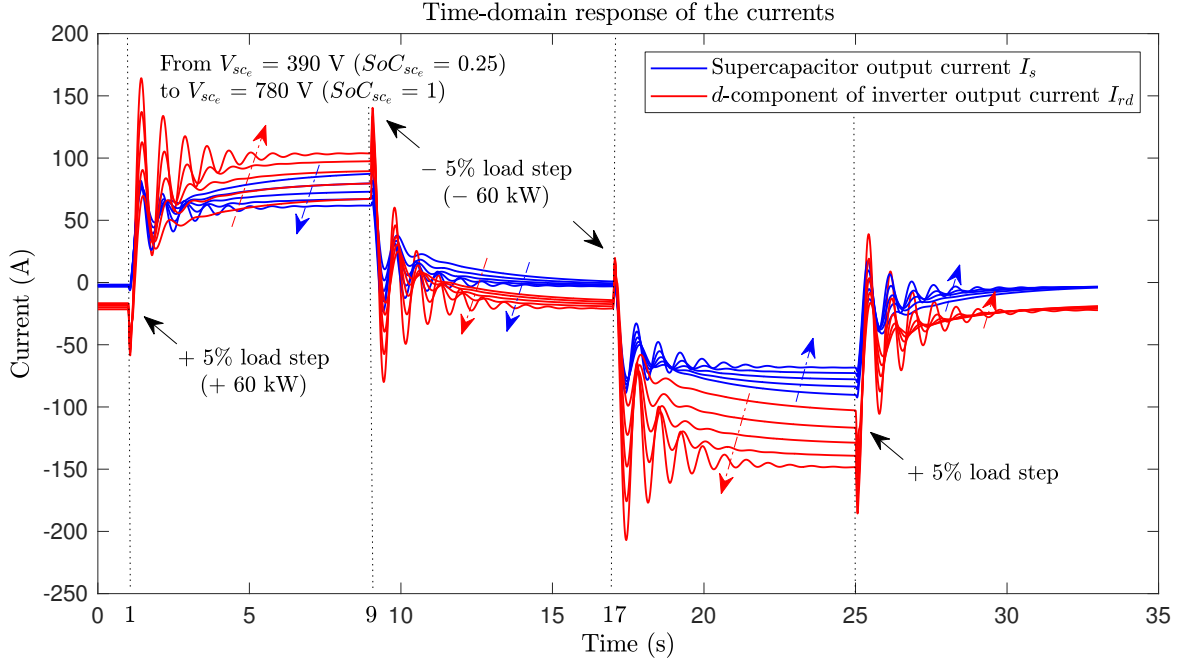


Figure 2.37 – Time-domain responses of the supercapacitor output current I_s and the d -component of the inverter output current I_{rd} under small load step disturbances of $\pm 5\%$ of the load rated active power (± 60 kW) taking into account the uncertainty in V_{sc_e} (or SoC_{sc_e}).

means that their imposed dynamic performances are met.

2.8 Chapter conclusion

In this chapter, frequency-control-oriented modeling has been detailed for the diesel-PV-storage hybrid power generation system operating in stand-alone mode. We have also proposed a systematic design procedure for computing a centralized, multi-variable \mathcal{H}_∞ robust controller for frequency regulation in stand-alone MGs highly penetrated by RESs. Effectiveness of the proposed robust control strategy has been validated *via* numerical simulation results. A complete time/frequency-domain analysis, including a robust performance analysis, has been performed for frequency robust control in stand-alone MGs with PV sources. This points out that the synthesized \mathcal{H}_∞ controller remains robust in performance to the large uncertainty in the initial value of SoC_{sc} (in particular $SoC_{sc_e} \in [25, 100]\%$), which is quite good for practical operation of the supercapacitor-based ESS as long as the corresponding variations of the supercapacitor output current are considered admissible.

Use of the \mathcal{H}_∞ robust control approach may not guarantee the desired dynamic performance specifications in the presence of large disturbance in the system. In this situation, design of an LPV control approach could be a feasible solution for addressing various oper-

ating conditions (*e.g.*, changes in ESS capacity, PV system output power, load power, *etc.*). The advantage of LPV control is that stability and performance of the closed loop can be guaranteed not only for all possible values of the parameters, but also during variations of the parameters. The LPV controller can automatically adapt its parameters for different operating points.

Voltage robust control in stand-alone microgrids

3.1 Introduction

This chapter addresses the voltage stability and regulation issues of islanded MGs with high penetration of renewable energy by making use of energy storage devices. In [97], the cooperative control strategy for sharing the reactive power demand among generation sources and fast-acting ESSs during islanded mode of operation in MGs has been proposed. By an adequate reactive-power-balance matching process, the PCC voltage magnitude can be regulated at the rated value, provided that the available capacity of the ESSs does not exceed their limitations. In this thesis framework, an \mathcal{H}_∞ -based multi-variable robust controller for PCC voltage magnitude regulation that copes with load reactive power variations in a diesel-PV-storage hybrid power generation system operating in stand-alone mode, is first proposed. A two-level control architecture, where this controller is placed on an upper control level and provides the references to current controllers placed on a lower level, is also adopted. Then, the performance and robustness of the proposed controller in the presence of various load disturbances and model uncertainties are studied based on MATLAB[®]/Simulink[®] time-domain simulations.

The remainder of this chapter is organized as follows. Section 3.2 describes the considered MG configuration and dynamic specifications for voltage control. Dynamic modeling of the MG for \mathcal{H}_∞ control is provided in Section 3.3. Section 3.4 is dedicated to an analysis of open-loop system behavior of the studied MG without ESS, as well as the whole MG. Section 3.5 details a robust design approach for voltage control along with some closed-loop time-domain simulations performed in the rated operating point. A robust performance analysis of the synthesized \mathcal{H}_∞ controller, subject to the uncertainties in the steady-state value of the supercapacitor voltage V_{sc} and the length of the transmission line l connecting the diesel engine generator to the PCC, is investigated in Section 3.6. Some concluding remarks are stated in Section 3.7.

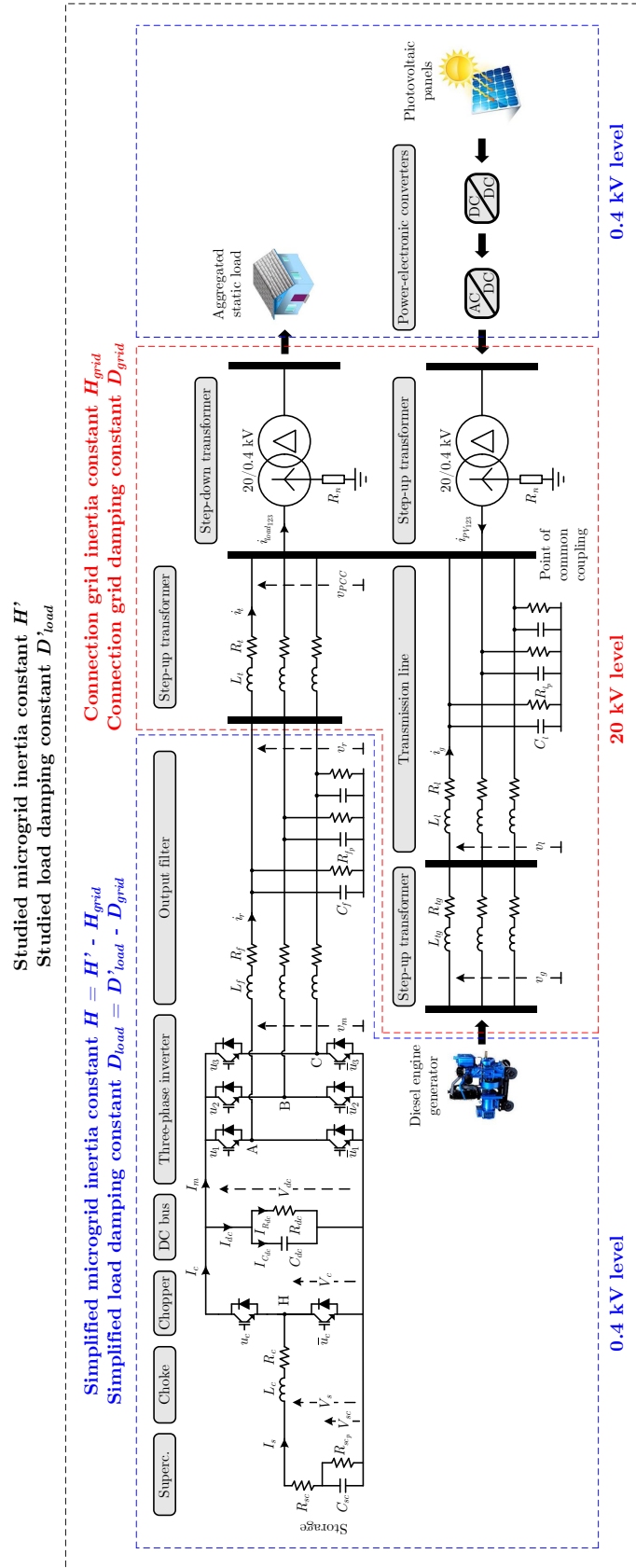


Figure 3.1 – Schematic diagram of the MG under consideration for voltage stability analysis.

3.2 Microgrid structure and dynamic specifications

3.2.1 System structure

A brief description of the studied MG structure has been provided in Section 1.6. The schematic diagram of the considered MG, which is used for voltage stability analysis, is shown in Figure 3.1.

3.2.2 Dynamic specifications for voltage control

In stand-alone MGs with high penetration of PV energy sources, the PCC voltage is risky to be unstable or its magnitude variations can be considerable and unacceptable. Properly designed ESSs can then be employed to stabilize the MG and/or improve the PCC voltage transient response by absorbing or injecting instantaneous reactive power subsequent to disturbances. In the considered MG, a control strategy where the ESS and the diesel engine generator have to fulfill distinct roles in voltage control is proposed. Thus, the ESS must act in high frequency by guaranteeing faster recovery of the PCC line-to-line voltage magnitude U_{PCC} consequent to a load or PV output reactive power variation, *i.e.*, to improve its dynamic performances (overshoot, response time, steady-state error). On the basis of grid code requirements [167], a template for the PCC line-to-line voltage magnitude deviation in response to a load reactive

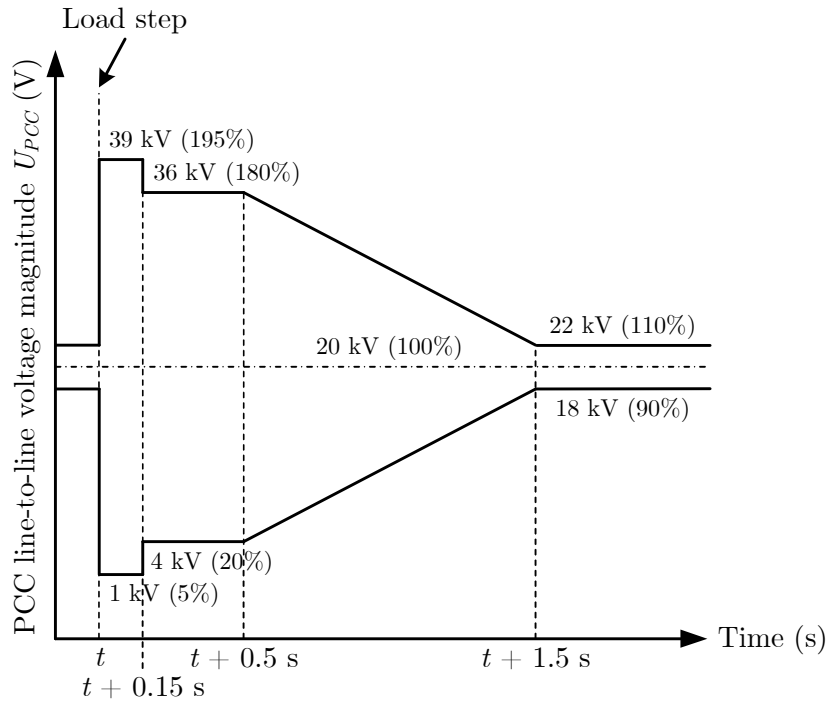


Figure 3.2 – Performance specification on the PCC line-to-line voltage magnitude variation in response to a load reactive power step disturbance in the time domain.

power step disturbance is defined in Figure 3.2.

Another control objective which must be taken into account is to regulate the DC-bus voltage V_{dc} at a reference value V_{dc}^{ref} that has been here chosen as 1000 V. The performance specification on this voltage variation has already been given in Figure 2.10 in Subsection 2.5.4.

3.3 Dynamic modeling of the microgrid

Voltage-control-oriented modeling describing the approximate dynamics of the real system is detailed in this section. The simplified model of each subsystem – the ESS, the diesel engine generator, the PV unit, and the aggregated static load – is first looked for, then a voltage-control-oriented model of the whole system, from which advanced or classical control techniques are easier to be realized, can be obtained.

3.3.1 Topological modeling

The topological model of the ESS has been presented in Table 2.1 in Subsection 2.5.4, except for its output filter and step-up transformer. Using the variables shown in Figure 3.1, the dynamic equations representing the physical behavior of each element of the ESS, the diesel engine generator system, and the power system are provided in Table 3.1, where the state variables of the topological model are: the supercapacitor voltage V_{sc} , the supercapacitor output current I_s , the DC-bus voltage V_{dc} , the inverter output currents i_{r123} , the filter output voltages v_{r123} , the ESS step-up transformer output currents i_{t123} , the diesel generator output currents i_{g123} , and the PCC voltages v_{PCC123} . v_{g123} are the diesel generator output voltages. v_{l123} are the step-up transformer output voltages of the diesel generator. i_{PV123} are the PV system output currents. $i_{load123}$ are the load currents. It should be noted here that all the parameters of the studied MG and the variables shown in Figure 3.1 are converted into the low-voltage level of 0.4 kV.

3.3.2 Nonlinear averaged modeling

The nonlinear averaged model of the ESS in the three-phase and dq reference frames has been given in Table 2.2 in Subsection 2.5.4, except for its output filter and step-up transformer.

In a similar way, if only the first-order harmonic of the AC variables $\langle x \rangle_1$ is taken into account, the generalized averaged models in the three-phase reference frame applied to the output filter and step-up transformer of the ESS, the diesel engine generator system, and the power system are obtained by averaging (3.1) – (3.5) respectively.

Applying the Park coordinates transformation (presented in Appendix C) to (3.6), (3.7), (3.10), (3.11), and (3.14), after some algebraic calculus, the generalized averaged models of the output filter and step-up transformer of the ESS, the diesel engine generator system, and

Table 3.1 – Topological model of the studied MG.

Element	Dynamic equation
Energy storage system	
Output filter	$\begin{bmatrix} \frac{dv_{r1}}{dt} \\ \frac{dv_{r2}}{dt} \\ \frac{dv_{r3}}{dt} \end{bmatrix} = \frac{1}{C_f} \begin{bmatrix} i_{r1} \\ i_{r2} \\ i_{r3} \end{bmatrix} - \frac{1}{R_{fp}C_f} \begin{bmatrix} v_{r1} \\ v_{r2} \\ v_{r3} \end{bmatrix} - \frac{1}{C_f} \begin{bmatrix} i_{t1} \\ i_{t2} \\ i_{t3} \end{bmatrix}. \quad (3.1)$
Step-up transformer	$\begin{bmatrix} \frac{di_{t1}}{dt} \\ \frac{di_{t2}}{dt} \\ \frac{di_{t3}}{dt} \end{bmatrix} = \frac{1}{L_t} \begin{bmatrix} v_{r1} \\ v_{r2} \\ v_{r3} \end{bmatrix} - \frac{R_t}{L_t} \begin{bmatrix} i_{t1} \\ i_{t2} \\ i_{t3} \end{bmatrix} - \frac{1}{L_t} \begin{bmatrix} v_{PCC1} \\ v_{PCC2} \\ v_{PCC3} \end{bmatrix}. \quad (3.2)$
Diesel engine generator system	
Step-up transformer	$\begin{bmatrix} \frac{di_{g1}}{dt} \\ \frac{di_{g2}}{dt} \\ \frac{di_{g3}}{dt} \end{bmatrix} = \frac{1}{L_{tg}} \begin{bmatrix} v_{g1} \\ v_{g2} \\ v_{g3} \end{bmatrix} - \frac{R_{tg}}{L_{tg}} \begin{bmatrix} i_{g1} \\ i_{g2} \\ i_{g3} \end{bmatrix} - \frac{1}{L_{tg}} \begin{bmatrix} v_{l1} \\ v_{l2} \\ v_{l3} \end{bmatrix}. \quad (3.3)$
Transmission line	$\begin{bmatrix} \frac{di_{g1}}{dt} \\ \frac{di_{g2}}{dt} \\ \frac{di_{g3}}{dt} \end{bmatrix} = \frac{1}{L_l} \begin{bmatrix} v_{l1} \\ v_{l2} \\ v_{l3} \end{bmatrix} - \frac{R_l}{L_l} \begin{bmatrix} i_{g1} \\ i_{g2} \\ i_{g3} \end{bmatrix} - \frac{1}{L_l} \begin{bmatrix} v_{PCC1} \\ v_{PCC2} \\ v_{PCC3} \end{bmatrix}. \quad (3.4)$
Power system	
Point of common coupling	$\begin{bmatrix} \frac{dv_{PCC1}}{dt} \\ \frac{dv_{PCC2}}{dt} \\ \frac{dv_{PCC3}}{dt} \end{bmatrix} = \frac{1}{C_l} \begin{bmatrix} i_{t1} \\ i_{t2} \\ i_{t3} \end{bmatrix} + \frac{1}{C_l} \begin{bmatrix} i_{g1} \\ i_{g2} \\ i_{g3} \end{bmatrix} - \frac{1}{R_{lp}C_l} \begin{bmatrix} v_{PCC1} \\ v_{PCC2} \\ v_{PCC3} \end{bmatrix} \\ + \frac{1}{C_l} \begin{bmatrix} i_{PV1} \\ i_{PV2} \\ i_{PV3} \end{bmatrix} - \frac{1}{C_l} \begin{bmatrix} i_{load1} \\ i_{load2} \\ i_{load3} \end{bmatrix}. \quad (3.5)$

the power system in the dq reference frame can thus be obtained in (3.8), (3.9), (3.12), (3.13), and (3.15) respectively.

From the equations in Table 3.2, after some simple algebra, the nonlinear averaged model

Table 3.2 – Nonlinear averaged model of the studied MG.

Element	Dynamic equation
Energy storage system (in three-phase reference frame)	
Output filter	$\begin{bmatrix} \frac{d\langle v_{r1}\rangle_1}{dt} \\ \frac{d\langle v_{r2}\rangle_1}{dt} \\ \frac{d\langle v_{r3}\rangle_1}{dt} \end{bmatrix} = \frac{1}{C_f} \begin{bmatrix} \langle i_{r1}\rangle_1 \\ \langle i_{r2}\rangle_1 \\ \langle i_{r3}\rangle_1 \end{bmatrix} - \frac{1}{R_{fp}C_f} \begin{bmatrix} \langle v_{r1}\rangle_1 \\ \langle v_{r2}\rangle_1 \\ \langle v_{r3}\rangle_1 \end{bmatrix} - \frac{1}{C_f} \begin{bmatrix} \langle i_{t1}\rangle_1 \\ \langle i_{t2}\rangle_1 \\ \langle i_{t3}\rangle_1 \end{bmatrix} \quad (3.6)$ $- \begin{bmatrix} j\omega_{grid}\langle v_{r1}\rangle_1 \\ j\omega_{grid}\langle v_{r2}\rangle_1 \\ j\omega_{grid}\langle v_{r3}\rangle_1 \end{bmatrix}.$
Step-up transformer	$\begin{bmatrix} \frac{d\langle i_{t1}\rangle_1}{dt} \\ \frac{d\langle i_{t2}\rangle_1}{dt} \\ \frac{d\langle i_{t3}\rangle_1}{dt} \end{bmatrix} = \frac{1}{L_t} \begin{bmatrix} \langle v_{r1}\rangle_1 \\ \langle v_{r2}\rangle_1 \\ \langle v_{r3}\rangle_1 \end{bmatrix} - \frac{R_t}{L_t} \begin{bmatrix} \langle i_{t1}\rangle_1 \\ \langle i_{t2}\rangle_1 \\ \langle i_{t3}\rangle_1 \end{bmatrix} - \frac{1}{L_t} \begin{bmatrix} \langle v_{PCC1}\rangle_1 \\ \langle v_{PCC2}\rangle_1 \\ \langle v_{PCC3}\rangle_1 \end{bmatrix} \quad (3.7)$ $- \begin{bmatrix} j\omega_{grid}\langle i_{t1}\rangle_1 \\ j\omega_{grid}\langle i_{t2}\rangle_1 \\ j\omega_{grid}\langle i_{t3}\rangle_1 \end{bmatrix}.$
Energy storage system (in dq reference frame)	
Output filter	$\begin{bmatrix} \frac{dV_{rd}}{dt} \\ \frac{dV_{rq}}{dt} \end{bmatrix} = \frac{1}{C_f} \begin{bmatrix} I_{rd} \\ I_{rq} \end{bmatrix} - \frac{1}{R_{fp}C_f} \begin{bmatrix} V_{rd} \\ V_{rq} \end{bmatrix} - \frac{1}{C_f} \begin{bmatrix} I_{td} \\ I_{tq} \end{bmatrix} + \begin{bmatrix} \omega_{grid}V_{rq} \\ -\omega_{grid}V_{rd} \end{bmatrix}. \quad (3.8)$
Step-up transformer	$\begin{bmatrix} \frac{dI_{td}}{dt} \\ \frac{dI_{tq}}{dt} \end{bmatrix} = \frac{1}{L_t} \begin{bmatrix} V_{rd} \\ V_{rq} \end{bmatrix} - \frac{R_t}{L_t} \begin{bmatrix} I_{td} \\ I_{tq} \end{bmatrix} - \frac{1}{L_t} \begin{bmatrix} V_{PCCd} \\ V_{PCCq} \end{bmatrix} + \begin{bmatrix} \omega_{grid}I_{tq} \\ -\omega_{grid}I_{td} \end{bmatrix}. \quad (3.9)$
Diesel engine generator system (in three-phase reference frame)	
Step-up transformer	$\begin{bmatrix} \frac{d\langle i_{g1}\rangle_1}{dt} \\ \frac{d\langle i_{g2}\rangle_1}{dt} \\ \frac{d\langle i_{g3}\rangle_1}{dt} \end{bmatrix} = \frac{1}{L_{tg}} \begin{bmatrix} \langle v_{g1}\rangle_1 \\ \langle v_{g2}\rangle_1 \\ \langle v_{g3}\rangle_1 \end{bmatrix} - \frac{R_{tg}}{L_{tg}} \begin{bmatrix} \langle i_{g1}\rangle_1 \\ \langle i_{g2}\rangle_1 \\ \langle i_{g3}\rangle_1 \end{bmatrix} - \frac{1}{L_{tg}} \begin{bmatrix} \langle v_{l1}\rangle_1 \\ \langle v_{l2}\rangle_1 \\ \langle v_{l3}\rangle_1 \end{bmatrix} \quad (3.10)$ $- \begin{bmatrix} j\omega_{grid}\langle i_{g1}\rangle_1 \\ j\omega_{grid}\langle i_{g2}\rangle_1 \\ j\omega_{grid}\langle i_{g3}\rangle_1 \end{bmatrix}.$

Element	Dynamic equation
Transmission line	$\begin{bmatrix} \frac{d\langle i_{g1}\rangle_1}{dt} \\ \frac{d\langle i_{g2}\rangle_1}{dt} \\ \frac{d\langle i_{g3}\rangle_1}{dt} \end{bmatrix} = \frac{1}{L_l} \begin{bmatrix} \langle v_{l1}\rangle_1 \\ \langle v_{l2}\rangle_1 \\ \langle v_{l3}\rangle_1 \end{bmatrix} - \frac{R_l}{L_l} \begin{bmatrix} \langle i_{g1}\rangle_1 \\ \langle i_{g2}\rangle_1 \\ \langle i_{g3}\rangle_1 \end{bmatrix} - \frac{1}{L_l} \begin{bmatrix} \langle v_{PCC1}\rangle_1 \\ \langle v_{PCC2}\rangle_1 \\ \langle v_{PCC3}\rangle_1 \end{bmatrix} \quad (3.11)$ $- \begin{bmatrix} j\omega_{grid} \langle i_{g1}\rangle_1 \\ j\omega_{grid} \langle i_{g2}\rangle_1 \\ j\omega_{grid} \langle i_{g3}\rangle_1 \end{bmatrix}.$
Diesel engine generator system (in dq reference frame)	
Step-up transformer	$\begin{bmatrix} \frac{dI_{gd}}{dt} \\ \frac{dI_{gq}}{dt} \end{bmatrix} = \frac{1}{L_{tg}} \begin{bmatrix} V_{gd} \\ V_{gq} \end{bmatrix} - \frac{R_{tg}}{L_{tg}} \begin{bmatrix} I_{gd} \\ I_{gq} \end{bmatrix} - \frac{1}{L_{tg}} \begin{bmatrix} V_{ld} \\ V_{lq} \end{bmatrix} + \begin{bmatrix} \omega_{grid} I_{gq} \\ -\omega_{grid} I_{gd} \end{bmatrix}. \quad (3.12)$
Transmission line	$\begin{bmatrix} \frac{dI_{gd}}{dt} \\ \frac{dI_{gq}}{dt} \end{bmatrix} = \frac{1}{L_l} \begin{bmatrix} V_{ld} \\ V_{lq} \end{bmatrix} - \frac{R_l}{L_l} \begin{bmatrix} I_{gd} \\ I_{gq} \end{bmatrix} - \frac{1}{L_l} \begin{bmatrix} V_{PCCd} \\ V_{PCCq} \end{bmatrix} + \begin{bmatrix} \omega_{grid} I_{gq} \\ -\omega_{grid} I_{gd} \end{bmatrix}. \quad (3.13)$
Power system (in three-phase reference frame)	
Point of common coupling	$\begin{bmatrix} \frac{d\langle v_{PCC1}\rangle_1}{dt} \\ \frac{d\langle v_{PCC2}\rangle_1}{dt} \\ \frac{d\langle v_{PCC3}\rangle_1}{dt} \end{bmatrix} = \frac{1}{C_l} \begin{bmatrix} \langle i_{t1}\rangle_1 \\ \langle i_{t2}\rangle_1 \\ \langle i_{t3}\rangle_1 \end{bmatrix} + \frac{1}{C_l} \begin{bmatrix} \langle i_{g1}\rangle_1 \\ \langle i_{g2}\rangle_1 \\ \langle i_{g3}\rangle_1 \end{bmatrix} \quad (3.14)$ $- \frac{1}{R_{lp} C_l} \begin{bmatrix} \langle v_{PCC1}\rangle_1 \\ \langle v_{PCC2}\rangle_1 \\ \langle v_{PCC3}\rangle_1 \end{bmatrix} + \frac{1}{C_l} \begin{bmatrix} \langle i_{PV1}\rangle_1 \\ \langle i_{PV2}\rangle_1 \\ \langle i_{PV3}\rangle_1 \end{bmatrix}$ $- \frac{1}{C_l} \begin{bmatrix} \langle i_{load1}\rangle_1 \\ \langle i_{load2}\rangle_1 \\ \langle i_{load3}\rangle_1 \end{bmatrix} - \begin{bmatrix} j\omega_{grid} \langle v_{PCC1}\rangle_1 \\ j\omega_{grid} \langle v_{PCC2}\rangle_1 \\ j\omega_{grid} \langle v_{PCC3}\rangle_1 \end{bmatrix}.$
Power system (in dq reference frame)	
Point of common coupling	$\begin{bmatrix} \frac{dV_{PCCd}}{dt} \\ \frac{dV_{PCCq}}{dt} \end{bmatrix} = \frac{1}{C_l} \begin{bmatrix} I_{td} \\ I_{tq} \end{bmatrix} + \frac{1}{C_l} \begin{bmatrix} I_{gd} \\ I_{gq} \end{bmatrix} - \frac{1}{R_{lp} C_l} \begin{bmatrix} V_{PCCd} \\ V_{PCCq} \end{bmatrix} + \frac{1}{C_l} \begin{bmatrix} I_{PVd} \\ I_{PVq} \end{bmatrix}$ $- \frac{1}{C_l} \begin{bmatrix} I_{loadd} \\ I_{loadq} \end{bmatrix} + \begin{bmatrix} \omega_{grid} V_{PCCq} \\ -\omega_{grid} V_{PCCd} \end{bmatrix}. \quad (3.15)$

of the considered MG is finally rewritten as follows (where the nonlinear averaged model of the ESS has been written in (2.40) – (2.44))

$$\frac{dV_{rd}}{dt} = \frac{1}{C_f} I_{rd} - \frac{1}{R_{fp} C_f} V_{rd} - \frac{1}{C_f} I_{td} + \omega_{grid} V_{rq}, \quad (3.16)$$

$$\frac{dV_{rq}}{dt} = \frac{1}{C_f} I_{rq} - \frac{1}{R_{fp} C_f} V_{rq} - \frac{1}{C_f} I_{tq} - \omega_{grid} V_{rd}, \quad (3.17)$$

$$\frac{dI_{td}}{dt} = \frac{1}{L_t} V_{rd} - \frac{R_t}{L_t} I_{td} - \frac{1}{L_t} V_{PCCd} + \omega_{grid} I_{tq}, \quad (3.18)$$

$$\frac{dI_{tq}}{dt} = \frac{1}{L_t} V_{rq} - \frac{R_t}{L_t} I_{tq} - \frac{1}{L_t} V_{PCCq} - \omega_{grid} I_{td}, \quad (3.19)$$

$$\frac{dI_{gd}}{dt} = \frac{1}{L_g} V_{gd} - \frac{R_g}{L_g} I_{gd} - \frac{1}{L_g} V_{PCCd} + \omega_{grid} I_{gq}, \quad (3.20)$$

$$\frac{dI_{gq}}{dt} = \frac{1}{L_g} V_{gq} - \frac{R_g}{L_g} I_{gq} - \frac{1}{L_g} V_{PCCq} - \omega_{grid} I_{gd}, \quad (3.21)$$

$$\frac{dV_{PCCd}}{dt} = \frac{1}{C_l} I_{td} + \frac{1}{C_l} I_{gd} - \frac{1}{R_{lp} C_l} V_{PCCd} + \frac{1}{C_l} I_{PVd} - \frac{1}{C_l} I_{loadd} + \omega_{grid} V_{PCCq}, \quad (3.22)$$

$$\frac{dV_{PCCq}}{dt} = \frac{1}{C_l} I_{tq} + \frac{1}{C_l} I_{gq} - \frac{1}{R_{lp} C_l} V_{PCCq} + \frac{1}{C_l} I_{PVq} - \frac{1}{C_l} I_{loadq} - \omega_{grid} V_{PCCd}, \quad (3.23)$$

where the state variables are: V_{sc} , I_s , V_{dc} , I_{rd} , I_{rq} , the direct and quadrature components of the filter output voltage V_{rd} and V_{rq} respectively, the direct and quadrature components of the ESS step-up transformer output current I_{td} and I_{tq} respectively, the direct and quadrature components of the diesel generator output current I_{gd} and I_{gq} respectively, the direct and quadrature components of the PCC voltage V_{PCCd} and V_{PCCq} respectively. V_{gd} and V_{gq} are the direct and quadrature components of the diesel generator output voltage respectively. I_{PVd} and I_{PVq} are the direct and quadrature components of the PV system output current respectively. I_{loadd} and I_{loadq} are the direct and quadrature components of the load current respectively.

The active and reactive power of the sources and load can be computed by the following equations

$$P_t = V_{PCCd} I_{td} + V_{PCCq} I_{tq}, \quad (3.24)$$

$$Q_t = V_{PCCq} I_{td} - V_{PCCd} I_{tq}, \quad (3.25)$$

$$P_g = V_{PCCd} I_{gd} + V_{PCCq} I_{gq}, \quad (3.26)$$

$$Q_g = V_{PCCq} I_{gd} - V_{PCCd} I_{gq}, \quad (3.27)$$

$$P_{PV} = V_{PCCd} I_{PVd} + V_{PCCq} I_{PVq}, \quad (3.28)$$

$$Q_{PV} = V_{PCCq} I_{PVd} - V_{PCCd} I_{PVq}, \quad (3.29)$$

$$P_{load} = V_{PCCd} I_{loadd} + V_{PCCq} I_{loadq}, \quad (3.30)$$

$$Q_{load} = V_{PCCq} I_{loadd} - V_{PCCd} I_{loadq}, \quad (3.31)$$

where P_t and Q_t are the ESS step-up transformer output active and reactive power respectively, P_g and Q_g are the diesel generator system output active and reactive power supplied

at the PCC respectively, P_{PV} and Q_{PV} are the PV system output active and reactive power respectively, and P_{load} and Q_{load} are the load active and reactive power respectively. Let us define here that

- For sources: $P > 0$ if they supply active power, $P < 0$ if they absorb active power; $Q > 0$ if they supply reactive power, $Q < 0$ if they absorb reactive power;
- For loads: $P > 0$ if they absorb active power, $P < 0$ if they supply active power; $Q > 0$ if they absorb reactive power, $Q < 0$ if they supply reactive power.

The equations which express power balance at the PCC are given by

$$P_t + \left(P_g - \frac{U_{PCC}^2}{R_{lp}} \right) + P_{PV} - P_{load} = 0, \quad (3.32)$$

$$Q_t + (Q_g + U_{PCC}^2 C_l \omega_{grid}) + Q_{PV} - Q_{load} = 0. \quad (3.33)$$

3.3.3 Equilibrium point computation

Some initial assumptions used for computing an equilibrium state of the studied MG (indicated by the subscript e) are first given as follows:

- 1 The supercapacitor voltage V_{sc} – which is an image of its state of charge SoC_{sc} – is considered to be initially known, *i.e.*, $V_{sc} = V_{sc_e}$ (or $SoC_{sc} = SoC_{sc_e}$);
- 2 The DC-bus voltage V_{dc} is assumed to be initially equal to its setpoint value, *i.e.*, $V_{dc} = V_{dc_e} = V_{dc}^{ref}$;
- 3 Without loss of generality, the dq reference frame is chosen to be synchronized with the filter output phase voltage vector $v_{r1} = \sqrt{2}V_r \cos(\omega_{grid}t)$. According to the inverse Park coordinates transformation one has $v_{r1} = \sqrt{\frac{2}{3}} [V_{rd} \cos(\omega_{grid}t) - V_{rq} \sin(\omega_{grid}t)]$, therefore one deduces $V_{rd} = \sqrt{3}V_r = U_r$ and $V_{rq} = V_{rq_e} = 0$;
- 4 The output reactive power of the three-phase inverter Q_r is assumed to be initially equal to zero, *i.e.*, $Q_r = Q_{r_e} = V_{rq_e} I_{rd_e} - V_{rd_e} I_{rq_e} = 0$, therefore one deduces $I_{rq_e} = 0$;
- 5 The PCC line-to-line voltage magnitude U_{PCC} is supposed to be initially equal to its reference value, *i.e.*,

$$U_{PCC} = U_{PCC_e} = \sqrt{V_{PCCd_e}^2 + V_{PCCq_e}^2} = U_{PCC}^{ref}; \quad (3.34)$$

- 6 The MG frequency f_{grid} is supposed to be well regulated at its rated value, *i.e.*, $f_{grid} = f_{grid_e} = f_{grid}^{ref}$ or $\omega_{grid} = \omega_{grid_e} = \omega_{grid}^{ref}$.

From (3.28) – (3.31), the active and reactive power of the PV source and load at the equilibrium state can be written as follows

$$P_{PV_e} = V_{PCCd_e} I_{PVd_e} + V_{PCCq_e} I_{PVq_e}, \quad (3.35)$$

$$Q_{PV_e} = V_{PCCq_e} I_{PVd_e} - V_{PCCd_e} I_{PVq_e}, \quad (3.36)$$

$$P_{load_e} = V_{PCCd_e} I_{loadd_e} + V_{PCCq_e} I_{loadq_e}, \quad (3.37)$$

$$Q_{load_e} = V_{PCCq_e} I_{loadd_e} - V_{PCCd_e} I_{loadq_e}. \quad (3.38)$$

The equilibrium point can be found by imposing all the derivative terms dX/dt in (2.40) – (2.44) to be equal to zero as in (2.48) – (2.52) and (3.16) – (3.23) to be equal to zero as follows

$$\left(\frac{dV_{rd}}{dt} \right)_e = 0 \Rightarrow \frac{1}{C_f} I_{rd_e} - \frac{1}{R_{fp} C_f} V_{rd_e} - \frac{1}{C_f} I_{td_e} + \omega_{grid_e} V_{rq_e} = 0, \quad (3.39)$$

$$\left(\frac{dV_{rq}}{dt} \right)_e = 0 \Rightarrow \frac{1}{C_f} I_{rq_e} - \frac{1}{R_{fp} C_f} V_{rq_e} - \frac{1}{C_f} I_{tq_e} - \omega_{grid_e} V_{rd_e} = 0, \quad (3.40)$$

$$\left(\frac{dI_{td}}{dt} \right)_e = 0 \Rightarrow \frac{1}{L_t} V_{rd_e} - \frac{R_t}{L_t} I_{td_e} - \frac{1}{L_t} V_{PCCd_e} + \omega_{grid_e} I_{tq_e} = 0, \quad (3.41)$$

$$\left(\frac{dI_{tq}}{dt} \right)_e = 0 \Rightarrow \frac{1}{L_t} V_{rq_e} - \frac{R_t}{L_t} I_{tq_e} - \frac{1}{L_t} V_{PCCq_e} - \omega_{grid_e} I_{td_e} = 0, \quad (3.42)$$

$$\left(\frac{dI_{gd}}{dt} \right)_e = 0 \Rightarrow \frac{1}{L_g} V_{gd_e} - \frac{R_g}{L_g} I_{gd_e} - \frac{1}{L_g} V_{PCCd_e} + \omega_{grid_e} I_{gq_e} = 0, \quad (3.43)$$

$$\left(\frac{dI_{gq}}{dt} \right)_e = 0 \Rightarrow \frac{1}{L_g} V_{gq_e} - \frac{R_g}{L_g} I_{gq_e} - \frac{1}{L_g} V_{PCCq_e} - \omega_{grid_e} I_{gd_e} = 0, \quad (3.44)$$

$$\begin{aligned} \left(\frac{dV_{PCCd}}{dt} \right)_e = 0 \Rightarrow & \frac{1}{C_l} I_{td_e} + \frac{1}{C_l} I_{gd_e} - \frac{1}{R_{lp} C_l} V_{PCCd_e} + \frac{1}{C_l} I_{PVd_e} - \frac{1}{C_l} I_{loadd_e} \\ & + \omega_{grid_e} V_{PCCq_e} = 0, \end{aligned} \quad (3.45)$$

$$\begin{aligned} \left(\frac{dV_{PCCq}}{dt} \right)_e = 0 \Rightarrow & \frac{1}{C_l} I_{tq_e} + \frac{1}{C_l} I_{gq_e} - \frac{1}{R_{lp} C_l} V_{PCCq_e} + \frac{1}{C_l} I_{PVq_e} - \frac{1}{C_l} I_{loadq_e} \\ & - \omega_{grid_e} V_{PCCd_e} = 0. \end{aligned} \quad (3.46)$$

One can note that (2.48) – (2.52) and (3.34) – (3.46) is a nonlinear system of 18 equations with 18 unknowns. The system can be written as a single expression using vectors, *i.e.*, $\mathbf{f}(\mathbf{X}_e) = 0$, where the vector \mathbf{X}_e contains 18 independent variables and the vector \mathbf{f} contains 18 functions $f_i(\mathbf{X}_e)$ ($i = \overline{1, 18}$) as follows

$$\mathbf{X}_e = [V_{rd_e} \quad I_{s_e} \quad I_{rd_e} \quad \alpha_{c_e} \quad \beta_{d_e} \quad \beta_{q_e} \quad V_{gd_e} \quad V_{gq_e} \quad V_{PCCd_e} \quad V_{PCCq_e} \quad I_{td_e} \quad I_{tq_e} \quad I_{gd_e} \quad I_{gq_e} \quad I_{PVd_e} \quad I_{PVq_e} \quad I_{loadd_e} \quad I_{loadq_e}]^T, \quad (3.47)$$

$$\mathbf{f}(\mathbf{X}_e) = [f_1(\mathbf{X}_e) \quad f_2(\mathbf{X}_e) \quad \cdots \quad f_{18}(\mathbf{X}_e)]^T. \quad (3.48)$$

The steady-state operating point of the studied MG is finally given in Table 3.3 by solving the nonlinear equation system $\mathbf{f}(\mathbf{X}_e) = 0$ with MG parameter values using the Newton-Raphson method taking into account the aforementioned initial assumptions. Note here that from (3.24) – (3.27), one has $P_{t_e} = V_{PCCd_e} I_{td_e} + V_{PCCq_e} I_{tq_e}$, $Q_{t_e} = V_{PCCq_e} I_{td_e} - V_{PCCd_e} I_{tq_e}$,

Table 3.3 – Steady-state real-unit values of the studied MG.

0.4 kV level						
Variable	V_{sc_e}	V_{dc_e}	V_{rd_e}	V_{rq_e}	U_{r_e}	I_{s_e}
Value	585 V	1000 V	400.13 V	0 V	400.13 V	-2.53 A
Variable	I_{rd_e}	I_{rq_e}	α_{c_e}	β_{d_e}	β_{q_e}	P_{s_e}
Value	-18.67 A	0 A	0.585	0.4	-0.0027	-1.48 kW
Variable	P_{r_e}	Q_{r_e}				
Value	-7.47 kW	0 kVAr				
20 kV level						
Variable	V_{gd_e}	V_{gq_e}	U_{g_e}	V_{PCCd_e}	V_{PCCq_e}	U_{PCC_e}
Value	20.66 kV	552.43 V	20.67 kV	20 kV	37.6 V	20 kV
Variable	I_{td_e}	I_{tq_e}	I_{gd_e}	I_{gq_e}	I_{PVd_e}	I_{PVq_e}
Value	-0.87 A	-0.38 A	52.54 A	-36.14 A	10.01 A	-7.48 A
Variable	I_{loadd_e}	I_{loadq_e}	P_{t_e}	Q_{t_e}	P_{g_e}	Q_{g_e}
Value	60.08 A	-44.89 A	-17.49 kW	7.66 kVAr	1049.5 kW	724.75 kVAr
Variable	P_{PV_e}	Q_{PV_e}	P_{load_e}	Q_{load_e}	f_{grid_e}	ω_{grid_e}
Value	200 kW	150 kVAr	1200 kW	900 kVAr	50 Hz	100π rad/s

$P_{g_e} = V_{PCCd_e}I_{gd_e} + V_{PCCq_e}I_{gq_e}$, $Q_{g_e} = V_{PCCq_e}I_{gd_e} - V_{PCCd_e}I_{gq_e}$. The value V_{sc_e} chosen for \mathcal{H}_∞ control design corresponds here to the midrange between the minimum and maximum supercapacitor voltages. The minimum value of the transmission line length l is chosen for \mathcal{H}_∞ control design. In this case, $l = l_{min} = 1$ km, where 10 km has been chosen as the maximum value of l in order to ensure the voltage drop on the transmission line at the high-voltage level of 20 kV being less than or equal to the admissible limit of 8% of the rated voltage.

3.3.4 Linear averaged modeling

The linear averaged model of the ESS has been written in (2.53) – (2.57) in Subsection 2.5.4, except for its output filter and step-up transformer. By linearizing the nonlinear averaged model of the considered MG (3.16) – (3.23) around the given steady-state point, supposing that the MG frequency f_{grid} is well regulated at its rated value, *i.e.*, $\Delta f_{grid} = 0$ or $\Delta\omega_{grid} = 0$, and the diesel engine generator output voltage is well regulated at its setpoint value, *i.e.*, $\Delta V_{gd} = 0$ and $\Delta V_{gq} = 0$, the linear averaged model can be expressed as follows

$$\frac{d\Delta V_{rd}}{dt} = \frac{1}{C_f} \Delta I_{rd} - \frac{1}{R_{f_p} C_f} \Delta V_{rd} - \frac{1}{C_f} \Delta I_{td} + \omega_{grid_e} \Delta V_{rq}, \quad (3.49)$$

$$\frac{d\Delta V_{rq}}{dt} = \frac{1}{C_f} \Delta I_{rq} - \frac{1}{R_{f_p} C_f} \Delta V_{rq} - \frac{1}{C_f} \Delta I_{tq} - \omega_{grid_e} \Delta V_{rd}, \quad (3.50)$$

$$\frac{d\Delta I_{td}}{dt} = \frac{1}{L_t} \Delta V_{rd} - \frac{R_t}{L_t} \Delta I_{td} - \frac{1}{L_t} \Delta V_{PCCd} + \omega_{grid_e} \Delta I_{tq}, \quad (3.51)$$

$$\frac{d\Delta I_{tq}}{dt} = \frac{1}{L_t} \Delta V_{rq} - \frac{R_t}{L_t} \Delta I_{tq} - \frac{1}{L_t} \Delta V_{PCCq} - \omega_{grid_e} \Delta I_{td}, \quad (3.52)$$

$$\frac{d\Delta I_{gd}}{dt} = -\frac{R_g}{L_g} \Delta I_{gd} - \frac{1}{L_g} \Delta V_{PCCd} + \omega_{grid_e} \Delta I_{gq}, \quad (3.53)$$

$$\frac{d\Delta I_{gq}}{dt} = -\frac{R_g}{L_g} \Delta I_{gq} - \frac{1}{L_g} \Delta V_{PCCq} - \omega_{grid_e} \Delta I_{gd}, \quad (3.54)$$

$$\begin{aligned} \frac{d\Delta V_{PCCd}}{dt} &= \frac{1}{C_l} \Delta I_{td} + \frac{1}{C_l} \Delta I_{gd} - \frac{1}{R_{lp} C_l} \Delta V_{PCCd} + \frac{1}{C_l} \Delta I_{PVd} - \frac{1}{C_l} \Delta I_{loadd} \\ &\quad + \omega_{grid_e} \Delta V_{PCCq}, \end{aligned} \quad (3.55)$$

$$\begin{aligned} \frac{d\Delta V_{PCCq}}{dt} &= \frac{1}{C_l} \Delta I_{tq} + \frac{1}{C_l} \Delta I_{gq} - \frac{1}{R_{lp} C_l} \Delta V_{PCCq} + \frac{1}{C_l} \Delta I_{PVq} - \frac{1}{C_l} \Delta I_{loadq} \\ &\quad - \omega_{grid_e} \Delta V_{PCCd}, \end{aligned} \quad (3.56)$$

where the state variables are: ΔV_{sc} , ΔI_s , ΔV_{dc} , ΔI_{rd} , ΔI_{rq} , the direct and quadrature components of the filter output voltage variation ΔV_{rd} and ΔV_{rq} respectively, the direct and quadrature components of the ESS step-up transformer output current variation ΔI_{td} and ΔI_{tq} respectively, the direct and quadrature components of the diesel generator output current variation ΔI_{gd} and ΔI_{gq} respectively, the direct and quadrature components of the PCC voltage variation ΔV_{PCCd} and ΔV_{PCCq} respectively. ΔI_{PVd} and ΔI_{PVq} are the direct and quadrature components of the PV system output current variation respectively. ΔI_{loadd} and ΔI_{loadq} are the direct and quadrature components of the load current variation respectively.

Similarly, the active and reactive power variations of the sources and load can be linearized from (3.24) – (3.31) as follows

$$\Delta P_t = V_{PCCd_e} \Delta I_{td} + I_{td_e} \Delta V_{PCCd} + V_{PCCq_e} \Delta I_{tq} + I_{tq_e} \Delta V_{PCCq}, \quad (3.57)$$

$$\Delta Q_t = V_{PCCq_e} \Delta I_{td} + I_{td_e} \Delta V_{PCCq} - V_{PCCd_e} \Delta I_{tq} - I_{tq_e} \Delta V_{PCCd}, \quad (3.58)$$

$$\Delta P_g = V_{PCCd_e} \Delta I_{gd} + I_{gd_e} \Delta V_{PCCd} + V_{PCCq_e} \Delta I_{gq} + I_{gq_e} \Delta V_{PCCq}, \quad (3.59)$$

$$\Delta Q_g = V_{PCCq_e} \Delta I_{gd} + I_{gd_e} \Delta V_{PCCq} - V_{PCCd_e} \Delta I_{gq} - I_{gq_e} \Delta V_{PCCd}, \quad (3.60)$$

$$\Delta P_{PV} = V_{PCCd_e} \Delta I_{PVd} + I_{PVd_e} \Delta V_{PCCd} + V_{PCCq_e} \Delta I_{PVq} + I_{PVq_e} \Delta V_{PCCq}, \quad (3.61)$$

$$\Delta Q_{PV} = V_{PCCq_e} \Delta I_{PVd} + I_{PVd_e} \Delta V_{PCCq} - V_{PCCd_e} \Delta I_{PVq} - I_{PVq_e} \Delta V_{PCCd}, \quad (3.62)$$

$$\Delta P_{load} = V_{PCCd_e} \Delta I_{loadd} + I_{loadd_e} \Delta V_{PCCd} + V_{PCCq_e} \Delta I_{loadq} + I_{loadq_e} \Delta V_{PCCq}, \quad (3.63)$$

$$\Delta Q_{load} = V_{PCCq_e} \Delta I_{loadd} + I_{loadd_e} \Delta V_{PCCq} - V_{PCCd_e} \Delta I_{loadq} - I_{loadq_e} \Delta V_{PCCd}, \quad (3.64)$$

where ΔP_t and ΔQ_t are the ESS step-up transformer output active and reactive power variations respectively, ΔP_g and ΔQ_g are the diesel generator system output active and reactive power variations supplied at the PCC respectively, ΔP_{PV} and ΔQ_{PV} are the PV system output active and reactive power variations respectively, and ΔP_{load} and ΔQ_{load} are the load active and reactive power variations respectively.

3.3.5 Per-unitized averaged modeling

The per-unitized nonlinear and linear averaged models of the ESS have been detailed in (2.61) – (2.65) and (2.69) – (2.73) respectively in Subsection 2.5.4, except for its output filter and step-up transformer. In a per-unit frame, the nonlinear averaged model of the studied MG, deduced from the real-unit nonlinear equation system (3.16) – (3.23), can be expressed by the following per-unitized set of equations

$$\frac{1}{\omega_b} \frac{dV_{rd}}{dt} = \frac{1}{C_f} I_{rd} - \frac{1}{R_{fp} C_f} V_{rd} - \frac{1}{C_f} I_{td} + \omega_{grid} V_{rq}, \quad (3.65)$$

$$\frac{1}{\omega_b} \frac{dV_{rq}}{dt} = \frac{1}{C_f} I_{rq} - \frac{1}{R_{fp} C_f} V_{rq} - \frac{1}{C_f} I_{tq} - \omega_{grid} V_{rd}, \quad (3.66)$$

$$\frac{1}{\omega_b} \frac{dI_{td}}{dt} = \frac{1}{L_t} V_{rd} - \frac{R_t}{L_t} I_{td} - \frac{1}{L_t} V_{PCCd} + \omega_{grid} I_{tq}, \quad (3.67)$$

$$\frac{1}{\omega_b} \frac{dI_{tq}}{dt} = \frac{1}{L_t} V_{rq} - \frac{R_t}{L_t} I_{tq} - \frac{1}{L_t} V_{PCCq} - \omega_{grid} I_{td}, \quad (3.68)$$

$$\frac{1}{\omega_b} \frac{dI_{gd}}{dt} = \frac{1}{L_g} V_{gd} - \frac{R_g}{L_g} I_{gd} - \frac{1}{L_g} V_{PCCd} + \omega_{grid} I_{gq}, \quad (3.69)$$

$$\frac{1}{\omega_b} \frac{dI_{gq}}{dt} = \frac{1}{L_g} V_{gq} - \frac{R_g}{L_g} I_{gq} - \frac{1}{L_g} V_{PCCq} - \omega_{grid} I_{gd}, \quad (3.70)$$

$$\frac{1}{\omega_b} \frac{dV_{PCCd}}{dt} = \frac{1}{C_l} I_{td} + \frac{1}{C_l} I_{gd} - \frac{1}{R_{lp} C_l} V_{PCCd} + \frac{1}{C_l} I_{PVd} - \frac{1}{C_l} I_{loadd} + \omega_{grid} V_{PCCq}, \quad (3.71)$$

$$\frac{1}{\omega_b} \frac{dV_{PCCq}}{dt} = \frac{1}{C_l} I_{tq} + \frac{1}{C_l} I_{gq} - \frac{1}{R_{lp} C_l} V_{PCCq} + \frac{1}{C_l} I_{PVq} - \frac{1}{C_l} I_{loadq} - \omega_{grid} V_{PCCd}, \quad (3.72)$$

where the state variables are: V_{sc} , I_s , V_{dc} , I_{rd} , I_{rq} , V_{rd} , V_{rq} , I_{td} , I_{tq} , I_{gd} , I_{gq} , V_{PCCd} , and V_{PCCq} . The equation system (3.65) – (3.72) implies that each derivative term of an original equation is premultiplied by the factor $1/\omega_b$ in its per-unit counterpart.

By per-unitizing (3.24) – (3.31), the active and reactive power of the sources and load can be written as follows

$$P_t = V_{PCCd} I_{td} + V_{PCCq} I_{tq}, \quad (3.73)$$

$$Q_t = V_{PCCq} I_{td} - V_{PCCd} I_{tq}, \quad (3.74)$$

$$P_g = V_{PCCd} I_{gd} + V_{PCCq} I_{gq}, \quad (3.75)$$

$$Q_g = V_{PCCq} I_{gd} - V_{PCCd} I_{gq}, \quad (3.76)$$

$$P_{PV} = V_{PCCd} I_{PVd} + V_{PCCq} I_{PVq}, \quad (3.77)$$

$$Q_{PV} = V_{PCCq} I_{PVd} - V_{PCCd} I_{PVq}, \quad (3.78)$$

$$P_{load} = V_{PCCd} I_{loadd} + V_{PCCq} I_{loadq}, \quad (3.79)$$

$$Q_{load} = V_{PCCq} I_{loadd} - V_{PCCd} I_{loadq}. \quad (3.80)$$

In a per-unit frame, the equilibrium point can easily be found by solving the nonlinear equation system $(d\mathbf{X}/dt)_e = 0$ derived from (2.61) – (2.65) and (3.16) – (3.23) or by per-unitizing the real-unit equilibrium one which has been computed above.

By linearizing the nonlinear averaged model of the considered MG (3.65) – (3.72) around the given equilibrium point, supposing that the MG frequency f_{grid} is well regulated at its rated value, *i.e.*, $\underline{\Delta f_{grid}} = 0$ or $\underline{\Delta \omega_{grid}} = 0$, and the diesel engine generator output voltage is well regulated at its setpoint value, *i.e.*, $\underline{\Delta V_{gd}} = 0$ and $\underline{\Delta V_{gq}} = 0$, or by per-unitizing the real-unit linear equation system (3.49) – (3.56), the linear averaged model can be described by the following per-unitized set of equations

$$\frac{1}{\omega_b} \frac{d\underline{\Delta V_{rd}}}{dt} = \frac{1}{C_f} \underline{\Delta I_{rd}} - \frac{1}{R_{fp} C_f} \underline{\Delta V_{rd}} - \frac{1}{C_f} \underline{\Delta I_{td}} + \underline{\omega_{grid_e}} \underline{\Delta V_{rq}}, \quad (3.81)$$

$$\frac{1}{\omega_b} \frac{d\underline{\Delta V_{rq}}}{dt} = \frac{1}{C_f} \underline{\Delta I_{rq}} - \frac{1}{R_{fp} C_f} \underline{\Delta V_{rq}} - \frac{1}{C_f} \underline{\Delta I_{tq}} - \underline{\omega_{grid_e}} \underline{\Delta V_{rd}}, \quad (3.82)$$

$$\frac{1}{\omega_b} \frac{d\underline{\Delta I_{td}}}{dt} = \frac{1}{L_t} \underline{\Delta V_{rd}} - \frac{R_t}{L_t} \underline{\Delta I_{td}} - \frac{1}{L_t} \underline{\Delta V_{PCCd}} + \underline{\omega_{grid_e}} \underline{\Delta I_{tq}}, \quad (3.83)$$

$$\frac{1}{\omega_b} \frac{d\underline{\Delta I_{tq}}}{dt} = \frac{1}{L_t} \underline{\Delta V_{rq}} - \frac{R_t}{L_t} \underline{\Delta I_{tq}} - \frac{1}{L_t} \underline{\Delta V_{PCCq}} - \underline{\omega_{grid_e}} \underline{\Delta I_{td}}, \quad (3.84)$$

$$\frac{1}{\omega_b} \frac{d\underline{\Delta I_{gd}}}{dt} = -\frac{R_g}{L_g} \underline{\Delta I_{gd}} - \frac{1}{L_g} \underline{\Delta V_{PCCd}} + \underline{\omega_{grid_e}} \underline{\Delta I_{gq}}, \quad (3.85)$$

$$\frac{1}{\omega_b} \frac{d\underline{\Delta I_{gq}}}{dt} = -\frac{R_g}{L_g} \underline{\Delta I_{gq}} - \frac{1}{L_g} \underline{\Delta V_{PCCq}} - \underline{\omega_{grid_e}} \underline{\Delta I_{gd}}, \quad (3.86)$$

$$\begin{aligned} \frac{1}{\omega_b} \frac{d\underline{\Delta V_{PCCd}}}{dt} &= \frac{1}{C_l} \underline{\Delta I_{td}} + \frac{1}{C_l} \underline{\Delta I_{gd}} - \frac{1}{R_{lp} C_l} \underline{\Delta V_{PCCd}} + \frac{1}{C_l} \underline{\Delta I_{PVd}} - \frac{1}{C_l} \underline{\Delta I_{loadd}} \\ &\quad + \underline{\omega_{grid_e}} \underline{\Delta V_{PCCq}}, \end{aligned} \quad (3.87)$$

$$\begin{aligned} \frac{1}{\omega_b} \frac{d\underline{\Delta V_{PCCq}}}{dt} &= \frac{1}{C_l} \underline{\Delta I_{tq}} + \frac{1}{C_l} \underline{\Delta I_{gq}} - \frac{1}{R_{lp} C_l} \underline{\Delta V_{PCCq}} + \frac{1}{C_l} \underline{\Delta I_{PVq}} - \frac{1}{C_l} \underline{\Delta I_{loadq}} \\ &\quad - \underline{\omega_{grid_e}} \underline{\Delta V_{PCCd}}, \end{aligned} \quad (3.88)$$

where the state variables are: $\underline{\Delta V_{sc}}$, $\underline{\Delta I_s}$, $\underline{\Delta V_{dc}}$, $\underline{\Delta I_{rd}}$, $\underline{\Delta I_{rq}}$, $\underline{\Delta V_{rd}}$, $\underline{\Delta V_{rq}}$, $\underline{\Delta I_{td}}$, $\underline{\Delta I_{tq}}$, $\underline{\Delta I_{gd}}$, $\underline{\Delta I_{gq}}$, $\underline{\Delta V_{PCCd}}$, and $\underline{\Delta V_{PCCq}}$.

By linearizing (3.73) – (3.80) or by per-unitizing (3.57) – (3.64), in a per-unit frame, the

active and reactive power variations of the sources and load can be written as follows

$$\underline{\Delta P}_t = \underline{V}_{PCCd_e} \underline{\Delta I}_{td} + \underline{I}_{td_e} \underline{\Delta V}_{PCCd} + \underline{V}_{PCCq_e} \underline{\Delta I}_{tq} + \underline{I}_{tq_e} \underline{\Delta V}_{PCCq}, \quad (3.89)$$

$$\underline{\Delta Q}_t = \underline{V}_{PCCq_e} \underline{\Delta I}_{td} + \underline{I}_{td_e} \underline{\Delta V}_{PCCq} - \underline{V}_{PCCd_e} \underline{\Delta I}_{tq} - \underline{I}_{tq_e} \underline{\Delta V}_{PCCd}, \quad (3.90)$$

$$\underline{\Delta P}_g = \underline{V}_{PCCd_e} \underline{\Delta I}_{gd} + \underline{I}_{gd_e} \underline{\Delta V}_{PCCd} + \underline{V}_{PCCq_e} \underline{\Delta I}_{gq} + \underline{I}_{gq_e} \underline{\Delta V}_{PCCq}, \quad (3.91)$$

$$\underline{\Delta Q}_g = \underline{V}_{PCCq_e} \underline{\Delta I}_{gd} + \underline{I}_{gd_e} \underline{\Delta V}_{PCCq} - \underline{V}_{PCCd_e} \underline{\Delta I}_{gq} - \underline{I}_{gq_e} \underline{\Delta V}_{PCCd}, \quad (3.92)$$

$$\underline{\Delta P}_{PV} = \underline{V}_{PCCd_e} \underline{\Delta I}_{PVd} + \underline{I}_{PVd_e} \underline{\Delta V}_{PCCd} + \underline{V}_{PCCq_e} \underline{\Delta I}_{PVq} + \underline{I}_{PVq_e} \underline{\Delta V}_{PCCq}, \quad (3.93)$$

$$\underline{\Delta Q}_{PV} = \underline{V}_{PCCq_e} \underline{\Delta I}_{PVd} + \underline{I}_{PVd_e} \underline{\Delta V}_{PCCq} - \underline{V}_{PCCd_e} \underline{\Delta I}_{PVq} - \underline{I}_{PVq_e} \underline{\Delta V}_{PCCd}, \quad (3.94)$$

$$\underline{\Delta P}_{load} = \underline{V}_{PCCd_e} \underline{\Delta I}_{loadd} + \underline{I}_{loadd_e} \underline{\Delta V}_{PCCd} + \underline{V}_{PCCq_e} \underline{\Delta I}_{loadq} + \underline{I}_{loadq_e} \underline{\Delta V}_{PCCq}, \quad (3.95)$$

$$\underline{\Delta Q}_{load} = \underline{V}_{PCCq_e} \underline{\Delta I}_{loadd} + \underline{I}_{loadd_e} \underline{\Delta V}_{PCCq} - \underline{V}_{PCCd_e} \underline{\Delta I}_{loadq} - \underline{I}_{loadq_e} \underline{\Delta V}_{PCCd}. \quad (3.96)$$

3.3.6 System modeling for \mathcal{H}_∞ control

By aggregating the state equations (2.69) – (2.73) and (3.81) – (3.88), the per-unitized linear averaged model of the whole system around the precomputed equilibrium point can finally be obtained as follows

$$\frac{d\underline{\Delta V}_{sc}}{dt} = -\frac{\omega_b}{\underline{C}_{sc}} \underline{\Delta I}_s - \frac{\omega_b}{\underline{R}_{sc_p} \underline{C}_{sc}} \underline{\Delta V}_{sc}, \quad (3.97)$$

$$\begin{aligned} \frac{d\underline{\Delta V}_{dc}}{dt} &= \frac{\omega_b}{\underline{C}_{dc}} \alpha_{c_e} \underline{\Delta I}_s + \frac{\omega_b}{\underline{C}_{dc}} \underline{I}_{s_e} \underline{\Delta \alpha}_c \\ &\quad - \frac{\omega_b}{\underline{C}_{dc}} \left(\beta_{d_e} \underline{\Delta I}_{rd} + \underline{I}_{rd_e} \underline{\Delta \beta}_d + \beta_{q_e} \underline{\Delta I}_{rq} + \underline{I}_{rq_e} \underline{\Delta \beta}_q \right) - \frac{\omega_b}{\underline{R}_{dc} \underline{C}_{dc}} \underline{\Delta V}_{dc}, \end{aligned} \quad (3.98)$$

$$\frac{d\underline{\Delta V}_{rd}}{dt} = \frac{\omega_b}{\underline{C}_f} \underline{\Delta I}_{rd} - \frac{\omega_b}{\underline{R}_{f_p} \underline{C}_f} \underline{\Delta V}_{rd} - \frac{\omega_b}{\underline{C}_f} \underline{\Delta I}_{td} + \omega_b \underline{\omega}_{grid_e} \underline{\Delta V}_{rq}, \quad (3.99)$$

$$\frac{d\underline{\Delta V}_{rq}}{dt} = \frac{\omega_b}{\underline{C}_f} \underline{\Delta I}_{rq} - \frac{\omega_b}{\underline{R}_{f_p} \underline{C}_f} \underline{\Delta V}_{rq} - \frac{\omega_b}{\underline{C}_f} \underline{\Delta I}_{tq} - \omega_b \underline{\omega}_{grid_e} \underline{\Delta V}_{rd}, \quad (3.100)$$

$$\begin{aligned} \frac{d\underline{\Delta V}_{PCCd}}{dt} &= \frac{\omega_b}{\underline{C}_l} \underline{\Delta I}_{td} + \frac{\omega_b}{\underline{C}_l} \underline{\Delta I}_{gd} - \frac{\omega_b}{\underline{R}_{l_p} \underline{C}_l} \underline{\Delta V}_{PCCd} + \frac{\omega_b}{\underline{C}_l} \underline{\Delta I}_{PVd} - \frac{\omega_b}{\underline{C}_l} \underline{\Delta I}_{loadd} \\ &\quad + \omega_b \underline{\omega}_{grid_e} \underline{\Delta V}_{PCCq}, \end{aligned} \quad (3.101)$$

$$\begin{aligned} \frac{d\underline{\Delta V}_{PCCq}}{dt} &= \frac{\omega_b}{\underline{C}_l} \underline{\Delta I}_{tq} + \frac{\omega_b}{\underline{C}_l} \underline{\Delta I}_{gq} - \frac{\omega_b}{\underline{R}_{l_p} \underline{C}_l} \underline{\Delta V}_{PCCq} + \frac{\omega_b}{\underline{C}_l} \underline{\Delta I}_{PVq} - \frac{\omega_b}{\underline{C}_l} \underline{\Delta I}_{loadq} \\ &\quad - \omega_b \underline{\omega}_{grid_e} \underline{\Delta V}_{PCCd}, \end{aligned} \quad (3.102)$$

$$\frac{d\underline{\Delta I}_{td}}{dt} = \frac{\omega_b}{\underline{L}_t} \underline{\Delta V}_{rd} - \frac{\omega_b \underline{R}_t}{\underline{L}_t} \underline{\Delta I}_{td} - \frac{\omega_b}{\underline{L}_t} \underline{\Delta V}_{PCCd} + \omega_b \underline{\omega}_{grid_e} \underline{\Delta I}_{tq}, \quad (3.103)$$

$$\frac{d\underline{\Delta I}_{tq}}{dt} = \frac{\omega_b}{\underline{L}_t} \underline{\Delta V}_{rq} - \frac{\omega_b \underline{R}_t}{\underline{L}_t} \underline{\Delta I}_{tq} - \frac{\omega_b}{\underline{L}_t} \underline{\Delta V}_{PCCq} - \omega_b \underline{\omega}_{grid_e} \underline{\Delta I}_{td}, \quad (3.104)$$

$$\frac{d\Delta I_{gd}}{dt} = -\frac{\omega_b R_g}{L_g} \Delta I_{gd} - \frac{\omega_b}{L_g} \Delta V_{PCCd} + \omega_b \omega_{gride} \Delta I_{gq}, \quad (3.105)$$

$$\frac{d\Delta I_{gq}}{dt} = -\frac{\omega_b R_g}{L_g} \Delta I_{gq} - \frac{\omega_b}{L_g} \Delta V_{PCCq} - \omega_b \omega_{gride} \Delta I_{gd}, \quad (3.106)$$

$$\frac{1}{\omega_b} \frac{d\Delta I_s}{dt} = \frac{1}{L_c} \Delta V_{sc} - \frac{R_{sc} + R_c}{L_c} \Delta I_s - \frac{1}{L_c} \alpha_{ce} \Delta V_{dc} - \frac{1}{L_c} V_{dc_e} \Delta \alpha_c, \quad (3.107)$$

$$\frac{1}{\omega_b} \frac{d\Delta I_{rd}}{dt} = \frac{1}{L_f} \beta_{de} \Delta V_{dc} + \frac{1}{L_f} V_{dc_e} \Delta \beta_d - \frac{R_f}{L_f} \Delta I_{rd} - \frac{1}{L_f} \Delta V_{rd} + \omega_{gride} \Delta I_{rq}, \quad (3.108)$$

$$\frac{1}{\omega_b} \frac{d\Delta I_{rq}}{dt} = \frac{1}{L_f} \beta_{qe} \Delta V_{dc} + \frac{1}{L_f} V_{dc_e} \Delta \beta_q - \frac{R_f}{L_f} \Delta I_{rq} - \frac{1}{L_f} \Delta V_{rq} - \omega_{gride} \Delta I_{rd}, \quad (3.109)$$

where the state variables are: ΔV_{sc} , ΔV_{dc} , ΔV_{rd} , ΔV_{rq} , ΔV_{PCCd} , ΔV_{PCCq} , ΔI_{td} , ΔI_{tq} , ΔI_{gd} , ΔI_{gq} , ΔI_s , ΔI_{rd} , and ΔI_{rq} . The external disturbances applied to the system are the direct and quadrature components of the load and PV system output current variations, *i.e.*, $\Delta I_{loadd} - \Delta I_{PVd}$ and $\Delta I_{loadq} - \Delta I_{PVq}$ respectively. It should be noted that this averaged model takes into consideration only the primary voltage control of the diesel engine generator.

Control design will hereafter be carried out based on this linear averaged model.

3.4 Open-loop system behavior

This section gives an analysis of open-loop system behavior of the studied MG without ESS, as well as the whole MG. First, a linear state-space representation around a given equilibrium point is provided. Second, system structural properties of the linear system are investigated. Next, an “analysis-of-zeros” method based on Monte Carlo simulation is detailed in order to emphasize the influence of system parameters on the dynamic behavior of open-loop system measured outputs. Some MATLAB[®]/Simulink[®] open-loop time-domain simulations are also performed to validate the results of the proposed “analysis-of-zeros” method.

3.4.1 Without energy storage system

Equilibrium point computation

In order to compute an equilibrium state of the studied MG without ESS (indicated by the subscript *e*), several initial assumptions are first given as follows:

- [1] Without loss of generality, the *dq* reference frame is chosen to be synchronized with the PCC phase voltage vector $v_{PCC1} = \sqrt{2}V_{PCC} \cos(\omega_{grid}t)$. According to the inverse Park coordinates transformation one has $v_{PCC1} = \sqrt{\frac{2}{3}} [V_{PCCd} \cos(\omega_{grid}t) - V_{PCCq} \sin(\omega_{grid}t)]$, therefore one deduces $V_{PCCd} =$

Table 3.4 – Steady-state real-unit values of the studied MG without ESS.

20 kV level						
Variable	V_{gd_e}	V_{gq_e}	U_{g_e}	V_{PCCd_e}	V_{PCCq_e}	U_{PCC_e}
Value	20.66 kV	501.14 V	20.67 kV	20 kV	0 kV	20 kV
Variable	I_{gd_e}	I_{gq_e}	I_{PVd_e}	I_{PVq_e}	I_{loadd_e}	I_{loadq_e}
Value	51.6 A	-36.62 A	10 A	-7.5 A	60 A	-45 A
Variable	P_{g_e}	Q_{g_e}	P_{PV_e}	Q_{PV_e}	P_{load_e}	Q_{load_e}
Value	1032 kW	732.41 kVAr	200 kW	150 kVAr	1200 kW	900 kVAr
Variable	f_{grid_e}	ω_{grid_e}				
Value	50 Hz	100π rad/s				

$\sqrt{3}V_{PCC} = U_{PCC}$ and $V_{PCCq} = 0$. Moreover, the PCC line-to-line voltage magnitude U_{PCC} is supposed to be initially equal to its reference value, *i.e.*, $U_{PCC} = U_{PCC_e} = U_{PCC}^{ref}$, thus one obtains $V_{PCCd} = V_{PCCd_e} = U_{PCC}^{ref}$ and $V_{PCCq} = V_{PCCq_e} = 0$;

- 2] The MG frequency f_{grid} is supposed to be well regulated at its rated value, *i.e.*, $f_{grid} = f_{grid_e} = f_{grid}^{ref}$ or $\omega_{grid} = \omega_{grid_e} = \omega_{grid}^{ref}$.

Solving the linear equation system (3.35) – (3.38) and (3.43) – (3.46) of the considered MG without ESS by some simple algebraic calculus and taking into account the aforementioned initial assumptions gives

$$\begin{aligned}
I_{PVd_e} &= \frac{P_{PV_e}}{V_{PCCd_e}}, \quad I_{PVq_e} = -\frac{Q_{PV_e}}{V_{PCCd_e}}, \quad I_{loadd_e} = \frac{P_{load_e}}{V_{PCCd_e}}, \quad I_{loadq_e} = -\frac{Q_{load_e}}{V_{PCCd_e}}, \\
I_{gd_e} &= \frac{1}{R_{l_p}} V_{PCCd_e} - I_{PVd_e} + I_{loadd_e}, \quad I_{gq_e} = -I_{PVq_e} + I_{loadq_e} + C_l \omega_{grid_e} V_{PCCd_e}, \\
V_{gd_e} &= R_g I_{gd_e} + V_{PCCd_e} - L_g \omega_{grid_e} I_{gq_e}, \quad V_{gq_e} = R_g I_{gq_e} + L_g \omega_{grid_e} I_{gd_e}.
\end{aligned}$$

By numerical application with MG parameter values, the steady-state operating point of the studied MG without ESS is finally given in Table 3.4. Note here that the minimum value of the transmission line length l is chosen for the steady-state point computation. In this case, $l = l_{min} = 1$ km, where 10 km is the maximum value of l .

In per-unit values, the steady-state point can easily be found by solving the linear equation system $(d\mathbf{X}/dt)_e = 0$ deduced from (3.69) – (3.72) and $(\mathbf{X})_e$ derived from (3.77) – (3.80) or by per-unitizing the real-unit steady-state one which has been computed above

$$\begin{aligned}
\underline{I}_{PVd_e} &= \frac{\underline{P}_{PV_e}}{\underline{V}_{PCCd_e}}, \quad \underline{I}_{PVq_e} = -\frac{\underline{Q}_{PV_e}}{\underline{V}_{PCCd_e}}, \quad \underline{I}_{loadd_e} = \frac{\underline{P}_{load_e}}{\underline{V}_{PCCd_e}}, \quad \underline{I}_{loadq_e} = -\frac{\underline{Q}_{load_e}}{\underline{V}_{PCCd_e}}, \\
\underline{I}_{gd_e} &= \frac{1}{\underline{R}_{l_p}} \underline{V}_{PCCd_e} - \underline{I}_{PVd_e} + \underline{I}_{loadd_e}, \quad \underline{I}_{gq_e} = -\underline{I}_{PVq_e} + \underline{I}_{loadq_e} + \underline{C}_l \omega_{grid_e} \underline{V}_{PCCd_e}, \\
\underline{V}_{gd_e} &= \underline{R}_g \underline{I}_{gd_e} + \underline{V}_{PCCd_e} - \underline{L}_g \omega_{grid_e} \underline{I}_{gq_e}, \quad \underline{V}_{gq_e} = \underline{R}_g \underline{I}_{gq_e} + \underline{L}_g \omega_{grid_e} \underline{I}_{gd_e}.
\end{aligned}$$

Linear state-space representation

The state-space representation of the per-unitized linear system (3.101), (3.102), (3.105), and (3.106) of the studied MG without ESS around the precomputed steady-state point can be written as follows

$$\begin{cases} \underline{\Delta \dot{\mathbf{x}}} = \mathbf{A}\underline{\Delta \mathbf{x}} + \mathbf{B}_2\underline{\Delta \mathbf{w}} \\ \underline{\Delta \mathbf{y}} = \mathbf{C}\underline{\Delta \mathbf{x}} + \mathbf{D}_2\underline{\Delta \mathbf{w}} \end{cases}, \quad (3.110)$$

where $\underline{\Delta \mathbf{x}} = \left[\underline{\Delta V_{PCCd}} \quad \underline{\Delta V_{PCCq}} \quad \underline{\Delta I_{gd}} \quad \underline{\Delta I_{gq}} \right]^T$ is the state vector, $\underline{\Delta \mathbf{w}} = \left[\underline{\Delta I_{loadd}} - \underline{\Delta I_{PVd}} \quad \underline{\Delta I_{loadq}} - \underline{\Delta I_{PVq}} \right]^T$ the disturbance input vector, and $\underline{\Delta \mathbf{y}} = \left[\underline{\Delta V_{PCCd}} \quad \underline{\Delta V_{PCCq}} \right]^T$ the measured output vector. Matrices \mathbf{A} , \mathbf{B}_2 , \mathbf{C} , and \mathbf{D}_2 in (3.110) are given as follows

$$\mathbf{A} = \begin{bmatrix} -\frac{\omega_b}{R_{lp}C_l} & \omega_b\omega_{grid_e} & \frac{\omega_b}{C_l} & 0 \\ -\omega_b\omega_{grid_e} & -\frac{\omega_b}{R_{lp}C_l} & 0 & \frac{\omega_b}{C_l} \\ -\frac{\omega_b}{L_g} & 0 & -\frac{\omega_b R_g}{L_g} & \omega_b\omega_{grid_e} \\ 0 & -\frac{\omega_b}{L_g} & -\omega_b\omega_{grid_e} & -\frac{\omega_b R_g}{L_g} \end{bmatrix}, \quad \mathbf{B}_2 = \begin{bmatrix} -\frac{\omega_b}{C_l} & 0 \\ 0 & -\frac{\omega_b}{C_l} \\ 0 & 0 \\ 0 & 0 \end{bmatrix}, \quad (3.111)$$

$$\mathbf{C} = \begin{bmatrix} 1 & 0 & 0 & 0 \\ 0 & 1 & 0 & 0 \end{bmatrix}, \quad \mathbf{D}_2 = \begin{bmatrix} 0 & 0 \\ 0 & 0 \end{bmatrix}.$$

Analysis of system structural properties

The structural properties: stability and observability of the linear system (3.110) are analyzed based on its matrices \mathbf{A} and \mathbf{C} . With MG parameter values in Appendix A, eigenvalues of the matrix \mathbf{A} are equal to $p_{1,2} = -335.3 \pm 13704j$ and $p_{3,4} = -335.3 \pm 13076j$. For small variations around the steady-state operating point the system is said to be stable since all eigenvalues have negative real parts. Next, the observability condition can be checked by using the MATLAB[®] function “obsv”. The rank of the observability matrix $\mathbf{Q}_o = \text{obsv}(\mathbf{A}, \mathbf{C})$ is equal to the rank of the matrix \mathbf{A} , *i.e.*, 4, so the system is well observable.

Analysis of zeros using Monte Carlo simulation

With MG parameter values, the zeros of the open-loop sensitivity functions $\underline{\Delta V_{PCCd}} / (\underline{\Delta I_{loadd}} - \underline{\Delta I_{PVd}})$ or $\underline{\Delta V_{PCCq}} / (\underline{\Delta I_{loadq}} - \underline{\Delta I_{PVq}})$, and $\underline{\Delta V_{PCCd}} / (\underline{\Delta I_{loadq}} - \underline{\Delta I_{PVq}})$ or $\underline{\Delta V_{PCCq}} / (\underline{\Delta I_{loadd}} - \underline{\Delta I_{PVd}})$ of the linear system (3.110) are given in Table 3.5. The transfer function $\underline{\Delta V_{PCCd}} / (\underline{\Delta I_{loadq}} - \underline{\Delta I_{PVq}})$ or

Table 3.5 – Zeros of the open-loop sensitivity functions of the per-unitized linear system without ESS.

Sensitivity function	$\frac{\Delta V_{PCCd}}{(\Delta I_{loadd} - \Delta I_{PVd})}$ or $\frac{\Delta V_{PCCq}}{(\Delta I_{loadq} - \Delta I_{PVq})}$	$\frac{\Delta V_{PCCd}}{(\Delta I_{loadq} - \Delta I_{PVq})}$ or $\frac{\Delta V_{PCCq}}{(\Delta I_{loadd} - \Delta I_{PVd})}$
Zero	$z_{1,2} = -335.1 \pm 13394j$ $z_3 = -99.3$	$z_1 = -13487$ $z_2 = 13289$

$\frac{\Delta V_{PCCq}}{(\Delta I_{loadd} - \Delta I_{PVd})}$ has a right-half-plane zero $z_2 = 13289$ (*i.e.*, positive real part). This results in the open-loop step response taking a particular shape, namely, the measured output variation ΔV_{PCCd} or ΔV_{PCCq} first evolves in the opposite sense in relation to the disturbance input variation $\Delta I_{loadq} - \Delta I_{PVq}$ or $\Delta I_{loadd} - \Delta I_{PVd}$ respectively, then come back to the positive sense. This is called a non-minimum phase response [180] and leads to an exhibition of non-minimum phase behavior in the PCC line-to-line voltage magnitude variation ΔU_{PCC} (with $U_{PCC} = \sqrt{V_{PCCd}^2 + V_{PCCq}^2}$). Moreover, the transfer function $\frac{\Delta V_{PCCd}}{(\Delta I_{loadd} - \Delta I_{PVd})}$ or $\frac{\Delta V_{PCCq}}{(\Delta I_{loadq} - \Delta I_{PVq})}$ has a left-half-plane complex conjugate zero pair $z_{1,2} = -335.1 \pm 13394j$ that induces oscillations in ΔV_{PCCd} or ΔV_{PCCq} in response to $\Delta I_{loadd} - \Delta I_{PVd}$ or $\Delta I_{loadq} - \Delta I_{PVq}$ respectively. This leads to an oscillation in ΔU_{PCC} , where the oscillation damping is characterized by the ratio $|\text{Im}(z_{1,2})/\text{Re}(z_{1,2})|$. Namely, the smaller this ratio is, the more damped the oscillation is. It should be noted here that this ratio, as well as the aforementioned zeros, are completely dependent on MG parameter values and the MG steady-state operating point. Hence, the minimization of this ratio by changing MG parameter values could be a feasible solution in order to minimize the oscillation amplitude in ΔU_{PCC} , as well as to limit the non-minimum phase behavior.

Given admissible variation ranges of MG parameter values, we propose an “analysis-of-zeros” method with the aim of finding out a combination of these MG parameter values that allows to minimize the oscillation amplitude in ΔU_{PCC} . This method is based on Monte Carlo simulation and carried out in the following steps:

- 1] Define a domain of possible values of m input independent random variables: MG parameter value random variables \mathcal{X}_i ($i = \overline{1, m}$) are here assumed to vary from -50% to $+50\%$ of their rated values \mathcal{X}_{i_n} , *i.e.*, $0.5\mathcal{X}_{i_n} \leq \mathcal{X}_i \leq 1.5\mathcal{X}_{i_n}$;
- 2] Sample the random variables \mathcal{X}_i that are distributed over the continuous ranges $[0.5\mathcal{X}_{i_n}, 1.5\mathcal{X}_{i_n}]$. This is randomly done with the MATLAB[®] random variable generator “rand”;
- 3] Compute a steady-state operating point $\underline{\mathbf{X}}_e$, as well as matrices \mathbf{A} , \mathbf{B}_2 , \mathbf{C} , and \mathbf{D}_2 of the linear system, with the sampled random variables \mathcal{X}_i generated in Step 2;
- 4] Analyze the structural properties of stability and observability of the linear system

based on its matrices \mathbf{A} and \mathbf{C} to verify if the system is stable and observable or not. If this is not fulfilled, Step 2 then Step 3 are re-conducted.

- 5] Determine open-loop sensitivity functions of the linear system, then for each sensitivity function $\underline{\Delta y}/\underline{\Delta w}$ identify all right-half-plane zeros which characterize non-minimum phase behavior, as well as all left-half-plane complex conjugate zero pairs $z_{k,k+1} = -\zeta_k \omega_{n_k} \pm j \omega_{n_k} \sqrt{1 - \zeta_k^2}$ ($k = \overline{1, q-1}$, where $q/2$ is the number of left-half-plane complex conjugate zero pairs of the system) which cause oscillation in the measured output variation Δy consequent to the disturbance input variation Δw ;
- 6] For each open-loop sensitivity function $\underline{\Delta y}/\underline{\Delta w}$ of the linear system compute the values of output variables $\mathcal{Y}_{k,k+1} = |\text{Im}(z_{k,k+1})/\text{Re}(z_{k,k+1})| = \left| \sqrt{1 - \zeta_k^2}/\zeta_k \right|$ of the left-half-plane complex conjugate zero pairs $z_{k,k+1}$, which characterize the oscillation amplitudes in the measured output channel variation Δy in response to the input channel disturbance Δw ;
- 7] Suppose that N samples of each random variable \mathcal{X}_i are generated, then all the samples of random variables constitute N sets of inputs, *i.e.*, $\mathbf{X}_r = (\mathcal{X}_{r-1}, \mathcal{X}_{r-2}, \dots, \mathcal{X}_{r-i}, \dots, \mathcal{X}_{r-m})$ ($r = \overline{1, N}$). Solve the problem from Step 2 to Step 6 N times deterministically yields N sample sets of output variables, *i.e.*, $\mathbf{Y}_r = (\mathcal{Y}_{r-1}, \mathcal{Y}_{r-2}, \dots, \mathcal{Y}_{r-k}, \dots, \mathcal{Y}_{r-q})$, which is available for statistical analysis and estimation of the characteristics of the output variables \mathbf{Y}_r . Let us remark here that the accuracy of Monte Carlo simulation depends on the number of simulations N . The higher the number of simulations is, the more accurate the estimate will be;
- 8] Among N sample sets of the output variables $\mathbf{Y}_r = (\mathcal{Y}_{r-1}, \mathcal{Y}_{r-2}, \dots, \mathcal{Y}_{r-k}, \dots, \mathcal{Y}_{r-q})$ identify the sample \mathcal{Y}_{r-k} that has the greater influence on the minimization of the oscillation amplitude in ΔU_{PCC} , then the corresponding sample set of the input variables $\mathbf{X}_r = (\mathcal{X}_{r-1}, \mathcal{X}_{r-2}, \dots, \mathcal{X}_{r-i}, \dots, \mathcal{X}_{r-m})$. This input set will be the desired combination of the MG parameter values.

By applying the aforescribed “analysis-of-zeros” method with the input-independent random variables being $\mathbf{X} = (L_g, R_g, C_l, R_{l_p})$ assumed to vary from -50% to $+50\%$ of their rated values \mathcal{X}_{i_n} and a sufficiently large number of samples of $N = 1000$, one can obtain 1000 samples $\mathcal{Y}_{1,2} = |\text{Im}(z_{1,2})/\text{Re}(z_{1,2})|$ of the left-half-plane complex conjugate zero pair $z_{1,2}$ of the open-loop sensitivity function $\underline{\Delta V_{PCCd}}/(\underline{\Delta I_{loadd}} - \underline{\Delta I_{PVd}})$ or $\underline{\Delta V_{PCCq}}/(\underline{\Delta I_{loadq}} - \underline{\Delta I_{PVq}})$, as depicted in Figure 3.3. As can be observed from this figure, the minimum sample of $|\text{Im}(z_{1,2})/\text{Re}(z_{1,2})|$ is equal to 14.1 at the 718th sampling time (*i.e.*, $\mathcal{Y}_{718-1,2} = 14.1$), which corresponds to the 718th sample set of the input variables \mathbf{X}_{718} , where their relative deviations from the rated values are given in Table 3.6. Therefore, this desired parameter combination of the studied MG without ESS allows to minimize the oscillation amplitude in ΔU_{PCC} .

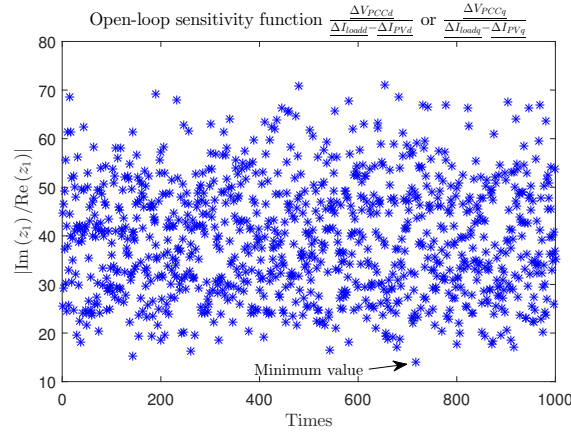


Figure 3.3 – Values $\mathcal{Y}_{1,2} = |\text{Im}(z_{1,2})/\text{Re}(z_{1,2})|$ of the left-half-plane complex conjugate zero pair $z_{1,2}$ of the open-loop sensitivity function $\frac{\Delta V_{PCCd}}{(\Delta I_{loadd} - \Delta I_{PVd})}$ or $\frac{\Delta V_{PCCq}}{(\Delta I_{loadq} - \Delta I_{PVq})}$.

Table 3.6 – Relative deviations of parameters of the studied MG without ESS from their rated values.

Parameter	L_g	R_g	C_l	R_{lp}
Relative deviation	+ 42.2%	+ 41.3%	- 46.6%	- 48.6%

Numerical simulation results

MATLAB[®]/Simulink[®] open-loop time-domain simulations using the nonlinear averaged model are performed to show the validity and effectiveness of the proposed “analysis-of-zeros” method. Without loss of generality, at $t = 1$ s a load step change of + 5% of the quadrature component of the load rated current I_{loadqe} (*i.e.*, -2.25 A), which corresponds to a load step change of + 5% of the load rated reactive power Q_{loade} (*i.e.*, + 45 kVAr), is applied as a disturbance. It should be noted that the direct component of the load current variation is considered to be approximately equal to zero, *i.e.*, $\Delta I_{loadd} \approx 0$.

Figure 3.4 displays the time-domain responses of the PCC line-to-line voltage magnitude U_{PCC} obtained with both nominal, as well as above computed sets of MG parameter values. One can see that the non-minimum phase behavior of the variation ΔU_{PCC} anticipated by the aforementioned analysis of zeros is confirmed by simulation since ΔU_{PCC} first evolves in the opposite sense in response to the variation ΔQ_{load} (resulting from the variations ΔI_{loadd} and ΔI_{loadq}). Additionally, the simulation results show that ΔU_{PCC} exhibits a considerable oscillation due to the presence of a left-half-plane complex conjugate zero pairs in the transfer function $\frac{\Delta V_{PCCd}}{(\Delta I_{loadd} - \Delta I_{PVd})}$ or $\frac{\Delta V_{PCCq}}{(\Delta I_{loadq} - \Delta I_{PVq})}$. It should be highlighted here that the oscillation amplitude in ΔU_{PCC} obtained with the desired combination

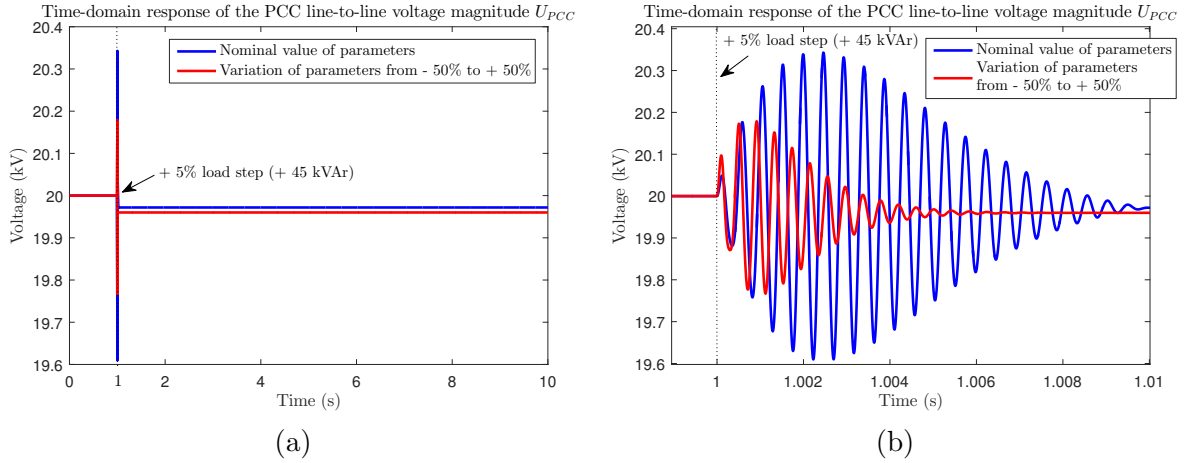


Figure 3.4 – (a) Open-loop time-domain response of the PCC line-to-line voltage magnitude U_{PCC} under a small load step disturbance of + 5% of the load rated reactive power (+ 45 kVAr) with respect to the rated operating point of the studied MG without ESS. (b) Temporal zoom in the time interval $t \in [0.999, 1.01]$ s.

of the MG parameter values has significantly been reduced compared to that performed with the rated values of the MG parameters. This demonstrates the effectiveness of the proposed “analysis-of-zeros” method. Nevertheless, the dynamic effects have not been canceled because this “analysis-of-zeros” method does not alter the natural properties of the linear system.

3.4.2 Whole system

Linear state-space representation

The steady-state point of the considered whole MG has already been computed in Subsection 3.3.3. Its per-unitized linear system (3.97) – (3.109) can be represented in the state-space form around this steady-state point as follows

$$\begin{cases} \underline{\Delta \dot{\mathbf{x}}} = \mathbf{A} \underline{\Delta \mathbf{x}} + \mathbf{B}_1 \underline{\Delta \mathbf{u}} + \mathbf{B}_2 \underline{\Delta \mathbf{w}} \\ \underline{\Delta \mathbf{y}} = \mathbf{C} \underline{\Delta \mathbf{x}} + \mathbf{D}_1 \underline{\Delta \mathbf{u}} + \mathbf{D}_2 \underline{\Delta \mathbf{w}} \end{cases}, \quad (3.112)$$

where $\underline{\Delta \mathbf{x}} = \left[\underline{\Delta V_{sc}} \quad \underline{\Delta V_{dc}} \quad \underline{\Delta V_{rd}} \quad \underline{\Delta V_{rq}} \quad \underline{\Delta V_{PCCd}} \quad \underline{\Delta V_{PCCq}} \quad \underline{\Delta I_{td}} \quad \underline{\Delta I_{tq}} \quad \underline{\Delta I_{gd}} \quad \underline{\Delta I_{gq}} \quad \underline{\Delta I_s} \quad \underline{\Delta I_{rd}} \quad \underline{\Delta I_{rq}} \right]^T$ is the state vector, $\underline{\Delta \mathbf{u}} = \left[\underline{\Delta \alpha_c} \quad \underline{\Delta \beta_d} \quad \underline{\Delta \beta_q} \right]^T$ the control input vector, $\underline{\Delta \mathbf{w}} = \left[\underline{\Delta I_{loadd}} - \underline{\Delta I_{PVd}} \quad \underline{\Delta I_{loadq}} - \underline{\Delta I_{PVq}} \right]^T$ the disturbance input vector, and $\underline{\Delta \mathbf{y}} = \left[\underline{\Delta V_{dc}} \quad \underline{\Delta V_{PCCd}} \quad \underline{\Delta V_{PCCq}} \right]^T$ the measured output vector. Matrices \mathbf{A} , \mathbf{B}_1 , \mathbf{B}_2 , \mathbf{C} , \mathbf{D}_1 , and \mathbf{D}_2 in (3.112) are given as follows

Analysis of system structural properties

The structural properties: stability, controllability and observability of the linear system (3.112) are analyzed based on its matrices \mathbf{A} , \mathbf{B}_1 , and \mathbf{C} . With MG parameter values in Appendix A, eigenvalues of the matrix \mathbf{A} are equal to $p_{1,2} = -306.6 \pm 17341j$, $p_{3,4} = -306.6 \pm 16712j$, $p_5 = -0.0031$, $p_{6,7} = -4.6 \pm 27.8j$, $p_{8,9} = -19.1 \pm 316.7j$, $p_{10,11} = -266.5 \pm 9968.2j$, and $p_{12,13} = -266.5 \pm 9339.8j$. Since all eigenvalues have negative real parts, therefore for small variations around the steady-state operating point the system is stable. Next, the controllability condition can be checked by using the MATLAB[®] function “ctrb”. The controllability matrix $\mathbf{Q}_c = \text{ctrb}(\mathbf{A}, \mathbf{B}_1)$ has the rank of 13, which is equal to the rank of the matrix \mathbf{A} , therefore the system is well controllable. Finally, the MATLAB[®] function “obsv” can be used to evaluate the observability condition. The observability matrix $\mathbf{Q}_o = \text{obsv}(\mathbf{A}, \mathbf{C})$ has the rank of 13, which is equal to the rank of the matrix \mathbf{A} , so the system is said to be completely observable.

Analysis of open-loop zeros using Monte Carlo simulation

With MG parameter values, the zeros of the open-loop sensitivity functions $\frac{\Delta V_{PCCd}}{(\Delta I_{loadd} - \Delta I_{PVd})}$ or $\frac{\Delta V_{PCCq}}{(\Delta I_{loadq} - \Delta I_{PVq})}$ and $\frac{\Delta V_{PCCd}}{(\Delta I_{loadq} - \Delta I_{PVq})}$ or $\frac{\Delta V_{PCCq}}{(\Delta I_{loadd} - \Delta I_{PVd})}$ of the linear system (3.112) are given in Table 3.7. An analysis of zeros analogous to the one detailed in Subsection 3.4.1 comes to the conclusion that there are dynamic effects (*e.g.*, non-minimum phase behavior, oscillation) exhibited in the PCC line-to-line voltage magnitude variation ΔU_{PCC} in response to the disturbance input variation $\Delta I_{loadq} - \Delta I_{PVq}$ or $\Delta I_{loadd} - \Delta I_{PVd}$.

Applying the “analysis-of-zeros” method proposed in Subsection 3.4.1 with the input-independent random variables being $\mathbf{X} = (C_{sc}, R_{sc}, R_{scp}, L_c, R_c, C_{dc}, R_{dc}, L_f, R_f, C_f, R_{fp}, L_t, R_t, L_g, R_g, C_l, R_{lp})$ supposed to vary

Table 3.7 – Zeros of the open-loop sensitivity functions of the per-unitized linear whole system.

Sensitivity function	$\frac{\Delta V_{PCCd}}{(\Delta I_{loadd} - \Delta I_{PVd})}$ or $\frac{\Delta V_{PCCq}}{(\Delta I_{loadq} - \Delta I_{PVq})}$	$\frac{\Delta V_{PCCd}}{(\Delta I_{loadq} - \Delta I_{PVq})}$ or $\frac{\Delta V_{PCCq}}{(\Delta I_{loadd} - \Delta I_{PVd})}$
Zero	$z_{1,2} = -306.3 \pm 17036j$ $z_{3,4} = -239.9 \pm 12105j$ $z_{5,6} = -265.8 \pm 9632.9j$ $z_{7,8} = -19 \pm 316.4j$ $z_9 = -96.6$ $z_{10,11} = -4.8 \pm 27.9j$ $z_{12} = -0.0078$	$z_1 = -13804$ $z_2 = 13661$ $z_{3,4} = -3606.9 \pm 11545j$ $z_{5,6} = 3103.6 \pm 11547j$ $z_{7,8} = -19.2 \pm 317j$ $z_{9,10} = -4.5 \pm 27.8j$ $z_{11} = -0.0028$

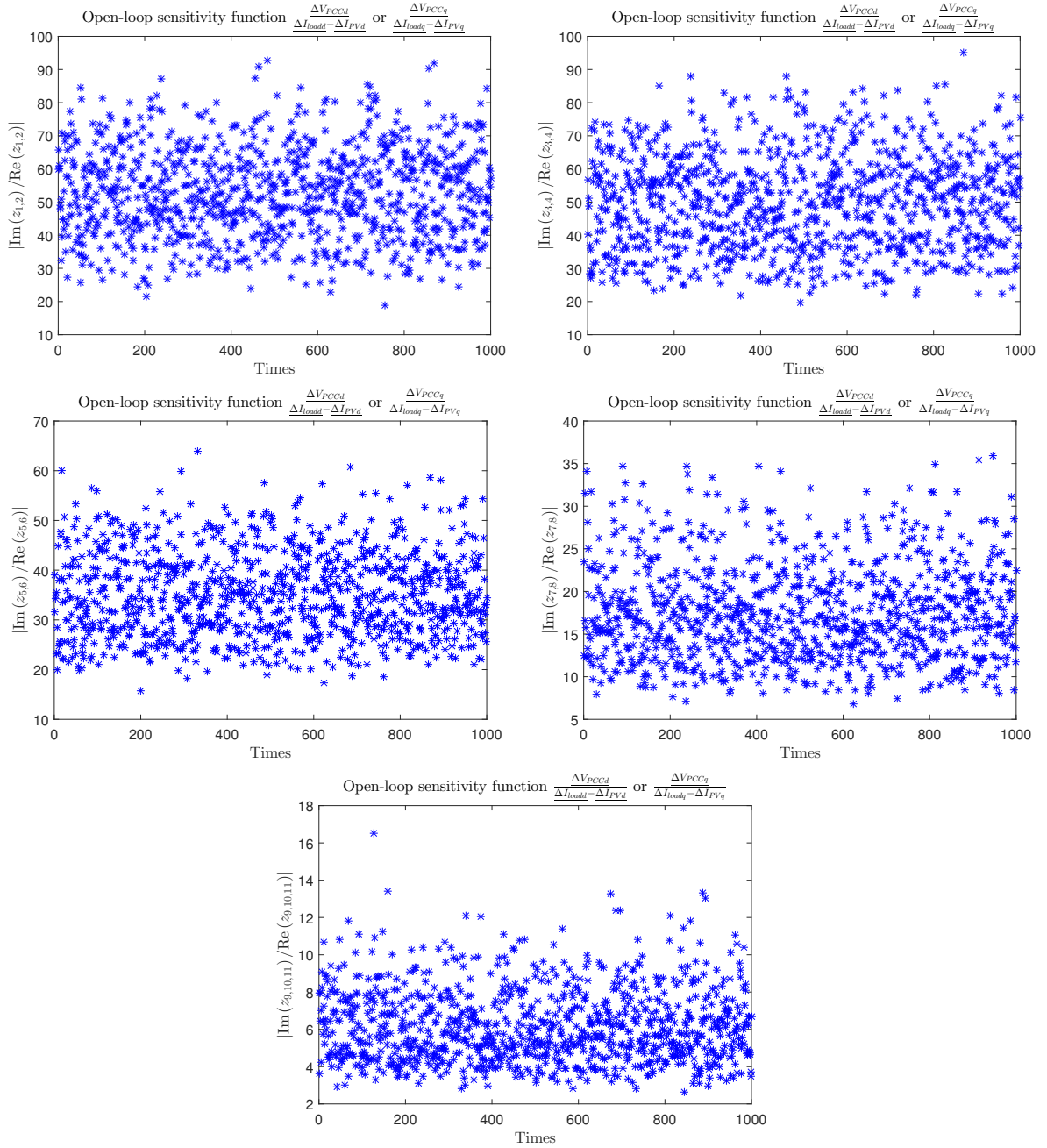


Figure 3.5 – Values $\mathcal{Y}_{k,k+1} = |\text{Im}(z_{k,k+1})/\text{Re}(z_{k,k+1})|$ of the left-half-plane complex conjugate zero pairs $z_{k,k+1}$ of the open-loop sensitivity function $\frac{\Delta V_{PCCd}}{\Delta I_{loadd} - \Delta I_{PVd}}$ or $\frac{\Delta V_{PCCq}}{\Delta I_{loadq} - \Delta I_{PVq}}$.

from -50% to $+50\%$ of their rated values \mathcal{X}_{i_n} and a sufficiently large number of samples of $N = 1000$ gives each 1000 samples $\mathcal{Y}_{k,k+1} = |\text{Im}(z_{k,k+1})/\text{Re}(z_{k,k+1})|$ of the left-half-plane complex conjugate zero pairs $z_{k,k+1}$ of the open-loop sensitivity functions $\frac{\Delta V_{PCCd}}{\Delta I_{loadd} - \Delta I_{PVd}}$ or $\frac{\Delta V_{PCCq}}{\Delta I_{loadq} - \Delta I_{PVq}}$ and

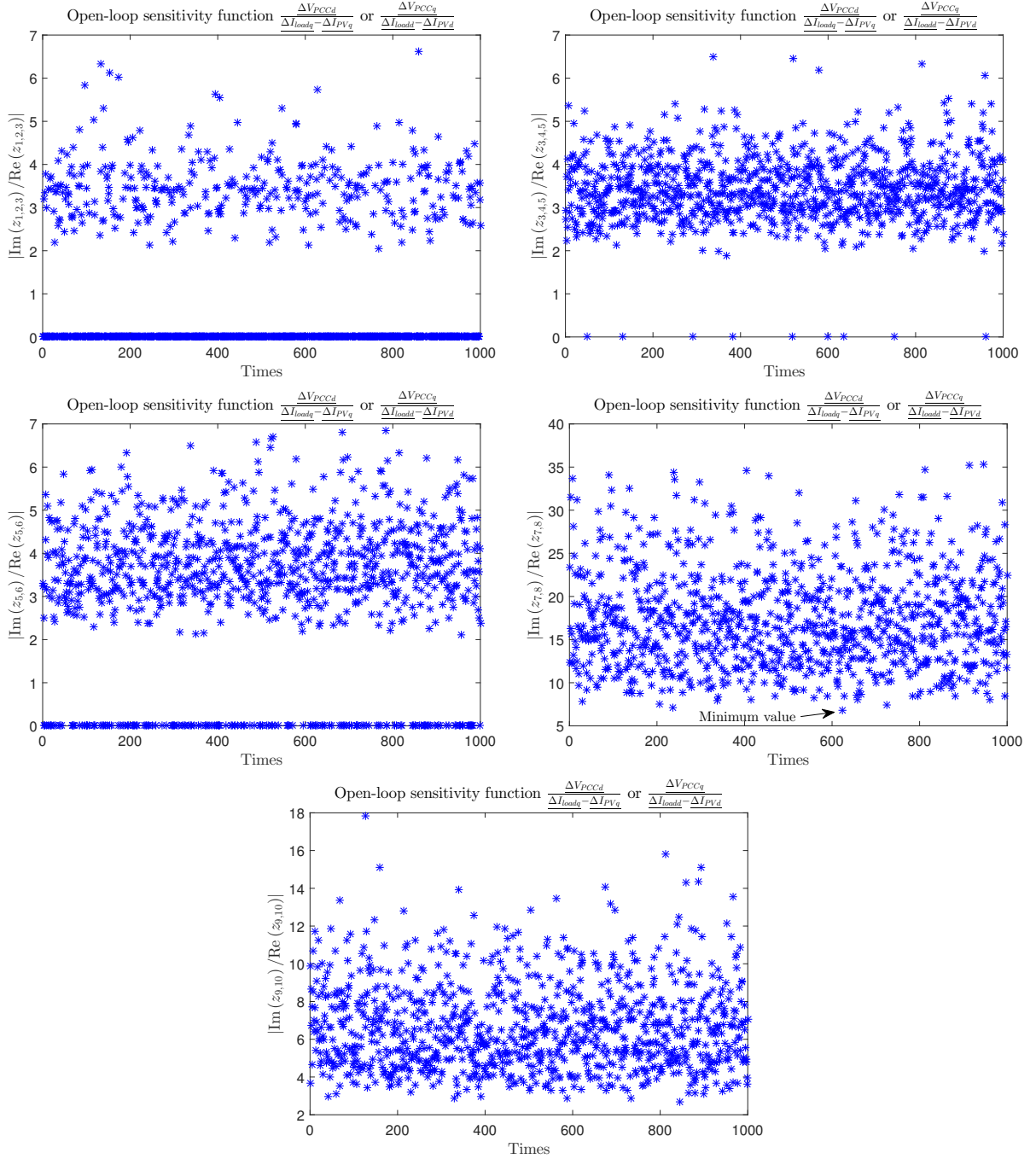


Figure 3.6 – Values $\mathcal{Y}_{k,k+1} = |\text{Im}(z_{k,k+1})/\text{Re}(z_{k,k+1})|$ of the left-half-plane complex conjugate zero pairs $z_{k,k+1}$ of the open-loop sensitivity function $\frac{\Delta V_{PCCd}}{(\Delta I_{loadq} - \Delta I_{PVq})}$ or $\frac{\Delta V_{PCCq}}{(\Delta I_{loadd} - \Delta I_{PVd})}$.

$\frac{\Delta V_{PCCd}}{(\Delta I_{loadq} - \Delta I_{PVq})}$ or $\frac{\Delta V_{PCCq}}{(\Delta I_{loadd} - \Delta I_{PVd})}$, as depicted in Figure 3.5 and Figure 3.6 respectively. Let us remark here that, since $V_{PCCq} \ll V_{PCCd}$, deducing

Table 3.8 – Relative deviations of parameters of the studied whole MG from their rated values.

Parameter	C_{sc}	R_{sc}	R_{sc_p}	L_c	R_c	C_{dc}
Relative deviation	+ 38.9%	+ 33%	– 20.9%	+ 20.2%	– 36.2%	– 39.7%
Parameter	R_{dc}	L_f	R_f	C_f	R_{f_p}	L_t
Relative deviation	– 34.4%	– 48.8%	+ 45.8%	– 29.6%	– 33.2%	– 19.4%
Parameter	R_t	L_g	R_g	C_l	R_{l_p}	
Relative deviation	+ 38.9%	+ 49.3%	+ 41.3%	– 23%	– 46.1%	

that $U_{PCC} \approx V_{PCCd}$ or $\Delta U_{PCC} \approx \Delta V_{PCCd}$, therefore the variation ΔU_{PCC} is much more influenced by ΔV_{PCCd} than by ΔV_{PCCq} . Moreover, only the quadrature component of the load current variation ΔI_{loadq} is regarded as a disturbance, whereas its direct component is approximately equal to zero, *i.e.*, $\Delta I_{loadd} \approx 0$. As a result, the dynamic effects exhibited in ΔU_{PCC} are mainly affected by the values $\mathcal{Y}_{k,k+1}$ of the left-half-plane complex conjugate zero pairs $z_{k,k+1}$ of the sensitivity function $\frac{\Delta V_{PCCd}}{(\Delta I_{loadq} - \Delta I_{PVq})}$ compared to the contributions of those of the left-half-plane complex conjugate zero pairs of the other transfer functions. As can be observed from Figure 3.6, the values $\mathcal{Y}_{7,8}$ are the highest among these values $\mathcal{Y}_{k,k+1}$, which means that $\mathcal{Y}_{7,8}$ have the most influence on the dynamic effects displayed in ΔU_{PCC} in comparison to the influences of the other values $\mathcal{Y}_{k,k+1}$. The minimum sample of $|\text{Im}(z_{7,8})/\text{Re}(z_{7,8})|$ is equal to 6.8 at the 623rd sampling time (*i.e.*, $\mathcal{Y}_{623-7,8} = 6.8$), which corresponds to the 623rd sample set of the input variables \mathbf{X}_{623} , where their relative deviations from the rated values are given in Table 3.8. This desired parameter combination of the studied whole MG allows to minimize the oscillation amplitude in ΔU_{PCC} .

Numerical simulation results

In order to validate the effectiveness of the proposed “analysis-of-zeros” method, MATLAB[®]/Simulink[®] open-loop time-domain simulations are performed on the nonlinear averaged model. Without loss of generality, a load step change of + 5% of the quadrature component of the load rated current I_{loadqe} (*i.e.*, –2.25 A) at $t = 1$ s is applied as a disturbance, whereas the direct component of the load current variation is considered to be approximately equal to zero, *i.e.*, $\Delta I_{loadd} \approx 0$, which corresponds to a load step change of + 5% of the load rated reactive power Q_{load_e} (*i.e.*, + 45 kVAr).

The time-domain responses of the PCC line-to-line voltage magnitude U_{PCC} obtained with both nominal, as well as above computed sets of MG parameter values, are displayed in Figure 3.7. Similar to the simulation results presented in Subsection 3.4.1, it can be seen that the dynamic effects exhibited in the variation ΔU_{PCC} anticipated by the aforementioned analysis of zeros are now confirmed by simulation. In addition, the desired combination of the MG parameter values has considerably improved the dynamic performance of ΔU_{PCC} in terms of oscillation amplitude compared to that obtained with the rated values of the

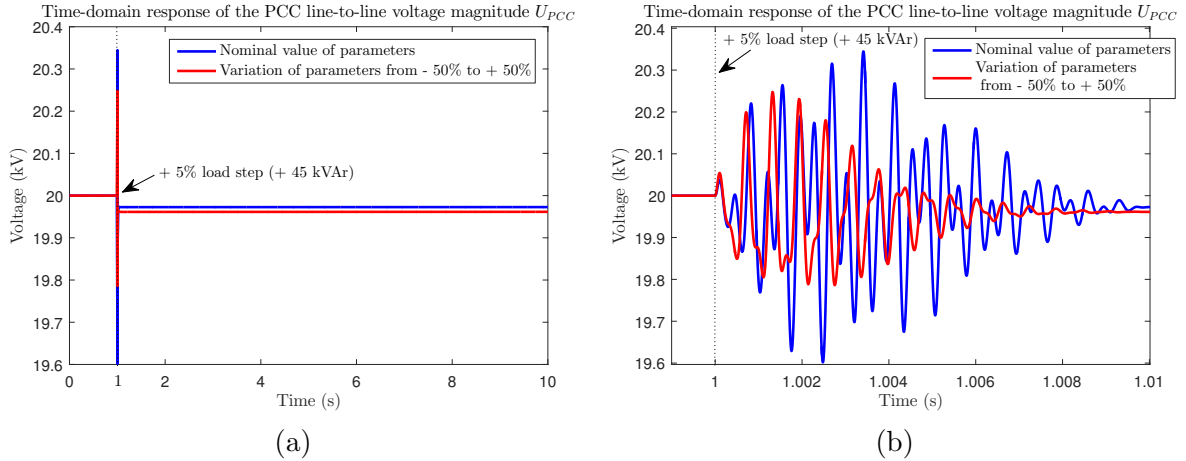


Figure 3.7 – (a) Open-loop time-domain response of the PCC line-to-line voltage magnitude U_{PCC} under a small load step disturbance of + 5% of the load rated reactive power (+ 45 kVAr) with respect to the rated operating point of the studied whole MG. (b) Temporal zoom in the time interval $t \in [0.999, 1.01]$ s.

MG parameters. This demonstrates once again the effectiveness of the proposed “analysis-of-zeros” method. However, employing MG parameter values computed by this method has still not canceled the dynamic effects since it does not alter the natural properties of the linear system.

3.5 Control design

This section presents a voltage robust control design approach used to satisfy the aforementioned dynamic specifications in Subsection 3.2.2. Similar to frequency robust control, here the basic idea is to consider the current variations $\underline{\Delta I}_s$, $\underline{\Delta I}_{rd}$, and $\underline{\Delta I}_{rq}$ in (3.107) – (3.109) as control inputs for the linear system (3.97) – (3.106), which should result from the disturbance rejection requirement $\underline{\Delta I}_{loadd} - \underline{\Delta I}_{PVd}$ and $\underline{\Delta I}_{loadq} - \underline{\Delta I}_{PVq}$. A hierarchical two-level control strategy, where the outer control loop deals with output regulation imposing low-frequency dynamics (*e.g.*, $\underline{\Delta V}_{dc}$, $\underline{\Delta V}_{PCCd}$, $\underline{\Delta V}_{PCCq}$) and the inner loop concerns current reference tracking of high-frequency dynamics (*e.g.*, $\underline{\Delta I}_s$, $\underline{\Delta I}_{rd}$, $\underline{\Delta I}_{rq}$), is also adopted for voltage control. The validity and effectiveness of the proposed robust control strategy are demonstrated through a series of closed-loop time-domain simulations carried out in MATLAB[®]/Simulink[®].

3.5.1 Proposed cascaded two-level control structure

The same idea of cascaded two-level control structure – where classical PI-based current tracking controllers are placed on the low control level and receive references from an \mathcal{H}_∞ -control-based upper level – is also hereafter adopted. The proposed global control structure is depicted in Figure 3.8.

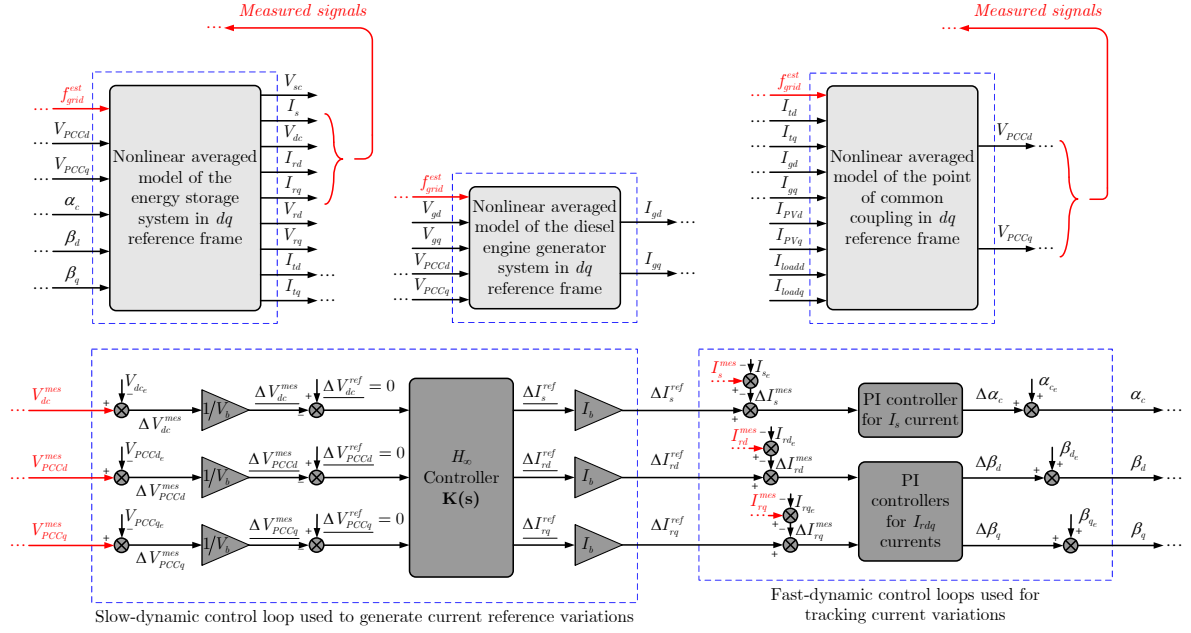


Figure 3.8 – Block diagram of the proposed global control structure.

3.5.2 Current control level

The current variations ΔI_s , ΔI_{rd} , and ΔI_{rq} must be controlled and prevented from exceeding admissible limits. All current control loops have fast closed-loop dynamics compared to the \mathcal{H}_∞ control loop, therefore, they are grouped together.

It should be highlighted that current control loops with the same closed-loop dynamic performance as those used for frequency control in Subsection 2.6.2 are here re-utilized at the low control level.

3.5.3 \mathcal{H}_∞ control level

Linear state-space representation

The current variations ΔI_s , ΔI_{rd} , and ΔI_{rq} are controlled by the very-fast-dynamic control loops tracking the current reference variations generated by the \mathcal{H}_∞ controller, therefore, the outer \mathcal{H}_∞ plant “sees” $\Delta I_s \equiv \Delta I_s^{ref}$, $\Delta I_{rd} \equiv \Delta I_{rd}^{ref}$, and $\Delta I_{rq} \equiv \Delta I_{rq}^{ref}$. The supercapacitor voltage V_{sc} is considered as a time-invariant parameter in the \mathcal{H}_∞ controller synthesis, *i.e.*, $\Delta V_{sc} = 0$ (its dynamic equation $\Delta \dot{V}_{sc} = f(\Delta V_{sc}, \Delta I_s)$ in (3.97) being neglected). Thus, the state-space form of the linear system (3.98) – (3.106) can be written as follows (with the terms $\frac{\omega_b}{C_{dc}} I_{se} \Delta \alpha_c$, $\frac{\omega_b}{C_{dc}} I_{rde} \Delta \beta_d$, and $\frac{\omega_b}{C_{dc}} I_{rqe} \Delta \beta_q$ in (3.98) being neglected in the outer \mathcal{H}_∞ control

loop design)

$$\begin{cases} \underline{\Delta \dot{\mathbf{x}}} = \mathbf{A}\underline{\Delta \mathbf{x}} + \mathbf{B}_1\underline{\Delta \mathbf{u}} + \mathbf{B}_2\underline{\Delta \mathbf{w}} \\ \underline{\Delta \mathbf{y}} = \mathbf{C}\underline{\Delta \mathbf{x}} + \mathbf{D}_1\underline{\Delta \mathbf{u}} + \mathbf{D}_2\underline{\Delta \mathbf{w}} \end{cases}, \quad (3.114)$$

where $\underline{\Delta \mathbf{x}} = [\underline{\Delta V_{dc}} \quad \underline{\Delta V_{rd}} \quad \underline{\Delta V_{rq}} \quad \underline{\Delta V_{PCCd}} \quad \underline{\Delta V_{PCCq}} \quad \underline{\Delta I_{td}} \quad \underline{\Delta I_{tq}} \quad \underline{\Delta I_{gd}} \quad \underline{\Delta I_{gq}}]^T$ is the state vector, $\underline{\Delta \mathbf{u}} = [\underline{\Delta I_s^{ref}} \quad \underline{\Delta I_{rd}^{ref}} \quad \underline{\Delta I_{rq}^{ref}}]^T$ the control input vector, $\underline{\Delta \mathbf{w}} = [\underline{\Delta I_{loadd}} - \underline{\Delta I_{PVd}} \quad \underline{\Delta I_{loadq}} - \underline{\Delta I_{PVq}}]^T$ the disturbance input vector, and $\underline{\Delta \mathbf{y}} = [\underline{\Delta V_{dc}} \quad \underline{\Delta V_{PCCd}} \quad \underline{\Delta V_{PCCq}}]^T$ the measured output vector. Matrices \mathbf{A} , \mathbf{B}_1 , \mathbf{B}_2 , \mathbf{C} , \mathbf{D}_1 , and \mathbf{D}_2 in (3.114) are given as follows

$$\mathbf{A} = \begin{bmatrix} -\frac{\omega_b}{R_{dc}C_{dc}} & 0 & 0 & 0 & 0 & 0 & 0 & 0 & 0 & 0 \\ 0 & -\frac{\omega_b}{R_{fp}C_f} & \omega_b\omega_{gride} & 0 & 0 & -\frac{\omega_b}{C_f} & 0 & 0 & 0 & 0 \\ 0 & -\omega_b\omega_{gride} & -\frac{\omega_b}{R_{fp}C_f} & 0 & 0 & 0 & -\frac{\omega_b}{C_f} & 0 & 0 & 0 \\ 0 & 0 & 0 & -\frac{\omega_b}{R_{lp}C_l} & \omega_b\omega_{gride} & \frac{\omega_b}{C_l} & 0 & \frac{\omega_b}{C_l} & 0 & 0 \\ 0 & 0 & 0 & -\omega_b\omega_{gride} & -\frac{\omega_b}{R_{lp}C_l} & 0 & \frac{\omega_b}{C_l} & 0 & 0 & \frac{\omega_b}{C_l} \\ 0 & \frac{\omega_b}{L_t} & 0 & -\frac{\omega_b}{L_t} & 0 & -\frac{\omega_b R_t}{L_t} & \omega_b\omega_{gride} & 0 & 0 & 0 \\ 0 & 0 & \frac{\omega_b}{L_t} & 0 & -\frac{\omega_b}{L_t} & -\omega_b\omega_{gride} & -\frac{\omega_b R_t}{L_t} & 0 & 0 & 0 \\ 0 & 0 & 0 & -\frac{\omega_b}{L_g} & 0 & 0 & 0 & -\frac{\omega_b R_g}{L_g} & \omega_b\omega_{gride} & 0 \\ 0 & 0 & 0 & 0 & -\frac{\omega_b}{L_g} & 0 & 0 & 0 & -\omega_b\omega_{gride} & -\frac{\omega_b R_g}{L_g} \end{bmatrix},$$

$$\mathbf{B}_1 = \begin{bmatrix} \frac{\omega_b}{C_{dc}}\alpha_{ce} & -\frac{\omega_b}{C_{dc}}\beta_{de} & -\frac{\omega_b}{C_{dc}}\beta_{qe} \\ 0 & \frac{\omega_b}{C_f} & 0 \\ 0 & 0 & \frac{\omega_b}{C_f} \\ 0 & 0 & 0 \\ 0 & 0 & 0 \\ 0 & 0 & 0 \\ 0 & 0 & 0 \\ 0 & 0 & 0 \end{bmatrix}, \quad \mathbf{B}_2 = \begin{bmatrix} 0 & 0 \\ 0 & 0 \\ 0 & 0 \\ -\frac{\omega_b}{C_l} & 0 \\ 0 & -\frac{\omega_b}{C_l} \\ 0 & 0 \\ 0 & 0 \\ 0 & 0 \\ 0 & 0 \end{bmatrix}, \quad \mathbf{C} = \begin{bmatrix} 1 & 0 & 0 & 0 & 0 & 0 & 0 & 0 & 0 & 0 \\ 0 & 0 & 0 & 1 & 0 & 0 & 0 & 0 & 0 & 0 \\ 0 & 0 & 0 & 0 & 1 & 0 & 0 & 0 & 0 & 0 \end{bmatrix},$$

$$\mathbf{D}_1 = \begin{bmatrix} 0 & 0 & 0 \\ 0 & 0 & 0 \\ 0 & 0 & 0 \end{bmatrix}, \quad \mathbf{D}_2 = \begin{bmatrix} 0 & 0 \\ 0 & 0 \\ 0 & 0 \end{bmatrix}. \quad (3.115)$$

Analysis of system structural properties

The structural properties: stability, controllability, and observability of the linear system (3.114) are analyzed based on its matrices \mathbf{A} , \mathbf{B}_1 , and \mathbf{C} . With MG parameter values,

eigenvalues of the matrix \mathbf{A} are equal to $p_{1,2} = -309.5 \pm 17234j$, $p_{3,4} = -309.5 \pm 16605j$, $p_{5,6} = -268 \pm 9403.7j$, $p_{7,8} = -268 \pm 8775.4j$, and $p_9 = -0.0307$. The system is stable for small variations around the steady-state operating point since all eigenvalues have negative real parts. Next, the MATLAB[®] function “ctrb” can be used to check the controllability condition. The controllability matrix $\mathbf{Q}_c = \text{ctrb}(\mathbf{A}, \mathbf{B}_1)$ has the rank of 9, which is equal to the rank of the matrix \mathbf{A} , therefore, the system is well controllable. Finally, the observability condition can be evaluated by using the MATLAB[®] function “obsv”. The rank of the observability matrix $\mathbf{Q}_o = \text{obsv}(\mathbf{A}, \mathbf{C})$ is equal to the rank of the matrix \mathbf{A} , *i.e.*, 9, so the system is said to be completely observable.

Analysis of open-loop zeros

With MG parameter values, the zeros of the open-loop sensitivity functions $\frac{\Delta V_{PCCd}}{(\Delta I_{loadd} - \Delta I_{PVd})}$ or $\frac{\Delta V_{PCCq}}{(\Delta I_{loadq} - \Delta I_{PVq})}$ and $\frac{\Delta V_{PCCd}}{(\Delta I_{loadq} - \Delta I_{PVq})}$ or $\frac{\Delta V_{PCCq}}{(\Delta I_{loadd} - \Delta I_{PVd})}$ of the linear system (3.114) are given in Table 3.9. The existence of undesired dynamic effects (*e.g.*, non-minimum phase behavior, oscillation) exhibited in the PCC line-to-line voltage magnitude variation ΔU_{PCC} in response to the disturbance input variation $\Delta I_{loadq} - \Delta I_{PVq}$ or $\Delta I_{loadd} - \Delta I_{PVd}$ can be proved in a similar way as the analysis of zeros presented in Subsection 3.4.1.

The zeros of the open-loop transfer functions $\frac{\Delta V_{PCCd}}{\Delta I_{rd}^{ref}}$ or $\frac{\Delta V_{PCCq}}{\Delta I_{rq}^{ref}}$ and $\frac{\Delta V_{PCCd}}{\Delta I_{rq}^{ref}}$ or $\frac{\Delta V_{PCCq}}{\Delta I_{rd}^{ref}}$ of the linear plant $\mathbf{G}(s)$ in (3.114) are also given in Table 3.9. The measured output variation ΔV_{PCCd} or ΔV_{PCCq} exhibits non-minimum phase behavior in response to the control input variation ΔI_{rq}^{ref} or ΔI_{rd}^{ref} respectively, as shown by the associated transfer function $\frac{\Delta V_{PCCd}}{\Delta I_{rq}^{ref}}$ or $\frac{\Delta V_{PCCq}}{\Delta I_{rd}^{ref}}$ respectively, having a

Table 3.9 – Zeros of the open-loop transfer functions of the per-unitized linear system (3.114).

Sensitivity function	$\frac{\Delta V_{PCCd}}{(\Delta I_{loadd} - \Delta I_{PVd})}$ or $\frac{\Delta V_{PCCq}}{(\Delta I_{loadq} - \Delta I_{PVq})}$	$\frac{\Delta V_{PCCd}}{(\Delta I_{loadq} - \Delta I_{PVq})}$ or $\frac{\Delta V_{PCCq}}{(\Delta I_{loadd} - \Delta I_{PVd})}$
Zero	$z_{1,2} = -309.2 \pm 16928j$ $z_{3,4} = -243 \pm 11504j$ $z_{5,6} = -267.3 \pm 9067.6j$ $z_7 = -99.4$	$z_1 = -13665$ $z_2 = 13529$ $z_{3,4} = -3706.6 \pm 10856j$ $z_{5,6} = 3191.2 \pm 10859j$
Transfer function	$\frac{\Delta V_{PCCd}}{\Delta I_{rd}^{ref}}$ or $\frac{\Delta V_{PCCq}}{\Delta I_{rq}^{ref}}$	$\frac{\Delta V_{PCCd}}{\Delta I_{rq}^{ref}}$ or $\frac{\Delta V_{PCCq}}{\Delta I_{rd}^{ref}}$
Zero	$z_{1,2} = -309.5 \pm 16906j$ $z_{3,4} = -267.8 \pm 9103.8j$ $z_5 = -99.6$	$z_{1,2} = -297.4 \pm 13018j$ $z_3 = -6969.9$ $z_4 = 6662.8$

right-half-plane zero $z_4 = 6662.8$. This results in a non-minimum phase behavior in ΔU_{PCC} . Suppose that the system operates in a closed loop with an \mathcal{H}_∞ controller. It will not be possible to compensate exactly this zero in closed loop, because the controller itself will be unstable. In this case, the control requires specific solutions that preserve control quality, meanwhile avoiding controller instabilities. An analysis of left-half-plane complex conjugate zero pairs similar to the one carried out in Subsection 3.4.1 allows to conclude that there is another dynamic effect (*e.g.*, oscillation) exhibited in ΔU_{PCC} in response to the control input variation ΔI_{rd}^{ref} or ΔI_{rq}^{ref} . The design procedure of an \mathcal{H}_∞ controller hereafter proposed will take into account influences of these dynamic effects.

We may sometimes use the term “transmission zeros” to distinguish them from the zeros of the elements of the transfer matrix $\mathbf{G}(s)$. The “transmission zeros” of the linear plant $\mathbf{G}(s)$ in (3.114) are equal to $z_{1,2} = -309.5 \pm 17234j$, $z_{3,4} = -309.5 \pm 16605j$, $z_{5,6} = -268 \pm 9403.7j$, $z_{7,8} = -268 \pm 8775.4j$, and $z_{9,10} = -99.1 \pm 314.2j$. Influence of these left-half-plane complex conjugate zero pairs, usually corresponding to “overshoots” (or oscillations) in the time response, can be compensated by control action.

Control configuration in the P – K form

Multi-variable \mathcal{H}_∞ control design for the linear system (3.114) is cast into the formalism in Figure 3.9. A linear approach using the small-signal state-space model of the system is here adopted. In this case, focus is on rejecting disturbance due to the direct and quadrature component variations of the load and PV system output currents. Moreover, it is supposed that the measurement noise is relatively small. The tracking problem is not considered and therefore the S/KS mixed-sensitivity optimization problem in the standard regulation form must typically be solved [180]. The inclusion of KS as a mechanism for limiting the size and bandwidth of the \mathcal{H}_∞ controller, and hence the control energy used, is also important. The key of this design method is the appropriate definition of weighting functions $W_{perf}(s)$ to guarantee the performance specifications and weighting functions $W_u(s)$ to translate the constraints imposed to the control inputs.

The generalized plant \mathbf{P} has five inputs, namely, the direct and quadrature components of the load and PV system output current variations, $\Delta I_{loadd} - \Delta I_{PVd}$ and $\Delta I_{loadq} - \Delta I_{PVq}$ respectively, acting as disturbance inputs $\Delta \mathbf{w}$ and the current reference variations ΔI_s^{ref} , ΔI_{rd}^{ref} , and ΔI_{rq}^{ref} , which are the control inputs $\Delta \mathbf{u}$. The measured output vector $\Delta \mathbf{y}$ is composed of the DC-bus voltage variation ΔV_{dc} and the direct and quadrature components of the PCC voltage variation, ΔV_{PCCd} and ΔV_{PCCq} respectively. The desired performances are expressed in the form of weighting functions on the chosen performance outputs. ΔV_{dc} , ΔV_{PCCd} , ΔV_{PCCq} , as well as ΔI_s^{ref} , ΔI_{rd}^{ref} , ΔI_{rq}^{ref} , are chosen as performance outputs. Their vector is noted $\Delta \mathbf{z}$ in Figure 3.9.

The S/KS mixed-sensitivity optimization of the \mathcal{H}_∞ control framework consists in finding a stabilizing controller which minimizes the norm $\left\| \begin{matrix} W_{perf}S \\ W_uKS \end{matrix} \right\|_\infty$.

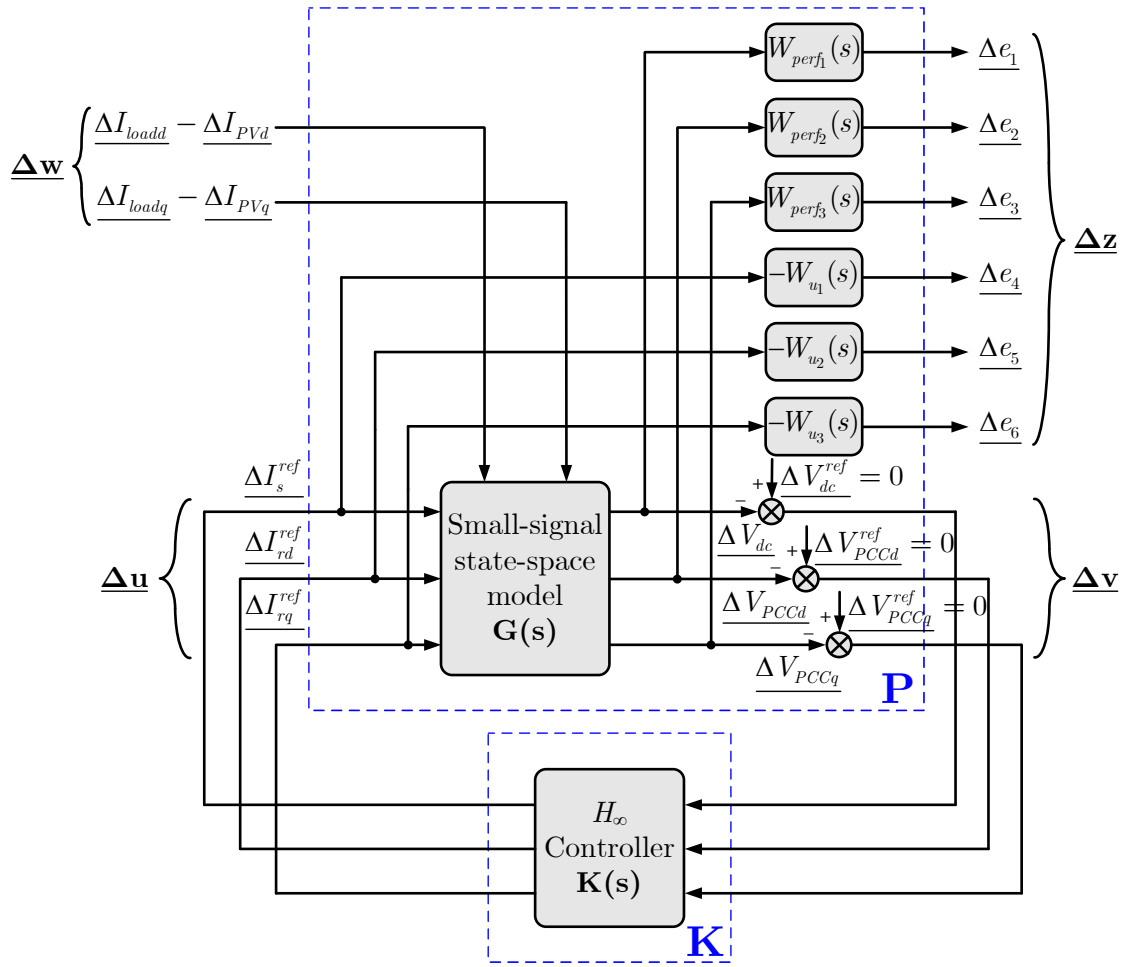


Figure 3.9 – Control configuration in the so-called $\mathbf{P} - \mathbf{K}$ form, where \mathbf{P} denotes the plant together with the weighting functions and \mathbf{K} denotes the \mathcal{H}_∞ controller.

Weighting functions selection

The representation of the direct and quadrature components of the PCC voltage V_{PCCd} and V_{PCCq} , where $U_{PCC} = \sqrt{V_{PCCd}^2 + V_{PCCq}^2}$, is shown in Figure 3.10. A performance specification on the direct component of the PCC voltage variation ΔV_{PCCd} in response to a load reactive power step disturbance, deduced from the grid code requirements on the PCC line-to-line voltage magnitude variation ΔU_{PCC} , is illustrated in Figure 3.11. It should be noted here that since $V_{PCCq} \ll V_{PCCd}$, meaning that $U_{PCC} \approx V_{PCCd}$ or $\Delta U_{PCC} \approx \Delta V_{PCCd}$, therefore the performance template for ΔV_{PCCd} is chosen to be quasi-identical to that for ΔU_{PCC} .

The choice of linear time-invariant weighting functions is the key to deal with the performance requirements. The DC-bus voltage variation ΔV_{dc} and the direct and quadrature components of the PCC voltage variation, ΔV_{PCCd} and ΔV_{PCCq} respectively, are bounded

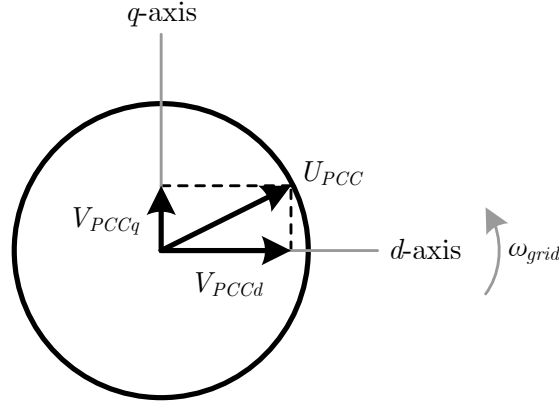


Figure 3.10 – Representation of the dq -components of the PCC voltage V_{PCCd} and V_{PCCq} .

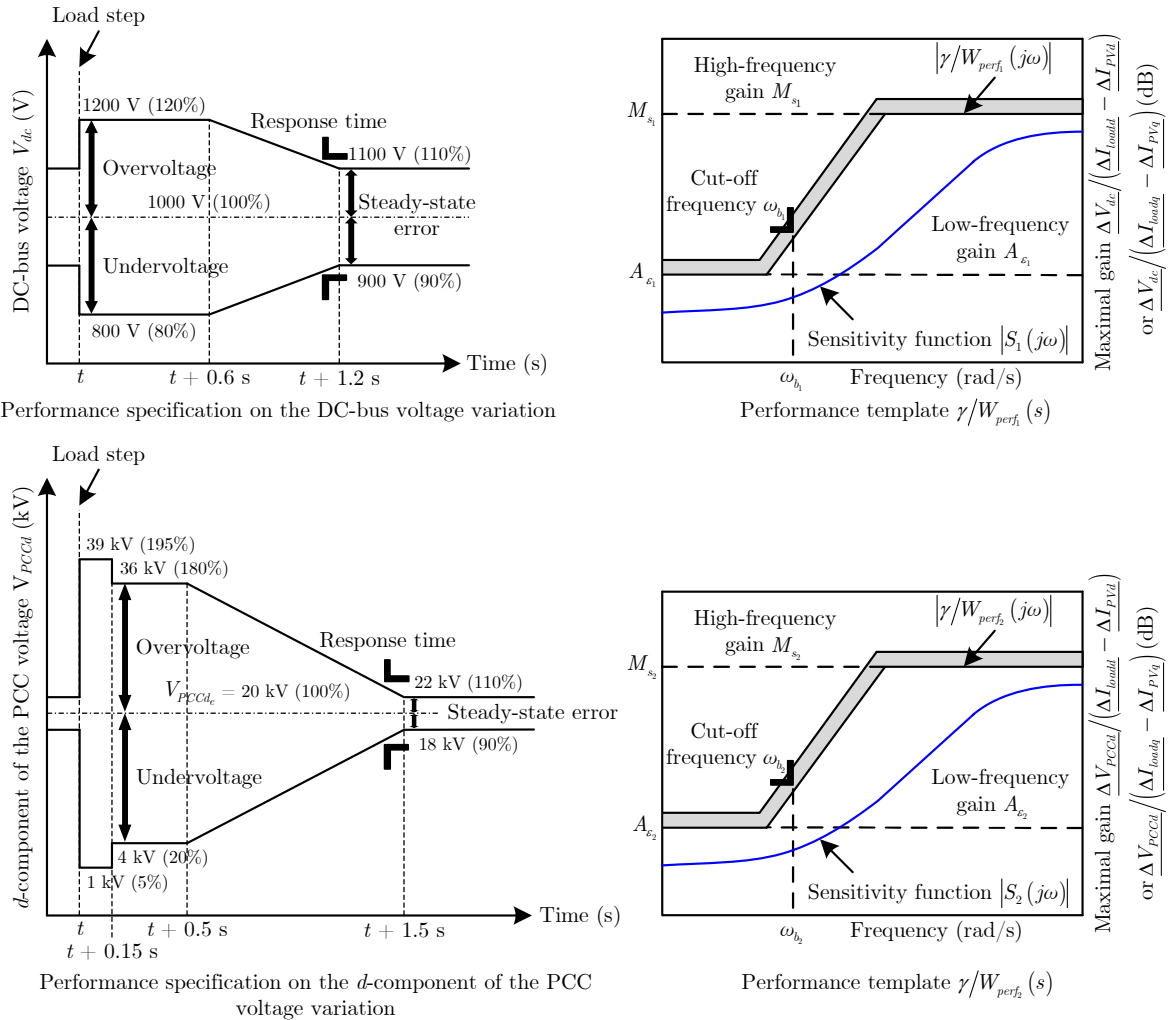


Figure 3.11 – Translations of temporal norms into frequency-domain specifications.

by first-order weighting functions $W_{perf}(s)$ of the following form [180]

$$\frac{1}{W_{perf}(s)} = \frac{s + \omega_b A_\varepsilon}{s/M_s + \omega_b}. \quad (3.116)$$

The function $1/W_{perf}(s)$ can be representative of time-domain response specifications, where the high-frequency gain M_s has an impact on the system overshoot, whereas the desired response time is tuned by the cut-off frequency ω_b and the steady-state error can be limited by appropriate choice of the low-frequency gain A_ε [74]. That makes equivalences between desired time-domain performances and frequency-domain specifications, as shown in Figure 3.11. In order to satisfy the tight control requirement at low frequencies in the presence of the right-half-plane zeros of the plant, the selection of the value ω_b of the function $1/W_{perf}(s)$ is of great importance. Let $\mathbf{G}(s)$ be a MIMO plant with one right-half-plane zero at $s = z$ and $W_{perf}(s)$ be a scalar weight, then closed-loop stability is ensured only if $\|W_{perf}(s)S(s)\|_\infty \geq |W_{perf}(z)|$ [180]. For the design problem, if the \mathcal{H}_∞ controller meets the requirements, then $\|W_{perf}(s)S(s)\|_\infty \leq 1$. Therefore, a necessary condition for closed-loop stability is $|W_{perf}(z)| \leq 1$, which corresponds to (with $W_{perf}(s)$ being given in (3.116)) [180]

$$\left| \frac{z/M_s + \omega_b}{z + \omega_b A_\varepsilon} \right| \leq 1. \quad (3.117)$$

Consider the case when z is real and positive, then (3.117) is equivalent to

$$\omega_b (1 - A_\varepsilon) \leq z \left(1 - \frac{1}{M_s} \right). \quad (3.118)$$

The first weighting function $W_{perf_1}(s)$ is designed such that to ensure a bandwidth for $\underline{\Delta V_{dc}}$ forty times smaller than the $\underline{\Delta I_{rd}}$ (or $\underline{\Delta I_{rd}}$) inner closed-loop one, *i.e.*, $\omega_{b_1} = 1/(40T_{0_{rdq}}) = 2.61$ rad/s (or a response time of approximately $t_{r_1} \approx 1.2$ s). $M_{s_1} = (0.2\underline{V_{dc_e}}) / (0.05 |I_{loadq_e}|) = 22.28$ is chosen to limit the DC-bus voltage overshoot at 20% of its rated value V_{dc_e} (*i.e.*, 200 V) in response to a load step of 5% of the quadrature component of the load rated current I_{loadq_e} (*i.e.*, -2.25 A), which corresponds to a load step of 5% of the load rated reactive power Q_{load_e} (*i.e.*, 45 kVar). Similarly, one imposes $A_{\varepsilon_1} = (0.1\underline{V_{dc_e}}) / (0.05 |I_{loadq_e}|) = 11.14$ to ensure a desired steady-state error being less than or equal to 10% of V_{dc_e} (*i.e.*, 100 V).

The parameters of the second weighting function $W_{perf_2}(s)$ designed for $\underline{\Delta V_{PCCd}}$ are chosen to guarantee its performance specification in Figure 3.11. $\omega_{b_2} = 1/(50T_{0_{rdq}}) = 2.09$ rad/s is chosen to ensure a response time of approximately $t_{r_2} \approx 1.5$ s (or a bandwidth fifty times smaller than the $\underline{\Delta I_{rd}}$ (or $\underline{\Delta I_{rd}}$) inner closed-loop one). Imposing $M_{s_2} = (0.8\underline{V_{PCCd_e}}) / (0.05 |I_{loadq_e}|) = 35.64$ allows limiting the overshoot of the direct component of the PCC rated voltage V_{PCCd_e} at 80% (*i.e.*, 16 kV) in response to a load step of 5% of I_{loadq_e} (*i.e.*, -2.25 A). $A_{\varepsilon_2} = (0.1\underline{V_{PCCd_e}}) / (0.05 |I_{loadq_e}|) = 4.46$ is chosen to ensure a desired steady-state error being less than or equal to 10% of V_{PCCd_e} (*i.e.*, 2 kV).

The third weighting function $W_{perf_3}(s)$ is designed such that to impose a bandwidth for $\underline{\Delta V_{PCCq}}$ fifty times smaller than the $\underline{\Delta I_{rd}}$ (or $\underline{\Delta I_{rd}}$) inner closed-loop one, *i.e.*, $\omega_{b_3} =$

$1/(50T_{0_{rdq}}) = 2.09$ rad/s (or a response time of approximately $t_{r_3} \approx 1.5$ s). In order not to impose too much constraint on ΔV_{PCCq} (or ΔV_{PCCd}), $M_{s_3} = \left(80V_{PCCq_e}\right) / \left(0.05 \left|I_{loadq_e}\right|\right) = 6.7$ is chosen, which allows limiting the overshoot at 3.01 kV on ΔV_{PCCq} in response to a load step of 5% of I_{loadq_e} (*i.e.*, -2.25 A). $A_{\varepsilon_3} = \left(80V_{PCCq_e}\right) / \left(0.05 \left|I_{loadq_e}\right|\right) = 6.7$ is chosen to ensure a desired steady-state error being less than or equal to 3.01 kV on ΔV_{PCCq} .

Let us note here that the selection of the values ω_{b_2} and ω_{b_3} of the functions $1/W_{perf_2}(s)$ and $1/W_{perf_3}(s)$ respectively satisfies the condition (3.118), which means that closed-loop stability is implicitly ensured in the presence of the right-half-plane zero $z_4 = 6662.8$ of the open-loop transfer function $\Delta V_{PCCd}/\Delta I_{rq}^{ref}$ or $\Delta V_{PCCq}/\Delta I_{rd}^{ref}$ of the linear plant $\mathbf{G}(s)$ in (3.114). In addition, the frequencies $|z_{k,k+1}|$ of the left-half-plane complex conjugate zero pairs $z_{k,k+1}$ of the transfer functions $\Delta V_{PCCd}/\Delta I_{rd}^{ref}$ or $\Delta V_{PCCq}/\Delta I_{rq}^{ref}$ and $\Delta V_{PCCd}/\Delta I_{rq}^{ref}$ or $\Delta V_{PCCq}/\Delta I_{rd}^{ref}$ are all higher than the frequency $|z_4|$ of z_4 , therefore the oscillation exhibited in ΔU_{PCC} in response to the control input variation ΔI_{rd}^{ref} or ΔI_{rq}^{ref} are implicitly filtered.

The active power injection or absorption of the ESS is controlled *via* I_s . The DC-bus voltage and the direct and quadrature components of the PCC voltage respectively are regulated *via* I_{rd} and I_{rq} . Thus, the supercapacitor output current reference variation ΔI_s^{ref} and the direct and quadrature components of the inverter output current reference variation, ΔI_{rd}^{ref} and ΔI_{rq}^{ref} respectively, are bounded by the following first-order weighting functions [180]

$$\frac{1}{W_u(s)} = \frac{A_u s + \omega_{bc}}{s + \omega_{bc}/M_u}. \quad (3.119)$$

Frequency-domain specifications on these current reference variations are presented in Figure 3.12.

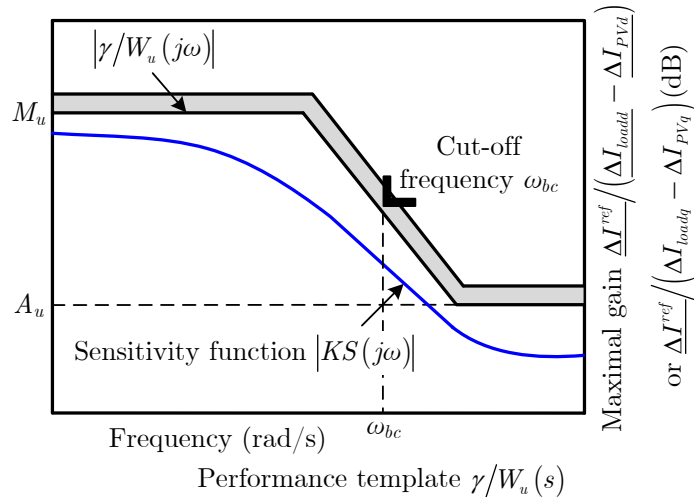


Figure 3.12 – Frequency-domain specifications on the supercapacitor output current reference variation ΔI_s^{ref} and the dq -component of the inverter output current reference variation ΔI_{rd}^{ref} and ΔI_{rq}^{ref} .

The first weighting function $W_{u_1}(s)$ is designed such that to impose a bandwidth for $\underline{\Delta I_s^{ref}}$ ten times smaller than the ΔI_s (or $\underline{\Delta I_s}$) inner closed-loop one, *i.e.*, $\omega_{bc_1} = 1/(10T_{0_s}) = 8.77$ rad/s. $M_{u_1} = \left(\frac{I_{s_{max}} - I_{s_e}}{0.05 |I_{loadq_e}|} \right) = 12.83$ is chosen to prevent the supercapacitor output current reference from exceeding its admissible limit $I_{s_{max}}$ consequent to a load step of 5% of I_{loadq_e} (*i.e.*, -2.25 A). A small value of $A_{u_1} = 0.01M_{u_1} = 0.128$ is imposed.

The parameters of the second weighting function $W_{u_2}(s)$ designed for $\underline{\Delta I_{rd}^{ref}}$ are chosen to impose a bandwidth ten times smaller than the ΔI_{rd} (or $\underline{\Delta I_{rd}}$) inner closed-loop one, *i.e.*, $\omega_{bc_2} = 1/(10T_{0_{rdq}}) = 10.43$ rad/s. $M_{u_2} = \left(\frac{I_{rd_{max}} - I_{rd_e}}{0.05 |I_{loadq_e}|} \right) = 11.31$ is imposed to limit the direct component of the inverter output current reference below its maximum value $I_{rd_{max}}$ consequent to a load step of 5% of I_{loadq_e} (*i.e.*, -2.25 A). A small value of $A_{u_2} = 0.01M_{u_2} = 0.113$ is chosen.

The third weighting function $W_{u_3}(s)$ is designed such that to impose a bandwidth for $\underline{\Delta I_{rq}^{ref}}$ ten times smaller than the ΔI_{rq} (or $\underline{\Delta I_{rq}}$) inner closed-loop one, *i.e.*, $\omega_{bc_3} = 1/(10T_{0_{rdq}}) = 10.43$ rad/s. Imposing $M_{u_3} = \left(\frac{I_{rq_{max}} - I_{rq_e}}{0.05 |I_{loadq_e}|} \right) = 7.39$ allows preventing the quadrature component of the inverter output current reference from exceeding its admissible limit $I_{rq_{max}}$ consequent to a load step of 5% of I_{loadq_e} (*i.e.*, -2.25 A). A small value of $A_{u_3} = 0.02M_{u_3} = 0.148$ is chosen.

\mathcal{H}_∞ controller synthesis

The robust control toolbox in the MATLAB[®] software environment is used to design a full-order \mathcal{H}_∞ controller based on the system modeling and the selected weighting functions. The obtained result corresponds to the minimization of the norm

$$\left\| \frac{W_{perf}S}{W_uKS} \right\|_\infty < \gamma. \quad (3.120)$$

Design procedure may yield unstable controllers. Therefore, the value γ_{min} must be slightly increased in this case to relax the constraint on the control and lead to stable controllers. The LMI algorithm under the MATLAB[®] software environment yields a solution after five iterations for a multi-variable full-order \mathcal{H}_∞ controller which has 15 states with a conditioning value of $\gamma = 160.87$ and an \mathcal{H}_∞ norm = 40.71. This optimization quality allows the synthesized \mathcal{H}_∞ controller to guarantee stable and robust performance in case of a load step of 5% of I_{loadq_e} (*i.e.*, -2.25 A) in the system, which is demonstrated in the sequel.

For the considered system shown in Figure 3.9, sensitivity functions $S_{11}(s)$, $S_{12}(s)$, $S_{21}(s)$, $S_{22}(s)$, $S_{31}(s)$, $S_{32}(s)$ and complementary sensitivity functions $KS_{11}(s)$, $KS_{12}(s)$, $KS_{21}(s)$, $KS_{22}(s)$, $KS_{31}(s)$, $KS_{32}(s)$ are defined as follows

$$S_{11}(s) = \frac{\underline{\Delta V_{dc}}}{\underline{\Delta I_{loadd}} - \underline{\Delta I_{PVd}}}, \quad S_{12}(s) = \frac{\underline{\Delta V_{dc}}}{\underline{\Delta I_{loadq}} - \underline{\Delta I_{PVq}}}. \quad (3.121)$$

$$S_{21}(s) = \frac{\underline{\Delta V_{PCCd}}}{\underline{\Delta I_{loadd}} - \underline{\Delta I_{PVd}}}, \quad S_{22}(s) = \frac{\underline{\Delta V_{PCCd}}}{\underline{\Delta I_{loadq}} - \underline{\Delta I_{PVq}}}. \quad (3.122)$$

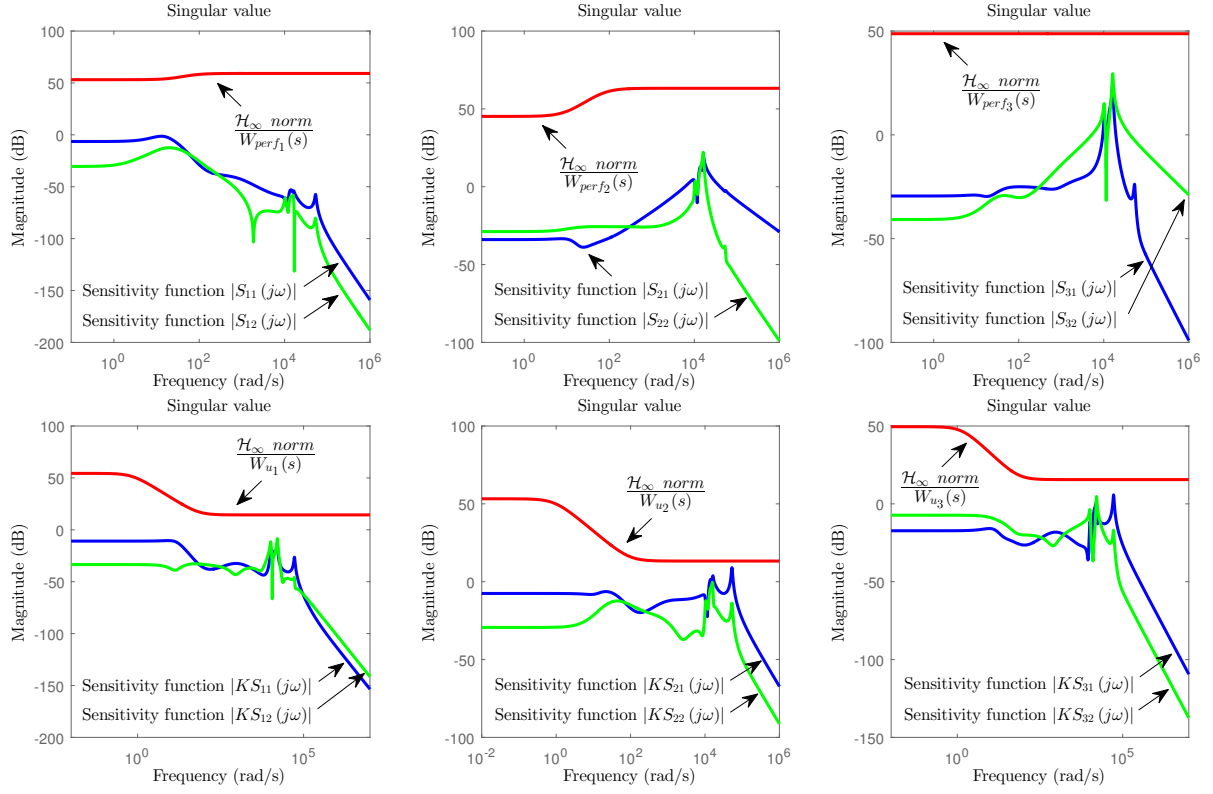


Figure 3.13 – Singular value plots of the sensitivity functions $S_{11}(s)$, $S_{12}(s)$, $S_{21}(s)$, $S_{22}(s)$, $S_{31}(s)$, $S_{32}(s)$; complementary sensitivity functions $KS_{11}(s)$, $KS_{12}(s)$, $KS_{21}(s)$, $KS_{22}(s)$, $KS_{31}(s)$, $KS_{32}(s)$; and corresponding templates.

$$S_{31}(s) = \frac{\Delta V_{PCCq}}{\Delta I_{loadq} - \Delta I_{PVd}}, \quad S_{32}(s) = \frac{\Delta V_{PCCq}}{\Delta I_{loadq} - \Delta I_{PVq}}. \quad (3.123)$$

$$KS_{11}(s) = \frac{\Delta I_s^{ref}}{\Delta I_{loadq} - \Delta I_{PVd}}, \quad KS_{12}(s) = \frac{\Delta I_s^{ref}}{\Delta I_{loadq} - \Delta I_{PVq}}. \quad (3.124)$$

$$KS_{21}(s) = \frac{\Delta I_{rd}^{ref}}{\Delta I_{loadq} - \Delta I_{PVd}}, \quad KS_{22}(s) = \frac{\Delta I_{rd}^{ref}}{\Delta I_{loadq} - \Delta I_{PVq}}. \quad (3.125)$$

$$KS_{31}(s) = \frac{\Delta I_{rq}^{ref}}{\Delta I_{loadq} - \Delta I_{PVd}}, \quad KS_{32}(s) = \frac{\Delta I_{rq}^{ref}}{\Delta I_{loadq} - \Delta I_{PVq}}. \quad (3.126)$$

The singular value plots of the sensitivity functions $S(s)$, complementary sensitivity functions $KS(s)$, and corresponding templates of the closed-loop system are illustrated in Figure 3.13. The results show how the shaping of \mathcal{H}_∞ performance is straightforward for the full-order \mathcal{H}_∞ controller using the weighting functions templates. It can be observed that, since the sensitivity functions are placed below the corresponding templates irrespective of the frequency value, the imposed control performance weights are well respected.

3.5.4 Numerical simulation results

A series of MATLAB[®]/Simulink[®] closed-loop time-domain simulations using the topological model, as well as the nonlinear and linear averaged models are performed to show the effectiveness of the proposed control approach. The topological model refers here to the complete model of the ESS considering the ideal PWM switching functions of the chopper and of the three-phase inverter as control inputs. Without loss of generality, a load step change of + 5% of the quadrature component of the load rated current I_{loadqe} (*i.e.*, -2.25 A) at $t = 1$ s is applied as a disturbance, whereas the direct component of the load current variation is regarded to be approximately equal to zero, *i.e.*, $\Delta I_{loadd} \approx 0$, which corresponds to a load step change of + 5% of the load rated reactive power (*i.e.*, + 45 kVAr). The supercapacitor voltage V_{sc} , initially regarded as a time-invariant parameter in the \mathcal{H}_∞ controller synthesis, is considered now as a time-variant one, *i.e.*, $\Delta V_{sc} \neq 0$ (its dynamic equation $\dot{V}_{sc} = f(V_{sc}, I_s)$ being taken into account in the simulation models).

Model validation and effectiveness of the proposed robust control strategy

Figure 3.14, Figure 3.15, Figure 3.16, and Figure 3.17(a) present a comparison of topological and averaged modeling for the time-domain responses of the PCC line-to-line voltage magnitude U_{PCC} , the direct and quadrature components of the PCC voltage V_{PCCd} and V_{PCCq} , and the DC-bus voltage V_{dc} respectively. The results show a good concordance with both of these models despite high-frequency oscillations seen in the topological model. Therefore, the averaged models themselves are validated when compared to the topological model results. It can be observed from Figure 3.15 and Figure 3.16 that the desired time-domain performances of V_{PCCd} and V_{PCCq} are successfully achieved in terms of overshoot, response time, and steady-state error with respect to the choice of the weighting functions $W_{perf_2}(s)$

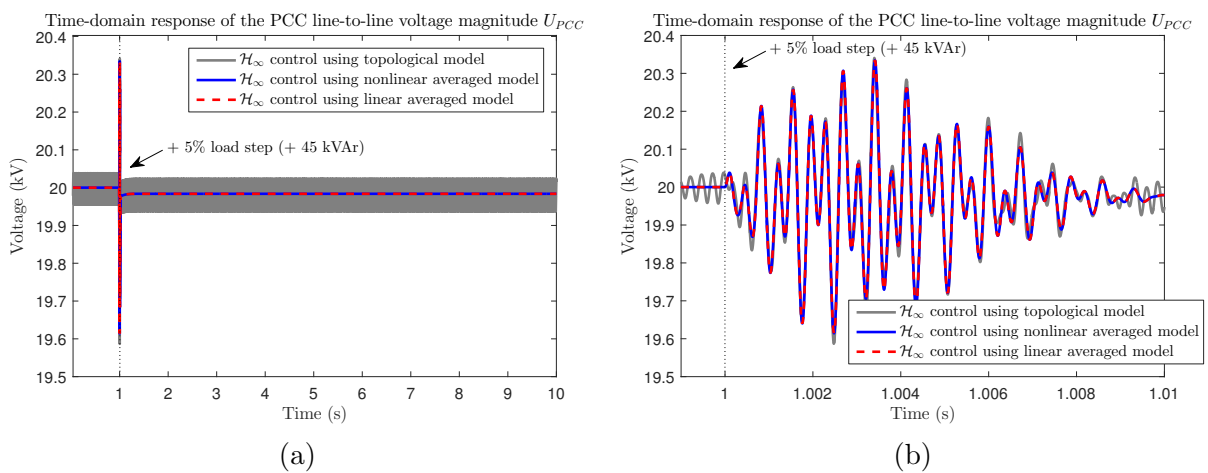


Figure 3.14 – (a) Time-domain response of the PCC line-to-line voltage magnitude U_{PCC} under a small load step disturbance of + 5% of the load rated reactive power (+ 45 kVAr) with respect to the rated operating point. (b) Temporal zoom in the time interval $t \in [0.999, 1.01]$ s.

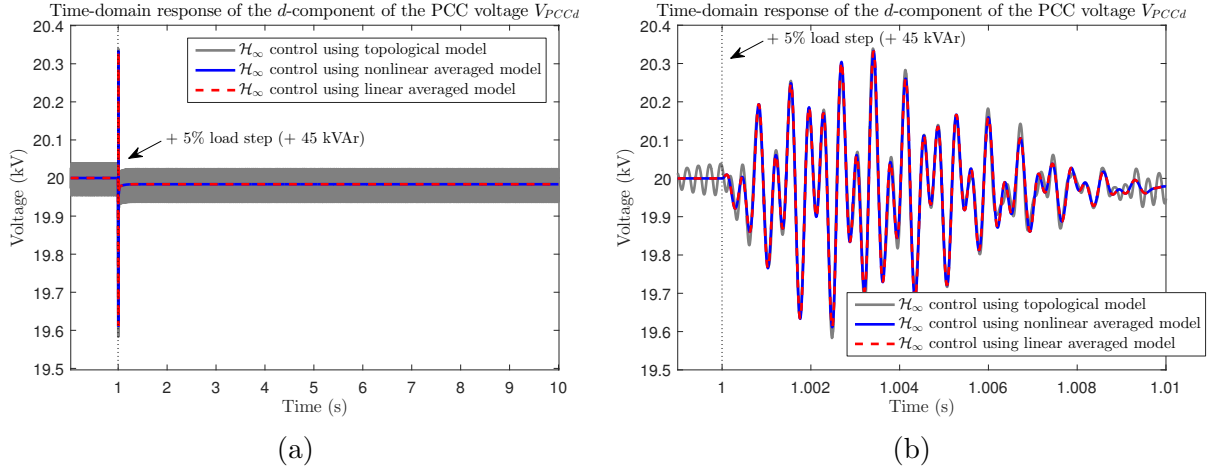


Figure 3.15 – (a) Time-domain response of the d -component of the PCC voltage V_{PCCd} under a small load step disturbance of + 5% of the load rated reactive power (+ 45 kVAR) with respect to the rated operating point. (b) Temporal zoom in the time interval $t \in [0.999, 1.01]$ s.

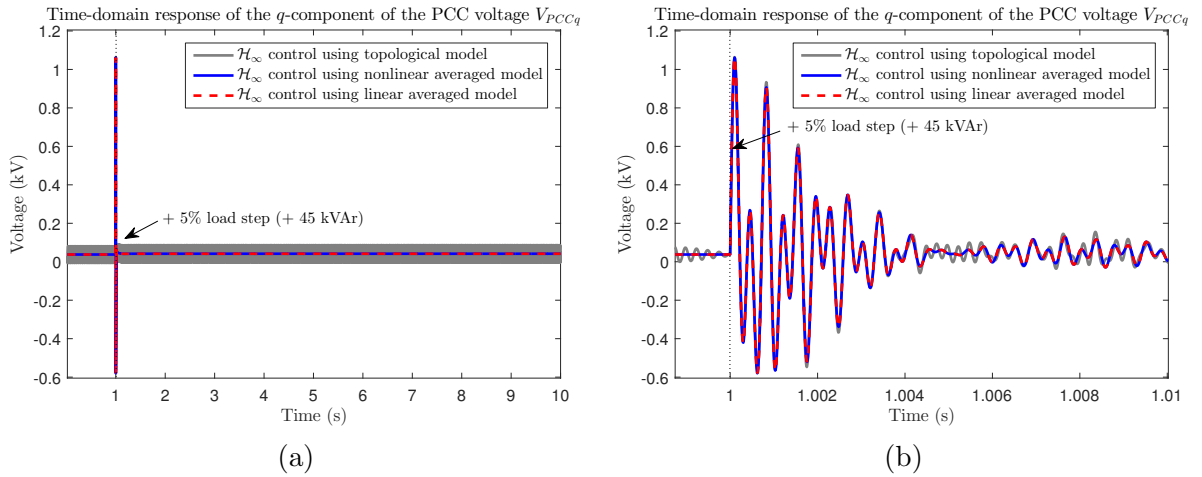


Figure 3.16 – (a) Time-domain response of the q -component of the PCC voltage V_{PCCq} under a small load step disturbance of + 5% of the load rated reactive power (+ 45 kVAR) with respect to the rated operating point. (b) Temporal zoom in the time interval $t \in [0.999, 1.01]$ s.

and $W_{perf_3}(s)$ respectively. Figure 3.14 shows that the dynamic performance specification imposed on U_{PCC} in Figure 3.2 is well respected. The system is also always stable. It should be noted here that, since focus is on primary voltage control only, the PCC voltage error cancellation cannot be obtained, which means that the PCC voltage cannot be brought back to its initial steady-state value after the disturbance. It can be seen from Figure 3.17(a) that the desired time-domain performances of V_{dc} corresponding to the tuning of the weighting function $W_{perf_1}(s)$ are satisfied. Hence, the synthesized \mathcal{H}_∞ controller guarantees the desired performance specifications.

Figure 3.17(b), Figure 3.18(a), and Figure 3.18(b) compare the time-domain responses

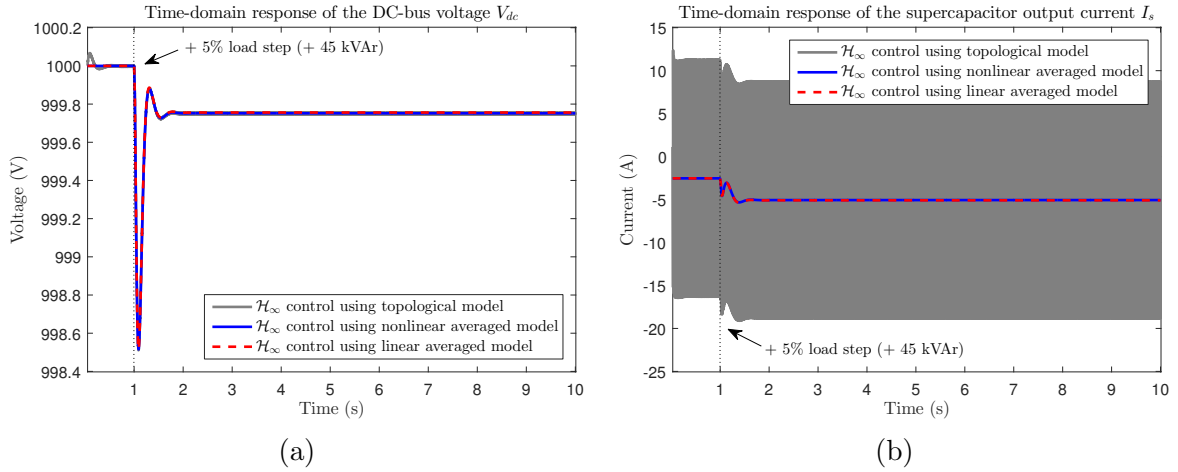


Figure 3.17 – Time-domain responses of (a) the DC-bus voltage V_{dc} and (b) the supercapacitor output current I_s under a small load step disturbance of + 5% of the load rated reactive power (+ 45 kVAr) with respect to the rated operating point.

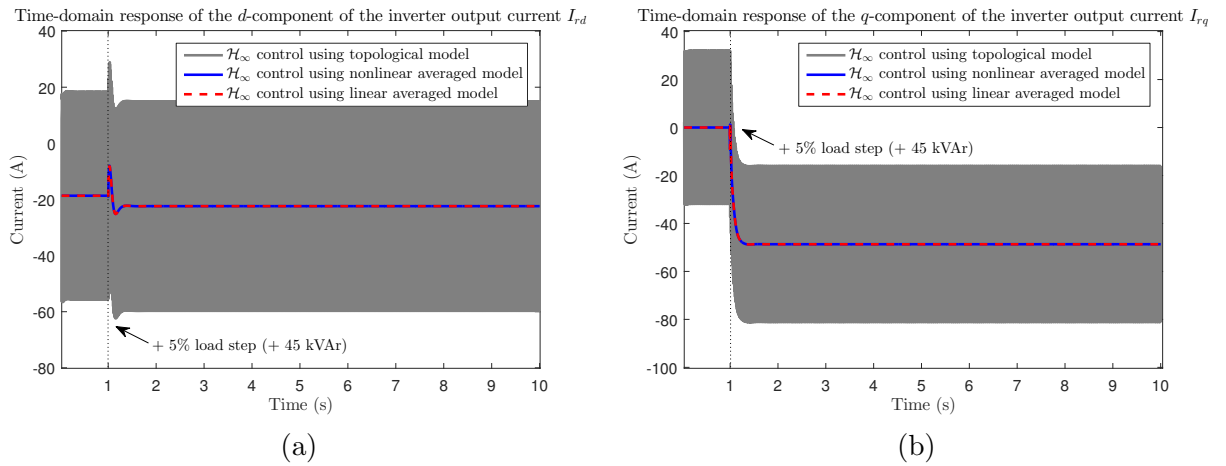


Figure 3.18 – Time-domain responses of (a) the d -component I_{rd} and (b) the q -component I_{rq} of the inverter output current under a small load step disturbance of + 5% of the load rated reactive power (+ 45 kVAr) with respect to the rated operating point.

of the supercapacitor output current I_s and the direct and quadrature components of the inverter output current I_{rd} and I_{rq} , respectively, obtained with both topological and averaged models. The results show a good agreement between these models, except for high-frequency oscillations observed in the topological model. Therefore, the averaged models precisely represent the dynamics of the ESS in that frequency bandwidth that is interesting for control purposes. Moreover, it can be seen that the admissible limit is guaranteed for these currents, which means that their imposed dynamic performance specifications are satisfied.

For the sake of simplicity and without loss of generality, the nonlinear averaged model will from now on be used for time-domain simulation.

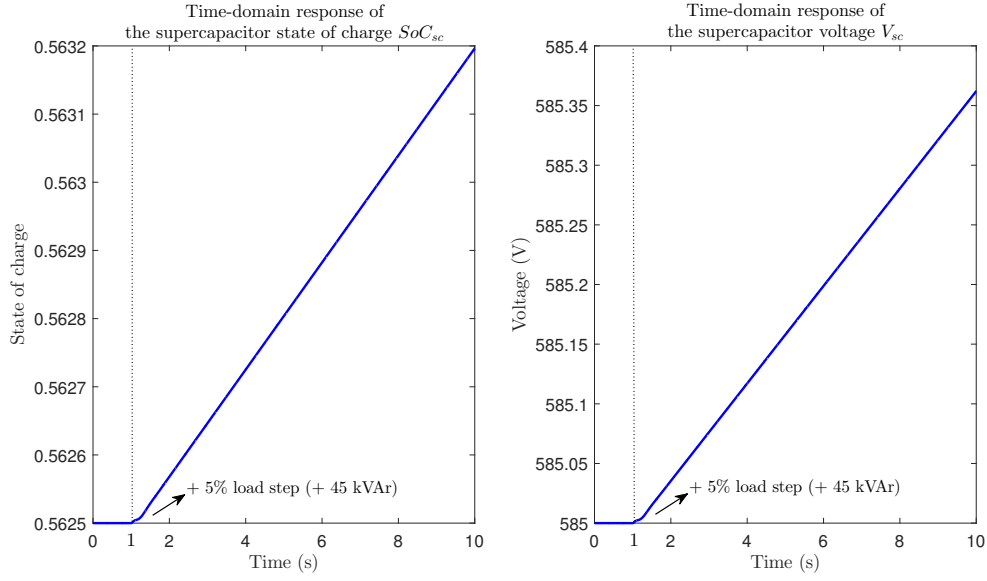


Figure 3.19 – Time-domain responses of the supercapacitor state of charge SoC_{sc} and voltage V_{sc} under a small load step disturbance of + 5% of the load rated reactive power (+ 45 kVAr) with respect to the rated operating point.

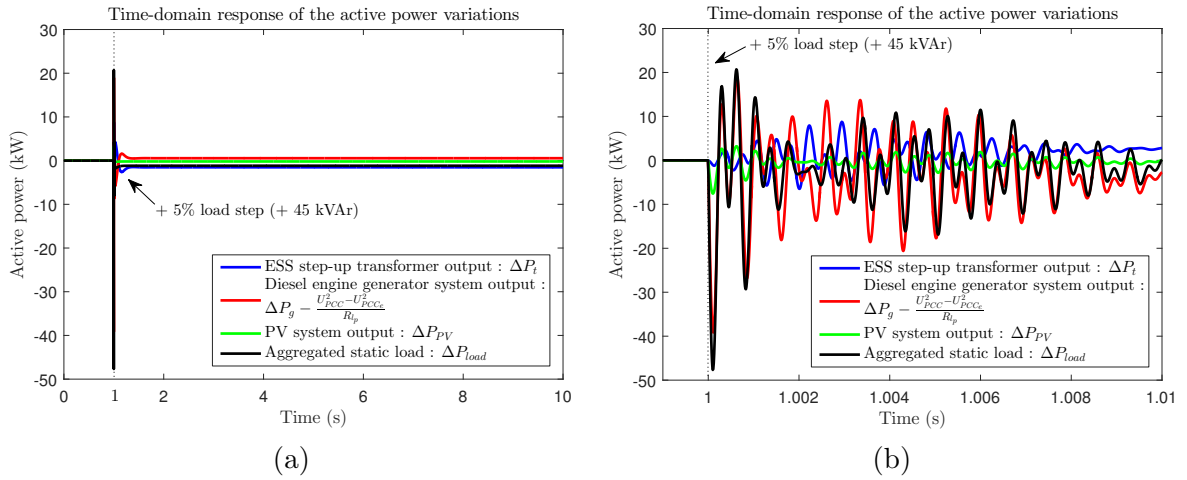


Figure 3.20 – (a) Active power variations of the sources and load under a small load step disturbance of + 5% of the load rated reactive power (+ 45 kVAr). (b) Temporal zoom in the time interval $t \in [0.999, 1.01]$ s.

Figure 3.19 illustrates the time-domain responses of the supercapacitor state of charge SoC_{sc} and voltage V_{sc} . These values tend to increase linearly and quite slowly since the steady-state value of I_s is negative and slightly lower than its initial value, which means that the supercapacitor is in charging mode.

The time-domain responses of the active power variations of the sources and load are illustrated in Figure 3.20. It can be observed that, due to large variations in U_{PCC} , V_{PCCd} ,

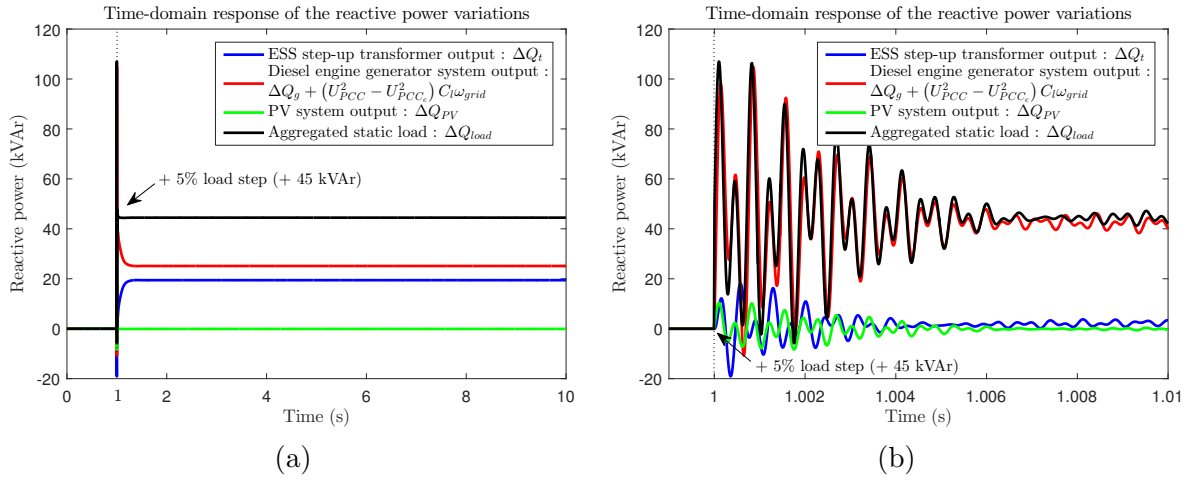


Figure 3.21 – (a) Reactive power variations of the sources and load under a small load step disturbance of + 5% of the load rated reactive power (+ 45 kVAr). (b) Temporal zoom in the time interval $t \in [0.999, 1.01]$ s.

and V_{PCCq} within a 10-ms interval consequent to the disturbance, the active power of the diesel engine generator system output P_g and the load P_{load} fluctuate considerably, however they return nearly to their initial values after 10 ms of disturbance; whereas the output active power of the ESS step-up transformer P_t and the PV system P_{PV} present slight fluctuations around their initial values within this interval.

Figure 3.21 shows the time-domain responses of the reactive power variations of the sources and load. In a similar way, one can see that the reactive power of the diesel engine generator system output Q_g and the load Q_{load} present dramatic fluctuations resulting from large variations in U_{PCC} , V_{PCCd} , and V_{PCCq} within a 10-ms interval subsequent to the disturbance; whereas the output reactive power of the ESS step-up transformer Q_t and the PV system Q_{PV} fluctuate slightly around their initial values within this interval. Moreover, the ESS participation in primary voltage control has reduced the reactive power variation of the diesel generator around the steady-state point after the disturbance, as shown in Figure 3.21(a).

Effectiveness of the proposed “analysis-of-zeros” method

Figure 3.22 presents a comparison of the closed-loop time-domain responses of the PCC line-to-line voltage magnitude U_{PCC} obtained with both nominal, as well as aforecomputed sets of MG parameter values in the proposed “analysis-of-zeros” method in Subsection 3.4.2. Analogous to the open-loop time-domain simulation results presented in Subsection 3.4.2, it can be observed that the undesired dynamic effects (*e.g.*, non-minimum phase behavior, oscillation) displayed in the variation ΔU_{PCC} in response to the disturbance input variation ΔI_{loadq} (or ΔQ_{load}) still exist in the closed-loop system, which means that the proposed control design procedure cannot alter the natural properties of the system. However, the dynamic performance of ΔU_{PCC} in terms of oscillation amplitude, performed with the desired set of

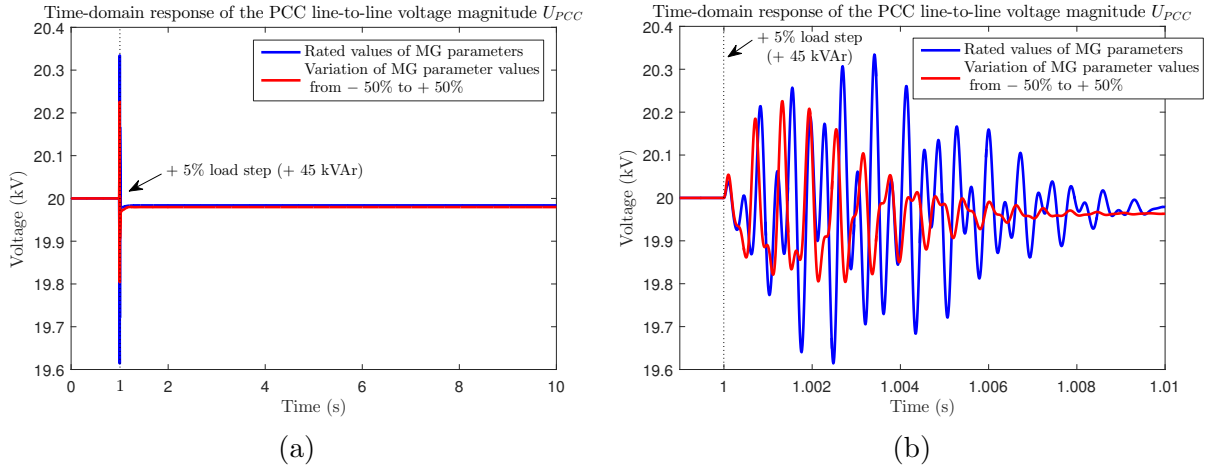


Figure 3.22 – (a) Time-domain response of the PCC line-to-line voltage magnitude U_{PCC} under a small load step disturbance of + 5% of the load rated reactive power (+ 45 kVAr) with respect to the rated operating point. (b) Temporal zoom in the time interval $t \in [0.999, 1.01]$ s.

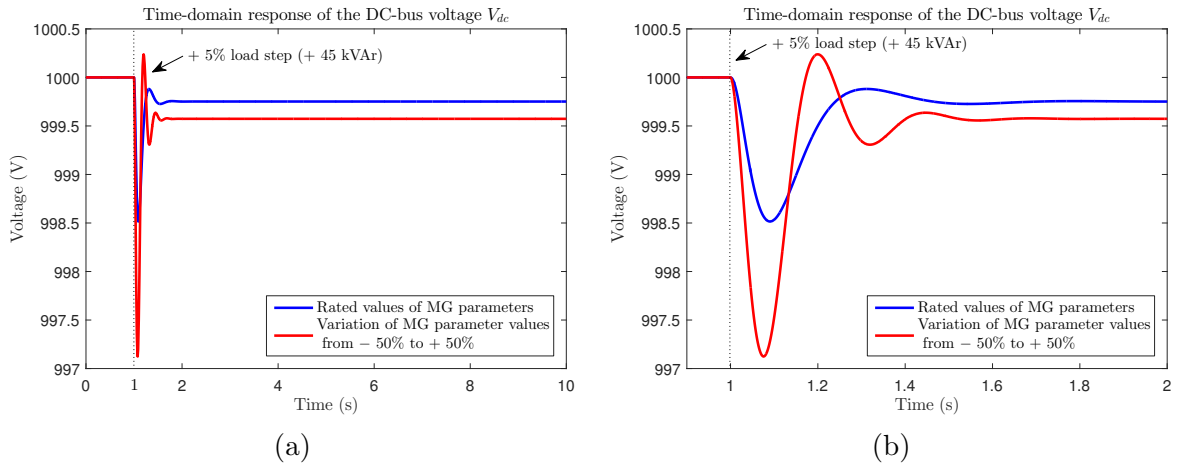


Figure 3.23 – (a) Time-domain response of the DC-bus voltage V_{dc} under a small load step disturbance of + 5% of the load rated reactive power (+ 45 kVAr) with respect to the rated operating point. (b) Temporal zoom in the time interval $t \in [0.9, 2]$ s.

the MG parameter values, has significantly been improved compared to that obtained with the rated values of the MG parameters, as shown in Figure 3.22. This shows once again the validity and effectiveness of the proposed “analysis-of-zeros” method.

The time-domain response of the DC-bus voltage V_{dc} performed with both nominal and desired sets of MG parameter values is depicted in Figure 3.23. It can be seen that the dynamic performance specification imposed on V_{dc} corresponding to the choice of the weighting function $W_{perf_1}(s)$ is well respected for both cases. Therefore, we can come to the conclusion that the \mathcal{H}_∞ controller synthesized with the rated values of MG parameters ensures the desired performance specifications. Let us remark here that, with the variation of MG parameters from -50% to $+50\%$ of their rated values, the time-domain response of V_{dc} presents a higher

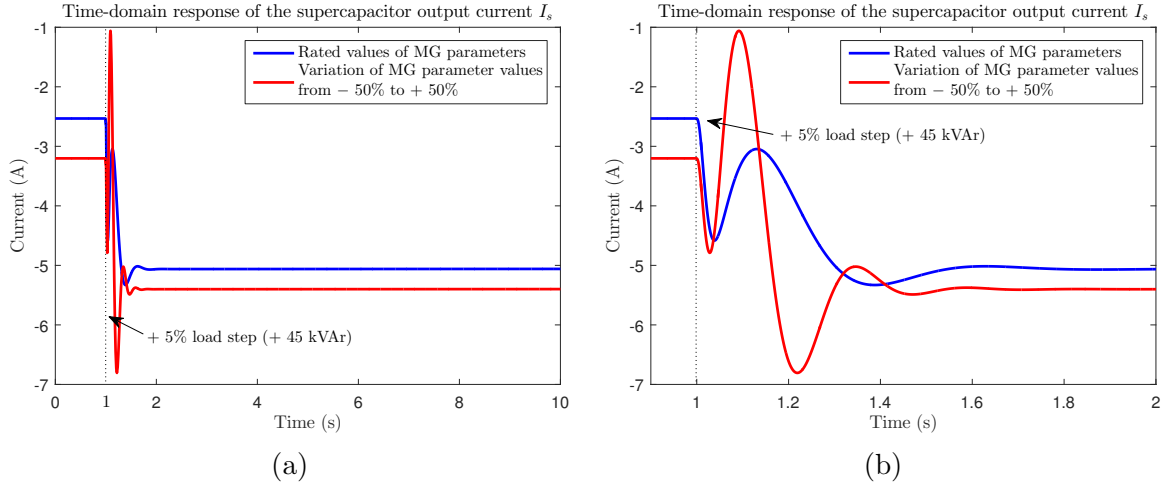


Figure 3.24 – (a) Time-domain response of the supercapacitor output current I_s under a small load step disturbance of + 5% of the load rated reactive power (+ 45 kVAr) with respect to the rated operating point. (b) Temporal zoom in the time interval $t \in [0.9, 2]$ s.

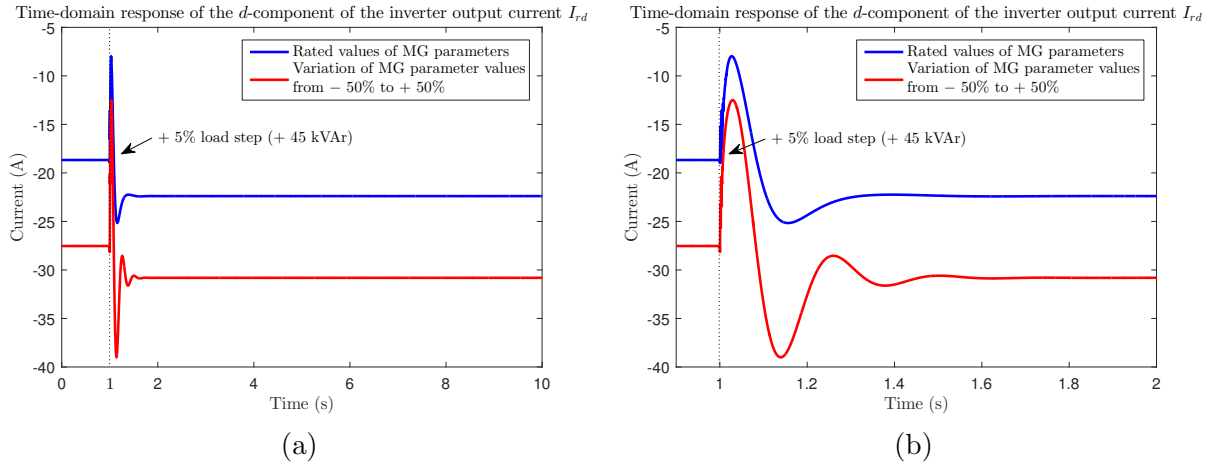


Figure 3.25 – (a) Time-domain response of the d -component of the inverter output current I_{rd} under a small load step disturbance of + 5% of the load rated reactive power (+ 45 kVAr) with respect to the rated operating point. (b) Temporal zoom in the time interval $t \in [0.9, 2]$ s.

overshoot and steady-state error. This can be explained due to a decrease in the value of the DC-bus capacitor C_{dc} from its rated value, as shown in Table 3.8.

Figure 3.24, Figure 3.25, and Figure 3.26 show the time-domain responses of the supercapacitor output current I_s and the direct and quadrature components of the inverter output current I_{rd} and I_{rq} , respectively, obtained with both nominal and desired sets of MG parameter values. It can be seen that, for both cases, the admissible limit is guaranteed for these currents with respect to the choice of the weighting functions $W_u(s)$, which means that their imposed dynamic performance specifications are well satisfied.

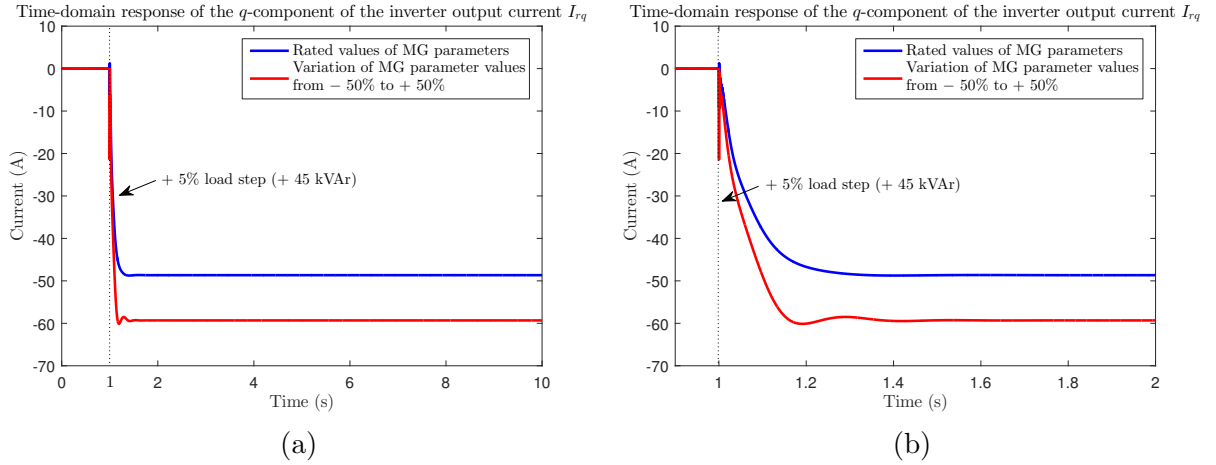


Figure 3.26 – (a) Time-domain response of the q -component of the inverter output current I_{rq} under a small load step disturbance of + 5% of the load rated reactive power (+ 45 kVAr) with respect to the rated operating point. (b) Temporal zoom in the time interval $t \in [0.9, 2]$ s.

3.6 Robust performance analysis

This section details a robust performance analysis of the \mathcal{H}_∞ controller, which was designed in the previous section while the system parameters are fixed at their rated values. First, the uncertainties in the steady-state value of the supercapacitor state of charge SoC_{sc_e} (or supercapacitor voltage V_{sc_e}) and the length of the transmission line l connecting the diesel engine generator to the PCC are considered. Then, a sensitivity analysis is performed so as to determine the maximum variation ranges of the values SoC_{sc_e} (or V_{sc_e}) and l for which the imposed closed-loop performances are guaranteed. Next, a series of MATLAB[®]/Simulink[®] closed-loop time-domain simulations are presented to validate the controller robustness and performance in the presence of various load disturbances and the uncertainties in SoC_{sc_e} and l .

3.6.1 Parametric uncertainties

In the case of the studied hybrid system, uncertainties could be associated first with the parameters of the ESS but could also be representative of the variation in the steady-state value of the supercapacitor state of charge SoC_{sc_e} (or supercapacitor voltage V_{sc_e}). They could also represent changes in the parameters of the diesel engine generator system (inductor L_{tg} and resistor R_{tg} of the step-up transformer; inductor L_l , resistor R_l , capacitor C_l , and parallel resistor R_{lp} of the transmission line). This results in changes in the steady-state operating point of the system.

Let us note that only the uncertainties in SoC_{sc_e} (or V_{sc_e}) and L_l , R_l , C_l , and R_{lp} (due to the change in the length of the transmission line l) are taken into account in the below sensitivity analysis. In order to ensure reliable, efficient, and safe operation of the supercapacitor

and prolong its lifespan, an admissible range of $[25, 100]\%$ should practically be required for SoC_{sc} . The limited variation range, corroborated with the equation for SoC estimation in (2.100), points out that the V_{sc} value must be controlled between 390 V and 780 V. The midrange between these two values, *i.e.*, $V_{sc} = 585$ V, is a suitable choice for designing the nominal \mathcal{H}_∞ controller whose robustness is further assessed. Moreover, the minimum value of the transmission line length $l = l_{min} = 1$ km is chosen for \mathcal{H}_∞ control design, where 10 km is the maximum value of l . This maximum value is limited at 10 km so as to ensure the voltage drop on the transmission line at the high-voltage level of 20 kV being less than or equal to the admissible limit of 8% of the rated voltage.

3.6.2 Sensitivity analysis

This subsection is devoted to the sensitivity analysis of robust performance of the synthesized \mathcal{H}_∞ controller to answer the question whether the closed-loop system remains robust or not (from a performance point of view) to a given parametric uncertainty level in the steady-state value of the supercapacitor voltage V_{sc_e} around its design value, 585 V, or to the variation in the transmission line length l from 1 to 10 km.

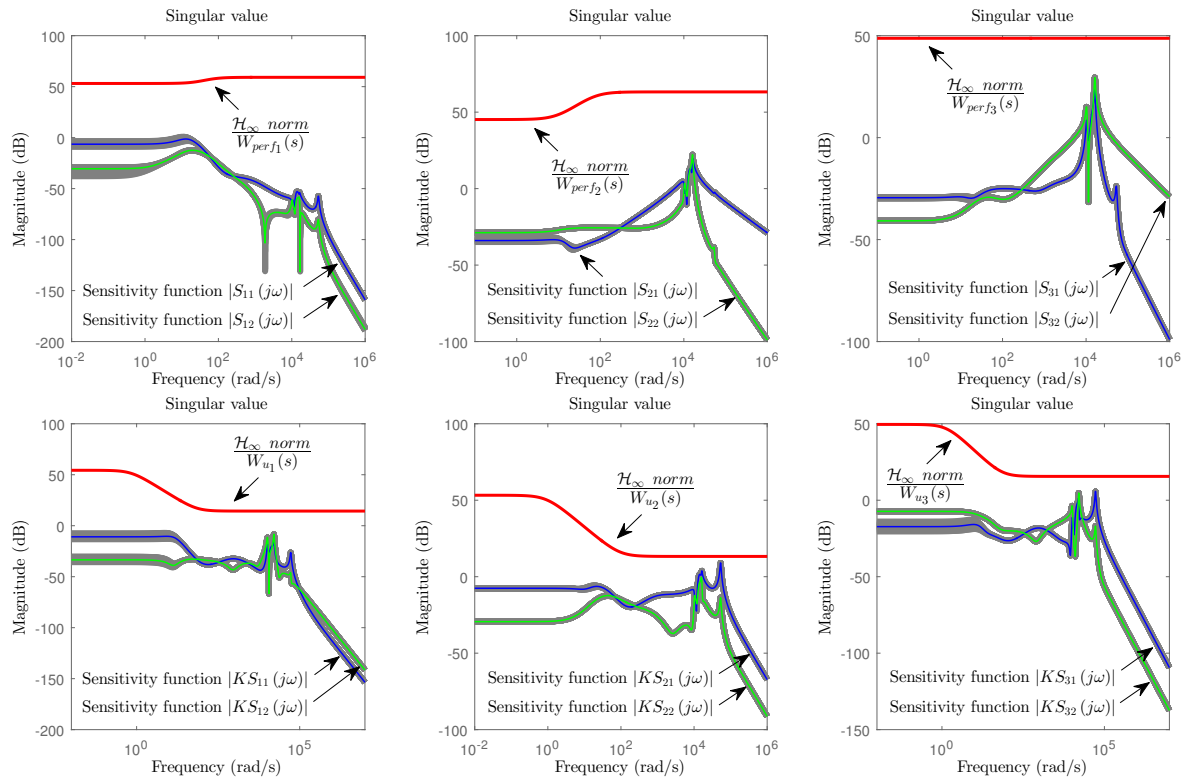


Figure 3.27 – Singular value plots of the sampled uncertain sensitivity functions $S_{11}(s)$, $S_{12}(s)$, $S_{21}(s)$, $S_{22}(s)$, $S_{31}(s)$, $S_{32}(s)$; complementary sensitivity functions $KS_{11}(s)$, $KS_{12}(s)$, $KS_{21}(s)$, $KS_{22}(s)$, $KS_{31}(s)$, $KS_{32}(s)$ obtained with 33.3% uncertainty in V_{sc_e} and $l \in [1, 10]$ km; and corresponding templates.

Figure 3.27 depicts the sampled uncertain sensitivity functions $S(s)$, complementary sensitivity functions $KS(s)$, obtained with 33.3% uncertainty in V_{sc_e} around its design value, 585 V (*i.e.*, $SoC_{sc_e} \in [25, 100]\%$ or $V_{sc_e} \in [390, 780]$ V) and $l \in [1, 10]$ km, together with the corresponding templates of the closed-loop system performed with the \mathcal{H}_∞ norm = 40.71. It can be seen that these functions are well placed below the corresponding weights regardless of the parametric uncertainties in V_{sc_e} and l , which means that the imposed overshoot performance specifications are satisfied.

Without loss of generality, MATLAB[®]/Simulink[®] closed-loop time-domain simulations using the nonlinear averaged model are performed with load step changes of + 5% of the quadrature component of the load rated current I_{loadq_e} (*i.e.*, -2.25 A) at $t = 1$ s, - 5% at $t = 9$ s, - 5% at $t = 17$ s, and + 5% at $t = 25$ s, whereas the direct component of the load current variation is regarded to be approximately equal to zero, *i.e.*, $\Delta I_{loadd} \approx 0$, which corresponds to load step changes of $\pm 5\%$ of the load rated reactive power (*i.e.*, ± 45 kVAr). The supercapacitor voltage V_{sc} appears as a time-variant parameter (*i.e.*, $\Delta V_{sc} \neq 0$) in the simulation model. The initial value of SoC_{sc} is varied between 25% and 100% in simulation. The length of the transmission line l is changed between 1 and 10 km.

Uncertainty in the supercapacitor state of charge SoC_{sc_e}

Figure 3.28, Figure 3.29, Figure 3.30, and Figure 3.31 present the time-domain responses of the PCC line-to-line voltage magnitude U_{PCC} , the direct and quadrature components of the PCC voltage V_{PCCd} and V_{PCCq} , and the DC-bus voltage V_{dc} , respectively, taking into account the uncertainty in V_{sc_e} (or SoC_{sc_e}), where the transmission line length is fixed at $l = 1$ km. Let us note here that the five curves in each above mentioned figure are practically

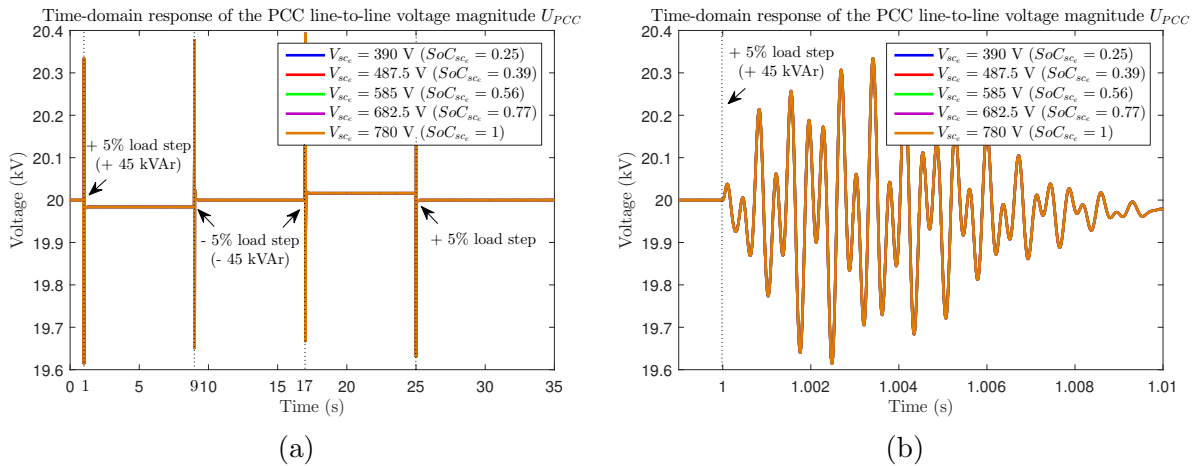


Figure 3.28 – (a) Time-domain response of the PCC line-to-line voltage magnitude U_{PCC} under small load step disturbances of $\pm 5\%$ of the load rated reactive power (± 45 kVAr) taking into account the uncertainty in V_{sc_e} (or SoC_{sc_e}). (b) Temporal zoom in the time interval $t \in [0.999, 1.01]$ s.

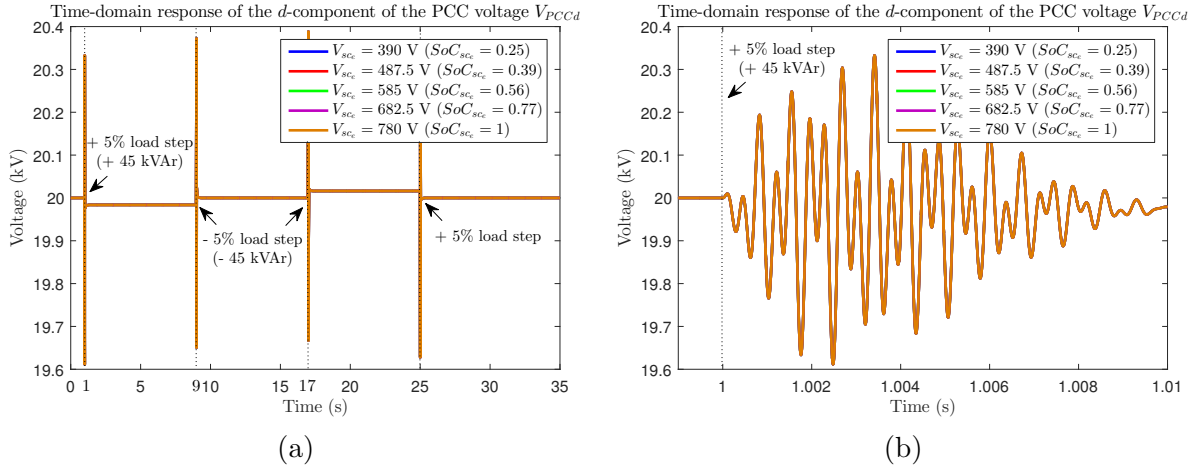


Figure 3.29 – (a) Time-domain response of the d -component of the PCC voltage V_{PCCd} under small load step disturbances of $\pm 5\%$ of the load rated reactive power (± 45 kVAr) taking into account the uncertainty in V_{sc_e} (or SoC_{sc_e}). (b) Temporal zoom in the time interval $t \in [0.999, 1.01]$ s.

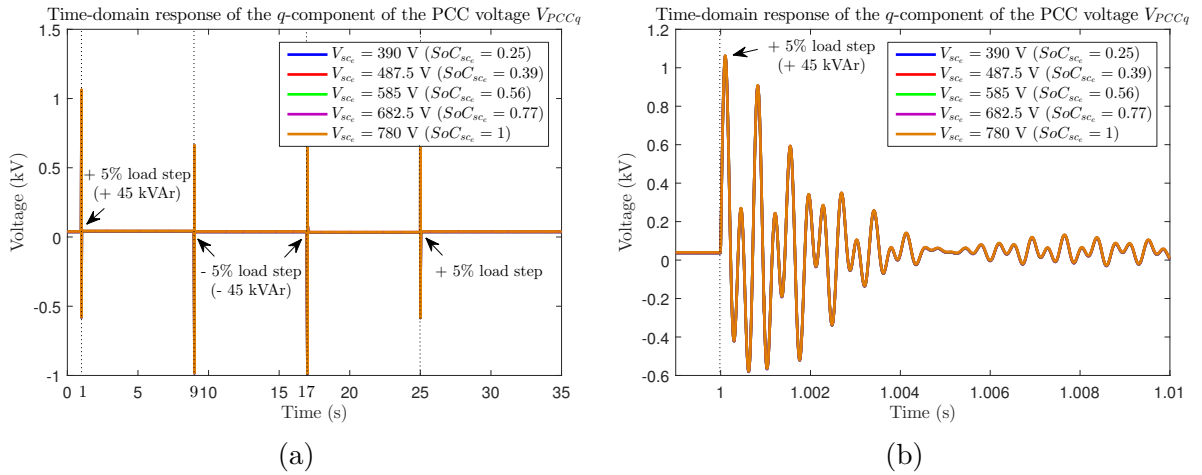


Figure 3.30 – (a) Time-domain response of the q -component of the PCC voltage V_{PCCq} under small load step disturbances of $\pm 5\%$ of the load rated reactive power (± 45 kVAr) taking into account the uncertainty in V_{sc_e} (or SoC_{sc_e}). (b) Temporal zoom in the time interval $t \in [0.999, 1.01]$ s.

superposed. As predicted by analyzing the sampled uncertain sensitivity functions $S(s)$ and corresponding templates in Figure 3.27, as well as seen in the above mentioned figures, the imposed closed-loop overshoot performances of U_{PCC} , V_{PCCd} , V_{PCCq} , and V_{dc} , with respect to the choice of the weighting functions $W_{perf}(s)$, are preserved regardless of the initial value of SoC_{sc_e} . Hence, the synthesized \mathcal{H}_∞ controller is robust in performance to $SoC_{sc_e} \in [25, 100]\%$ (or $V_{sc_e} \in [390, 780]$ V).

The time-domain responses of the supercapacitor output current I_s and the direct and

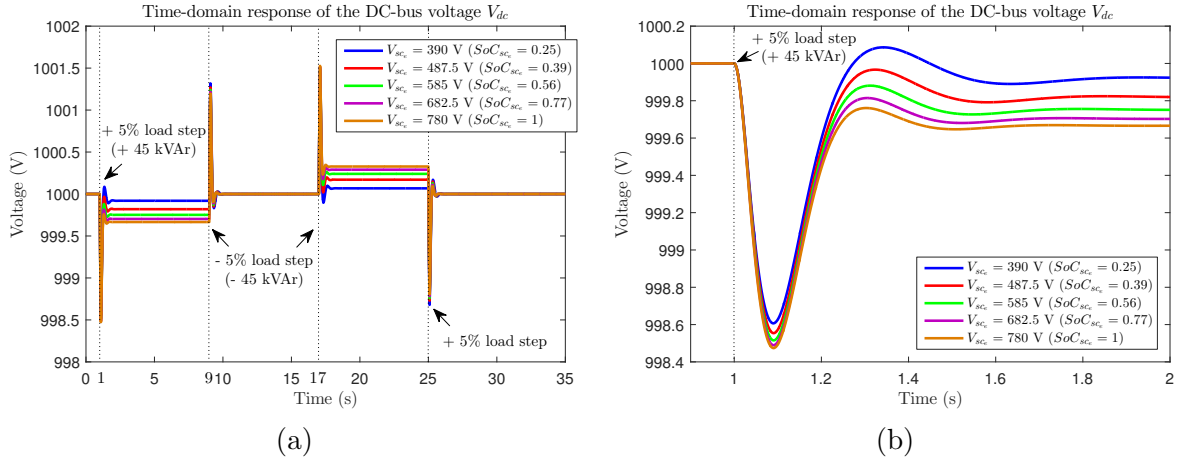


Figure 3.31 – (a) Time-domain response of the DC-bus voltage V_{dc} under small load step disturbances of $\pm 5\%$ of the load rated reactive power (± 45 kVAr) taking into account the uncertainty in V_{sc_e} (or SoC_{sc_e}). (b) Temporal zoom in the time interval $t \in [0.9, 2]$ s.

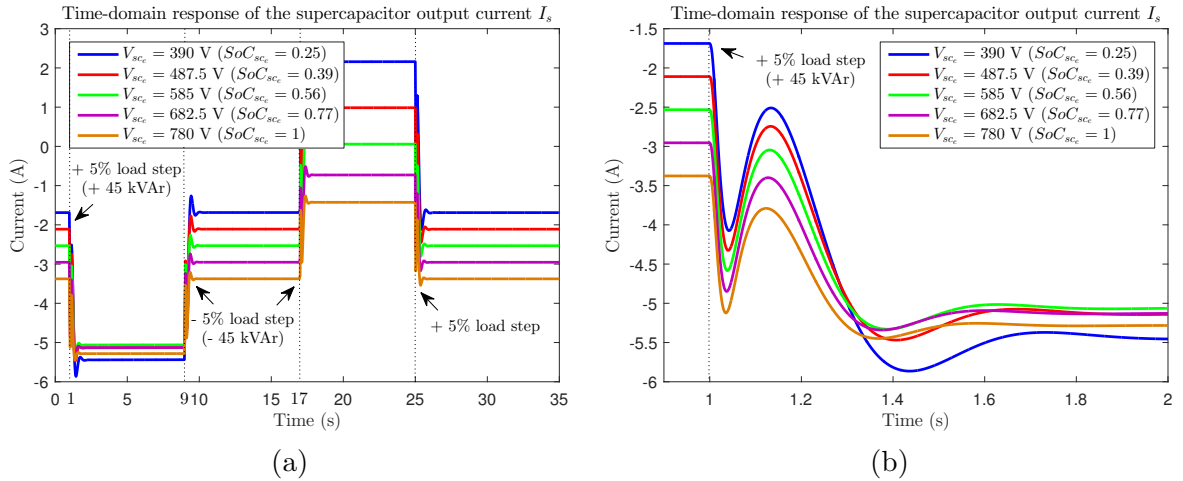


Figure 3.32 – (a) Time-domain response of the supercapacitor output current I_s under small load step disturbances of $\pm 5\%$ of the load rated reactive power (± 45 kVAr) taking into account the uncertainty in V_{sc_e} (or SoC_{sc_e}). (b) Temporal zoom in the time interval $t \in [0.9, 2]$ s.

quadrature components of the inverter output current I_{rd} and I_{rq} taking into account the uncertainty in V_{sc_e} (or SoC_{sc_e}) are given in Figure 3.32, Figure 3.33, and Figure 3.34, respectively. Similarly, as anticipated by analyzing the sampled uncertain complementary sensitivity functions $KS(s)$ and corresponding templates in Figure 3.27, as well as depicted in the aforementioned figures, the admissible limit is ensured for these currents with respect to the choice of the weighting functions $W_u(s)$, which means that their imposed dynamic performances are fulfilled.

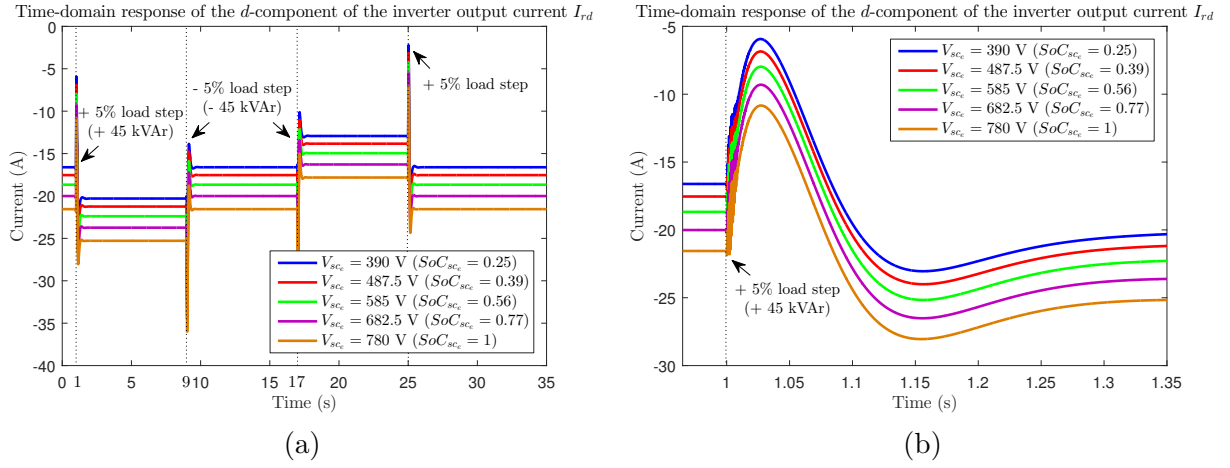


Figure 3.33 – (a) Time-domain response of the d -component of the inverter output current I_{rd} under small load step disturbances of $\pm 5\%$ of the load rated reactive power (± 45 kVAR) taking into account the uncertainty in V_{sc_e} (or SoC_{sc_e}). (b) Temporal zoom in the time interval $t \in [0.965, 1.35]$ s.

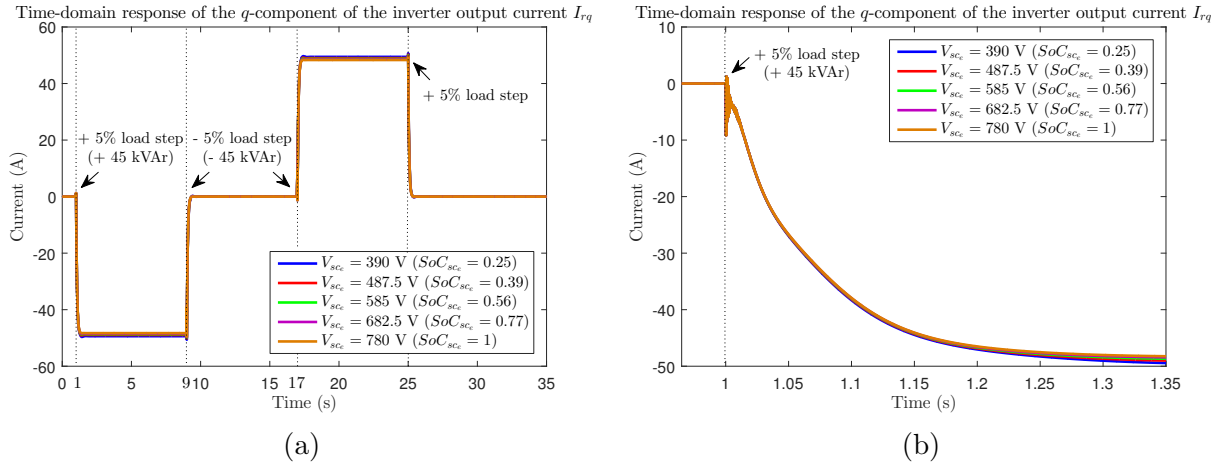


Figure 3.34 – (a) Time-domain response of the q -component of the inverter output current I_{rq} under small load step disturbances of $\pm 5\%$ of the load rated reactive power (± 45 kVAR) taking into account the uncertainty in V_{sc_e} (or SoC_{sc_e}). (b) Temporal zoom in the time interval $t \in [0.965, 1.35]$ s.

Uncertainty in the transmission line length l

The time-domain responses of the PCC line-to-line voltage magnitude U_{PCC} , the direct and quadrature components of the PCC voltage V_{PCCd} and V_{PCCq} , and the DC-bus voltage V_{dc} , taking into account the uncertainty in l , where the steady-state value of the supercapacitor voltage is chosen at $V_{sc_e} = 585$ V (or supercapacitor state of charge $SoC_{sc_e} = 0.56$), are illustrated in Figure 3.35, Figure 3.36, Figure 3.37, and Figure 3.38, respectively. As envisaged in the analysis of the sampled uncertain sensitivity functions $S(s)$ and corresponding templates

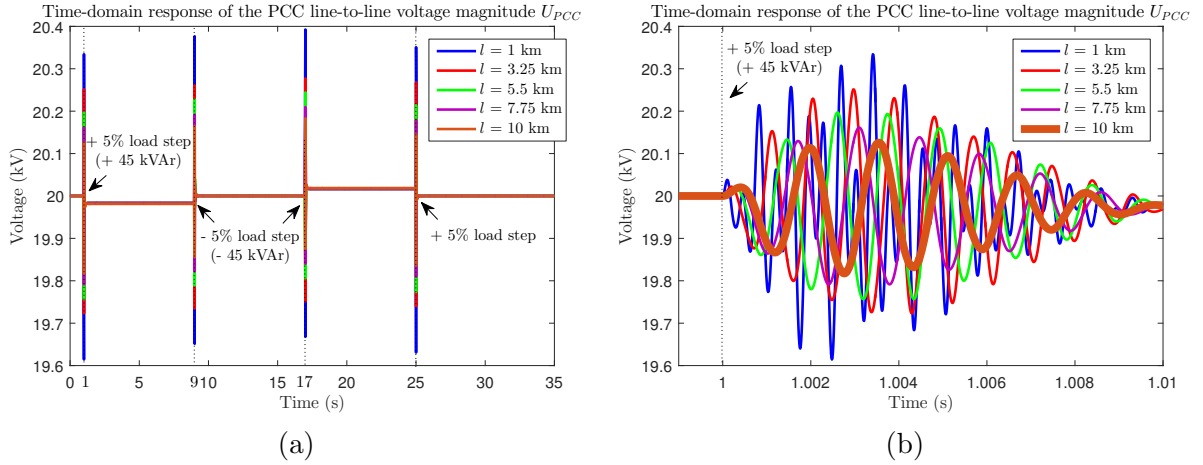


Figure 3.35 – (a) Time-domain response of the PCC line-to-line voltage magnitude U_{PCC} under small load step disturbances of $\pm 5\%$ of the load rated reactive power (± 45 kVAR) taking into account the uncertainty in l . (b) Temporal zoom in the time interval $t \in [0.999, 1.01]$ s.

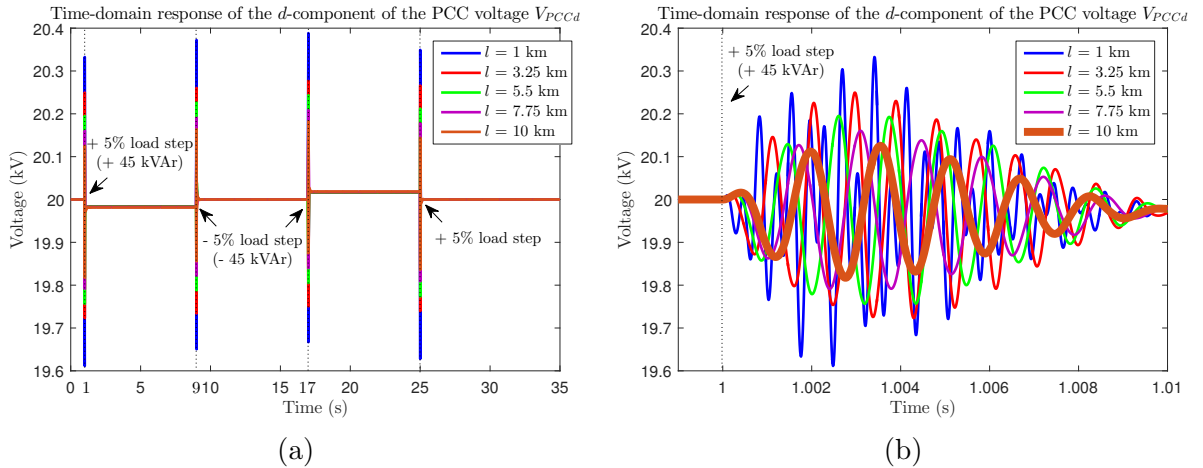


Figure 3.36 – (a) Time-domain response of the d -component of the PCC voltage V_{PCCd} under small load step disturbances of $\pm 5\%$ of the load rated reactive power (± 45 kVAR) taking into account the uncertainty in l . (b) Temporal zoom in the time interval $t \in [0.999, 1.01]$ s.

in Figure 3.27, as well as observed from the previously mentioned figures, the imposed closed-loop overshoot performances of U_{PCC} , V_{PCCd} , V_{PCCq} , and V_{dc} , corresponding to the tuning of the weighting functions $W_{perf}(s)$, are maintained irrespective of the value of l . Therefore, the designed \mathcal{H}_∞ controller is demonstrated to be robust in performance to $l \in [1, 10]$ km. Let us remark here that the longer the length of the transmission line l is, the more damped the oscillations of U_{PCC} , V_{PCCd} , and V_{PCCq} are, as shown in Figure 3.35, Figure 3.36, and Figure 3.37, respectively. This can be explained due to the fact that if the length of the transmission line is increased, its resistance value is therefore higher, which induces a rise in the damping coefficient of the system.

Figure 3.39, Figure 3.40, and Figure 3.41 show the time-domain responses of the superca-

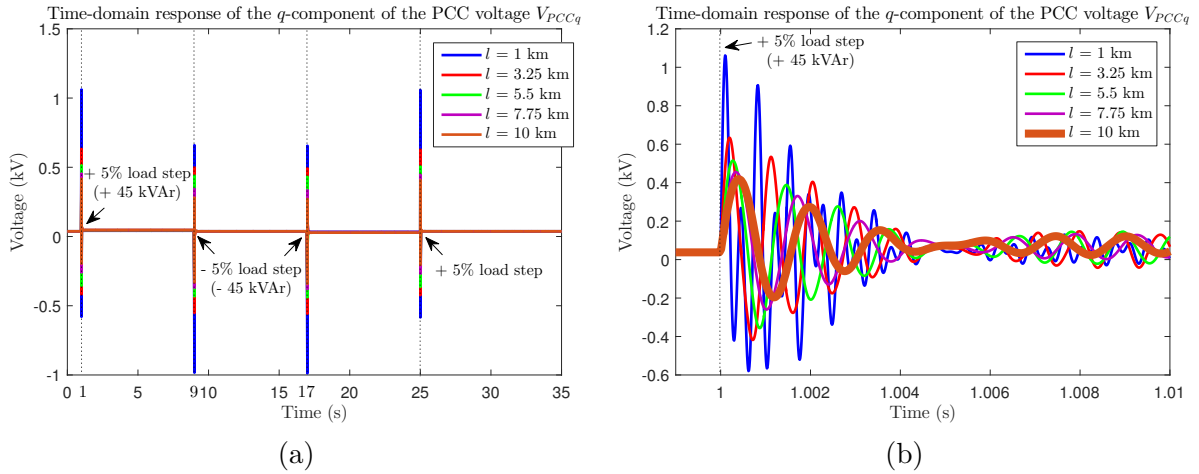


Figure 3.37 – (a) Time-domain response of the q -component of the PCC voltage V_{PCCq} under small load step disturbances of $\pm 5\%$ of the load rated reactive power (± 45 kVAr) taking into account the uncertainty in l . (b) Temporal zoom in the time interval $t \in [0.999, 1.01]$ s.

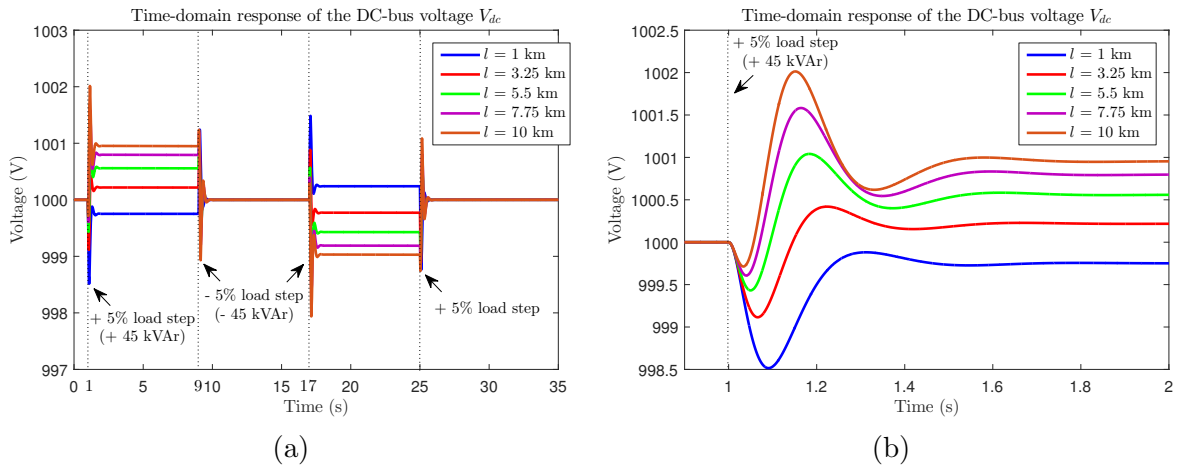


Figure 3.38 – (a) Time-domain response of the DC-bus voltage V_{dc} under small load step disturbances of $\pm 5\%$ of the load rated reactive power (± 45 kVAr) taking into account the uncertainty in l . (b) Temporal zoom in the time interval $t \in [0.9, 2]$ s.

pacitor output current I_s and the direct and quadrature components of the inverter output current I_{rd} and I_{rq} , respectively, taking into account the uncertainty in l . Similarly, as foreseen in the analysis of the sampled uncertain complementary sensitivity functions $KS(s)$ and corresponding templates in Figure 3.27, as well as shown in the aforementioned figures, the admissible limit is guaranteed for these currents corresponding to the tuning of the weighting functions $W_u(s)$, which means that their imposed dynamic performances are satisfied.

Figure 3.42 presents the time-domain responses of the supercapacitor state of charge SoC_{sc} and voltage V_{sc} . Consequent to small load step disturbances of $\pm 5\%$ of the load rated reactive power (± 45 kVAr), these values tend to increase or decrease linearly and quite slowly since

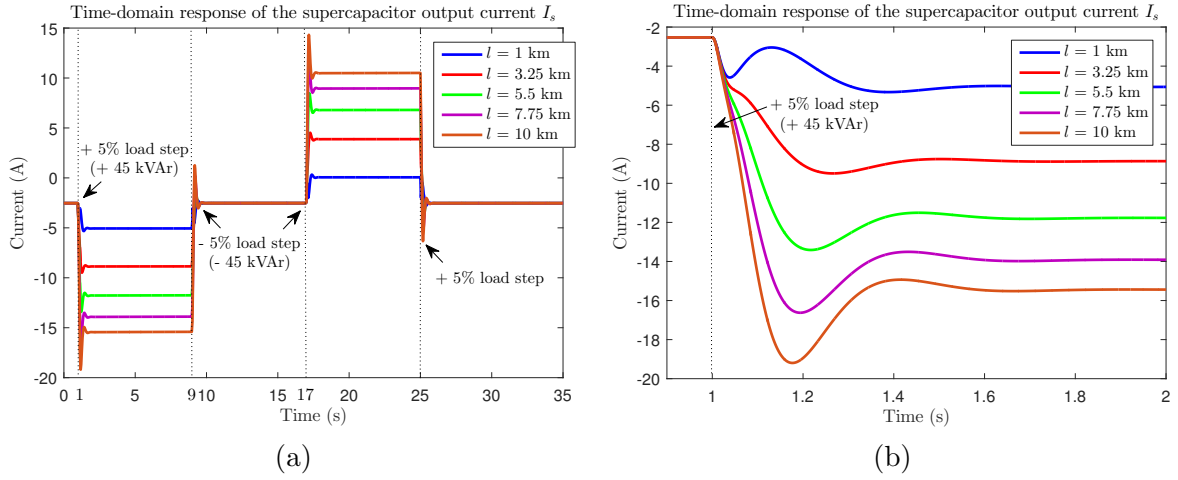


Figure 3.39 – (a) Time-domain response of the supercapacitor output current I_s under small load step disturbances of $\pm 5\%$ of the load rated reactive power (± 45 kVAR) taking into account the uncertainty in l . (b) Temporal zoom in the time interval $t \in [0.9, 2]$ s.

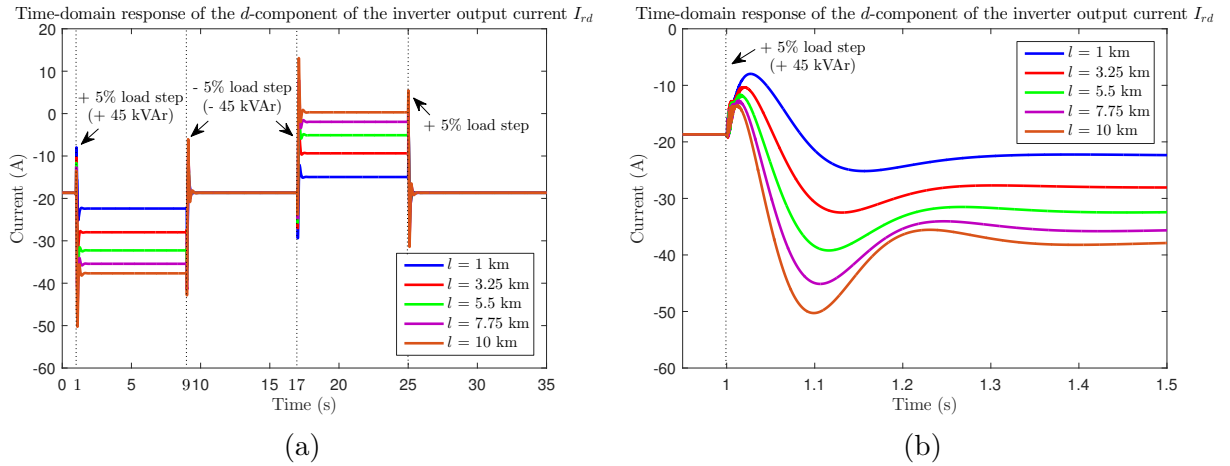


Figure 3.40 – (a) Time-domain response of the d -component of the inverter output current I_{rd} under small load step disturbances of $\pm 5\%$ of the load rated reactive power (± 45 kVAR) taking into account the uncertainty in l . (b) Temporal zoom in the time interval $t \in [0.95, 1.5]$ s.

the steady-state value of I_s is only slightly lower or higher than its initial value, as observed from Figure 3.39, which means that the supercapacitor is in slightly charging or discharging mode.

The time-domain responses of the active power variations of the ESS step-up transformer output ΔP_t and the diesel engine generator system output $\Delta P_g - (U_{PCC}^2 - U_{PCC_e}^2)/R_{l_p}$ are depicted in Figure 3.43 and Figure 3.44, respectively. It can be seen that, due to large oscillations in U_{PCC} , V_{PCC_d} , and V_{PCC_q} within a 10-ms interval in response to the disturbance, as shown in Figure 3.35, Figure 3.36, and Figure 3.37, respectively, there is a dramatic

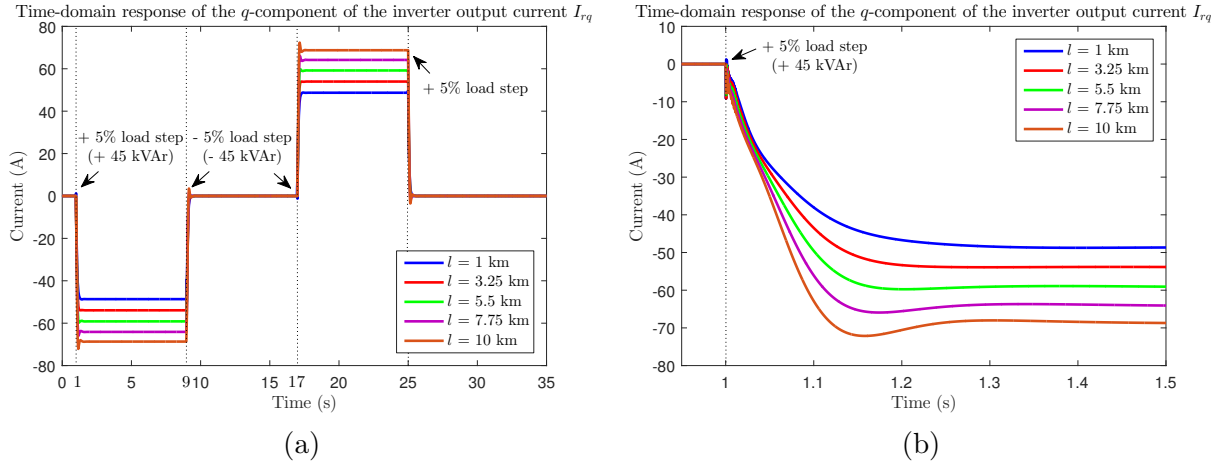


Figure 3.41 – (a) Time-domain response of the q -component of the inverter output current I_{rq} under small load step disturbances of $\pm 5\%$ of the load rated reactive power (± 45 kVAR) taking into account the uncertainty in l . (b) Temporal zoom in the time interval $t \in [0.95, 1.5]$ s.

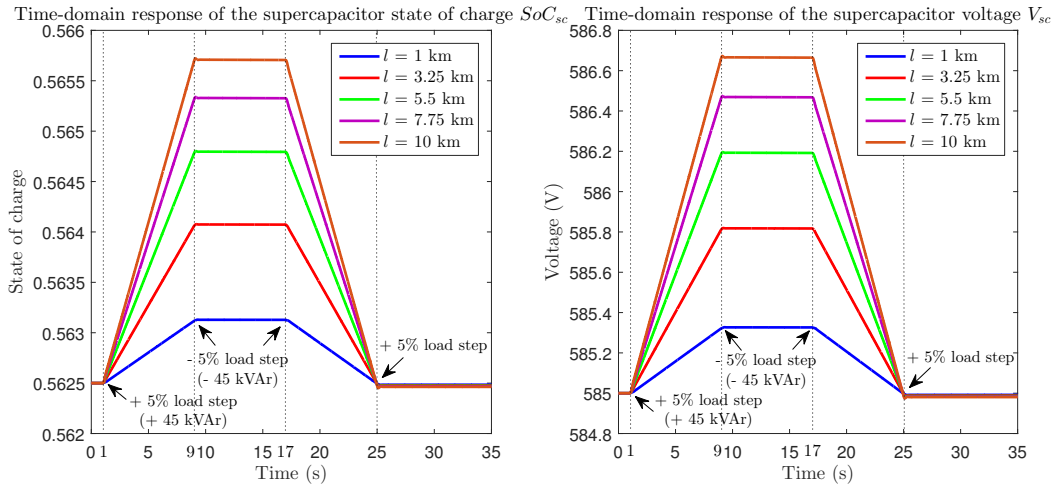


Figure 3.42 – Time-domain responses of the supercapacitor state of charge SoC_{sc} and voltage V_{sc} under small load step disturbances of $\pm 5\%$ of the load rated reactive power (± 45 kVAR) taking into account the uncertainty in l .

fluctuation in the active power of the diesel engine generator system output P_g , nevertheless it returns nearly to its initial value after 10 ms of disturbance; whereas the active power of the ESS step-up transformer output P_t presents a slight fluctuation around its initial value within this interval.

Figure 3.45 and Figure 3.46 depict the time-domain responses of the reactive power variations of the ESS step-up transformer output ΔQ_t and the diesel engine generator system output $\Delta Q_g + (U_{PCC}^2 - U_{PCC_e}^2) C_l \omega_{grid}$. In a similar way, one can see that the reactive power of the diesel engine generator system output Q_g presents a considerable fluctuation which is

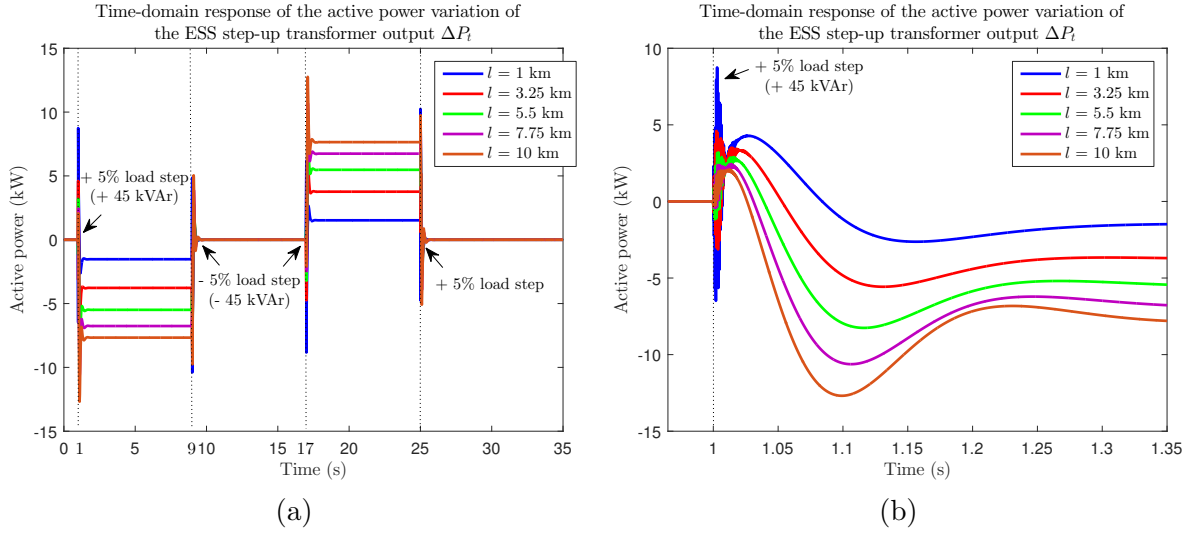


Figure 3.43 – (a) Active power variation of the ESS step-up transformer output ΔP_t under small load step disturbances of $\pm 5\%$ of the load rated reactive power (± 45 kVAr) taking into account the uncertainty in l . (b) Temporal zoom in the time interval $t \in [0.965, 1.35]$ s.

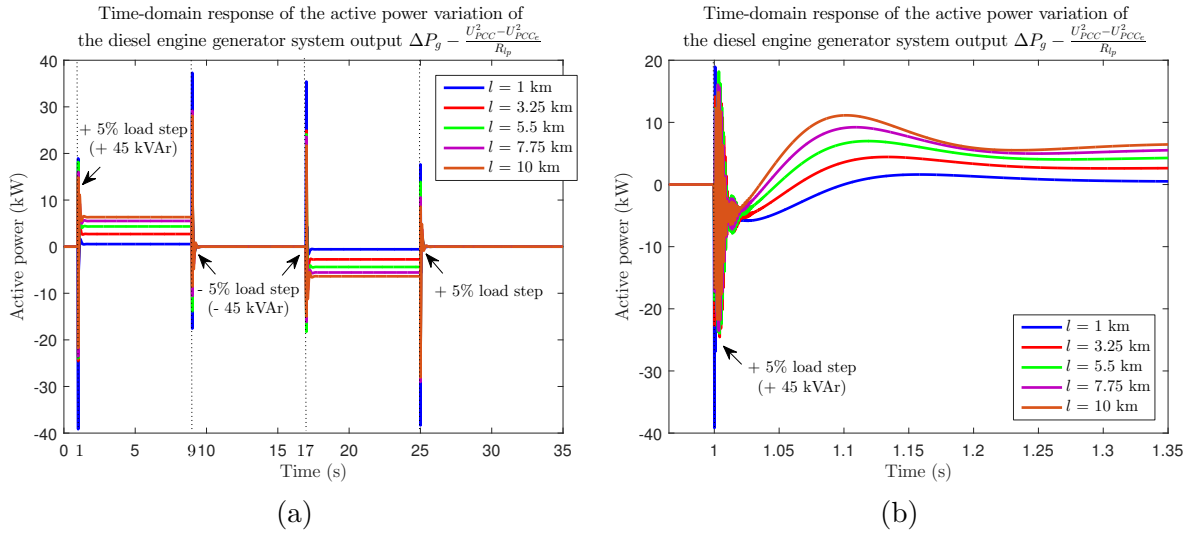


Figure 3.44 – (a) Active power variation of the diesel engine generator system output $\Delta P_g - (U_{PCC}^2 - U_{PCC_e}^2) / R_{lp}$ under small load step disturbances of $\pm 5\%$ of the load rated reactive power (± 45 kVAr) taking into account the uncertainty in l . (b) Temporal zoom in the time interval $t \in [0.965, 1.35]$ s.

caused by large oscillations in U_{PCC} , V_{PCCd} , and V_{PCCq} within a 10-ms interval subsequent to the disturbance, as shown in Figure 3.35, Figure 3.36, and Figure 3.37, respectively; whereas the reactive power of the ESS step-up transformer output Q_t fluctuates slightly around its initial value within this interval. In addition, the ESS participation in primary voltage control has decreased the reactive power variation of the diesel generator around the steady-state point after the disturbance, as seen in Figure 3.45 and Figure 3.46. It should be noted here

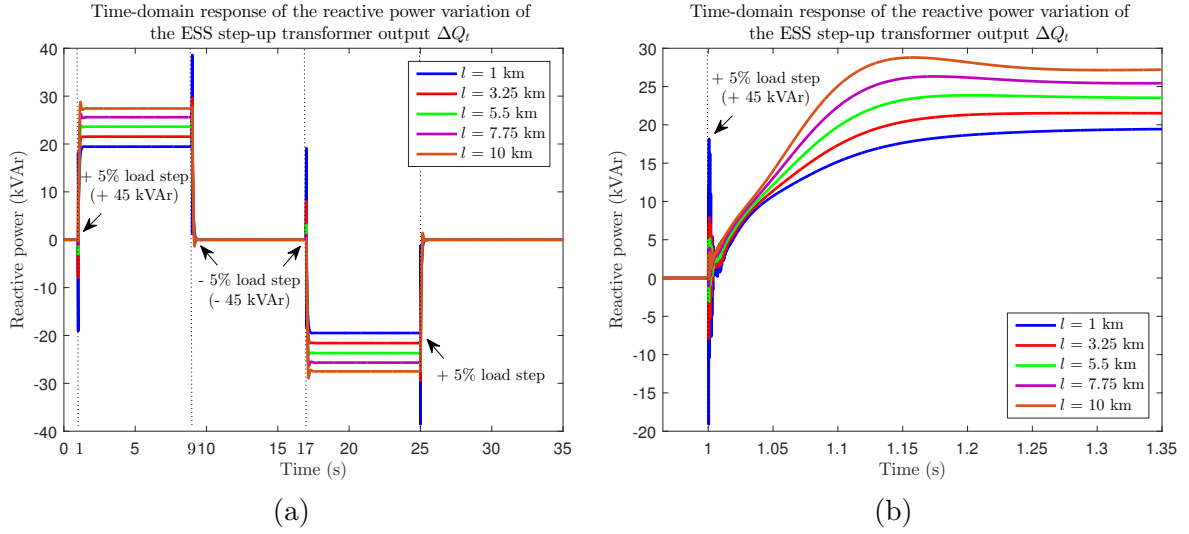


Figure 3.45 – (a) Reactive power variation of the ESS step-up transformer output ΔQ_t under small load step disturbances of $\pm 5\%$ of the load rated reactive power (± 45 kVAr) taking into account the uncertainty in l . (b) Temporal zoom in the time interval $t \in [0.965, 1.35]$ s.

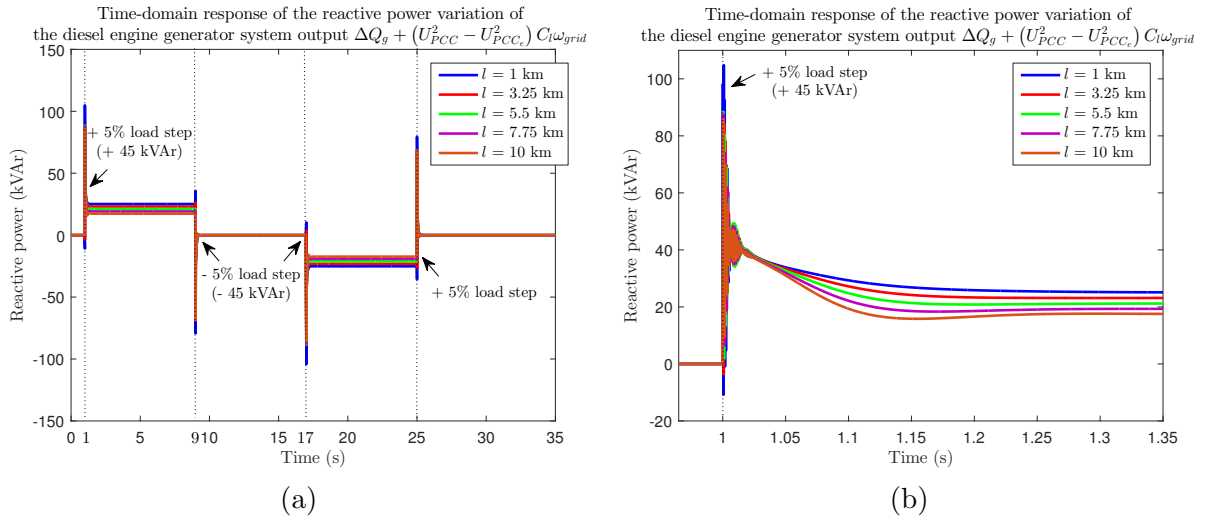


Figure 3.46 – (a) Reactive power variation of the diesel engine generator system output $\Delta Q_g + (U_{PCC}^2 - U_{PCC_e}^2) C_l \omega_{grid}$ under small load step disturbances of $\pm 5\%$ of the load rated reactive power (± 45 kVAr) taking into account the uncertainty in l . (b) Temporal zoom in the time interval $t \in [0.965, 1.35]$ s.

that the longer the length of the transmission line l is, the higher the reactive power variation of the ESS step-up transformer output ΔQ_t is and the lower the reactive power variation of the diesel engine generator system output $\Delta Q_g + (U_{PCC}^2 - U_{PCC_e}^2) C_l \omega_{grid}$ is, around their initial values after the disturbance.

3.7 Chapter conclusion

In this chapter, we have presented voltage-control-oriented modeling for the diesel-PV-storage hybrid power generation system operating in stand-alone mode. In particular, topological, as well as nonlinear and linear averaged models of each subsystem have first been provided, then a voltage-control-oriented model of the whole system has been obtained by aggregating these sub-models. We have also studied the influence of system parameters on the dynamic behavior of open-loop system measured outputs by means of an “analysis-of-zeros” method based on Monte Carlo simulation. Next, a voltage robust control design approach based on a cascaded two-level control structure – where classical PI-based current tracking controllers are placed on the low control level and receive references from an \mathcal{H}_∞ -control-based upper level – has been developed in order to satisfy the required dynamic specifications. Effectiveness of the proposed voltage robust control strategy, as well as the “analysis-of-zeros” method have been validated *via* MATLAB[®]/Simulink[®] closed-loop time-domain simulations. Finally, we have performed a sensitivity analysis of robust performance of the synthesized \mathcal{H}_∞ controller to a given parametric uncertainty level in the steady-state value of the supercapacitor state of charge SoC_{sc_e} (or supercapacitor voltage V_{sc_e}) or to the variation in the transmission line length l connecting the diesel engine generator to the PCC. Through a series of MATLAB[®]/Simulink[®] closed-loop time-domain simulations in the presence of various load disturbances, it has been pointed out that the synthesized \mathcal{H}_∞ controller remains robust in performance to a large uncertainty in the initial value of SoC_{sc} (in particular $SoC_{sc_e} \in [25, 100] \%$), as well as to the uncertainty in l (in particular $l \in [1, 10]$ km).

Frequency robust control real-time validation using a rapid-prototyping test bench

4.1 Introduction

This chapter presents the experimental validation of the frequency robust control strategy in stand-alone MGs which was previously proposed and tested in simulation in Chapter 2.

Compared to the final prototype system which requires relatively huge material and human investment, the rapid prototype system based on a real-time digital simulator allows, on the one hand, to save on the material, and on the other hand, to multiply the number of tests and configurations (*i.e.*, test bench flexibility) [52] in order to determine more precisely the validation range for our study. The use of real-time numerical simulation in MG research and development is then extensively adopted by MG manufacturers, researchers, developers, and operators so as to allow the design of MG control, protection, and power devices to be evaluated under realistic operating conditions before they are installed and commissioned in the real MG system. The interest of this approach comes from the PHIL concept which is often associated with it. This type of integrated simulation contains in closed loop one part numerically simulated and the other part using actual devices. The aim is to reproduce the laboratory-scale dynamic behavior of a real MG system [52]. This solution allows in our case to study and to validate the proposed frequency robust control strategy in stand-alone MGs while preserving the flexibility of the test system. In addition, the impact of real conditions, *e.g.*, environment, measurement sensors, system nonlinearities, model uncertainties, *etc.*, on the control strategy and architecture, together with their limitations can also be investigated through this approach.

The main advantages of using a test bench instead of a real MG system are then as follows [52]:

- Possibility to simulate various elements inside an MG system by intervening only on models;
- Ability to simulate as many energy management strategies and control architectures as one desires with a minimum of interventions;

- Reduced price compared to testing on a real MG system;
- Simplicity and ease of implementation;
- Testing is non-destructive;
- It is much less dangerous.

The experiment and validation of the proposed frequency robust control strategy, as well as the realization of dedicated electrical architectures, are not easy due to the complexity of the MG under consideration, but also because of the multiplicity of scenarios and the disparity of use(r)s. To overcome these challenges, the hybrid real-time simulator allows the connection of a real system (supercapacitor-based energy storage device, power-electronic converters, *etc.*) to a numerically simulated grid which can be deported in the form of models of complex, expensive, and/or fragile elements, *e.g.*, diesel engine generator, PV system, *etc.* This simulator allowed us to test power-electronic converters, regulation systems, control systems of power-electronic-based devices, and finally supercapacitor packs [52].

The experimental bench consists of a numerically simulated diesel-PV-load grid and a real supercapacitor-based ESS including a PWM-controlled two-quadrant chopper and a PWM-controlled three-phase voltage-source inverter. The emulated diesel-PV-load grid is interfaced to the PCC *via* a power amplifier. The goal displayed and achieved was to set up a complete energy structure representative of a stand-alone MG with a classical source, a renewable source, an energy storage unit, and an aggregated load. The different control levels and the proposed frequency robust control strategy are implemented in the real-time simulator, which therefore plays the role of a centralized controller. Finally, the structure can be adapted to other configurations of stand-alone MGs and other frequency control strategies in MGs without major modifications.

It should be noted here that the parameters and the rated apparent power of the real supercapacitor-based ESS in the experimental bench is much more lower than those of our initial case study presented in Chapter 2. Therefore, based on the analogous scaling law, some adaptations on the parameters and the rated apparent power of each unit in the emulated diesel-PV-load grid must be carried out to make this system precisely compatible with the real supercapacitor-based ESS in terms of voltage and current levels. As a result, the equilibrium point of the system under test is also different from the steady-state one of the simulated stand-alone MG presented in Chapter 2. The parameters of the experimental bench are given in Appendix D.

This chapter begins with a description of the laboratory-scale prototype system, together with the constitutive components of the software and hardware architectures of the test bench, as well as the control architecture in Section 4.2. Section 4.3 is devoted to our case study allowing to demonstrate both the performance of the test bench and the real-time validation of the frequency robust control strategy which was proposed in Chapter 2 under various test scenarios. Some concluding remarks are drawn in Section 4.4.

4.2 Implementation of a laboratory-scale prototype system

This section describes in detail the procedure according to which the experimental bench based on the PHIL configuration is utilized. First, the software architecture is presented. Next, the procedure allowing to manage the interaction among the different constitutive elements of the test bench and then the steps to achieve a robust control strategy for this kind of MG application are provided.

The objective of this study is to analyze and validate the proposed frequency robust control strategy in stand-alone MGs under realistic operating conditions. In order to realize this work, the construction of a test bench was envisaged. Here the aim is to add modules to the existing test bench at G2Elab, then arrange, interconnect, and control them.

4.2.1 Description of the laboratory-scale prototype system

A schematic diagram of the test bench implemented and completed during this thesis is depicted in Figure 4.1. The test bench comprises two main subsystems: a subsystem that concerns first of all the real supercapacitor-based ESS including a PWM-controlled two-quadrant chopper and a PWM-controlled three-phase voltage-source inverter, and subsequently the emulation of the remainder of the studied MG composed of a diesel engine generator, a PV system, and an aggregated static load *via* a real-time digital simulator and a power amplifier. Each subsystem is divided into two entities, namely a first software layer and a second hardware layer. The term “emulation” means the physical simulation of a component; it is therefore not a pure numerical simulation [52].

- **Real supercapacitor-based energy storage system:** the first software part contains the control architecture of the test bench. The second hardware part comprises the elements which allow to implement the power interface with the emulated diesel-PV-load grid.
- **Emulated diesel-photovoltaic-load grid:** the first software layer consists of models of the diesel engine generator, the PV system, and the aggregated load based on their aforescribed models in Chapter 2, together with the control architecture of the experimental bench. The second hardware layer includes the elements which allow to realize the power interface with the real supercapacitor-based ESS environment.

The software parts which control the hardware one of the test bench are represented by the real-time digital simulators, namely RT-LAB[®] and dSPACE[®]. It should be noted here that due to the inherent characteristics of the actual test bench, these two simulators are simultaneously employed. The models of the diesel generator, the PV system, and the aggregated load, along with the control architecture are developed under MATLAB[®]/Simulink[®].

The power interface consists in a power amplifier. The role of the power interface is to allow the emulation of the diesel-PV-load grid, as well as the interconnection with the real

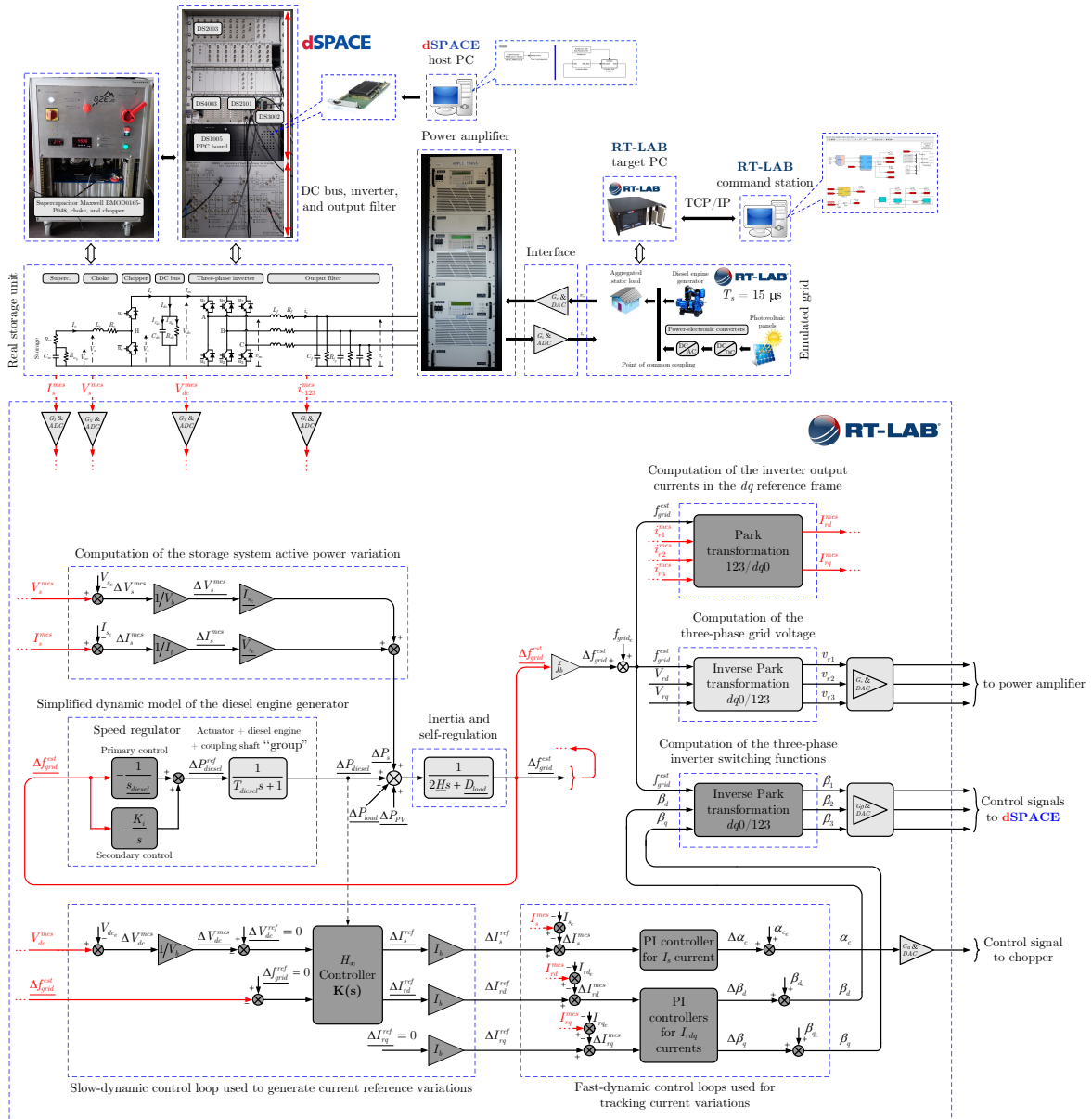


Figure 4.1 – Schematic diagram of the test bench for the stand-alone MG application based on the PHIL configuration.

supercapacitor-based ESS.

4.2.2 Correspondence with the physical elements

As mentioned in Subsection 4.2.1, the studied test bench has two major subsystems, namely the real supercapacitor-based ESS environment and the emulation of the diesel-PV-load grid.

In order to study the behavior of the test bench for stand-alone MGs and to validate the numerical simulations, experimental tests are set up and implemented on the bench depicted in Figure 4.1. This subsection aims at identifying which elements are physical and which ones are simulated or emulated on the test bench. The definition of the term “emulate” is “to seek to imitate”. The emulation is therefore an imitation of the physical behavior of a system by a software/hardware system [52].

Real supercapacitor-based energy storage system environment

As aforementioned in the previous subsections, the test bench contains two main parts, namely a software part (software architecture) and a hardware part (material architecture). The correspondence with the physical elements of the real supercapacitor-based ESS environment is shown in Figure 4.2.

- **Software architecture**

The software architecture of the test bench concerning the real supercapacitor-

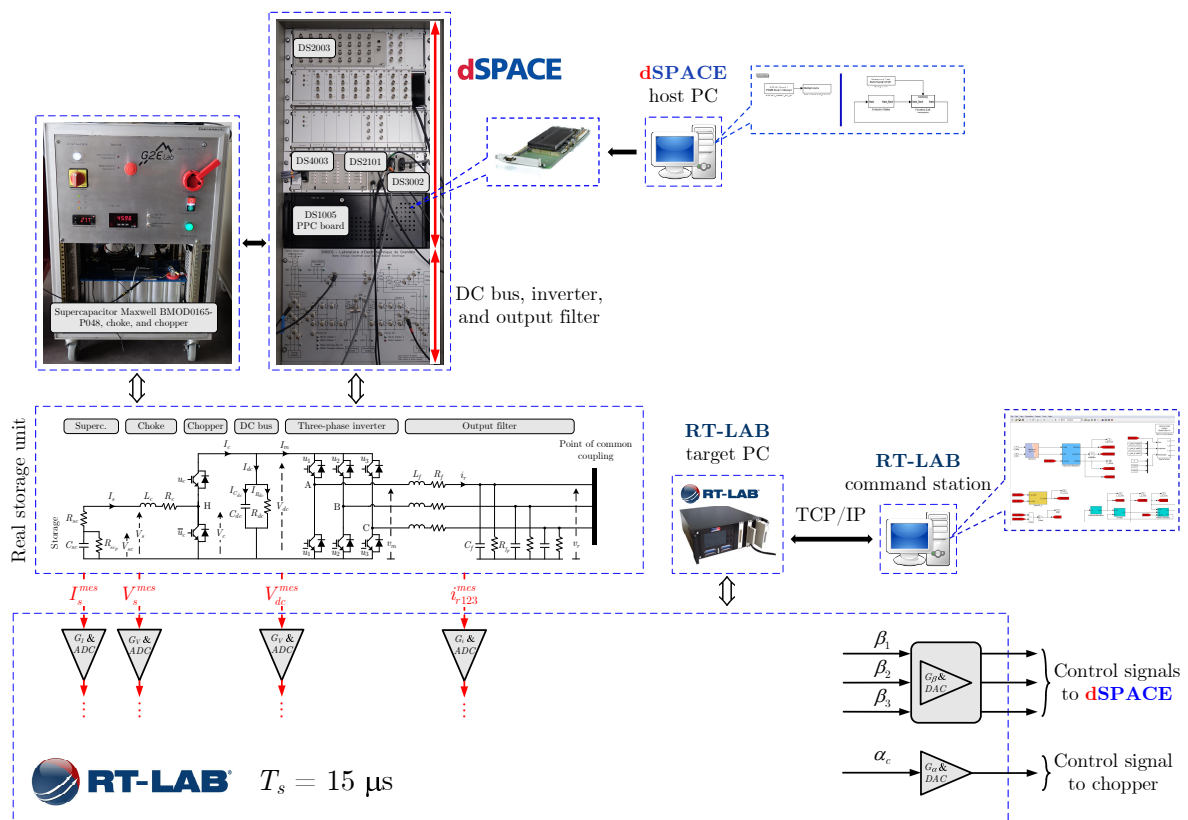


Figure 4.2 – Correspondence with the physical elements of the real supercapacitor-based ESS environment.

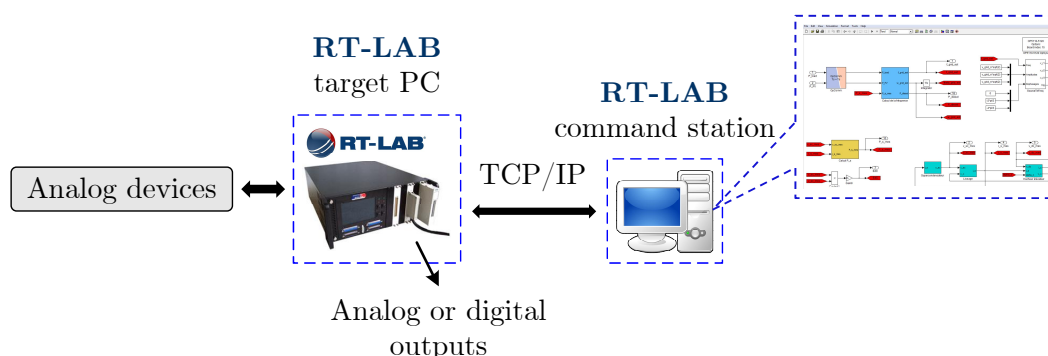


Figure 4.3 – Structure of the RT-LAB[®] real-time digital simulator.

based ESS environment consists in the RT-LAB[®] real-time digital simulator, developed by OPAL-RT Technologies. One of its key features is the integration of MATLAB[®]/Simulink[®] models. RT-LAB[®] allows to convert Simulink[®] models into real-time executable code *via* Real-Time Workshop and to execute them on one or several processors. This process is particularly useful for hybrid simulation or HIL and for the rapid prototyping of control systems. RT-LAB[®] governs the synchronization, the interactions with the user, the interface with the hardware by means of input/output cards, and the data exchanges for the distributed execution, seamlessly for the user [52].

All associated computation is performed using the RT-LAB[®] platform. The existing RT-LAB[®] hardware platform at the laboratory comprises two major parts as illustrated in Figure 4.3 [52]:

- A command station which has two functions. The first function is model design and development, model implementation and validation, code generation, non-real-time system analysis. The second function is the interface between the user and the system (*i.e.*, human-machine interface);
- A computing station that allows to execute real-time computation. The real-time cluster is connected to the command station *via* an Ethernet link. The computing station is based on Intel Xeon E5 with 24 processor cores (24 CPUs) up to 3.5 GHz, with the Linux-based operating system, which supports the real-time execution of the compiled model. The input/output cards of the computing station allow its connection with analog devices. Their type depends on the envisaged application. Also, there are analog/digital cards and digital/digital cards. In terms of HIL or PHIL interconnection, the system comprises 16 analog input cards, 16 analog output cards, 8 digital input cards, and 16 digital output cards. The parameters of the RT-LAB[®] real-time digital simulator have been set as follows: the discretization time step $T_s = 15 \mu s$, the analog outputs of $\pm 16 V$, and the computation method “ode4 (Runge-Kutta)”.

In this application, the control architecture of the real supercapacitor-based ESS is implemented in the RT-LAB[®] real-time digital simulator, as depicted in Figure 4.1. The

interaction with the power elements of the test bench is realized *via* analog input/output cards.

Another element of the test bench software architecture of the real supercapacitor-based ESS environment is the dSPACE[®] real-time digital simulator and the TMS320F24 signal processor. The dSPACE[®] system, based on the MATLAB[®]/Simulink[®] environment, consists of a processor card and a number of input/output cards. From the dSPACE[®] host PC, the system allows to convert Simulink[®] models into real-time executable code *via* Real-Time Workshop and to execute them on one or several processors. The RTI 1005 dSPACE[®] system currently available in the laboratory is composed of a DS1005 PowerPC processor card (motherboard) – PowerPC 750 operating at 480 MHz, a DS2003 measurement acquisition card with 32 analog inputs, a DS2101 display card with a block of 5 analog outputs, a DS3002 speed card with 6 high resolution inputs for incremental encoders, a DS4003 card with 96 logic inputs/outputs, and finally a DS5101 card (PWM card) which has 16 PWM outputs with a resolution of 25 ns. The dSPACE[®] system as a rapid-prototyping system allows the implementation of numerical models and also any control structures for electrical systems. The parameters of the dSPACE[®] real-time digital simulator have been set as follows: the discretization time step $T_s = 100 \mu\text{s}$, the analogue outputs of $\pm 10 \text{ V}$, and the computation method “ode1 (Euler)” [52].

In the control architecture of the real supercapacitor-based ESS implemented in the RT-LAB[®] real-time digital simulator, the chopper duty cycle α_c and the switching functions of the three-phase inverter β_{123} – digital control signals – are amplified and then converted into analog control signals by means of analog output cards. The analog control signal α_c is transmitted to an Arduino-based microprocessor integrated in the supercapacitor-choke-chopper system, which then allows to convert it into PWM control signals for the top and bottom switches of the chopper. Meanwhile, the analog control signals β_{123} are transmitted to the dSPACE[®] system (more particularly to the DS2003 measurement acquisition card), then *via* the DS5101 card (PWM card) the DS5101PWM block will automatically generate the switching commands for the corresponding top and bottom phase switches of the three-phase inverter. This block allows adjusting the dead time of switches. In addition, the measured voltage and current signals, namely the supercapacitor output current I_s^{mes} , supercapacitor voltage V_s^{mes} , DC-bus voltage V_{dc}^{mes} , and inverter output currents i_{r123}^{mes} – analog signals coming from the real supercapacitor-based ESS – are transmitted to the RT-LAB[®] system and then converted into digital signals *via* analog input cards. These digital signals are then amplified to be compatible with the implemented control architecture.

- **Material architecture**

The elements of the material architecture are the power interface, the current and voltage sensors, as well as the protection devices. The hardware systems of the real-time digital simulators – RT-LAB[®] and dSPACE[®] – are considered as an integrated part of the material architecture.

The supercapacitor-choke-chopper system contains a supercapacitor (type Maxwell BoostCap BMOD0165-P048 165 F), a Buck-Boost converter (type IGBTs Semikron

- *Software architecture*

The software architecture of the test bench for the emulation of the diesel-PV-load grid consists in the RT-LAB[®] real-time digital simulator. Here *via* this simulator and a power amplifier, the diesel engine generator, the PV system, and the aggregated load can be emulated based on their aforerepresented models in Chapter 2.

In the control architecture of the emulated diesel-PV-load grid implemented in the RT-LAB[®] real-time digital simulator, the three-phase voltages at the PCC v_{r123} – digital signals – are reduced and then converted into analog signals by means of analog output cards. The analog signals v_{r123} are transmitted to the power amplifier, then amplified to set the output voltages for the emulated grid.

- *Material architecture*

In order to implement the interconnection between the emulated diesel-PV-load grid and the real supercapacitor-based ESS, a power amplifier is required. The power amplifier currently available in the test bench is the AMX-Series AC Power Source, model 360-AMX – 18 kVA. It is configured with an UPC32 programmable controller. The maximum apparent power injected and absorbed by the power amplifier are set as 18 kVA and 6 kVA, respectively. The power amplifier is the component of the interface that transforms and amplifies the analog output signals of the simulator (voltage signals of ± 10 V) into electrical quantities (voltages or currents) that can rise up to 125 V rms and 16 A rms. The output bandwidth of the power amplifier is variable from 20 to 5000 Hz, allowing a representation of physical phenomena in low and medium frequencies.

4.3 Frequency robust control real-time validation

This section is devoted to the PHIL validation of the frequency robust control strategy in stand-alone MGs which was proposed in Chapter 2. First, dynamic specifications of the system under test are introduced. Then, an equilibrium point computation for this system is presented. Next, a brief description of the control design procedure for the considered system is given. Finally, an experimental validation of the proposed frequency robust control strategy under various test scenarios is detailed.

4.3.1 Dynamic specifications

The participation of both the ESS and the diesel engine generator in primary frequency control has been proposed in Section 2.4 in order to improve dynamic performances (lower overshoot, faster response time, smaller steady-state error) of the MG frequency f_{grid} in case of load active power variations. Here the control design is performed for a given MG frequency performance requirement in response to a load step disturbance of $\pm 5\%$ of the load rated active power (± 150 W). This performance specification, shown in Figure 4.5, is defined based on its time-domain response in the case where only the diesel generator participates in primary control.

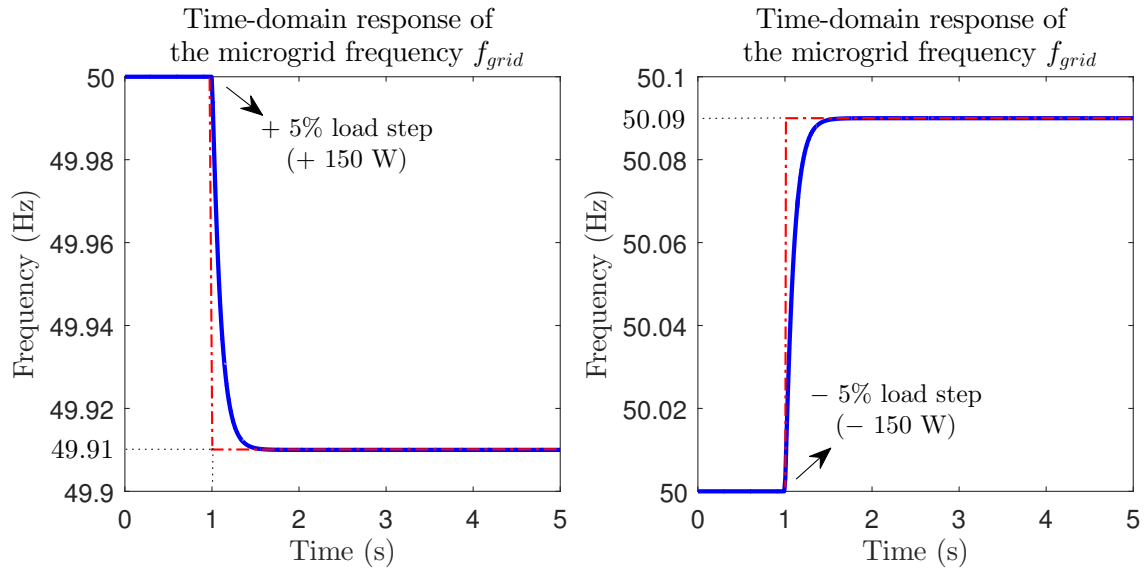


Figure 4.5 – Performance specification on the MG frequency variation in response to a load step disturbance of $\pm 5\%$ of the load rated active power (± 150 W) in the time domain.

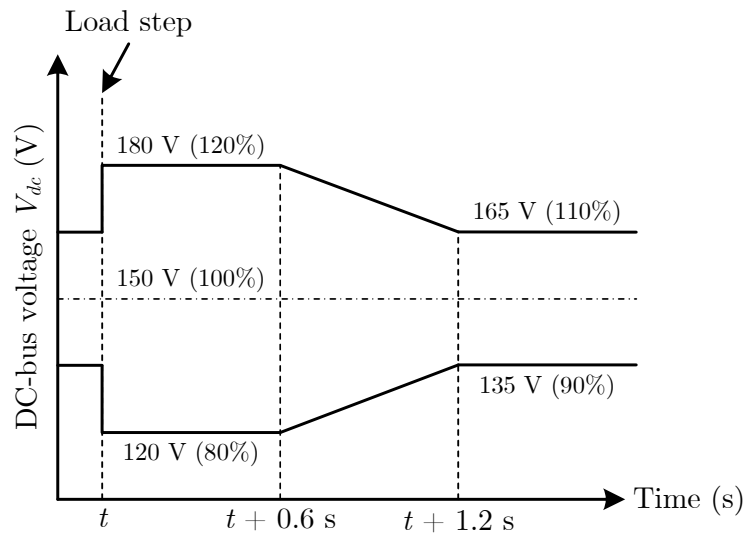


Figure 4.6 – Performance specification on the DC-bus voltage variation in response to a load step disturbance in the time domain.

Another dynamic specification which must be taken into account is to regulate the DC-bus voltage V_{dc} at a reference value V_{dc}^{ref} that has been here chosen as 150 V so as to ensure secure and reliable operation of the DC-bus capacitor (chemical capacitor that can accept a maximum voltage of 250 V). A performance specification on the DC-bus voltage variation, relied on the aforeproposed one in Subsection 2.5.4, is depicted in Figure 4.6. It should be noted that this specification is defined for any load step disturbance and then it is not possible to translate it exactly into small-signal specifications. However, large-signal standards can be guaranteed by imposing suitable small-signal performances.

4.3.2 Equilibrium point computation

In order to compute an equilibrium state of the ESS (indicated by the subscript e), several initial conditions are first given as follows. The DC-bus voltage V_{dc} is assumed to be initially equal to its setpoint value, *i.e.*, $V_{dc} = V_{dc_e} = V_{dc}^{ref} = 150$ V. Note here that we do not choose the value V_{sc_e} in the midrange between the minimum and maximum supercapacitor voltages for \mathcal{H}_∞ control design, as applied in Subsection 2.5.4, but the value V_{sc_e} chosen corresponds to the maximum supercapacitor voltage, *i.e.*, $V_{sc_e} \approx V_{s_e} = V_{s_{max}} = 48$ V, meaning that the supercapacitor is fully charged before tests. The aim is to prevent the PWM duty cycle of the chopper α_c from attaining its saturation threshold in case of large load disturbances. Indeed, since the chopper duty cycle α_c is directly proportional to the supercapacitor voltage V_{sc} , a large load variation may result in a dramatic decrease in V_{sc} , which rapidly drives α_c to its practical limits (*i.e.*, $\alpha_c \in [0.2, 0.8]$).

Due to hardware limitation, in this study the PWM-controlled two-quadrant chopper of the test bench will operate in boost mode only, which means that the real supercapacitor-based ESS is always in discharging mode. The boost converter operates in discontinuous conduction mode when the current I_m demanded by the load is low, and it operates in continuous conduction mode for larger currents. The limit between continuous and discontinuous conduction modes is reached when the current through the choke I_s falls to zero just at the switching moment. In this case, the output current $I_{m_{lim}}$ (output current at the limit of continuous and discontinuous conduction) can be expressed as follows [51]

$$I_{m_{lim}} = \frac{V_s}{2L_c f_{PWM_c}} \frac{V_s}{V_{dc}} \left(1 - \frac{V_s}{V_{dc}}\right). \quad (4.1)$$

At the equilibrium state of the ESS, one has

$$I_{m_{lim_e}} = \frac{V_{s_e}}{2L_c f_{PWM_c}} \frac{V_{s_e}}{V_{dc_e}} \left(1 - \frac{V_{s_e}}{V_{dc_e}}\right). \quad (4.2)$$

By replacing parameter values of the test bench from Appendix D to (4.2), one obtains $I_{m_{lim_e}} = 0.43$ A. Moreover, one also has $P_s = V_s I_s \approx P_{dc} = V_{dc} I_m$, therefore the supercapacitor output current at the limit of continuous and discontinuous conduction $I_{s_{lim}}$ can be deduced as follows

$$I_{s_{lim}} \approx \frac{V_{dc} I_{m_{lim}}}{V_s}. \quad (4.3)$$

At the equilibrium state of the ESS, one has

$$I_{s_{lim_e}} = \frac{V_{dc_e} I_{m_{lim_e}}}{V_{s_e}}. \quad (4.4)$$

By numerical application to (4.4), one obtains $I_{s_{lim_e}} = 1.33$ A. In order to ensure that the boost converter always operates in continuous conduction mode, the value I_{s_e} must be larger than its limit $I_{s_{lim_e}}$. Thus, in this study, we choose $I_{s_e} = 2$ A.

Finally, similar to the equilibrium point computation which has been presented in Subsection 2.5.4, the steady-state operating point of the supercapacitor-based ESS is given in Table 4.1.

Table 4.1 – Steady-state real-unit values of the supercapacitor-based ESS.

Variable	$V_{sc_e} \approx V_{s_e}$	V_{dc_e}	V_{rd_e}	V_{rq_e}	I_{s_e}
Value	48 V	150 V	80 V	0 V	2 A
Variable	I_{rd_e}	I_{rq_e}	α_{c_e}	β_{d_e}	β_{q_e}
Value	0.98 A	0 A	0.32	0.536	0.0143
Variable	P_{s_e}	P_{r_e}	Q_{r_e}	f_{grid_e}	ω_{grid_e}
Value	96 W	78 W	0 VAr	50 Hz	100π rad/s

4.3.3 Control design

A cascaded two-level control structure – where classical PI-based current tracking controllers are placed on the low control level and receive references from an \mathcal{H}_∞ -control-based upper level – is implemented to ensure the above mentioned dynamic specifications.

At the low level, we impose the closed-loop dynamics twenty times faster than the original current plants, *i.e.*, $T_{0_s} = T_s/20 = 1.2$ ms, $T_{0_{rdq}} = T_{rdq}/20 = 0.8$ ms and the damping ratios $\zeta_{0_s} = \zeta_{0_{rdq}} = 0.8$.

At the upper level, similar to the \mathcal{H}_∞ control design which has been carried out in Subsection 2.6.3, the design of the multi-variable \mathcal{H}_∞ controller for the linear system is cast into the **P** – **K** formalism, where weighting functions $W_{perf}(s)$ are chosen to guarantee the performance objectives and the practical implementation constraints imposed to the control inputs are dealt with by choice of weighting functions $W_u(s)$. The linear time-invariant weighting functions, used for S/KS mixed-sensitivity optimization process to reject disturbance due to the load active power variation, are written as follows

$$\frac{1}{W_{perf}(s)} = \frac{s + \omega_b A_\varepsilon}{s/M_s + \omega_b}, \quad (4.5)$$

$$\frac{1}{W_{u_1}(s)} = A_{u_1} \frac{\left(\frac{M_{u_1}}{\omega_{bc11}}s + 1\right) \left(\frac{A_{u_1}}{\omega_{bc12}}s + 1\right)}{\left(\frac{A_{u_1}}{\omega_{bc11}}s + 1\right) \left(\frac{M_{u_1}}{\omega_{bc12}}s + 1\right)}, \quad \frac{\omega_{bc11}}{A_{u_1}} < \frac{\omega_{bc12}}{M_{u_1}}, \quad (4.6)$$

$$\frac{1}{W_{u_2}(s)} = \frac{A_{u_2}s + \omega_{bc2}}{s + \omega_{bc2}/M_{u_2}}. \quad (4.7)$$

The first weighting function $W_{perf_1}(s)$ is designed such that to ensure a bandwidth for $\frac{\Delta V_{dc}}{\Delta I_{rd}}$ two hundred and forty times smaller than the ΔI_{rd} (or $\frac{\Delta I_{rd}}{\Delta I_{rd}}$) inner closed-loop one, *i.e.*, $\omega_{b_1} = 1/(240T_{0_{rdq}}) = 5.22$ rad/s (or a response time of approximately $t_{r_1} \approx 0.6$ s). $M_{s_1} = (0.05V_{dc_e}) / (0.05P_{load_e}) = 3.125$ is chosen to limit the DC-bus voltage overshoot at 5% of its rated value V_{dc_e} (*i.e.*, 7.5 V) in response to a load step of 5% of the load rated active power P_{load_e} (*i.e.*, 150 W). Similarly, one imposes $A_{\varepsilon_1} = (0.025V_{dc_e}) / (0.05P_{load_e}) = 1.563$ to ensure a desired steady-state error being less than or equal to 2.5% of V_{dc_e} (*i.e.*, 3.75 V).

The parameters of the second weighting function $W_{perf_2}(s)$ designed for $\underline{\Delta f_{grid}}$ are chosen to improve the transient response of the MG frequency compared to its performance specification in Figure 4.5. $\omega_{b_2} = \omega_{b_1} = 1/(240T_{0_{rdq}}) = 5.22$ rad/s is chosen to ensure a response time of approximately $t_{r_2} \approx 0.6$ s. Imposing $M_{s_2} = [(50.08 - 50)/f_b] / (0.05\underline{P_{load_e}}) = 0.053$ allows limiting the frequency overshoot at 0.08 Hz in response to a load step of 5% of P_{load_e} (*i.e.*, 150 W). $A_{\varepsilon_2} = [(50.04 - 50)/f_b] / (0.05\underline{P_{load_e}}) = 0.027$ is chosen to ensure a desired steady-state error being less than or equal to 0.04 Hz.

The parameters of the weighting function $W_{u_1}(s)$ designed for $\underline{\Delta I_s^{ref}}$ are chosen as follows. $M_{u_1} = (I_{s_{max}} - I_{s_e}) / (0.05\underline{P_{load_e}}) = 33.425$ is chosen to prevent the supercapacitor output current reference from exceeding its admissible limit $I_{s_{max}}$ consequent to a load step of 5% of P_{load_e} (*i.e.*, 150 W). A small value of $A_{u_1} = 0.1M_{u_1} = 3.343$ is imposed. In our case study, the own frequency of the selected supercapacitor technology is $f_p = 0.48$ Hz (or $\omega_p = 3.04$ rad/s), therefore, one chooses $\omega_{bc_{11}}/A_{u_1} = 3.04$ rad/s resulting in $\omega_{bc_{11}} = 10.17$ rad/s. Additionally, $\omega_{bc_{12}}/M_{u_1} = \omega_{c_{max}}/2 = 4.11$ rad/s is chosen (with $\omega_{c_{max}} = 8.21$ rad/s being already computed in Subsection 2.5.3), which leads to $\omega_{bc_{12}} = 137.21$ rad/s.

The parameters of the weighting function $W_{u_2}(s)$ designed for $\underline{\Delta I_{rd}^{ref}}$ are chosen as follows. $M_{u_2} = (I_{rd_{max}} - I_{rd_e}) / (0.05\underline{P_{load_e}}) = 9.99$ is imposed to limit the current reference below its maximum value $I_{rd_{max}}$ consequent to a load step of 5% of P_{load_e} (*i.e.*, 150 W). A small value of $A_{u_2} = 0.1M_{u_2} = 1$ is chosen. $\omega_{bc_2} = 1/(400T_{PWM_i}) = 25$ rad/s, where $T_{PWM_i} = 1/f_{PWM_i}$, is chosen to impose a bandwidth four hundred times smaller than the PWM switching frequency of the three-phase inverter f_{PWM_i} .

The LMI algorithm under the MATLAB[®] software environment yields a solution after eight iterations for a multi-variable full-order \mathcal{H}_∞ controller which has 8 states with an optimal value of $\gamma = 1.449$ and an \mathcal{H}_∞ norm = 0.603. This optimization quality allows the designed \mathcal{H}_∞ controller to ensure stable and robust performance in case of a load step of 5% of P_{load_e} (*i.e.*, 150 W) in the system, which is demonstrated in the sequel.

A series of experiments are hereafter performed to show the validity and effectiveness of the proposed frequency robust control approach. Without loss of generality, load step changes from $\pm 5\%$ to $\pm 30\%$ of the load rated active power are applied as disturbances. The supercapacitor voltage V_{sc} , initially regarded as a time-invariant parameter in the \mathcal{H}_∞ controller synthesis, appears now as a time-variant one in the test bench, *i.e.*, $\Delta V_{sc} \neq 0$ (its dynamic equation $\dot{V}_{sc} = f(V_{sc}, I_s)$ being taken into account in the experiment).

4.3.4 Experimental validation under small load step disturbances of $\pm 5\%$ of the load rated active power (± 150 W)

First of all, the experimental results are presented and discussed under small load step disturbances of $\pm 5\%$ of the load rated active power (± 150 W).

Figure 4.7 and Figure 4.8 present a comparison of the experimental result and simulation results obtained with topological and nonlinear averaged modeling for the time-domain responses of the MG frequency f_{grid} and DC-bus voltage V_{dc} , respectively, under small load step disturbances of $\pm 5\%$ of the load rated active power (± 150 W). It should be noted here that f_{grid} has been estimated *via* the dynamic model of the MG (*i.e.*, *via* the equation (2.11) which expresses the time derivative of the system frequency). A good concordance of these results can be observed in the sense that, despite high-frequency oscillations seen in the experimental result of V_{dc} , the averaged model approximates very well the converter's low-frequency behavior, the one generally used for control purposes. Therefore, the experimental result itself is validated when compared to the simulation results. From Figure 4.7 it can be observed

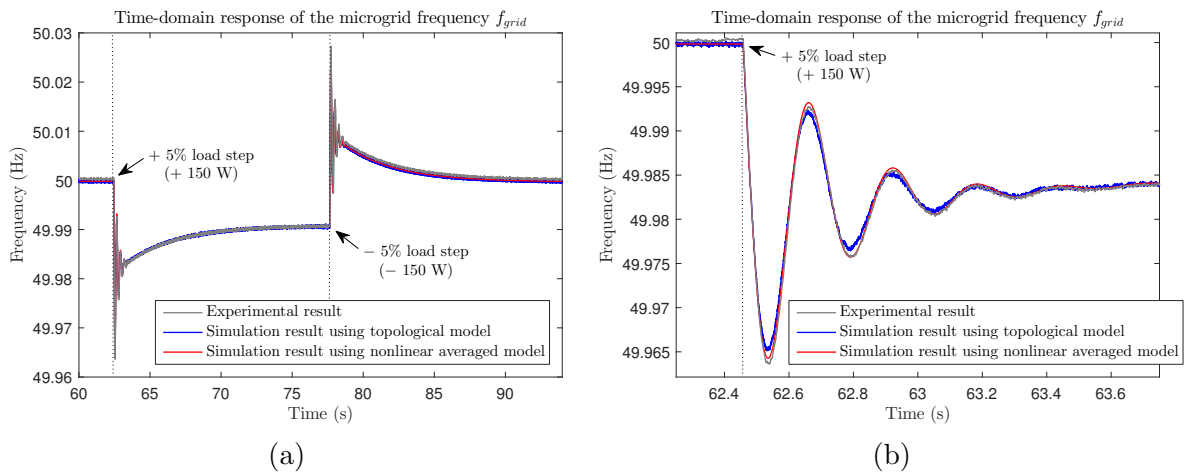


Figure 4.7 – (a) MG frequency time-domain response f_{grid} under small load step disturbances of $\pm 5\%$ of the load rated active power (± 150 W) with respect to the rated operating point. (b) Temporal zoom in the time interval $t \in [62.25, 63.75]$ s.

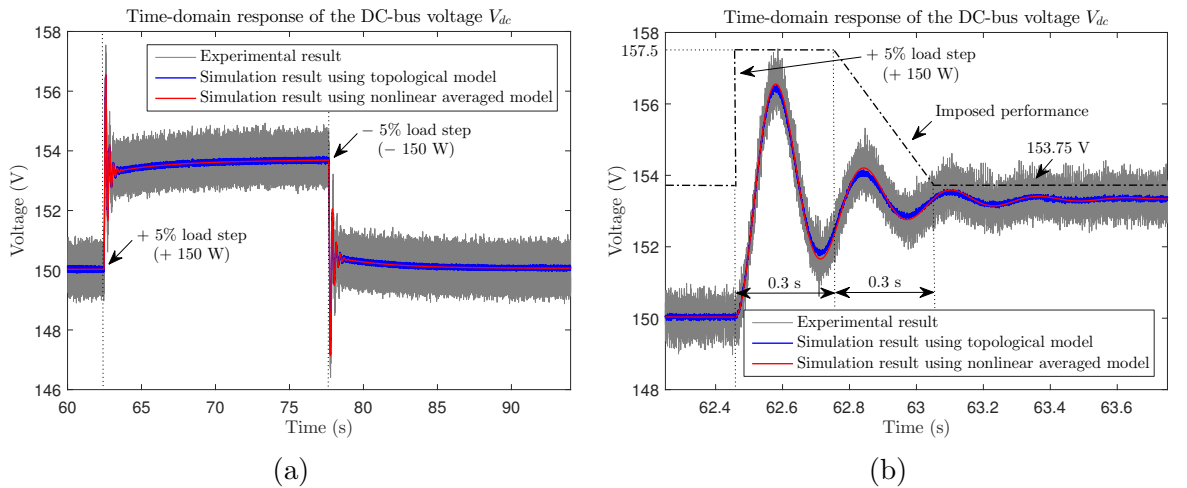


Figure 4.8 – (a) DC-bus voltage time-domain response V_{dc} under small load step disturbances of $\pm 5\%$ of the load rated active power (± 150 W) with respect to the rated operating point. (b) Temporal zoom in the time interval $t \in [62.25, 63.75]$ s.

that the imposed time-domain performances of f_{grid} are successfully guaranteed with respect to the choice of the weighting function $W_{perf_2}(s)$ (*i.e.*, maximum overshoot of 0.08 Hz, response time of approximately 0.6 s, admissible steady-state error of 0.04 Hz). Compared with the case in which only the diesel engine generator participates in primary frequency control, the storage device participation has significantly improved the dynamic performances (*i.e.*, lower overshoot, faster response time, smaller steady-state error) of f_{grid} . The system is also always stable. It can be seen from Figure 4.8 that the imposed time-domain performances of V_{dc} corresponding to the tuning of the weighting function $W_{perf_1}(s)$ (*i.e.*, maximum overshoot of 7.5 V, response time of approximately 0.6 s, admissible steady-state error of 3.75 V) are satisfied with both experiment and simulation, except for the steady-state error of V_{dc} observed in the experiment. Hence, the synthesized \mathcal{H}_∞ controller ensures the imposed performance specifications. The difference between the experimental result and simulation results can easily be explained due to some unavoidable reasons (*e.g.*, measurement error and/or noise, slight parameter difference between the model and the real system, unknown and/or neglected (unmodeled) dynamics of the real system).

Figure 4.9, Figure 4.10, and Figure 4.11 show the experimental results for the time-domain responses of the supercapacitor output current I_s and the direct and quadrature components of the inverter output current I_{rd} and I_{rq} , together with their references, respectively, under small load step disturbances of $\pm 5\%$ of the load rated active power (± 150 W). Let us note here that the initial real value of the direct current $I_{rde}^{real} = -0.4$ A is slightly different from that previously computed in Subsection 4.3.2, $I_{rde}^{com} = 0.98$ A. This is due to slight parameter difference between the model and the real system, as well as unknown and/or neglected (unmodeled) dynamics of the real system. In spite of high-frequency oscillations observed in the measured currents due to measurement noise, converters' high-frequency behavior, and

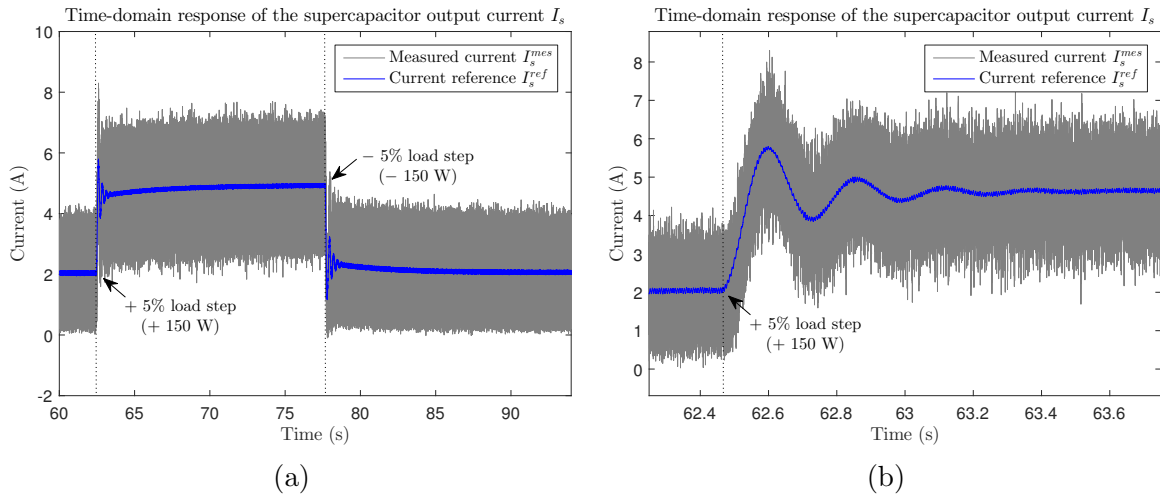


Figure 4.9 – (a) Experimental result for the time-domain response of the supercapacitor output current I_s under small load step disturbances of $\pm 5\%$ of the load rated active power (± 150 W) with respect to the rated operating point. (b) Temporal zoom in the time interval $t \in [62.25, 63.75]$ s.

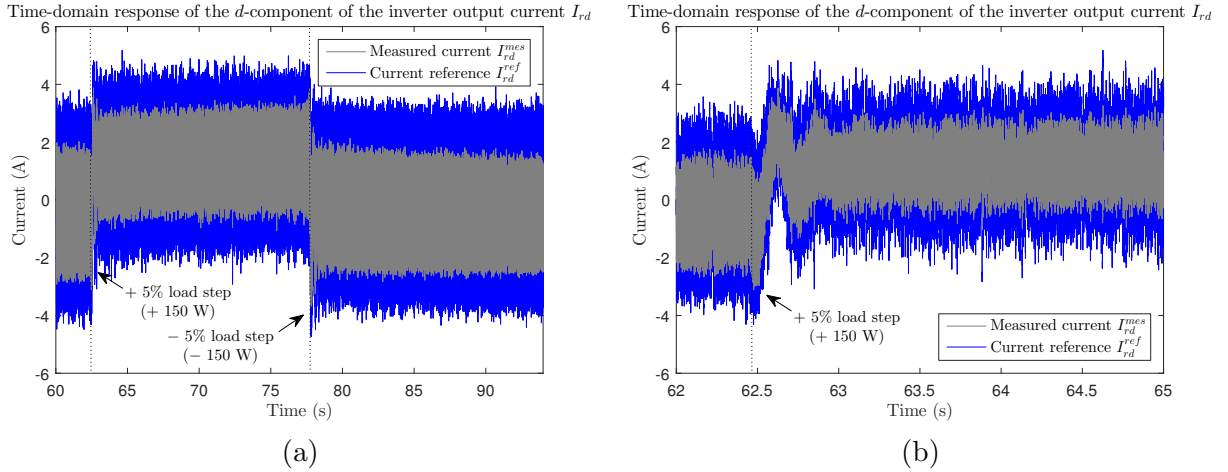


Figure 4.10 – (a) Experimental result for the time-domain response of the d -component of the inverter output current I_{rd} under small load step disturbances of $\pm 5\%$ of the load rated active power (± 150 W) with respect to the rated operating point. (b) Temporal zoom in the time interval $t \in [62, 65]$ s.

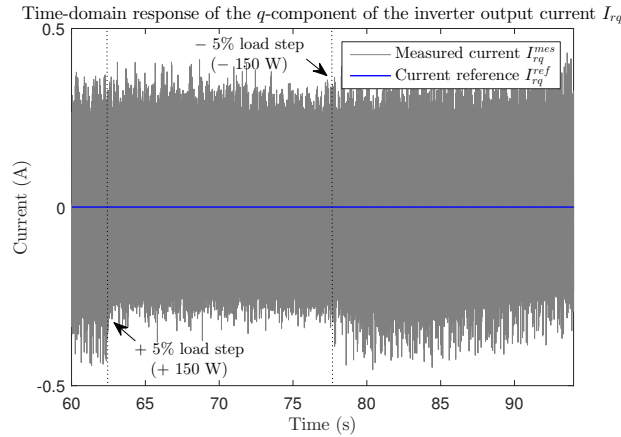


Figure 4.11 – Experimental result for the time-domain response of the q -component of the inverter output current I_{rq} under small load step disturbances of $\pm 5\%$ of the load rated active power (± 150 W) with respect to the rated operating point.

unadapted design of the test bench (more particularly the choke), these currents are able to satisfactorily track their references. Therefore, the synthesized classical PI-based current tracking controllers effectively ensure their imposed closed-loop dynamic performances. Nevertheless, let us remark here that the measured current I_{rd}^{mes} is “smoother” than the current reference I_{rd}^{ref} , as shown in Figure 4.10. This is due to the fact that the current loop cannot follow the very high-frequency variations of the reference. Moreover, it can be seen that the admissible limit is guaranteed for these currents with respect to the choice of the weighting functions $W_u(s)$, which means that their imposed dynamic performance specifications are well guaranteed.

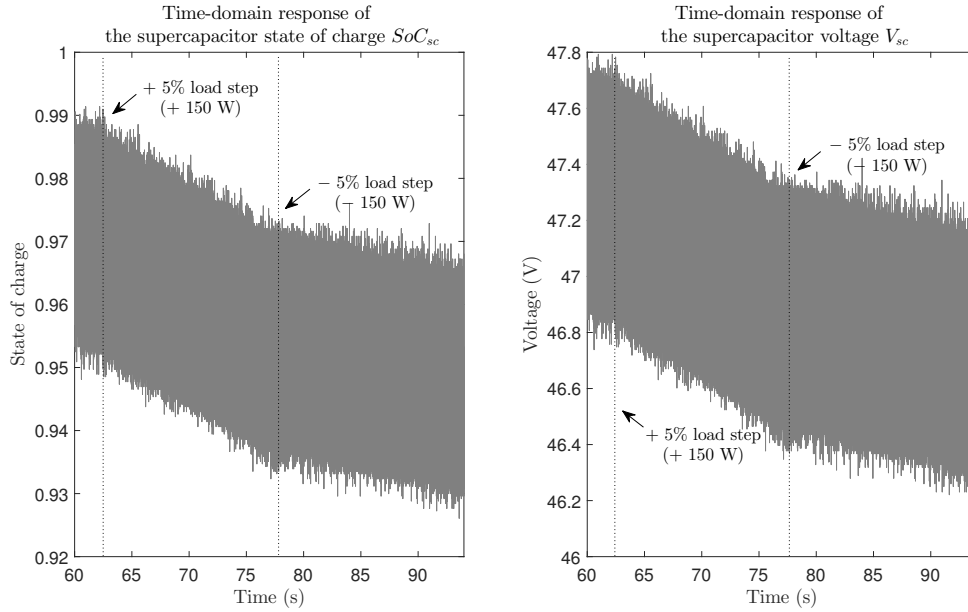


Figure 4.12 – Experimental results for the time-domain responses of the supercapacitor state of charge SoC_{sc} and voltage V_{sc} under small load step disturbances of $\pm 5\%$ of the load rated active power (± 150 W) with respect to the rated operating point.

Figure 4.12 illustrates the experimental results for the time-domain responses of the supercapacitor state of charge SoC_{sc} and voltage V_{sc} under small load step disturbances of $\pm 5\%$ of the load rated active power (± 150 W). During the first period before the disturbances, these values tend to decrease linearly and quite slowly. The supercapacitor is slightly discharged to compensate for losses in the ESS. Consequent to the load active power step disturbance of 150 W, the supercapacitor voltage decreases more rapidly – according to the bandwidth imposed for the weighting function that shapes supercapacitor current variation, $W_{u_1}(s)$ – which means that the supercapacitor is in discharging mode to compensate for the load active power variation. When the load active power comes back to its initial value, the supercapacitor also returns to the slowly discharging mode which is similar to the state observed before the disturbances. Let us note here that there are high-frequency oscillations shown in V_{sc} due to measurement noise and converters' high-frequency behavior.

The ESS participation in primary frequency control has reduced the active power variation of the diesel engine generator, as shown in Figure 4.13. It should also be noted here that the PV output active power variation $\Delta P_{PV} = 0$ does not reduce generality, as these variations may always be included in the aggregated load. In this \mathcal{H}_∞ robust control approach, it can be seen that the primary control is mainly realized by the storage device, whereas there is only a slight change in the active power of the diesel generator during this time interval, which allows to ensure an optimal operation of the diesel generator around its steady-state operating point. In addition, there are high-frequency oscillations displayed in the active power variation of the storage device ΔP_s . This is due to measurement noise and converter's high-frequency behavior.

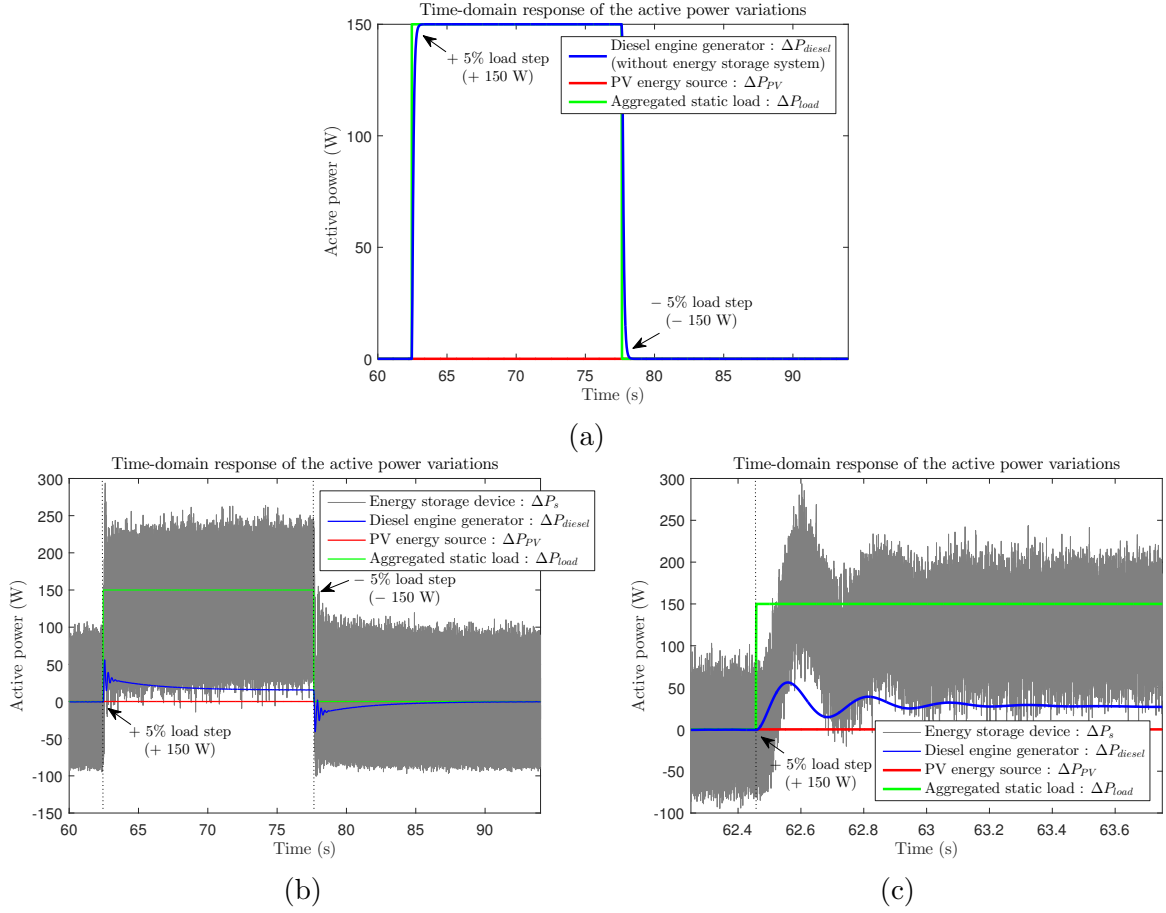


Figure 4.13 – Experimental results for the active power variations of the sources and load, (a) without ESS and (b) with ESS, under small load step disturbances of $\pm 5\%$ of the load rated active power (± 150 W) with respect to the rated operating point. (c) Temporal zoom for (b) in the time interval $t \in [62.25, 63.75]$ s.

These results allows us to revisit the storage device initial choice and sizing. From the time-domain response of the active power variation of the storage device, its sizing can be defined from the maximum active power variation of the load or PV energy source. Then, if a small variation of the MG transient frequency is required, an important peak of power provided by the storage device is needed. A trade-off between the MG admissible frequency variation and the rated power of the storage device is necessary. As the MG frequency variation with the ESS by \mathcal{H}_∞ control is fixed by the definition of the weighting function $W_{perf_2}(s)$, the imposed performance specification should be relaxed so as to increase the MG admissible frequency variation, leading to power and energy reduction and therefore, the cost used by the storage device. For example, the imposed steady-state value of the MG frequency can be increased from 0.04 Hz to 0.06 Hz (nearer to that of the MG frequency time-domain response without ESS) to reduce the power supplied by the storage device. The imposed performance of the MG frequency variation focuses on primary frequency control only. Therefore, the ESS does not participate in secondary frequency control. If the ESS is used to participate in secondary

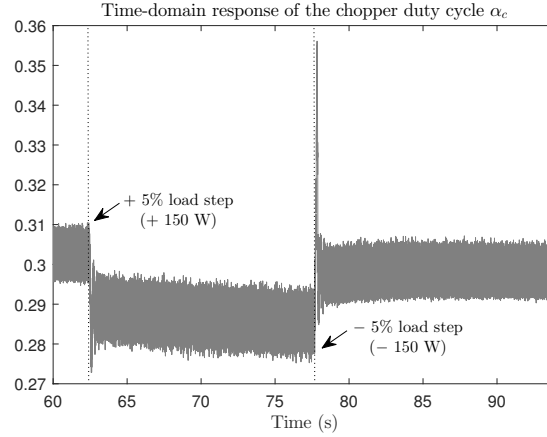


Figure 4.14 – Experimental result for the time-domain response of the chopper duty cycle α_c under small load step disturbances of $\pm 5\%$ of the load rated active power (± 150 W) with respect to the rated operating point.

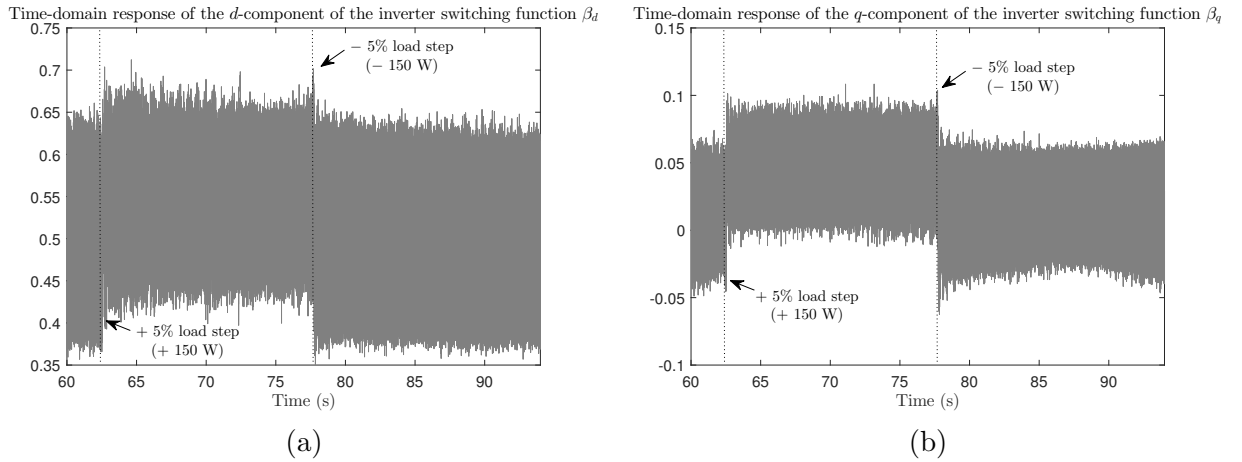


Figure 4.15 – Experimental results for the time-domain responses of (a) the d -component β_d and (b) the q -component β_q of the inverter switching function under small load step disturbances of $\pm 5\%$ of the load rated active power (± 150 W) with respect to the rated operating point.

frequency control, the weighting function of the MG frequency variation $W_{perf_2}(s)$ should be redesigned with a small steady-state value of the MG frequency variation (smaller A_{ε_2}). Nevertheless, in this case, a high energy density of the storage device should be required and induces an increase in the investment cost [142].

Figure 4.14, Figure 4.15(a), and Figure 4.15(b) illustrate the experimental results for the time-domain responses of the chopper duty cycle α_c and the direct and quadrature components of the inverter switching function β_d and β_q , respectively, under small load step disturbances of $\pm 5\%$ of the load rated active power (± 150 W). Let us remark here that, due to slight parameter difference between the model and the real system, as well as unknown and/or neglected (unmodeled) dynamics of the real system, the initial real values

$\alpha_{c_e}^{real} = 0.303$, $\beta_{d_e}^{real} = 0.51$, and $\beta_{q_e}^{real} = 0.01$ are slightly different from those previously computed in Subsection 4.3.2, $\alpha_{c_e}^{com} = 0.32$, $\beta_{d_e}^{com} = 0.536$, and $\beta_{q_e}^{com} = 0.0143$. Moreover, there are high-frequency oscillations observed in α_c , β_d , and β_q , which are caused by measurement noise and converters' high-frequency behavior. Consequent to the load active power step disturbances of ± 150 W, α_c , β_d , and β_q vary between their imposed lower and upper bounds and do not exceed their saturation thresholds. Nevertheless, it should be noted here that, as observed from Figure 4.14, the time-domain response of α_c presents a large variation from its steady-state operating point following the load active power step disturbance of -150 W. This may be due to the some unmodeled dynamic effect exhibited in the supercapacitor voltage variation ΔV_{sc} , as well as to the time variance of actual parameters of the supercapacitor together with its converter. Moreover, it should be noted here that α_c does not come back to its initial steady-state value, and this is due to supercapacitor voltage decreasing. As can be observed from Figure 4.14, due to the unadapted sizing of the supercapacitor in relation to the existing system, the value α_{c_e} is rather close to its limit ($\alpha_c \in [0.2, 0.8]$), therefore from the energy point of view, this cannot ensure an optimal operation of the storage device in case of large load active power disturbances in the system which rapidly drive α_c to its limit.

In summary, under small load step disturbances of $\pm 5\%$ of the load rated active power (± 150 W), the proposed frequency robust control approach has been demonstrated to be effective, where the designed \mathcal{H}_∞ controller is able to ensure the imposed dynamic performance specifications. In the sequel, the experimental results are presented and discussed under more stressed conditions where larger load active power step changes are applied as disturbances.

4.3.5 Experimental validation under more stressed conditions (large load active power step disturbances)

The PI and \mathcal{H}_∞ controllers previously synthesized are now implemented in experiment under larger load active power variations. The idea is to evaluate more accurately the domain where the implemented robust control ensures stable and robust performance.

Table 4.2 presents some remarkable experimental results performed with load step disturbances from $\pm 5\%$ to $\pm 30\%$ of the load rated active power (from ± 150 W to ± 900 W). A comparative analysis among these results is hereafter presented and discussed.

Table 4.2 – Experimental results performed with load step disturbances from $\pm 5\%$ to $\pm 30\%$ of the load rated active power (from ± 150 W to ± 900 W), where σ means the overshoot and ε stands for the steady-state error.

Step disturbances ΔP_{load}	$\pm 5\% P_{load_e}$ (± 150 W)	$\pm 10\% P_{load_e}$ (± 300 W)	$\pm 20\% P_{load_e}$ (± 600 W)	$\pm 30\% P_{load_e}$ (± 900 W)
Performance specification on f_{grid}	✓	✓	✗	✗
Time-domain response of f_{grid}	$\sigma_{f_{grid}} = 0.036$ Hz $\varepsilon_{f_{grid}} = 0.009$ Hz	$\sigma_{f_{grid}} = 0.073$ Hz $\varepsilon_{f_{grid}} = 0.019$ Hz	$\sigma_{f_{grid}} = 0.146$ Hz $\varepsilon_{f_{grid}} = 0.041$ Hz	$\sigma_{f_{grid}} = 0.219$ Hz $\varepsilon_{f_{grid}} = 0.063$ Hz
Performance specification on V_{dc}	✓	✓	✓	✗
Time-domain response of V_{dc}	$ \sigma_{V_{dc}} = 7.5$ V $ \varepsilon_{V_{dc}} = 4.7$ V	$ \sigma_{V_{dc}} = 13.9$ V $ \varepsilon_{V_{dc}} = 8.4$ V	$ \sigma_{V_{dc}} = 26.5$ V $ \varepsilon_{V_{dc}} = 16.1$ V	$ \sigma_{V_{dc}} = 38.7$ V $ \varepsilon_{V_{dc}} = 23.8$ V
Performance specification on I_s	✓	✓	✓	✓
Time-domain response of I_s	$ \Delta I_{s,max} = 6.3$ A	$ \Delta I_{s,max} = 10$ A	$ \Delta I_{s,max} = 17$ A	$ \Delta I_{s,max} = 24.2$ A
Performance specification on I_{rd}	✓	✓	✓	✓
Time-domain response of I_{rd}	$ \Delta I_{rd,max} = 4.3$ A	$ \Delta I_{rd,max} = 6.8$ A	$ \Delta I_{rd,max} = 10.5$ A	$ \Delta I_{rd,max} = 14.2$ A
Time-domain response of ΔP_s	$ \Delta P_{s,max} = 294$ W	$ \Delta P_{s,max} = 466$ W	$ \Delta P_{s,max} = 797$ W	$ \Delta P_{s,max} = 1128$ W

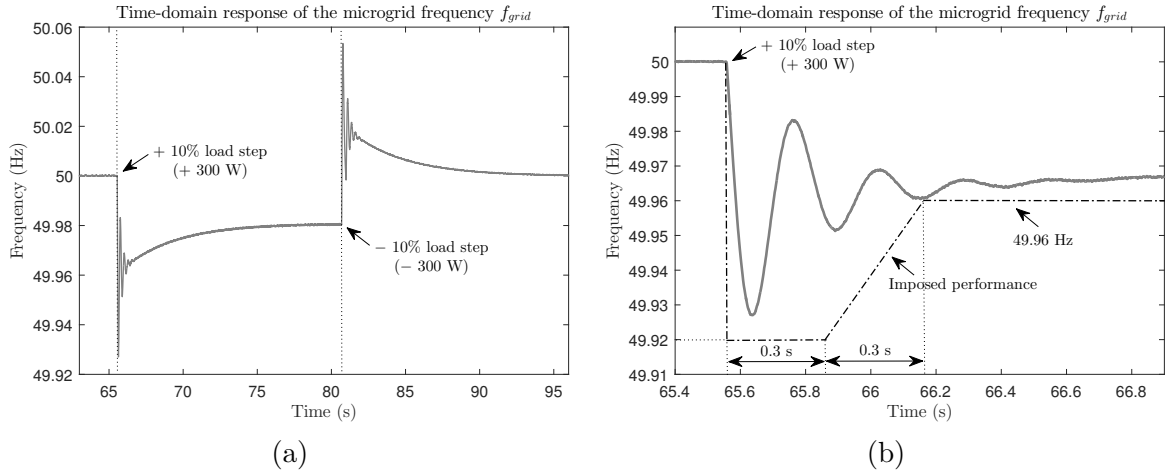


Figure 4.16 – (a) Experimental result for the MG frequency time-domain response f_{grid} under load step disturbances of $\pm 10\%$ of the load rated active power (± 300 W) with respect to the rated operating point. (b) Temporal zoom in the time interval $t \in [65.4, 66.9]$ s.

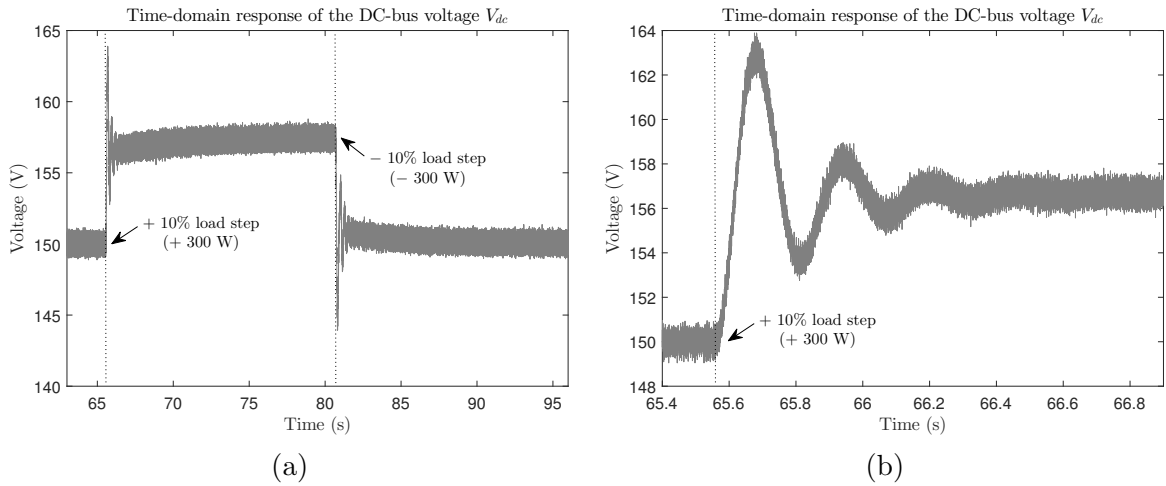


Figure 4.17 – (a) Experimental result for the DC-bus voltage time-domain response V_{dc} under load step disturbances of $\pm 10\%$ of the load rated active power (± 300 W) with respect to the rated operating point. (b) Temporal zoom in the time interval $t \in [65.4, 66.9]$ s.

Figure 4.16 and Figure 4.17 illustrate the experimental results for the time-domain responses of the MG frequency f_{grid} and DC-bus voltage V_{dc} , respectively, under load step disturbances of $\pm 10\%$ of the load rated active power (± 300 W). Although the \mathcal{H}_∞ controller is designed with respect to the performance specification in the frequency domain in the small-signal case (*i.e.*, a variation of $\pm 5\%$ (± 150 W) of the load rated active power), the imposed performance specification of f_{grid} corresponding to the choice of the weighting function $W_{perf_2}(s)$ (*i.e.*, maximum overshoot of 0.08 Hz, response time of approximately 0.6 s, admissible steady-state error of 0.04 Hz) is still respected in the time domain under larger load step disturbances of $\pm 10\%$ of the load rated active power (± 300 W), as shown in Figure 4.16. On the other hand, it can be seen from Figure 4.17 that the imposed time-domain performances

of V_{dc} corresponding to the tuning of the weighting function $W_{perf_1}(s)$ (*i.e.*, maximum overshoot of 7.5 V, response time of approximately 0.6 s, admissible steady-state error of 3.75 V) are not satisfied under load active power step disturbances of ± 300 W. However, the performance specification of V_{dc} imposed in Figure 4.6 (*i.e.*, maximum overshoot at 20% of its rated value V_{dc_e} (*i.e.*, 30 V), response time of approximately 1.2 s, admissible steady-state error at 10% of V_{dc_e} (*i.e.*, 15 V)) in response to any load active power step disturbances in the time domain is well guaranteed in this case. Thus, we can come to the conclusion that the action domain of the synthesized \mathcal{H}_∞ controller ensures robust performance with respect to the imposed weighting functions up to $\pm 10\%$ of load active power variations (± 300 W) around its steady-state operating point.

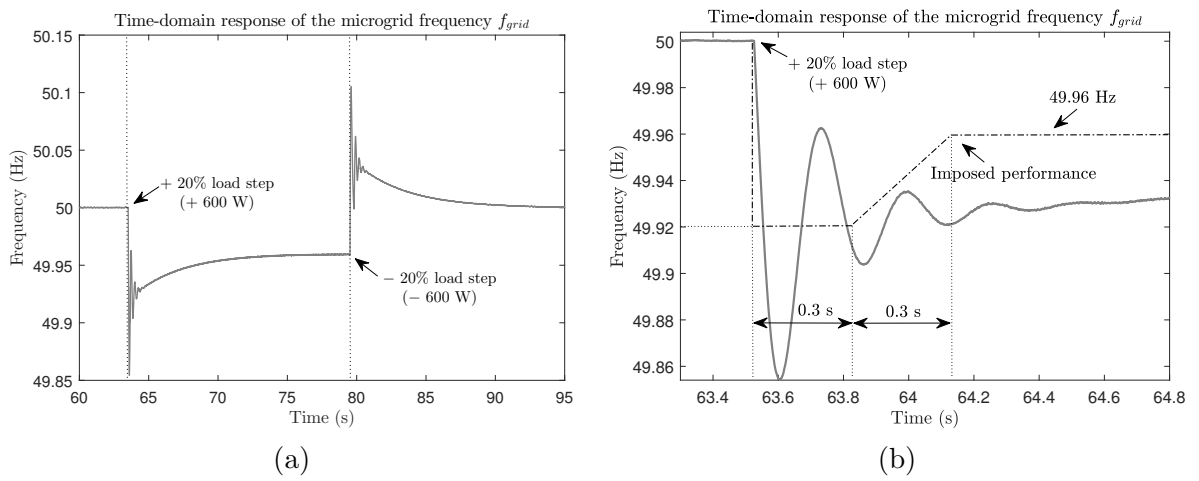


Figure 4.18 – (a) Experimental result for the MG frequency time-domain response f_{grid} under load step disturbances of $\pm 20\%$ of the load rated active power (± 600 W) with respect to the rated operating point. (b) Temporal zoom in the time interval $t \in [63.3, 64.8]$ s.

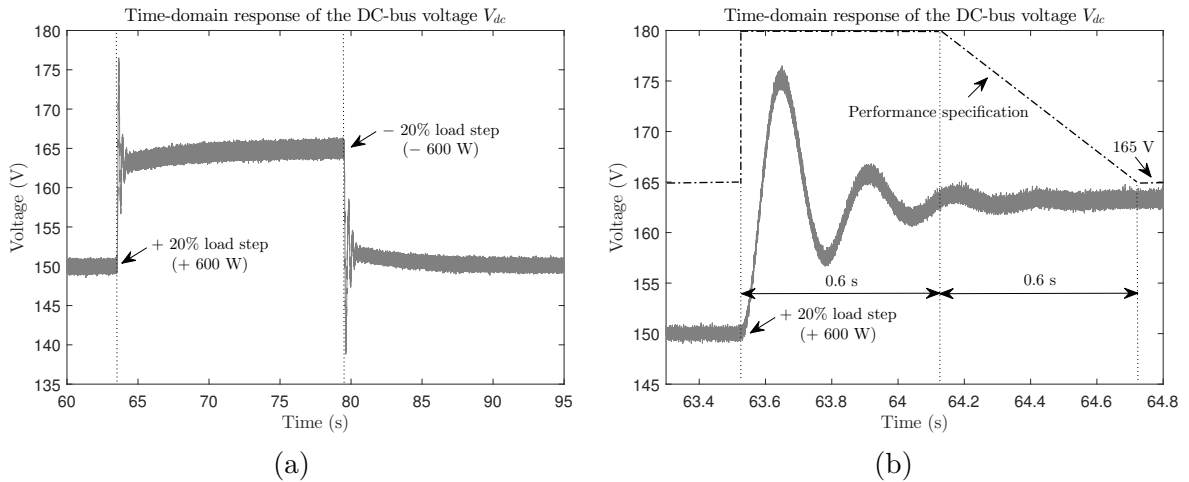


Figure 4.19 – (a) Experimental result for the DC-bus voltage time-domain response V_{dc} under load step disturbances of $\pm 20\%$ of the load rated active power (± 600 W) with respect to the rated operating point. (b) Temporal zoom in the time interval $t \in [63.3, 64.8]$ s.

Figure 4.18 and Figure 4.19 show the experimental results for the time-domain responses of the MG frequency f_{grid} and DC-bus voltage V_{dc} , respectively, under load step disturbances of $\pm 20\%$ of the load rated active power (± 600 W). In this case, the designed \mathcal{H}_∞ controller cannot guarantee the imposed performance specification of f_{grid} , as observed in Figure 4.18. On the other hand, the performance specification of V_{dc} imposed in Figure 4.6 is still satisfied, as depicted in Figure 4.19. Therefore, we can conclude that the synthesized \mathcal{H}_∞ controller ensures the performance specification of V_{dc} up to $\pm 20\%$ of load active power variations (± 600 W) around its steady-state operating point.

Figure 4.20 and Figure 4.21 present the experimental results for the time-domain responses

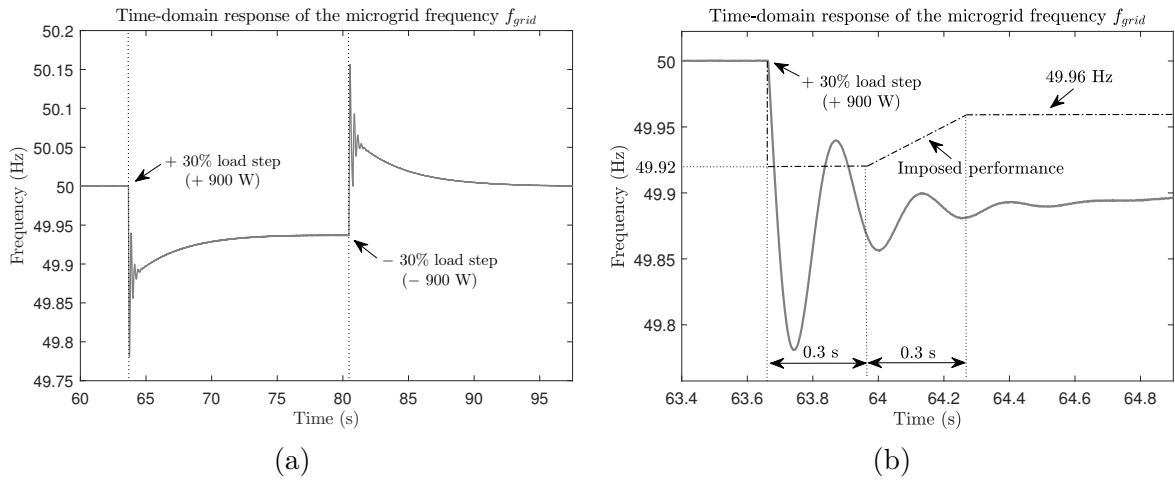


Figure 4.20 – (a) Experimental result for the MG frequency time-domain response f_{grid} under load step disturbances of $\pm 30\%$ of the load rated active power (± 900 W) with respect to the rated operating point. (b) Temporal zoom in the time interval $t \in [63.4, 64.9]$ s.

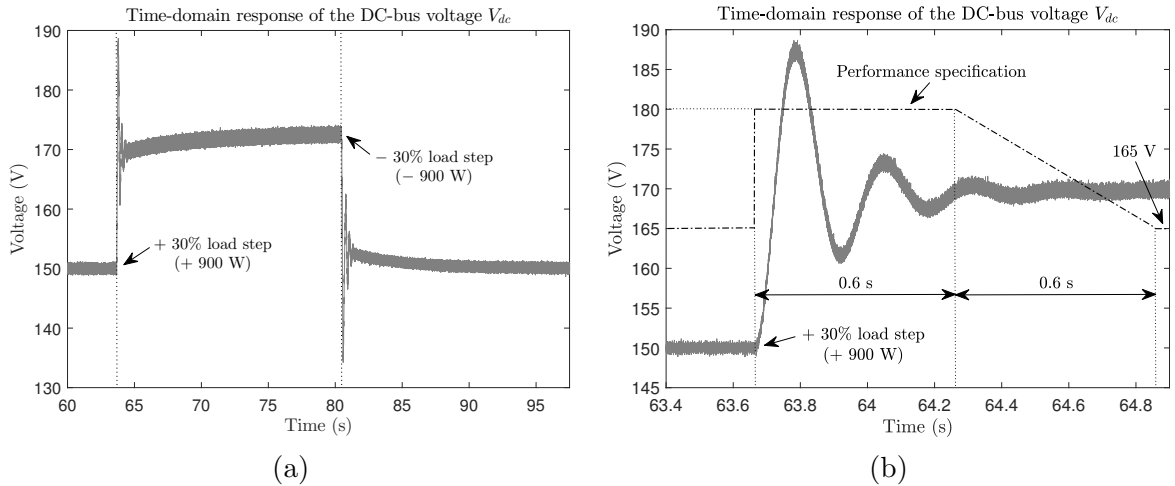


Figure 4.21 – (a) Experimental result for the DC-bus voltage time-domain response V_{dc} under load step disturbances of $\pm 30\%$ of the load rated active power (± 900 W) with respect to the rated operating point. (b) Temporal zoom in the time interval $t \in [63.4, 64.9]$ s.

of the MG frequency f_{grid} and DC-bus voltage V_{dc} , respectively, under load step disturbances of $\pm 30\%$ of the load rated active power (± 900 W). In this case, the performance specification of V_{dc} imposed in Figure 4.6 is no longer respected, as shown in Figure 4.21. Thus, under large load step disturbances which are more than or equal to $\pm 20\%$ of the load rated active power (± 600 W), the designed \mathcal{H}_∞ controller cannot guarantee the imposed performance specifications of f_{grid} and V_{dc} .

Figure 4.22, Figure 4.23, Figure 4.24, and Figure 4.25 present the experimental results for

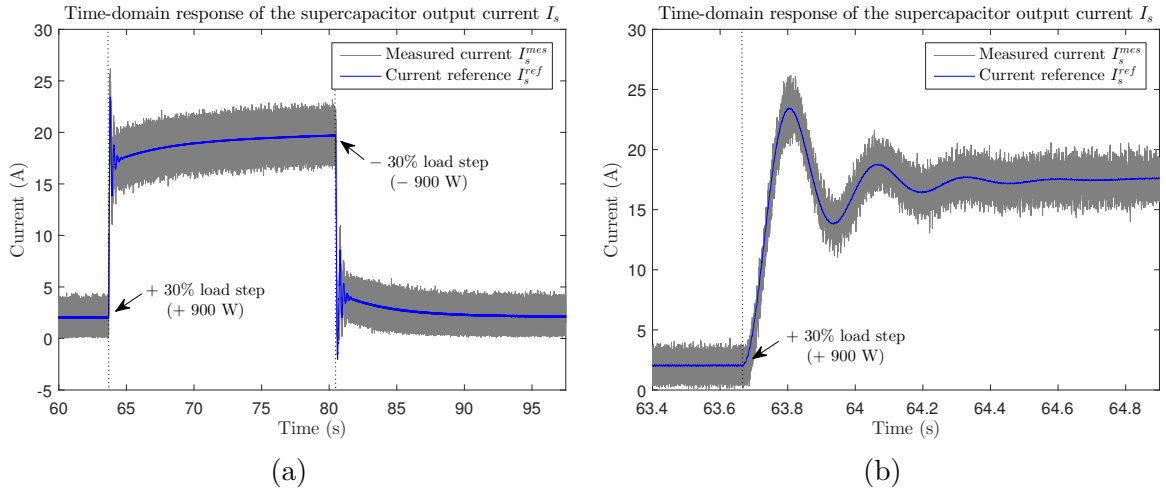


Figure 4.22 – (a) Experimental result for the time-domain response of the supercapacitor output current I_s under load step disturbances of $\pm 30\%$ of the load rated active power (± 900 W) with respect to the rated operating point. (b) Temporal zoom in the time interval $t \in [63.4, 64.9]$ s.

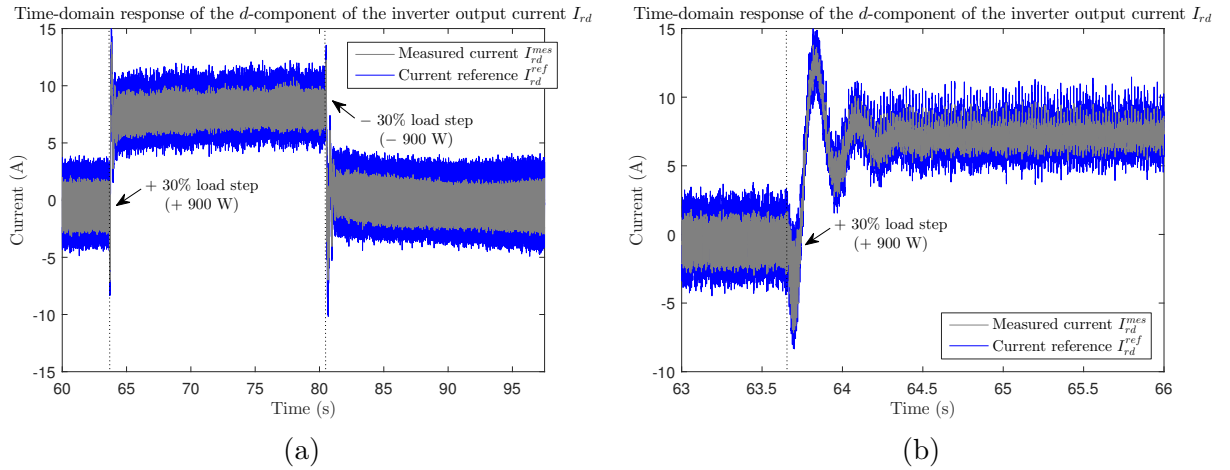


Figure 4.23 – (a) Experimental result for the time-domain response of the d -component of the inverter output current I_{rd} under load step disturbances of $\pm 30\%$ of the load rated active power (± 900 W) with respect to the rated operating point. (b) Temporal zoom in the time interval $t \in [63, 66]$ s.

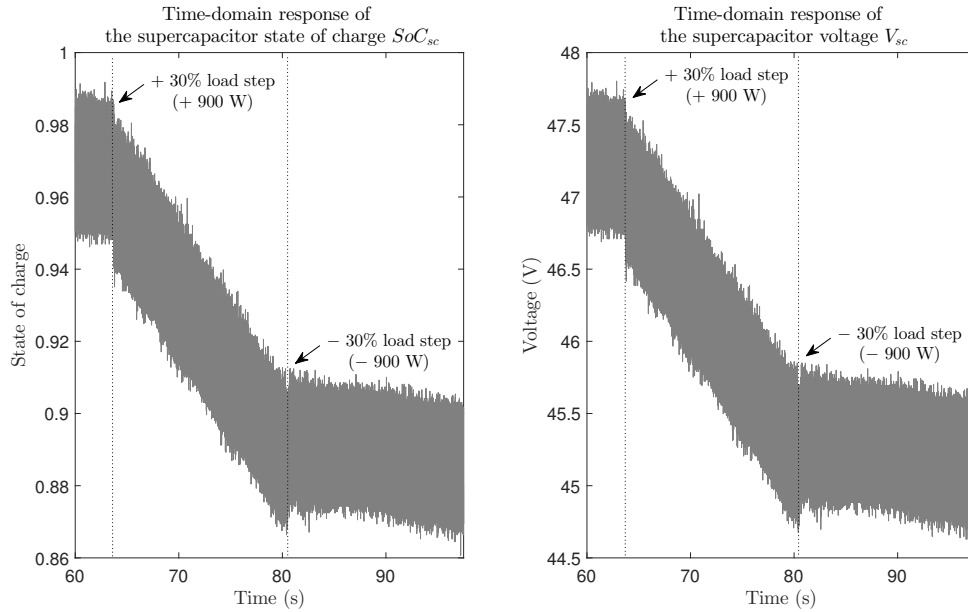


Figure 4.24 – Experimental results for the time-domain responses of the supercapacitor state of charge SoC_{sc} and voltage V_{sc} under load step disturbances of $\pm 30\%$ of the load rated active power (± 900 W) with respect to the rated operating point.

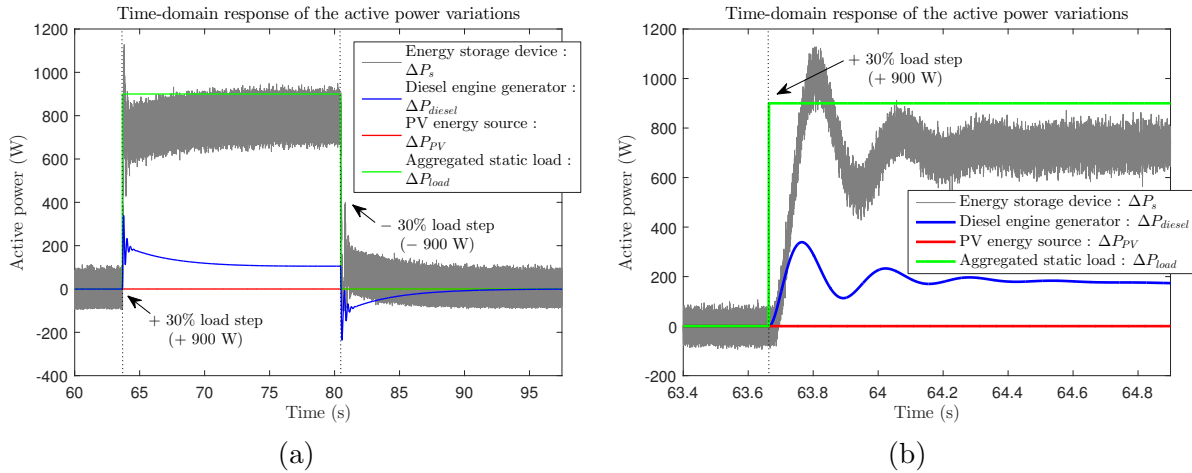


Figure 4.25 – (a) Experimental results for the active power variations of the sources and load under load step disturbances of $\pm 30\%$ of the load rated active power (± 900 W) with respect to the rated operating point. (b) Temporal zoom in the time interval $t \in [63.4, 64.9]$ s.

the time-domain responses of the supercapacitor output current I_s , the direct component of the inverter output current I_{rd} , together with their references, as well as the supercapacitor state of charge SoC_{sc} and voltage V_{sc} , and the active power variations of the sources and load, respectively, under load step disturbances of $\pm 30\%$ of the load rated active power (± 900 W). Concluding remarks similar to those in the aforementioned case in Subsection 4.3.4 can be deduced. As can be observed from Figure 4.22 and Figure 4.23, the admissible limit is ensured

for I_s and I_{rd} with respect to the choice of the weighting functions $W_u(s)$, which means that their imposed dynamic performance specifications are well satisfied up to $\pm 30\%$ of load active power variations (± 900 W). Consequent to the large load active power step disturbance of 900 W, the supercapacitor voltage V_{sc} decreases more rapidly than that previously presented in Figure 4.12 where a small load step of 150 W is applied as a disturbance. Moreover, it can be observed from Figure 4.25 that, consequent to the load active power step disturbance of 900 W, the maximum active power variation of the energy storage device is approximately equal to 1128 W, *i.e.*, $\Delta P_{s_{max}} = 1128$ W or $P_{s_{max}} = 1224$ W. This value is very close to its maximum possible active power of approximately 1500 W. Therefore, in order to ensure secure and reliable operation of the ESS, it should not be used to provide active power demand in case of large load step disturbances which are more than 30% of the load rated active power (900 W).

Some other experimental results in relation with the illustration in Table 4.2 are reported in Appendix E.

In short, the designed \mathcal{H}_∞ controller guarantees robust performance up to only $\pm 10\%$ of load active power variations (± 300 W) around its steady-state operating point. Use of an LPV control approach could be a feasible solution to ensure robust performance in case of larger load active power variations. Moreover, variations of the operating point (*e.g.*, changes in the steady-state value of the supercapacitor state of charge SoC_{sc_e} or voltage V_{sc_e} , PV system output power variations, *etc.*) should also be analyzed to test the control robustness.

4.4 Chapter conclusion

In this chapter, based on real-time digital simulators, namely RT-LAB[®] and dSPACE[®], a rapid-prototyping test bench composed of a real supercapacitor-based ESS and an emulated diesel-PV-load grid, has been implemented for the experimental validation of the proposed frequency robust control strategy in stand-alone MGs under realistic operating conditions. We have first set up a PHIL configuration in which the constitutive elements of the software and material architectures of the test bench, as well as the control architecture have been arranged and implemented. This test concept confers a great flexibility to the experiments. The changes in test scenarios can easily be implemented in MATLAB[®]/Simulink[®]. Similarly, the configuration of the system under test can also easily be modified. Moreover, this test bench allows to study other frequency control strategies. It is only required to change the control architecture under RT-LAB[®] or dSPACE[®].

Then, for the system under test, some preliminary steps needed for experimental validation, *e.g.*, definition of dynamic specifications, equilibrium point computation, control design, have been carried out. Next, we have performed a series of experiments to show the validity and effectiveness of the frequency robust control approach. The experimental results are demonstrated to be quasi-identical to the simulation ones, except for high-frequency oscillations or stresses observed in experiment due to some unavoidable reasons such as measurement error and/or noise, slight parameter difference between the model and the real system

and/or their variance in time, unknown and/or neglected (unmodeled) dynamics of the real system, converters' high-frequency behavior, unadapted design of the test bench, *etc.* The experimental results point out that the synthesized \mathcal{H}_∞ controller is able to ensure stable and robust performance up to $\pm 10\%$ of load active power variations (± 300 W) around its steady-state operating point. However, if time-domain specifications of the DC-link voltage V_{dc} are reasonably relaxed, then the designed controller performs robustly up to $\pm 20\%$ of load active power variations (± 600 W). In addition, it has been proved that the dynamic performance specifications imposed on the supercapacitor output current I_s and the direct component of the inverter output current I_{rd} are well guaranteed up to $\pm 30\%$ of load active power variations (± 900 W).

The control design parameters can effectively help at supercapacitor choice and resizing. Indeed, as the MG frequency variation with the ESS by \mathcal{H}_∞ control is fixed by the choice of the weighting function $W_{perf_2}(s)$, the imposed performance specification can be relaxed in order to increase the MG admissible frequency variation, resulting in power and energy reduction of the storage device, and therefore decreasing its investment cost.

Some other developments (*e.g.*, variations of the operating point, influence of parametric uncertainties, variations of system parameters, device aging, *etc.*) are also possible in order to test the control robustness. This will be detailed in the general conclusion and perspectives of this manuscript.

General conclusion and perspectives

General conclusion

This thesis has proposed an \mathcal{H}_∞ -based multi-variable robust control design approach for frequency and voltage stability in stand-alone MGs with a high penetration rate of RESs. A diesel-PV-supercapacitor hybrid power generation system operating in stand-alone mode has been considered as a sufficiently representative example of such MGs, with at least two power sources, either classical or renewable, and an energy storage unit, to be coordinated so as to satisfy voltage and primary frequency ancillary services. The considered problem has been formulated and solved in a systematic manner, where the following remarkable results have been obtained:

- Topological, as well as nonlinear and linear averaged models of each subsystem, then frequency-control-oriented modeling of the diesel-PV-storage hybrid power generation system operating in stand-alone mode have been detailed. Then, we have proposed a systematic design of a cascaded two-level robust control structure – where classical PI-based current tracking controllers are placed on the low control level and receive references from an \mathcal{H}_∞ -control-based upper level – for frequency stability in this kind of system. We have also carried out a robust performance analysis of the designed \mathcal{H}_∞ controller in the presence of various load disturbances, PV output active power variations, and model uncertainties so as to determine the maximum parameter variation range for which the imposed closed-loop performances are respected for the considered operating point. Numerical simulations performed with MATLAB[®]/Simulink[®] have shown the validity and effectiveness of the proposed frequency robust control strategy on a MVA-rated MG;
- We have also proposed voltage-control-oriented modeling for the diesel-PV-storage hybrid power generation system operating in stand-alone mode. In particular, topological, as well as nonlinear and linear averaged models of each subsystem have first been presented, then a voltage-control-oriented model of the whole system has been obtained by aggregating these sub-models. *Via* an “analysis-of-zeros” method based on Monte Carlo simulation, the influence of system parameters on the dynamic behavior of open-loop system measured outputs has been studied. Next, a voltage robust control design approach with the same idea of cascaded two-level structure – where an \mathcal{H}_∞ controller is placed on an upper control level and provides the references to current controllers placed on a lower level – has been developed in order to satisfy the required dynamic specifications. We have then validated the effectiveness of the proposed voltage robust control strategy, as well as the “analysis-of-zeros” method *via* MATLAB[®]/Simulink[®] closed-loop time-domain simulations. Finally, we have performed a sensitivity analysis of robust performance of the designed \mathcal{H}_∞ controller in the presence of various load reactive power disturbances and model uncertainties *via* a series of MATLAB[®]/Simulink[®]

closed-loop time-domain simulations;

- The proposed frequency robust control strategy in stand-alone MGs has experimentally been validated using a PHIL rapid-prototyping platform composed of a real supercapacitor-based ESS and an emulated diesel-PV-load grid based on real-time digital simulators, namely RT-LAB[®] and dSPACE[®]. First, for the system under test, some preliminary steps required for experimental validation, *e.g.*, definition of dynamic specifications, equilibrium point computation, control design, have been realized. Next, a series of experiments have been performed to show the validity and effectiveness of the frequency robust control approach. The experimental results have been demonstrated to be very close to the simulation ones, except for high-frequency oscillations or stresses observed in experiment due to some inherent experimental conditions which could be improved by the total re-design of the test bench.

Perspectives

The work presented in this manuscript opens a great number of perspectives both in short-term and long-term.

Short-term perspectives

- In the \mathcal{H}_∞ control design procedure, the choice of weighting functions parameters is still a challenging task, especially in case of high-order systems and when a large set of parameters have to be determined (*i.e.*, numerous control objectives need to be fulfilled at the same time). As a result, a further investigation on how to choose these parameters in a systematic and optimal manner (*i.e.*, automation for their design or expert modeling), for instance, through a genetic-algorithm-based multi-objective optimization method, is necessary, from which an useful guide can be created for practical control engineers in the future;
- It may be interesting to study the link between time-domain specifications (or desired control objectives) of the MG and frequency-domain specifications (*via* weighting functions in the \mathcal{H}_∞ control structure), from which one can optimally choose the forms and the parameters of these weighting functions;
- Frequency and voltage stability issues in stand-alone MGs, together with their control structures, have separately been addressed in this thesis framework. In reality, both of these control objectives must simultaneously be satisfied. In order to achieve this, a novel cascaded two-level control structure – based on the same idea, that is, where classical PI-based current tracking controllers are placed on the low control level and receive references from an \mathcal{H}_∞ -control-based upper level – should be used. Moreover, inside the upper control level, two different \mathcal{H}_∞ controllers, namely \mathcal{H}_∞ frequency and \mathcal{H}_∞ voltage ones, are superposed. This idea is illustrated in Figure 4.26. This novel

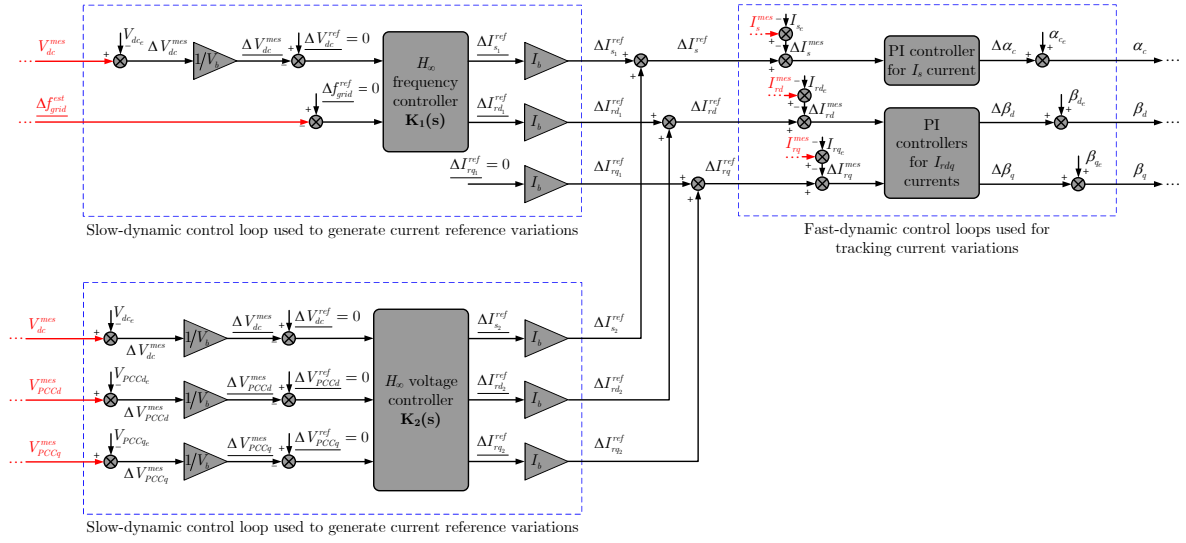


Figure 4.26 – Block diagram of the novel global control structure for MG frequency and PCC voltage regulation.

control structure will allow to regulate the MG frequency and the PCC voltage in case of *simultaneous* active and reactive power disturbances in the system;

- Practical validation of the voltage robust control strategy proposed in Chapter 3 on the real-time test bench is also envisaged, while evolving a little bit our emulated MG;
- A reduced-order version of the full-order \mathcal{H}_∞ controller should also be computed, which is a valuable step to reduce complexity and computational burden from a practical implementation point of view;
- Another interesting prospect is the ability to come back over grid code requirements on MG frequency and PCC voltage deviations in order to improve dynamic and long-term performances;
- Use of the \mathcal{H}_∞ robust control approach may not guarantee the desired dynamic performance specifications in the presence of large disturbance in the system. In this case, design of an LPV control approach may be an interesting solution so as to ensure good performance despite variations of the operating point (*e.g.*, ESS capacity, PV system output power, load power, *etc.*), while simultaneously taking into account the influence of time-varying system parameters and possibly device aging. The LPV controller can automatically adapt its parameters for different operating points;
- A coordinated control strategy of the diesel engine generator, ESS, PV system, and demand-side management using \mathcal{H}_∞ robust control should also be studied, which is a promising solution for stabilizing the MG frequency and PCC voltage.

Long-term perspectives

- An MG can be either connected or disconnected from a host grid. When operating in grid-connected mode, the MG voltage and frequency are set by the host grid. In this case, DG units and ESSs usually operate in current-controlled mode. Their interface converters are mainly designed to deliver power to an infinite-power grid. Therefore, a control strategy, different from that already applied in isolated mode of MG operation, will be required for these grid-feeding power converters to make them perfectly synchronized with the AC voltage at the PCC and to allow regulating accurately their active and reactive power exchanged with the utility grid. It is usually said that the MG operates in this case in P/Q mode. Moreover, the smooth transition between two modes of operation should also be studied;
- Application of the μ -synthesis control technique, where uncertainties in an MG can be modeled as a structured/parametric type, may be a very promising solution in order to avoid nonexact conservative results which are sometimes obtained with an unstructured-uncertainty-based control technique. This structured/parametric-uncertainty-based robust control strategy provides quite better performance and control accuracy than the case of the μ -controller with unstructured uncertainty, as well as the \mathcal{H}_∞ controller, as stated in the work of Bevrani *et al.* [14];
- Experimental testing on a dedicated benchmark system is also envisaged in order to analyze comparatively different control approaches (*e.g.*, robust control, adaptive control, artificial-intelligence-based control, model predictive control, sliding mode control, *etc.*) in terms of effectiveness, flexibility, simplicity, ease of implementation, and impact on the lifespan of devices, especially the ESS;
- True technical and economic assessment of the proposed robust control approach compared to more classical control methods should also be envisaged;
- A further investigation on how to deploy the proposed robust control methodology on complex MGs for multi-converter and multi-source systems should also be taken into account.

Résumé en français

L'architecture des réseaux électriques ainsi que leur gestion sont conçues et adaptées dans des conditions réalistes pour alimenter de manière optimale les consommateurs quelles que soient les modes de production et de consommation. Initialement conçue pour alimenter des consommateurs à partir de centrales de production nucléaires, thermique, ou hydraulique, l'architecture des réseaux électriques vont dans l'avenir connaître des évolutions majeurs, avec notamment l'arrivée de nombreux acteurs économiques et unités de production de faible puissance (unités de cogénération, générateurs à base d'énergie renouvelable ou non conventionnelle) non interfacés avec un poste de supervision conduisant à de profondes mutations sur la gestion des systèmes électriques actuels, y compris les variables techniques, environnementales, et financières. Une évolution vers de nouvelles architectures bien adaptées à ces nouveaux modes de production dispersée sera à imaginer pour les temps futurs. La définition de microréseaux, comme ceux déjà présents dans les îles ou les zones isolées, pourrait être une réponse à ce développement [105], [71].

Les microréseaux présentent deux caractéristiques intrinsèques essentielles qui en font un intérêt majeur pour le développement des réseaux électriques du futur:

- La proximité entre une production locale d'électricité et les différents consommateurs conduit à une minimisation immédiate des pertes liées au transport de l'énergie;
- La capacité de fonctionnement distinctive en mode autonome de microréseaux a permis de prendre des mesures de fiabilité plus élevées pour répondre aux demandes d'énergie lorsque le réseau principal n'est pas disponible.

Les futurs systèmes énergétiques seront ainsi des systèmes multi-convertisseurs et multi-sources, avec notamment l'insertion massive des sources d'énergie renouvelable et de stockage interfacées par des convertisseurs d'électronique de puissance et la tendance actuelle à privilégier l'électricité comme vecteur énergétique. Cela concernera notamment les microréseaux d'énergie, les réseaux de bâtiments ou d'éco-quartiers, et les futurs réseaux intelligents (au niveau de la distribution et même du transport). Ces systèmes électriques, intégrant les microréseaux, devront être ainsi partiellement ou totalement re-conçus pour intégrer ces nouvelles sources intermittentes qui perturberont la qualité d'alimentation en énergie en raison de leur très faible puissance de court-circuit. De plus, le développement d'interfaces d'électronique de puissance peut potentiellement induire un fonctionnement instable en raison des interactions dynamiques et harmoniques générées par les convertisseurs. Les incertitudes liées aux conditions météorologiques ou au dimensionnement paramétrique jouent également un rôle majeur dans l'absence de fiabilité des microréseaux, ce qui induit un surdimensionnement des différents composants dans les microréseaux, tels que les dispositifs de stockage.

Les problématiques de recherche associées aux microréseaux concernent ainsi le

développement de stratégies de pilotage optimales permettant de maximiser la qualité de l'énergie, sécuriser les approvisionnements, gérer les intermittences et leurs impacts sur le réseau en recourant par exemple aux dispositifs de stockage, maximiser le rendement, les performances, les fiabilités, et les coûts associés au système. Les principales difficultés seront associées à la nécessité d'appréhender les interactions et les couplages entre les différents composants au sein de ces systèmes, et donc de disposer de modèles statiques, dynamiques, et harmoniques permettant de prendre en compte l'évolution des configurations du réseau en fonction des aléas climatiques ou des stratégies de pilotage de charge. Dans les microréseaux autonomes, les problèmes de stabilité et de pilotage sont parmi les principaux défis en raison de la faible inertie, des incertitudes, et de la nature intermittente des ressources énergétiques dispersées [151]. Le maintien des écarts de fréquence et de tension dans leur plage prédéfinie est toujours critique en mode de fonctionnement autonome. Des systèmes de stockage d'énergie à haute fréquence – *e.g.*, des batteries au lithium-ion, des volants d'inertie, ou des supercondensateurs – sont donc devenus nécessaires, conduisant à de nouvelles configurations de réseau, pour lesquelles des structures de contrôle avancées plus complexes sont nécessaires pour alimenter les microréseaux avec des spécifications de performance souhaitables dans une large gamme de conditions de fonctionnement malgré de multiples contraintes telles que des perturbations inattendues et des incertitudes de modèle. Ce genre de problème conduit bien sûr à quelques questions comme suit:

- Par conséquent, quelle technologie de stockage d'énergie convient pour la stabilité de fréquence et de tension dans un microréseau autonome en tenant compte de la fréquence de coupure de chaque technologie de stockage (*i.e.*, compromis entre son énergie et sa puissance disponibles), son coût et sa durée de vie, ainsi que le coût global de possession ?
- Quelle technique de contrôle avancée est appropriée pour gérer de manière systématique de multiples demandes afin de garantir la stabilité et la performance globale robuste ?
- Comment traduire les demandes d'ingénierie spécifiques de l'opération du microréseau dans un formalisme de contrôle ? Plus particulièrement, comment définir les spécifications optimales sur les performances du réseau afin d'optimiser le comportement des microréseaux ?
- Comment prendre en compte les impacts des perturbations inattendues et des incertitudes du modèle dans la synthèse du contrôleur ?

L'objectif de cette thèse est donc de proposer des solutions à ces problématiques et notamment de définir une procédure de conception de contrôle robuste et systématique pour la stabilité de fréquence et de tension dans les microréseaux autonomes avec un fort taux de pénétration photovoltaïque en recourant aux dispositifs de stockage. Il serait également important de valider cette approche de contrôle à l'aide d'un banc expérimental.

Ce projet de doctorat, un travail conjoint, a reçu le soutien financier du Ministère de l'Enseignement Supérieur et de la Recherche et a été préparé au sein du Laboratoire de Génie Électrique de Grenoble (G2Elab) et du Laboratoire de Grenoble Images Parole Signal Automatique (GIPSA-lab), Institut Polytechnique de Grenoble (Grenoble INP).

Certaines études sur le contrôle robuste de divers systèmes ont déjà été menées au G2Elab et au GIPSA-lab.

A la thèse de doctorat de Sautreuil [173], une nouvelle méthodologie pour la conception des équipements a été proposée, en utilisant la robustesse comme indicateur de leur « capacité d'intégration » dans le système. L'accent est mis sur comment un contrôle dynamique robuste peut résoudre le problème d'intégration du sous-système à un poids minimum. Cette méthode est ensuite appliquée à trois structures de conversion AC/DC pour le système de génération d'avions futurs (une unité de redresseur de transformateur automatique, une unité de redresseur à diodes à 6 phases, et un redresseur commandé par ondes), où l'auteur établit les liens entre des normes, la robustesse, et la masse.

Hernández-Torres a présenté dans sa thèse de doctorat [74] la conception de plusieurs stratégies de contrôle robustes multi-variables pour un générateur de puissance hybride comprenant une pile à combustible et une source auxiliaire de stockage d'énergie. Différentes stratégies de contrôle sont proposées pour les convertisseurs d'élevateur du bus continu. Cette méthodologie de contrôle est également adoptée pour une opération en mode isolé du réseau considérant le contrôle supplémentaire d'un onduleur de source de tension. L'analyse de robustesse aux incertitudes paramétriques par la μ -analyse est également étudiée. En outre, pour le sous-système de compression d'air, une approche de contrôle LPV basée sur l'ordonnancement de gain a été proposée. Le contrôle LPV est également considéré pour gérer certaines incertitudes du système données.

A la thèse de doctorat de Mongkoltanatas [142], l'utilisation du stockage d'énergie pour maintenir la stabilité de fréquence dans les microréseaux isolés avec un fort taux de pénétration d'énergies renouvelables est étudiée. L'auteur a mis l'accent sur le dimensionnement approprié du stockage d'énergie et la comparaison de différentes stratégies pour la participation au réglage primaire de fréquence du stockage dans les microréseaux isolés avec un fort taux de pénétration photovoltaïque. Un contrôleur \mathcal{H}_∞ est également conçu pour la participation au réglage primaire de fréquence du système de stockage d'énergie.

Nwesaty a présenté dans sa thèse de doctorat [150] une conception de contrôle LPV/ \mathcal{H}_∞ des systèmes de gestion d'énergie embarqués pour les véhicules électriques. Une stratégie de partage de puissance générique et non liée au cycle de charge parmi trois différents types de sources commandées par courant et fonctionnées en parallèle – pile à combustible, batterie, et supercondensateur – basée sur un contrôleur MIMO LPV/ \mathcal{H}_∞ est proposée par rapport aux caractéristiques de fréquence de sources. Au moyen d'un algorithme génétique dont le critère d'optimisation exprime les demandes de séparation de fréquence, les paramètres de fonctions de pondération peuvent être obtenus. De plus, un contrôleur LPV/ \mathcal{H}_∞ d'ordre réduit est également calculé pour traiter une implémentation embarquée avec un fardeau de calcul limité.

Ce travail est alors compatible avec ces précédentes thèses de doctorat, mais en mettant l'accent sur les services système de tension et de fréquence primaire et une validation en temps réel pour prouver l'intérêt d'un tel système de gestion d'énergie avancé.

Structure de la thèse

Ce manuscrit est organisé en quatre chapitres comme suit.

Suite à cette introduction, le premier chapitre, noté « *Background* », est consacré à l'introduction du sujet du fonctionnement et du contrôle des microréseaux. Plus précisément, un compte rendu de la recherche dans le contexte des microréseaux, y compris le concept des microréseaux, la classification des microréseaux, le fonctionnement et le contrôle des microréseaux, le stockage d'énergie dans les microréseaux et les applications des générateurs synchrones virtuels pour les microréseaux, est d'abord fourni. Ensuite, une identification et une classification des stratégies de contrôle les plus largement utilisées dans les microréseaux sont présentées. Ensuite, un état de l'art sur les techniques de contrôle classiques et avancées appliquées aux microréseaux, tels que le contrôle PI/PID, le régulateur quadratique linéaire, le contrôle par mode glissant, le contrôle prédictif par modèle, le contrôle basé sur l'intelligence artificielle, le contrôle adaptatif, et le contrôle robuste, ainsi qu'une analyse comparative entre ces techniques de contrôle, sont introduits. Le contrôle robuste, plus précisément le contrôle \mathcal{H}_∞ , qui s'avère plus avantageux que d'autres techniques de contrôle, est utilisé pour les études de stabilité de fréquence et de tension dans notre étude de cas – un système de génération de puissance hybride diesel-photovoltaïque-stockage fonctionnant en mode autonome – dans les prochains chapitres. Enfin, quelques notions de base sur la théorie du contrôle \mathcal{H}_∞ , ainsi que les méthodes disponibles pour la conception de contrôle et l'analyse de robustesse, sont détaillées.

Le deuxième chapitre, intitulé « *Robust control for primary frequency ancillary service in stand-alone microgrids* », présente d'abord la modélisation orientée fréquence-contrôle et puis propose une conception systématique d'une structure de contrôle robuste multi-variable pour la stabilité de fréquence dans un système de génération de puissance hybride diesel-photovoltaïque-stockage fonctionnant en mode autonome. La structure de contrôle proposée repose sur une architecture à deux niveaux: les contrôleurs d'asservissement de courant basés sur le contrôle PI classique sont placés sur le niveau de contrôle inférieur et reçoivent des références d'un niveau supérieur qui, lui, est basé sur le contrôle \mathcal{H}_∞ . Une méthodologie compréhensive qui traduit les demandes d'ingénierie spécifiques du fonctionnement du microréseau dans le formalisme de contrôle \mathcal{H}_∞ est détaillée. Il est également montré comment les spécifications de performance dynamiques en boucle fermée doivent à leur tour être prises en compte dans la configuration et le dimensionnement initiaux du microréseau, c'est-à-dire en choisissant de manière appropriée et en évaluant le système de stockage d'énergie. Ensuite, une analyse de performance robuste du contrôleur \mathcal{H}_∞ synthétisé en présence de diverses perturbations de charge, de variations de puissance active de la source photovoltaïque, et d'incertitudes de modèle est effectuée afin de déterminer la plage de variation maximale des paramètres pour laquelle les performances imposées en boucle fermée sont respectées pour le point de fonctionnement considéré. Les simulations numériques effectuées avec MATLAB[®]/Simulink[®] montrent l'efficacité de la stratégie de contrôle robuste de la fréquence proposée sur un microréseau d'ordre de quelques MVA.

Le troisième chapitre, intitulé « *Voltage robust control in stand-alone microgrids* »,

présente d'abord la modélisation orientée tension-contrôle pour le système de génération de puissance hybride diesel-photovoltaïque-stockage étudié fonctionnant en mode autonome. Ensuite, l'influence des paramètres du système sur le comportement dynamique des sorties mesurées du système en boucle ouverte est étudiée au moyen d'une méthode « analyse de zéros » basée sur la simulation de Monte Carlo. Nous nous concentrons ensuite sur le calcul d'un contrôleur de tension multi-variable basé sur \mathcal{H}_∞ afin de forcer robustement l'amplitude de tension du point de couplage commun à satisfaire les spécifications dynamiques requises. La même idée de la structure de contrôle à deux niveaux en cascade – où ce contrôleur est placé sur un niveau de contrôle supérieur et fournit les références aux contrôleurs de courant placés sur un niveau inférieur – est également adoptée. L'efficacité de la stratégie de contrôle robuste de tension proposée et de la méthode « analyse de zéros » est validée *via* des simulations de domaine temporel en boucle fermée MATLAB[®]/Simulink[®]. Enfin, une analyse de sensibilité de la performance robuste du contrôleur \mathcal{H}_∞ synthétisé en présence de diverses perturbations de charge et d'incertitudes de modèle est étudiée basée sur des simulations de domaine temporel MATLAB[®]/Simulink[®].

Dans le quatrième chapitre, nommé « *Frequency robust control real-time validation using a rapid-prototyping test bench* », un banc de test de prototypage rapide composé d'un système de stockage d'énergie réel à base de supercondensateur et d'un réseau diesel-photovoltaïque-charge émulé, est mis en œuvre pour la validation expérimentale de la stratégie de contrôle robuste de la fréquence proposée dans les microréseaux autonomes sous des conditions de fonctionnement réalistes. Les tests sont exécutés sur des simulateurs numériques en temps réel, à savoir RT-LAB[®] et dSPACE[®]. Nous avons d'abord mis en place une configuration PHIL dans laquelle les éléments constitutifs des architectures logicielles et matérielles du banc d'essai, ainsi que l'architecture de contrôle, sont organisés et implémentés. Ensuite, pour le système testé, certaines étapes préliminaires nécessaires pour la validation expérimentale, *e.g.*, la définition des spécifications dynamiques, le calcul du point d'équilibre, la conception du contrôle, sont réalisées. Enfin, une série de essais sous divers scénarios de test est effectuée pour montrer la validité et l'efficacité de l'approche de contrôle robuste de la fréquence proposée.

Le manuscrit se termine par une conclusion générale recueillant les résultats les plus pertinents, puis décrivant quelques travaux de recherche futurs.

Contribution de la thèse

Cette thèse fournit une application efficace du contrôle robuste multi-variable pour un système de génération de puissance hybride diesel-photovoltaïque-stockage fonctionnant en mode autonome ou des microréseaux isolés. La méthodologie utilisée dans la stratégie de contrôle vise à fournir une approche systématique, où la conception de contrôle est facile à réaliser. Un accent est mis sur le contrôle \mathcal{H}_∞ . Plus précisément, les principales contributions sont les suivantes.

Contrôle robuste pour le service système de fréquence primaire

- Nous présentons d'abord une modélisation orientée fréquence-contrôle et puis proposons une conception systématique d'une structure de contrôle robuste à deux niveaux en cascade pour la stabilité de fréquence dans un système de génération de puissance hybride diesel-photovoltaïque-stockage fonctionnant en mode autonome;
- Nous développons une méthodologie compréhensive dans laquelle les demandes d'ingénierie spécifiques du fonctionnement du microréseau sont traduites dans le formalisme de contrôle \mathcal{H}_∞ ;
- Nous effectuons une analyse de performance robuste du contrôleur \mathcal{H}_∞ synthétisé en présence de diverses perturbations et d'incertitudes de modèle;
- Nous présentons une validation expérimentale de la stratégie de contrôle robuste de la fréquence proposée dans des microréseaux autonomes sur un banc de test PHIL à prototypage rapide.

Contrôle robuste de tension

- Nous proposons une modélisation orientée tension-contrôle pour un système de génération de puissance hybride diesel-photovoltaïque-supercondensateur fonctionnant en mode autonome;
- Nous proposons une méthode « analyse de zéros » basée sur la simulation de Monte Carlo pour le système en boucle ouverte;
- Nous développons une stratégie de contrôle robuste hiérarchique à deux niveaux pour la stabilité de tension dans les microréseaux autonomes afin de satisfaire les spécifications de performance dynamique requises;
- Nous effectuons une analyse de sensibilité de la performance robuste du contrôleur \mathcal{H}_∞ synthétisé en présence de diverses perturbations et d'incertitudes de modèle.

Méthodologie

- Nous développons une méthode de co-conception complète pour les systèmes de stockage d'énergie;
- Nous développons une approche de contrôle robuste sur les microréseaux complexes.

Parameters of the studied microgrid for frequency and voltage control

Table A.1 – Parameters of the studied MG for frequency control.

Symbol	Description	Value	Unity
Microgrid			
S_b	Power base unit	2	MVA
H	Simplified equivalent inertia constant	2	MW.s
$\underline{H} = \frac{H}{S_b}$	Per-unitized simplified equivalent inertia constant	1	pu
Diesel engine generator			
$P_{diesel, rated}$	Rated active power	1.6	MW
$P_{diesele}$	Initial active power	1	MW
s_{diesel}	Droop value for primary frequency control	1.5	Hz/MW
$\underline{s}_{diesel} = s_{diesel} \frac{S_b}{f_b}$	Per-unitized droop value for primary frequency control	0.06	pu
K_i	Inverse of the response time for secondary frequency control	0.08	MW/Hz
$\underline{K}_i = K_i \frac{f_b}{S_b}$	Inverse of the response time in a per-unit frame for secondary frequency control	2	pu
T_{diesel}	Time constant	0.22	s
Photovoltaic energy source			
$P_{PV, rated}$	Rated active power	0.25	MW
P_{PVe}	Initial active power	0.2	MW
Aggregated load			
$P_{load, rated}$	Rated active power	1.85	MW
P_{load_e}	Initial active power	1.2	MW
D_{load}	Simplified damping constant	0	MW/Hz
$\underline{D}_{load} = D_{load} \frac{f_b}{S_b}$	Per-unitized simplified damping constant	0	pu

Table A.2 – Parameters of the supercapacitor-based ESS for frequency and voltage control.

Symbol	Description	Value	Unity
General characteristics			
S_{rated}	Rated apparent power	600	kVA
P_{rated}	Rated active power	500	kW
U_{rated}	Rated output phase-to-phase voltage of the three-phase inverter	400	V
I_{rated}	Rated output phase current of the three-phase inverter	≈ 870	A
I_{rdmax}	Maximum value of the d -component of the inverter output current (computed)	1250	A
η_{ess}	DC/AC global efficiency of the energy conversion chain	≈ 95	%
Choke			
L_c	Inductance	2.2	mH
R_c	Resistance	2.5	m Ω
Chopper			
f_{sc}	IGBTs Semikron SKiiP 2403GB122-4DW with $U_{max} = 1200$ V and $I_{max} = 2400$ A PWM switching frequency	4	kHz
DC bus			
C_{dc}	Capacitance	195	mF
R_{dc}	Resistance	167	Ω
V_{dc}^{ref}	Setpoint value of the voltage	1000	V
Three-phase inverter			
f_{si}	IGBTs Semikron SKiiP 1803GB122-3DW with $U_{max} = 1200$ V and $I_{max} = 1800$ A PWM switching frequency	4	kHz
Output filter			
L_f	Inductance	0.46	mH
R_f	Series resistance	4.8	m Ω
C_f	Capacitance	153	μ F
R_{fp}	Parallel resistance	16	Ω
Supercapacitor bank			
C_{sc}	16s \times 6p Maxwell BMOD0165-P048 Capacitance	61.9	F
R_{sc}	Series resistance	16.8	m Ω
R_{scp}	Parallel resistance	231	Ω
V_{scmin}	Minimum voltage (chosen)	390	V
V_{scmax}	Maximum voltage (chosen)	780	V
I_{smax}	Maximum value of the output current (computed)	≈ 1440	A
P_{smax}	Maximum active power	≈ 526	kW

Table A.3 – Parameters of the studied MG for voltage control.

Symbol	Description	Value	Unity
Microgrid			
S_b	Power base unit	2	MVA
$H' = H + H_{grid}$	Studied equivalent inertia constant		MW.s
$\underline{H}' = \frac{H'}{S_b}$	Per-unitized studied equivalent inertia constant		pu
Diesel engine generator system			
P_{rated}	Rated output active power	1.6	MW
Q_{rated}	Rated output reactive power	1.2	MVAr
Photovoltaic system			
$P_{PV_{rated}}$	Rated output active power	0.25	MW
$Q_{PV_{rated}}$	Rated output reactive power	0.1875	MVAr
Aggregated load			
$P_{load_{rated}}$	Rated active power	1.85	MW
$Q_{load_{rated}}$	Rated reactive power	1.3875	MVAr
$D'_{load} = D_{load} + D_{grid}$	Studied damping constant		MW/Hz
$\underline{D}'_{load} = D'_{load} \frac{f_b}{S_b}$	Per-unitized studied damping constant		pu

Table A.4 – Parameters of the diesel engine generator system for voltage control.

Symbol	Description	Value	Unity
Step-up transformer TRIHAL 0.4/20 kV 2000 kVA			
$S_{t_{rated}}$	Rated apparent power	2000	kVA
$U_{1_{rated}}$	Rated primary phase-to-phase voltage	20	kV
U_{2_0}	No-load secondary phase-to-phase voltage	410	V
ΔP_0	No-load loss	4000	W
u_{sc}	Short-circuit voltage	6	%
i_0	No-load current	1.1	%
ΔV_2	Voltage drop at full load with $\cos\varphi = 1$	1.18	%
ΔV_2	Voltage drop at full load with $\cos\varphi = 0.8$	4.44	%
Transmission line 20 kV			
R_{l_0}	Resistance per kilometer	1.466	Ω/km
L_{l_0}	Inductance per kilometer	0.48	mH/km
C_{l_0}	Capacitance per kilometer	0.14	$\mu\text{F}/\text{km}$
R_{l_p}	Parallel resistance	12.5	k Ω

Table A.5 – Parameters of the ESS step-up transformer for voltage control.

Symbol	Description	Value	Unity
Step-up transformer TRIHAL 0.4/20 kV 630 kVA			
$S_{t_{rated}}$	Rated apparent power	630	kVA
$U_{1_{rated}}$	Rated primary phase-to-phase voltage	20	kV
U_{2_0}	No-load secondary phase-to-phase voltage	410	V
ΔP_0	No-load loss	1650	W
u_{sc}	Short-circuit voltage	6	%
i_0	No-load current	1.3	%
ΔV_2	Voltage drop at full load with $\cos\varphi = 1$	1.41	%
ΔV_2	Voltage drop at full load with $\cos\varphi = 0.8$	4.59	%

Per-unit values for the studied microgrid

Table B.1 – Per-unit values for the studied MG.

Symbol and expression	Description	Value	Unity
S_b	Power base unit	2	MVA
Base values for AC-side quantities			
$V_b = \sqrt{3}V_r^{ref} = U_r^{ref}$	Voltage base unit	400	V
$I_b = S_b/V_b$	Current base unit	5000	A
$Z_b = V_b/I_b$	Impedance base unit	0.08	Ω
$f_b = f_{grid}^{ref}$	Frequency base unit	50	Hz
$\omega_b = 2\pi f_b$	Pulsation base unit	100π	rad/s
$L_b = Z_b/\omega_b$	Inductance base unit	0.2546	mH
$C_b = 1/(Z_b\omega_b)$	Capacitance base unit	0.0398	F
Base values for DC-side quantities			
$V_{b-dc} = V_b$	Voltage base unit	400	V
$I_{b-dc} = S_b/V_{b-dc} = I_b$	Current base unit	5000	A
$Z_{b-dc} = V_{b-dc}/I_{b-dc} = Z_b$	Impedance base unit	0.08	Ω
$L_{b-dc} = Z_{b-dc}/\omega_b = L_b$	Inductance base unit	0.2546	mH
$C_{b-dc} = 1/(Z_{b-dc}\omega_b) = C_b$	Capacitance base unit	0.0398	F
Per-unit values			
$\underline{V} = V/V_b$	Per-unitized voltage		pu
$\underline{I} = I/I_b$	Per-unitized current		pu
$\underline{Z} = Z/Z_b$	Per-unitized impedance		pu
$\underline{f}_{grid} = f_{grid}/f_b$	Per-unitized frequency		pu
$\underline{\omega}_{grid} = \omega_{grid}/\omega_b$	Per-unitized pulsation		pu
$\underline{L} = L/L_b$	Per-unitized inductance		pu
$\underline{C} = C/C_b$	Per-unitized capacitance		pu
$\underline{P} = P/S_b$	Per-unitized active power		pu
$\underline{Q} = Q/S_b$	Per-unitized reactive power		pu

Park and inverse Park coordinates transformations

The Park coordinates transformation used is defined by

$$\begin{bmatrix} X_d \\ X_q \end{bmatrix} = \sqrt{\frac{2}{3}} \begin{bmatrix} \cos(\omega_{grid}t) & \cos\left(\omega_{grid}t - \frac{2\pi}{3}\right) & \cos\left(\omega_{grid}t - \frac{4\pi}{3}\right) \\ -\sin(\omega_{grid}t) & -\sin\left(\omega_{grid}t - \frac{2\pi}{3}\right) & -\sin\left(\omega_{grid}t - \frac{4\pi}{3}\right) \end{bmatrix} \begin{bmatrix} X_1 \\ X_2 \\ X_3 \end{bmatrix}. \quad (C.1)$$

The inverse Park coordinates transformation used is defined by

$$\begin{bmatrix} X_1 \\ X_2 \\ X_3 \end{bmatrix} = \sqrt{\frac{2}{3}} \begin{bmatrix} \cos(\omega_{grid}t) & -\sin(\omega_{grid}t) \\ \cos\left(\omega_{grid}t - \frac{2\pi}{3}\right) & -\sin\left(\omega_{grid}t - \frac{2\pi}{3}\right) \\ \cos\left(\omega_{grid}t - \frac{4\pi}{3}\right) & -\sin\left(\omega_{grid}t - \frac{4\pi}{3}\right) \end{bmatrix} \begin{bmatrix} X_d \\ X_q \end{bmatrix}. \quad (C.2)$$

Parameters of the test bench for frequency control real-time validation

Table D.1 – Parameters of the test bench for frequency control real-time validation.

Symbol	Description	Value	Unity
Microgrid			
S_b	Power base unit	5	kVA
H	Simplified equivalent inertia constant	5	kW.s
$\underline{H} = H/S_b$	Per-unitized simplified equivalent inertia constant	1	pu
Diesel engine generator			
$P_{diesel_{rated}}$	Rated active power	4	kW
P_{diesel_e}	Initial active power	2.5	kW
s_{diesel}	Droop value for primary frequency control	0.6	Hz/kW
$\underline{s_{diesel}} = s_{diesel} \frac{S_b}{f_b}$	Per-unitized droop value for primary frequency control	0.06	pu
K_i	Inverse of the response time for secondary frequency control	0.2	kW/Hz
$\underline{K_i} = K_i \frac{f_b}{S_b}$	Inverse of the response time in a per-unit frame for secondary frequency control	2	pu
T_{diesel}	Time constant	0.022	s
Photovoltaic energy source			
$P_{PV_{rated}}$	Rated active power	0.625	kW
P_{PV_e}	Initial active power	0.5	kW
Aggregated load			
$P_{load_{rated}}$	Rated active power	4.625	kW
P_{load_e}	Initial active power	3	kW
D_{load}	Simplified damping constant	0	kW/Hz
$\underline{D_{load}} = D_{load} \frac{f_b}{S_b}$	Per-unitized simplified damping constant	0	pu

Table D.2 – Parameters of the real supercapacitor-based ESS for frequency control real-time validation.

Symbol	Description	Value	Unity
General characteristics			
S_{rated}	Rated apparent power	≈ 1751	VA
P_{rated}	Rated active power	≈ 1459	W
U_{rated}	Rated output phase-to-phase voltage of the three-phase inverter (chosen)	80	V
I_{rated}	Rated output phase current of the three-phase inverter	≈ 12.6	A
I_{rdmax}	Maximum value of the d -component of the inverter output current (computed)	≈ 18.2	A
η_{ess}	DC/AC global efficiency of the energy conversion chain	≈ 95	%
Choke			
L_c	Inductance (catalog)	390	μH
R_c	Resistance (catalog)	11	$\text{m}\Omega$
Chopper			
f_{sc}	IGBTs Semikron SKM200GB123D with $U_{max} = 1200$ V and $I_{max} = 200$ A PWM switching frequency	≈ 31.4	kHz
DC bus			
C_{dc}	Capacitance (catalog)	5300	μF
R_{dc}	Resistance (estimated)	1285	Ω
V_{dc}^{ref}	Setpoint value of the voltage (chosen)	150	V
Three-phase inverter			
f_{si}	IGBTs Semikron SKM50GAL123D with $U_{max} = 1200$ V and $I_{max} = 50$ A PWM switching frequency	10	kHz
Output filter			
L_f	Inductance (catalog)	7	mH
R_f	Resistance (estimated)	440	$\text{m}\Omega$
C_f	Capacitance (catalog)	56	μF
Supercapacitor bank			
C_{sc}	Maxwell BoostCap BMOD0165-P048 Capacitance (catalog)	165	F
R_{sc}	Series resistance (estimated)	5.12	$\text{m}\Omega$
R_{scp}	Parallel resistance (estimated)	1453.9	Ω
V_{scmin}	Minimum voltage (chosen)	24	V
V_{scmax}	Maximum voltage (chosen)	48	V
I_{smax}	Maximum value of the output current (computed)	≈ 64.7	A
P_{smax}	Maximum active power (designed)	≈ 1536	W

Some other experimental results for frequency robust control real-time validation

E.1 Experimental results under load step disturbances of $\pm 10\%$ of the load rated active power (± 300 W)

Figure E.1, Figure E.2, Figure E.3, and Figure E.4 show the experimental results for the time-domain responses of the supercapacitor output current I_s , the direct component of the inverter output current I_{rd} , together with their references, as well as the supercapacitor state of charge SoC_{sc} and voltage V_{sc} , and the active power variations of the sources and load, respectively, under load step disturbances of $\pm 10\%$ of the load rated active power (± 300 W).

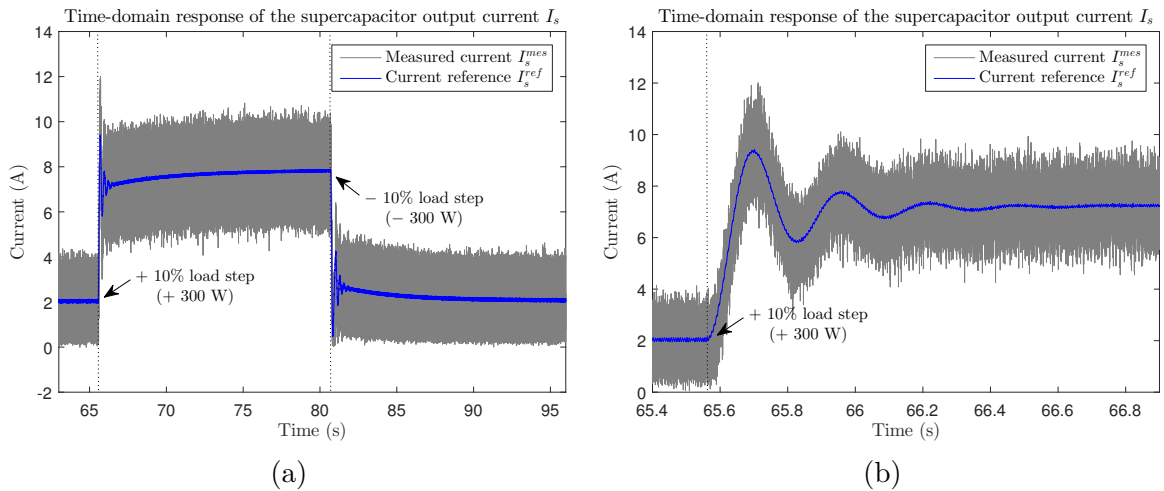


Figure E.1 – (a) Experimental result for the time-domain response of the supercapacitor output current I_s under load step disturbances of $\pm 10\%$ of the load rated active power (± 300 W) with respect to the rated operating point. (b) Temporal zoom in the time interval $t \in [65.4, 66.9]$ s.

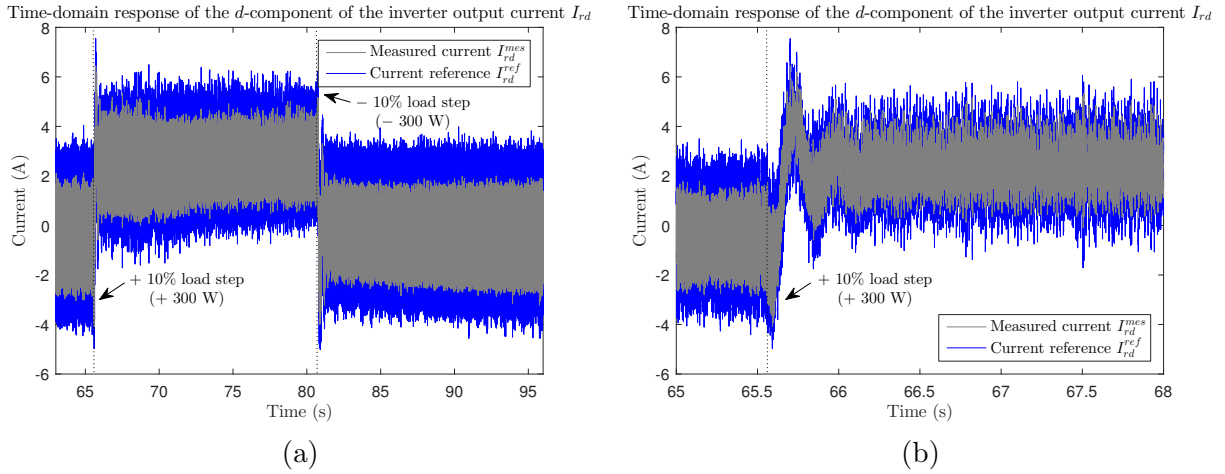


Figure E.2 – (a) Experimental result for the time-domain response of the d -component of the inverter output current I_{rd} under load step disturbances of $\pm 10\%$ of the load rated active power (± 300 W) with respect to the rated operating point. (b) Temporal zoom in the time interval $t \in [65, 68]$ s.

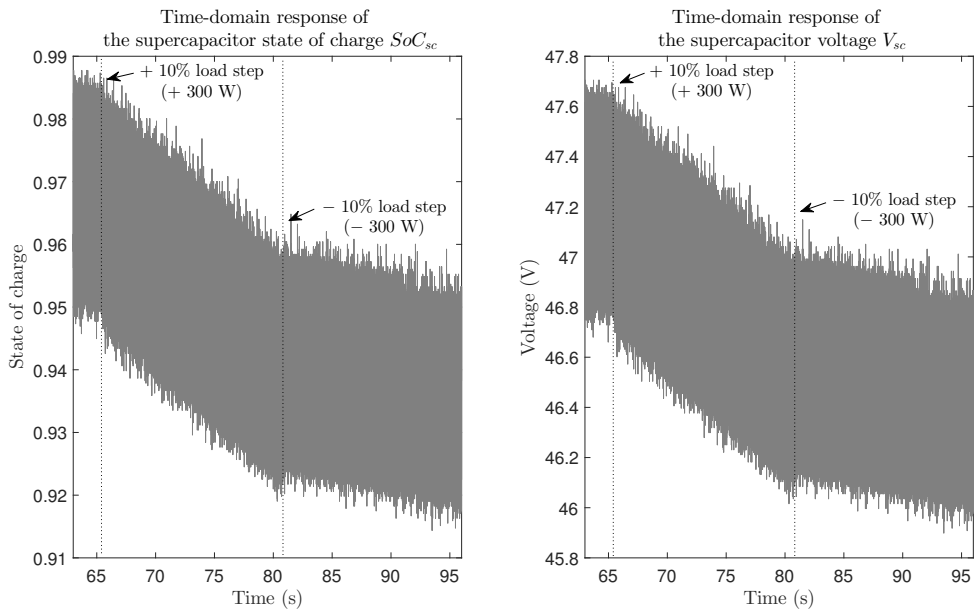


Figure E.3 – Experimental results for the time-domain responses of the supercapacitor state of charge SoC_{sc} and voltage V_{sc} under load step disturbances of $\pm 10\%$ of the load rated active power (± 300 W) with respect to the rated operating point.

E.2. Experimental results under load step disturbances of $\pm 20\%$ of the load rated active power (± 600 W)

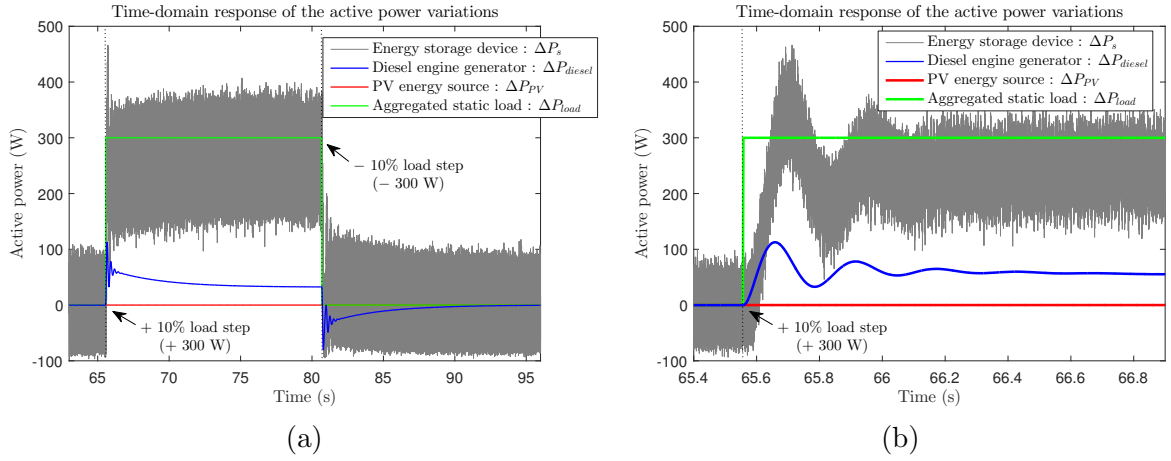


Figure E.4 – (a) Experimental results for the active power variations of the sources and load under load step disturbances of $\pm 10\%$ of the load rated active power (± 300 W) with respect to the rated operating point. (b) Temporal zoom in the time interval $t \in [65.4, 66.9]$ s.

E.2 Experimental results under load step disturbances of $\pm 20\%$ of the load rated active power (± 600 W)

Figure E.5, Figure E.6, Figure E.7, and Figure E.8 present the experimental results for the time-domain responses of the supercapacitor output current I_s , the direct component of the inverter output current I_{rd} , together with their references, as well as the supercapacitor state of charge SoC_{sc} and voltage V_{sc} , and the active power variations of the sources and load, respectively, under load step disturbances of $\pm 20\%$ of the load rated active power (± 600 W).

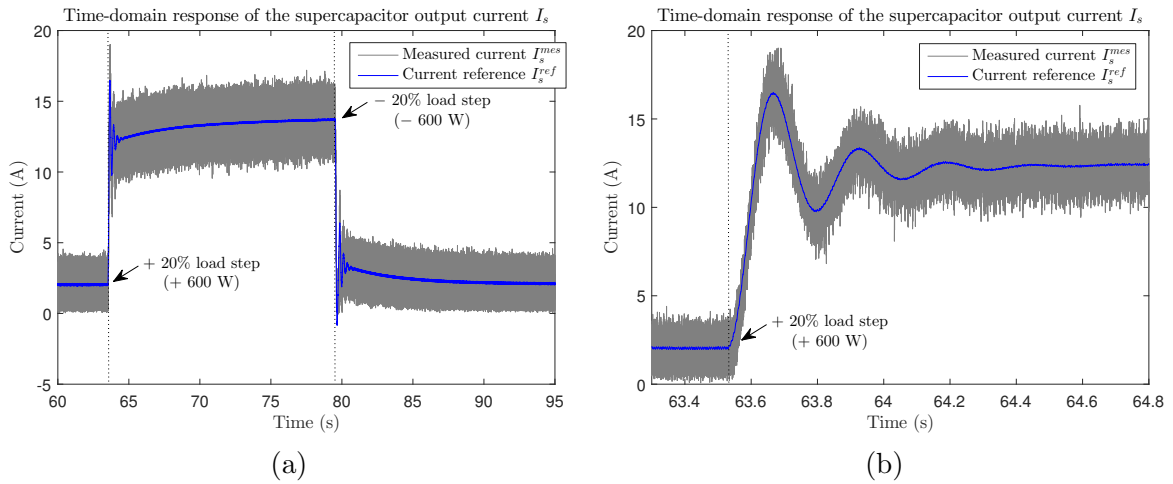


Figure E.5 – (a) Experimental result for the time-domain response of the supercapacitor output current I_s under load step disturbances of $\pm 20\%$ of the load rated active power (± 600 W) with respect to the rated operating point. (b) Temporal zoom in the time interval $t \in [63.3, 64.8]$ s.

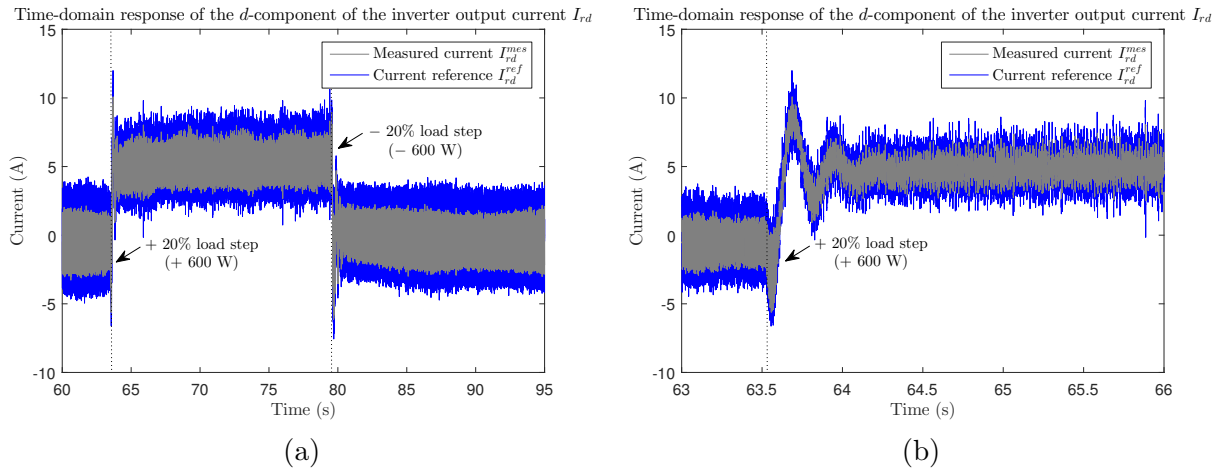


Figure E.6 – (a) Experimental result for the time-domain response of the d -component of the inverter output current I_{rd} under load step disturbances of $\pm 20\%$ of the load rated active power (± 600 W) with respect to the rated operating point. (b) Temporal zoom in the time interval $t \in [63, 66]$ s.

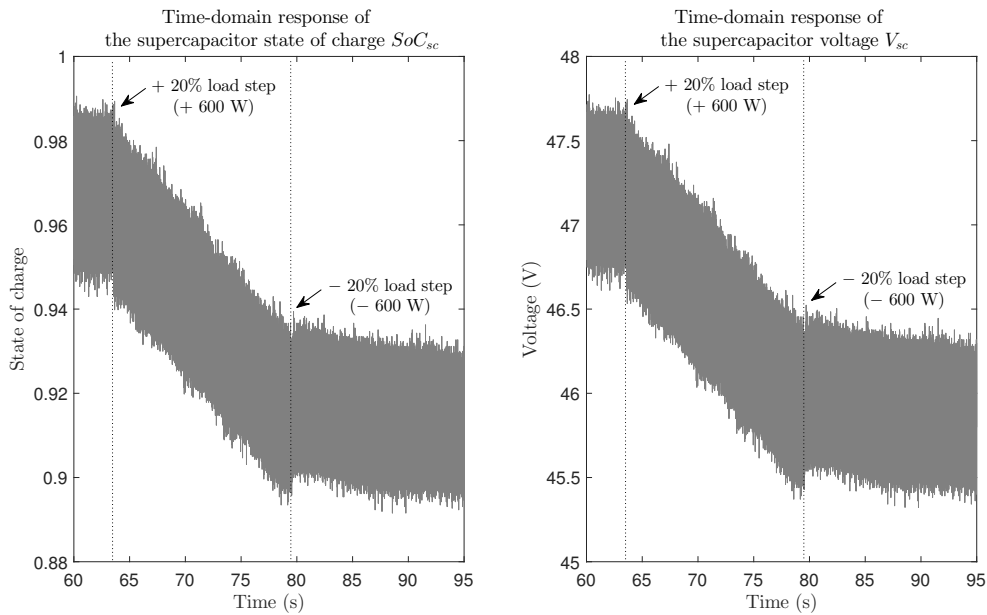


Figure E.7 – Experimental results for the time-domain responses of the supercapacitor state of charge SoC_{sc} and voltage V_{sc} under load step disturbances of $\pm 20\%$ of the load rated active power (± 600 W) with respect to the rated operating point.

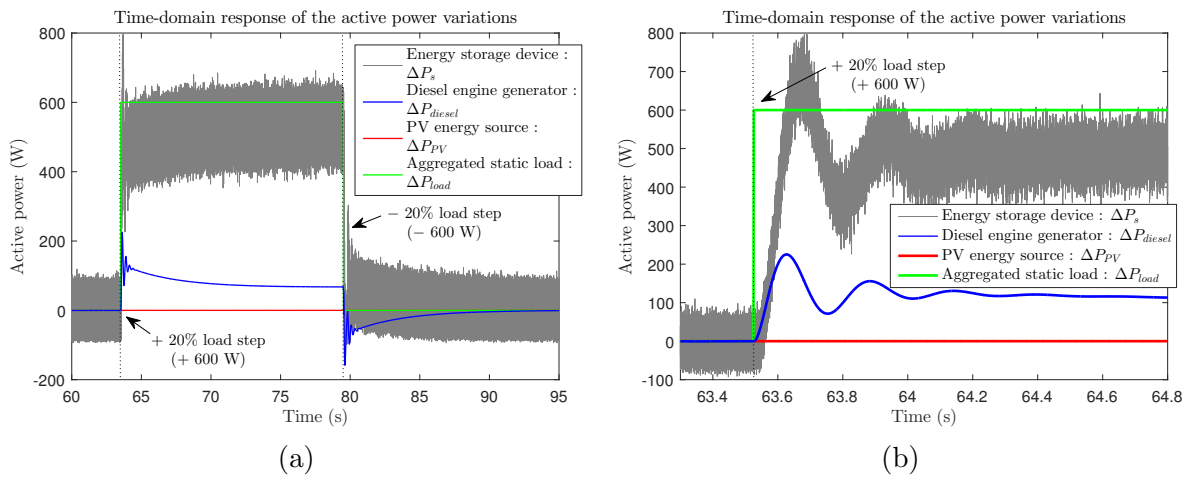


Figure E.8 – (a) Experimental results for the active power variations of the sources and load under load step disturbances of $\pm 20\%$ of the load rated active power (± 600 W) with respect to the rated operating point. (b) Temporal zoom in the time interval $t \in [63.3, 64.8]$ s.

Bibliography

- [1] M. I. Abouheaf, M. S. Mahmoud, and S. Azher Hussain. “A novel approach to control of autonomous microgrid systems.” In: *International Journal of Energy Engineering* 5.5 (2015), pp. 125–136 (cit. on p. 41).
- [2] N. Hatziargyriou et al. *Microgrids architectures and control*. IEEE Press, John Wiley & Sons, 2014 (cit. on pp. 9–12).
- [3] T. Funabashi et al. *Integration of distributed energy resources in power systems*. Academic Press, 2016 (cit. on pp. 23–25).
- [4] M. A. E. Alali. “Contribution à l’étude des compensateurs actifs des réseaux électriques basse tension.” PhD thesis. Université Louis Pasteur, Strasbourg I, 2002 (cit. on p. 71).
- [5] E. Ancillotti, R. Bruno, and M. Conti. “The role of communication systems in smart grids: Architectures, technical solutions and research challenges.” In: *Computer Communications* 36.17 (2013), pp. 1665–1697 (cit. on p. 15).
- [6] M. Babazadeh and H. Karimi. “A robust two-degree-of-freedom control strategy for an islanded microgrid.” In: *IEEE Transactions on Power Delivery* 28.3 (2013), pp. 1339–1347 (cit. on p. 44).
- [7] A. J. Babqi and A. H. Etemadi. “MPC-based microgrid control with supplementary fault current limitation and smooth transition mechanisms.” In: *IET Generation, Transmission Distribution* 11.9 (2017), pp. 2164–2172 (cit. on p. 36).
- [8] S. Bacha, I. Munteanu, and A. I. Bratcu. *Power electronic converters modeling and control*. Springer, 2014 (cit. on pp. 72, 80, 83).
- [9] H. R. Baghaee et al. “A decentralized robust mixed $\mathcal{H}_2/\mathcal{H}_\infty$ voltage control scheme to improve small/large-signal stability and FRT capability of islanded multi-DER microgrid considering load disturbances.” In: *IEEE Systems Journal* PP.99 (2017), pp. 1–12 (cit. on p. 44).
- [10] H. R. Baghaee et al. “A generalized descriptor-system robust \mathcal{H}_∞ control of autonomous microgrids to improve small and large signal stability considering communication delays and load nonlinearities.” In: *International Journal of Electrical Power & Energy Systems* 92.Supplement C (2017), pp. 63–82 (cit. on p. 44).
- [11] B. Bahrani, H. Karimi, and R. Iravani. “Nondetection zone assessment of an active islanding detection method and its experimental evaluation.” In: *IEEE Transactions on Power Delivery* 26.2 (2011), pp. 517–525 (cit. on p. 20).
- [12] J. N. Baker and A. Collinson. “Electrical energy storage at the turn of the Millennium.” In: *Power Engineering Journal* 13.3 (1999), pp. 107–112 (cit. on pp. 21, 23).
- [13] J. P. Barton and D. G. Infield. “Energy storage and its use with intermittent renewable energy.” In: *IEEE Transactions on Energy Conversion* 19.2 (2004), pp. 441–448 (cit. on p. 23).

- [14] H. Bevrani, M. R. Feizi, and S. Ataei. “Robust frequency control in an islanded microgrid: \mathcal{H}_∞ and μ -synthesis approaches.” In: *IEEE Transactions on Smart Grid* 7.2 (2016), pp. 706–717 (cit. on pp. 43, 53, 100, 196).
- [15] H. Bevrani, T. Ise, and Y. Miura. “Virtual synchronous generators: A survey and new perspectives.” In: *International Journal of Electrical Power & Energy Systems* 54 (2014), pp. 244–254 (cit. on pp. 23–25).
- [16] H. Bevrani and S. Shokoohi. “An intelligent droop control for simultaneous voltage and frequency regulation in islanded microgrids.” In: *IEEE Transactions on Smart Grid* 4.3 (2013), pp. 1505–1513 (cit. on p. 37).
- [17] H. Bevrani et al. “Intelligent frequency control in an AC microgrid: Online PSO-based fuzzy tuning approach.” In: *IEEE Transactions on Smart Grid* 3.4 (2012), pp. 1935–1944 (cit. on p. 37).
- [18] A. Bidram and A. Davoudi. “Hierarchical structure of microgrids control system.” In: *IEEE Transactions on Smart Grid* 3.4 (2012), pp. 1963–1976 (cit. on pp. 18–20, 28, 30).
- [19] A. Bidram, A. Davoudi, and F. L. Lewis. “A multiobjective distributed control framework for islanded AC microgrids.” In: *IEEE Transactions on Industrial Informatics* 10.3 (2014), pp. 1785–1798 (cit. on p. 28).
- [20] F. Blaabjerg et al. “Overview of control and grid synchronization for distributed power generation systems.” In: *IEEE Transactions on Industrial Electronics* 53.5 (2006), pp. 1398–1409 (cit. on p. 27).
- [21] D. Boroyevich et al. “Future electronic power distribution systems a contemplative view.” In: *2010 12th International Conference on Optimization of Electrical and Electronic Equipment*. 2010, pp. 1369–1380 (cit. on pp. 13, 14).
- [22] A. M. Bouzid et al. “A survey on control of electric power distributed generation systems for microgrid applications.” In: *Renewable and Sustainable Energy Reviews* 44 (2015), pp. 751–766 (cit. on p. 27).
- [23] K. De Brabandere et al. “A voltage and frequency droop control method for parallel inverters.” In: *IEEE Transactions on Power Electronics* 22.4 (2007), pp. 1107–1115 (cit. on p. 29).
- [24] J. Bryan, R. Duke, and S. Round. “Decentralized generator scheduling in a nanogrid using DC bus signaling.” In: *IEEE Power Engineering Society General Meeting, 2004*. 2004, 977–982 Vol.1 (cit. on p. 13).
- [25] CEN-CENELEC-ETSI. *Smart grid reference architecture*. Tech. rep. Smart Grid Coordination Group, 2012 (cit. on pp. 12, 14).
- [26] S. Chattopadhyay, M. Mitra, and S. Sengupta. *Electric power quality*. Springer, Dordrecht, 2011 (cit. on p. 20).
- [27] D. Chen and L. Xu. “Autonomous DC voltage control of a DC microgrid with multiple slack terminals.” In: *IEEE Transactions on Power Systems* 27.4 (2012), pp. 1897–1905 (cit. on p. 29).

- [28] H. Chen et al. “Progress in electrical energy storage system: A critical review.” In: *Progress in Natural Science* 19.3 (2009), pp. 291–312 (cit. on pp. 21, 22).
- [29] Y. Chen et al. “Comparison of methods for implementing virtual synchronous machine on inverters.” In: *International Conference on Renewable Energies and Power Quality*. 2012, pp. 734–739 (cit. on p. 23).
- [30] Y. Chen et al. “Improving the grid power quality using virtual synchronous machines.” In: *2011 International Conference on Power Engineering, Energy and Electrical Drives*. 2011, pp. 1–6 (cit. on p. 24).
- [31] Z. Chen et al. “Adaptive sliding-mode voltage control for inverter operating in islanded mode in microgrid.” In: *International Journal of Electrical Power & Energy Systems* 66.Supplement C (2015), pp. 133–143 (cit. on p. 40).
- [32] M. Chilali and P. Gahinet. “ \mathcal{H}_∞ design with pole placement constraints: An LMI approach.” In: *IEEE Transactions on Automatic Control* 41.3 (1996), pp. 358–367 (cit. on pp. 41, 51).
- [33] I. Y. Chung et al. “Control methods of inverter-interfaced distributed generators in a microgrid system.” In: *IEEE Transactions on Industry Applications* 46.3 (2010), pp. 1078–1088 (cit. on p. 37).
- [34] European Commission. *European smartgrids technology platform: Vision and strategy for Europe’s electricity networks of the future*. Tech. rep. Directorate-General for Research, EUR 22040, 2006 (cit. on pp. 9, 10).
- [35] M. Cucuzzella, G. P. Incremona, and A. Ferrara. “Decentralized sliding mode control of islanded AC microgrids with arbitrary topology.” In: *IEEE Transactions on Industrial Electronics* 64.8 (2017), pp. 6706–6713 (cit. on p. 35).
- [36] M. Cucuzzella, G. P. Incremona, and A. Ferrara. “Design of robust higher order sliding mode control for microgrids.” In: *IEEE Journal on Emerging and Selected Topics in Circuits and Systems* 5.3 (2015), pp. 393–401 (cit. on p. 34).
- [37] S. D’Arco and J. A. Suul. “Equivalence of virtual synchronous machines and frequency-droops for converter-based microgrids.” In: *IEEE Transactions on Smart Grid* 5.1 (2014), pp. 394–395 (cit. on p. 23).
- [38] D. Das, G. Gurralla, and U. J. Shenoy. “Linear quadratic regulator based bumpless transfer in microgrids.” In: *IEEE Transactions on Smart Grid* PP.99 (2017), pp. 1–1 (cit. on p. 34).
- [39] M. Davari and Y. A. R. I. Mohamed. “Robust multi-objective control of VSC-based DC-voltage power port in hybrid AC/DC multi-terminal micro-grids.” In: *IEEE Transactions on Smart Grid* 4.3 (2013), pp. 1597–1612 (cit. on pp. 31, 44, 52).
- [40] G. Delille, B. Francois, and G. Malarange. “Dynamic frequency control support by energy storage to reduce the impact of wind and solar generation on isolated power system’s inertia.” In: *IEEE Transactions on Sustainable Energy* 3.4 (2012), pp. 931–939 (cit. on p. 62).

- [41] G. M. A. Delille. “Contribution du stockage à la gestion avancée des systèmes électriques, approches organisationnelles et technico-économiques dans les réseaux de distribution.” PhD thesis. École Centrale de Lille, 2010 (cit. on pp. 18, 56, 66).
- [42] N. L. Diaz et al. “Intelligent distributed generation and storage units for DC microgrids – A new concept on cooperative control without communications beyond droop control.” In: *IEEE Transactions on Smart Grid* 5.5 (2014), pp. 2476–2485 (cit. on p. 29).
- [43] J. C. Doyle et al. “State-space solutions to standard \mathcal{H}_2 and \mathcal{H}_∞ control problems.” In: *IEEE Transactions on Automatic Control* 34.8 (1989), pp. 831–847 (cit. on p. 51).
- [44] T. Dragičević, J. M. Guerrero, and J. C. Vasquez. “A distributed control strategy for coordination of an autonomous LVDC microgrid based on power-line signaling.” In: *IEEE Transactions on Industrial Electronics* 61.7 (2014), pp. 3313–3326 (cit. on p. 29).
- [45] T. Dragičević et al. “Supervisory control of an adaptive-droop regulated DC microgrid with battery management capability.” In: *IEEE Transactions on Power Electronics* 29.2 (2014), pp. 695–706 (cit. on p. 29).
- [46] G. Duc and S. Font. *Commande \mathcal{H}_∞ et μ -analyse, des outils pour la robustesse*. Hermes Science Publication, 1999 (cit. on pp. 45, 46, 48, 49, 52, 53, 55).
- [47] N. Eghtedarpour and E. Farjah. “Power control and management in a hybrid AC/DC microgrid.” In: *IEEE Transactions on Smart Grid* 5.3 (2014), pp. 1494–1505 (cit. on p. 30).
- [48] S. Eren et al. “An adaptive droop DC-bus voltage controller for a grid-connected voltage source inverter with LCL filter.” In: *IEEE Transactions on Power Electronics* 30.2 (2015), pp. 547–560 (cit. on p. 29).
- [49] X. Fang et al. “Smart grid – The new and improved power grid: A survey.” In: *IEEE Communications Surveys Tutorials* 14.4 (2012), pp. 944–980 (cit. on p. 10).
- [50] H. Farhangi. “The path of the smart grid.” In: *IEEE Power and Energy Magazine* 8.1 (2010), pp. 18–28 (cit. on p. 10).
- [51] J-P. Ferrieux and F. Forest. *Alimentations à découpage, convertisseurs à résonance: Principes, composants, modélisation*. Dunod, 2006 (cit. on p. 175).
- [52] A. Florescu. “Gestion optimisée des flux énergétiques dans le véhicule électrique.” PhD thesis. Université de Grenoble, 2012 (cit. on pp. 165–167, 169–171).
- [53] J. Gao et al. “A survey of communication/networking in smart grids.” In: *Future Generation Computer Systems* 28.2 (2012), pp. 391–404 (cit. on p. 15).
- [54] S. K. Ghai et al. “DC picogrids: A case for local energy storage for uninterrupted power to DC appliances.” In: *Proceedings of the Fourth International Conference on Future Energy Systems*. e-Energy '13. 2013, pp. 27–38 (cit. on p. 13).
- [55] S. Gholami, S. Saha, and M. Aldeen. “Robust multiobjective control method for power sharing among distributed energy resources in islanded microgrids with unbalanced and nonlinear loads.” In: *International Journal of Electrical Power & Energy Systems* 94.Supplement C (2018), pp. 321–338 (cit. on p. 44).

- [56] K. Glover and J. C. Doyle. “State-space formulae for all stabilizing controllers that satisfy an \mathcal{H}_∞ -norm bound and relations to risk sensitivity.” In: 11.3 (1988), pp. 167–172 (cit. on p. 51).
- [57] R. B. Godoy et al. “Differential-evolution-based optimization of the dynamic response for parallel operation of inverters with no controller interconnection.” In: *IEEE Transactions on Industrial Electronics* 59.7 (2012), pp. 2859–2866 (cit. on p. 36).
- [58] T. Goya et al. “Frequency control in isolated island by using parallel operated battery systems applying \mathcal{H}_∞ control theory based on droop characteristics.” In: *IET Renewable Power Generation* 5.2 (2011), pp. 160–166 (cit. on p. 42).
- [59] S. Grillo et al. “DC islands in AC smart grids.” In: *IEEE Transactions on Power Electronics* 29.1 (2014), pp. 89–98 (cit. on p. 29).
- [60] Y. Gu, W. Li, and X. He. “Frequency-coordinating virtual impedance for autonomous power management of DC microgrid.” In: *IEEE Transactions on Power Electronics* 30.4 (2015), pp. 2328–2337 (cit. on p. 31).
- [61] Y. Gu et al. “Mode-adaptive decentralized control for renewable DC microgrid with enhanced reliability and flexibility.” In: *IEEE Transactions on Power Electronics* 29.9 (2014), pp. 5072–5080 (cit. on p. 30).
- [62] J. M. Guerrero, L. Hang, and J. Uceda. “Control of distributed uninterruptible power supply systems.” In: *IEEE Transactions on Industrial Electronics* 55.8 (2008), pp. 2845–2859 (cit. on p. 27).
- [63] J. M. Guerrero et al. “Advanced control architectures for intelligent microgrids – Part II: Power quality, energy storage, and AC/DC microgrids.” In: *IEEE Transactions on Industrial Electronics* 60.4 (2013), pp. 1263–1270 (cit. on p. 29).
- [64] J. M. Guerrero et al. “Hierarchical control of droop-controlled AC and DC microgrids – A general approach toward standardization.” In: *IEEE Transactions on Industrial Electronics* 58.1 (2011), pp. 158–172 (cit. on pp. 19, 20, 29, 30).
- [65] V. C. Gungor et al. “A survey on smart grid potential applications and communication requirements.” In: *IEEE Transactions on Industrial Informatics* 9.1 (2013), pp. 28–42 (cit. on p. 15).
- [66] A. Haddadi et al. “A μ -based approach to small-signal stability analysis of an interconnected distributed energy resource unit and load.” In: *IEEE Transactions on Power Delivery* 30.4 (2015), pp. 1715–1726 (cit. on pp. 44, 53).
- [67] M. Hamzeh et al. “Robust control of an islanded microgrid under unbalanced and nonlinear load conditions.” In: *IEEE Journal of Emerging and Selected Topics in Power Electronics* 4.2 (2016), pp. 512–520 (cit. on p. 44).
- [68] H. Han et al. “An improved droop control strategy for reactive power sharing in islanded microgrid.” In: *IEEE Transactions on Power Electronics* 30.6 (2015), pp. 3133–3141 (cit. on p. 29).
- [69] Y. Han et al. “Robust control for microgrid frequency deviation reduction with attached storage system.” In: *IEEE Transactions on Smart Grid* 6.2 (2015), pp. 557–565 (cit. on pp. 42, 53, 59, 100).

- [70] M. A. Hassan and M. A. Abido. “Optimal design of microgrids in autonomous and grid-connected modes using particle swarm optimization.” In: *IEEE Transactions on Power Electronics* 26.3 (2011), pp. 755–769 (cit. on p. 37).
- [71] N. Hatziargyriou et al. “Microgrids.” In: *IEEE Power and Energy Magazine* 5.4 (2007), pp. 78–94 (cit. on pp. 1, 10, 13, 18, 197).
- [72] N. Hatziargyriou et al. *Microgrids: Large scale integration of micro-generation to low voltage grids*. Tech. rep. Deliverable DC1 Part 1, Contract No: ENK5-CT-2002-00610, 2004 (cit. on pp. 10, 13).
- [73] J. He, Y. W. Li, and F. Blaabjerg. “Flexible microgrid power quality enhancement using adaptive hybrid voltage and current controller.” In: *IEEE Transactions on Industrial Electronics* 61.6 (2014), pp. 2784–2794 (cit. on p. 40).
- [74] D. Hernández-Torres. “Commande robuste de générateurs électrochimiques hybrides.” PhD thesis. Université de Grenoble, 2011 (cit. on pp. 3, 49, 50, 53, 55, 71, 86, 141, 199).
- [75] M. J. Hossain et al. “Robust control for power sharing in microgrids with low-inertia wind and PV generators.” In: *IEEE Transactions on Sustainable Energy* 6.3 (2015), pp. 1067–1077 (cit. on p. 44).
- [76] A. M. Howlader et al. “A robust \mathcal{H}_∞ controller based frequency control approach using the wind-battery coordination strategy in a small power system.” In: *International Journal of Electrical Power & Energy Systems* 58.Supplement C (2014), pp. 190–198 (cit. on p. 42).
- [77] P. H. Huang et al. “A novel droop-based average voltage sharing control strategy for DC microgrids.” In: *IEEE Transactions on Smart Grid* 6.3 (2015), pp. 1096–1106 (cit. on p. 29).
- [78] “IEEE standard for interconnecting distributed resources with electric power systems.” In: *IEEE Std 1547-2003* (2003), pp. 1–28 (cit. on p. 20).
- [79] A. Ipakchi and F. Albuyeh. “Grid of the future.” In: *IEEE Power and Energy Magazine* 7.2 (2009), pp. 52–62 (cit. on p. 9).
- [80] IRENA. *Off-grid renewable energy systems: Status and methodological issues*. Tech. rep. 2015 (cit. on pp. 13, 14).
- [81] K. Jalili and S. Bernet. “Design of LCL filters of active-front-end two-Level voltage-source converters.” In: *IEEE Transactions on Industrial Electronics* 56.5 (2009), pp. 1674–1689 (cit. on p. 71).
- [82] J. Johnston et al. “Beyond power over ethernet: The development of digital energy networks for buildings.” In: *CIBSE Technical Symposium 2012 - Buildings Systems and Services for the 21st Century*. 2012, Session 5 Power and Energy Design (cit. on p. 13).
- [83] A. Kahrobaeian and Y. A. R. I. Mohamed. “Direct single-loop μ -synthesis voltage control for suppression of multiple resonances in microgrids with power-factor correction capacitors.” In: *IEEE Transactions on Smart Grid* 4.2 (2013), pp. 1151–1161 (cit. on pp. 43, 53).

- [84] A. Kahrobaeian and Y. A. R. I. Mohamed. “Robust single-loop direct current control of LCL-filtered converter-based DG units in grid-connected and autonomous microgrid modes.” In: *IEEE Transactions on Power Electronics* 29.10 (2014), pp. 5605–5619 (cit. on pp. 44, 53).
- [85] A. Kahrobaeian and Y. A. R. I. Mohamed. “Suppression of interaction dynamics in DG converter-based microgrids via robust system-oriented control approach.” In: *IEEE Transactions on Smart Grid* 3.4 (2012), pp. 1800–1811 (cit. on p. 43).
- [86] H. Kakigano et al. “Fundamental characteristics of DC microgrid for residential houses with cogeneration system in each house.” In: *2008 IEEE Power and Energy Society General Meeting - Conversion and Delivery of Electrical Energy in the 21st Century*. 2008, pp. 1–8 (cit. on p. 13).
- [87] U. K. Kalla et al. “Adaptive sliding mode control of standalone single-phase microgrid using hydro, wind and solar PV array based generation.” In: *IEEE Transactions on Smart Grid* PP.99 (2017), pp. 1–1 (cit. on p. 40).
- [88] R. M. Kamel, A. Chaouachi, and K. Nagasaka. “Three control strategies to improve the microgrid transient dynamic response during isolated mode: A comparative study.” In: *IEEE Transactions on Industrial Electronics* 60.4 (2013), pp. 1314–1322 (cit. on p. 37).
- [89] H. Karimi, H. Nikkhajoei, and R. Iravani. “Control of an electronically-coupled distributed resource unit subsequent to an islanding event.” In: *IEEE Transactions on Power Delivery* 23.1 (2008), pp. 493–501 (cit. on p. 19).
- [90] F. Katiraei, M. R. Iravani, and P. W. Lehn. “Micro-grid autonomous operation during and subsequent to islanding process.” In: *IEEE Transactions on Power Delivery* 20.1 (2005), pp. 248–257 (cit. on p. 19).
- [91] F. Katiraei et al. “Microgrids management.” In: *IEEE Power and Energy Magazine* 6.3 (2008), pp. 54–65 (cit. on p. 18).
- [92] T. Kerdphol et al. “RBF neural network-based online intelligent management of a battery energy storage system for stand-alone microgrids.” In: *Energy, Sustainability and Society* 6.1 (2016), p. 5 (cit. on p. 38).
- [93] S. K. Khadem, M. Basu, and M. F. Conlon. “Parallel operation of inverters and active power filters in distributed generation system – A review.” In: *Renewable and Sustainable Energy Reviews* 15.9 (2011), pp. 5155–5168 (cit. on p. 28).
- [94] M. H. Khooban and T. Niknam. “A new intelligent online fuzzy tuning approach for multi-area load frequency control: Self adaptive modified bat algorithm.” In: *International Journal of Electrical Power & Energy Systems* 71 (2015), pp. 254–261 (cit. on p. 33).
- [95] S. S. Khorramabadi and A. Bakhshai. “Critic-based self-tuning PI structure for active and reactive power control of VSCs in microgrid systems.” In: *IEEE Transactions on Smart Grid* 6.1 (2015), pp. 92–103 (cit. on p. 38).

- [96] J. Kim et al. “Mode adaptive droop control with virtual output impedances for an inverter-based flexible AC microgrid.” In: *IEEE Transactions on Power Electronics* 26.3 (2011), pp. 689–701 (cit. on pp. 29, 31, 39).
- [97] J. Y. Kim et al. “Cooperative control strategy of energy storage system and microsources for stabilizing the microgrid during islanded operation.” In: *IEEE Transactions on Power Electronics* 25.12 (2010), pp. 3037–3048 (cit. on pp. 23, 107).
- [98] M. C. Kinn. “Proposed components for the design of a smart nano-grid for a domestic electrical system that operates at below 50V DC.” In: *2011 2nd IEEE PES International Conference and Exhibition on Innovative Smart Grid Technologies*. 2011, pp. 1–7 (cit. on p. 13).
- [99] N. Kumar, A. V. Vasilakos, and J. J. P. C. Rodrigues. “A multi-tenant cloud-based DC nano grid for self-sustained smart buildings in smart cities.” In: *IEEE Communications Magazine* 55.3 (2017), pp. 14–21 (cit. on p. 13).
- [100] P. Kundur. *Power system stability and control*. McGraw-Hill, 1994 (cit. on pp. 63–66).
- [101] A. Kuperman and I. Aharon. “Battery-ultracapacitor hybrids for pulsed current loads: A review.” In: *Renewable and Sustainable Energy Reviews* 15.2 (2011), pp. 981–992 (cit. on pp. 67, 70).
- [102] E. Kuznetsova et al. “Reinforcement learning for microgrid energy management.” In: *Energy* 59.Supplement C (2013), pp. 133–146 (cit. on p. 41).
- [103] M. A. Torres L. et al. “Self-tuning virtual synchronous machine: A control strategy for energy storage systems to support dynamic frequency control.” In: *IEEE Transactions on Energy Conversion* 29.4 (2014), pp. 833–840 (cit. on p. 23).
- [104] Q. L. Lam et al. “Multi-variable H-infinity robust control applied to primary frequency regulation in microgrids with large integration of photovoltaic energy source.” In: *2015 IEEE International Conference on Industrial Technology (ICIT)*. 2015, pp. 2921–2928 (cit. on pp. 53, 100).
- [105] R. H. Lasseter. “Microgrids.” In: *2002 IEEE Power Engineering Society Winter Meeting. Conference Proceedings (Cat. No.02CH37309)*. Vol. 1. 2002, 305–308 vol.1 (cit. on pp. 1, 10, 13, 18, 197).
- [106] C. T. Lee, C. C. Chu, and P. T. Cheng. “A new droop control method for the autonomous operation of distributed energy resource interface converters.” In: *IEEE Transactions on Power Electronics* 28.4 (2013), pp. 1980–1993 (cit. on p. 29).
- [107] F. Li et al. “Optimal control in microgrid using multi-agent reinforcement learning.” In: *ISA Transactions* 51.6 (2012), pp. 743–751 (cit. on p. 41).
- [108] F. Li et al. “Smart transmission grid: Vision and framework.” In: *IEEE Transactions on Smart Grid* 1.2 (2010), pp. 168–177 (cit. on p. 10).
- [109] P. Li et al. “Modelling robustness for a flexible grid-tied photovoltaic generation system.” In: *IET Renewable Power Generation* 9.4 (2015), pp. 315–322 (cit. on pp. 44, 53).
- [110] P. Li et al. “The \mathcal{H}_∞ control method of grid-tied photovoltaic generation.” In: *IEEE Transactions on Smart Grid* 6.4 (2015), pp. 1670–1677 (cit. on p. 44).

- [111] Y. Li, D. M. Vilathgamuwa, and P. C. Loh. “Design, analysis, and real-time testing of a controller for multibus microgrid system.” In: *IEEE Transactions on Power Electronics* 19.5 (2004), pp. 1195–1204 (cit. on p. 20).
- [112] Y. W. Li and C. N. Kao. “An accurate power control strategy for power-electronics-interfaced distributed generation units operating in a low-voltage multibus microgrid.” In: *IEEE Transactions on Power Electronics* 24.12 (2009), pp. 2977–2988 (cit. on p. 31).
- [113] Y. W. Li, D. M. Vilathgamuwa, and P. C. Loh. “Robust control scheme for a microgrid with PFC capacitor connected.” In: *IEEE Transactions on Industry Applications* 43.5 (2007), pp. 1172–1182 (cit. on p. 43).
- [114] Z. Li et al. “Control of a grid-forming inverter based on sliding-mode and mixed $\mathcal{H}_2/\mathcal{H}_\infty$ control.” In: *IEEE Transactions on Industrial Electronics* 64.5 (2017), pp. 3862–3872 (cit. on p. 43).
- [115] L. Liang, Y. Hou, and D. J. Hill. “Design guidelines for MPC-based frequency regulation for islanded microgrids with storage, voltage, and ramping constraints.” In: *IET Renewable Power Generation* 11.8 (2017), pp. 1200–1210 (cit. on p. 36).
- [116] J. Liu, Y. Miura, and T. Ise. “Comparison of dynamic characteristics between virtual synchronous generator and droop control in inverter-based distributed generators.” In: *IEEE Transactions on Power Electronics* 31.5 (2016), pp. 3600–3611 (cit. on p. 23).
- [117] J. Liu et al. “Enhanced virtual synchronous generator control for parallel inverters in microgrids.” In: *IEEE Transactions on Smart Grid* 8.5 (2017), pp. 2268–2277 (cit. on p. 23).
- [118] X. Liu, P. Wang, and P. C. Loh. “A hybrid AC/DC microgrid and its coordination control.” In: *IEEE Transactions on Smart Grid* 2.2 (2011), pp. 278–286 (cit. on p. 28).
- [119] Y. Liu et al. “A control strategy for microgrid inverters based on adaptive three-order sliding mode and optimized droop controls.” In: *Electric Power Systems Research* 117.Supplement C (2014), pp. 192–201 (cit. on p. 40).
- [120] P. C. Loh et al. “Autonomous control of interlinking converter with energy storage in hybrid AC–DC microgrid.” In: *IEEE Transactions on Industry Applications* 49.3 (2013), pp. 1374–1382 (cit. on p. 29).
- [121] P. C. Loh et al. “Autonomous operation of hybrid microgrid with AC and DC subgrids.” In: *IEEE Transactions on Power Electronics* 28.5 (2013), pp. 2214–2223 (cit. on pp. 29, 30).
- [122] J. A. Peças Lopes et al. “Integrating distributed generation into electric power systems: A review of drivers, challenges and opportunities.” In: *Electric Power Systems Research* 77.9 (2007), pp. 1189–1203 (cit. on p. 10).
- [123] X. Lu et al. “An improved droop control method for DC microgrids based on low bandwidth communication with DC bus voltage restoration and enhanced current sharing accuracy.” In: *IEEE Transactions on Power Electronics* 29.4 (2014), pp. 1800–1812 (cit. on p. 29).

- [124] X. Lu et al. “Hierarchical control of parallel AC-DC converter interfaces for hybrid microgrids.” In: *IEEE Transactions on Smart Grid* 5.2 (2014), pp. 683–692 (cit. on p. 29).
- [125] M. S. Mahmoud, N. M. Alyazidi, and M. I. Abouheaf. “Adaptive intelligent techniques for microgrid control systems: A survey.” In: *International Journal of Electrical Power & Energy Systems* 90 (2017), pp. 292–305 (cit. on pp. 32–39, 41, 44).
- [126] M. S. Mahmoud and S. A. Hussain. “Adaptive PI secondary control for smart autonomous microgrid systems.” In: *International Journal of Adaptive Control and Signal Processing* 29.11 (2015), pp. 1442–1458 (cit. on p. 39).
- [127] R. Majumder et al. “Improvement of stability and load sharing in an autonomous microgrid using supplementary droop control loop.” In: *IEEE Transactions on Power Systems* 25.2 (2010), pp. 796–808 (cit. on p. 29).
- [128] A. Majzoobi and A. Khodaei. “Application of microgrids in supporting distribution grid flexibility.” In: *IEEE Transactions on Power Systems* 32.5 (2017), pp. 3660–3669 (cit. on p. 10).
- [129] A. Maknouninejad et al. “Optimal, nonlinear, and distributed designs of droop controls for DC microgrids.” In: *IEEE Transactions on Smart Grid* 5.5 (2014), pp. 2508–2516 (cit. on p. 29).
- [130] D. Maksimović et al. “Modeling and simulation of power electronic converters.” In: *Proceedings of the IEEE* 89.6 (2001), pp. 898–912 (cit. on p. 72).
- [131] B. Marinescu and H. Bourles. “Robust predictive control for the flexible coordinated secondary voltage control of large-scale power systems.” In: *IEEE Transactions on Power Systems* 14.4 (1999), pp. 1262–1268 (cit. on p. 20).
- [132] F. Martin-Martínez, A. Sánchez-Mirallas, and M. Rivier. “A literature review of microgrids: A functional layer based classification.” In: *Renewable and Sustainable Energy Reviews* 62 (2016), pp. 1133–1153 (cit. on pp. 14–17).
- [133] A. Mehrizi-Sani and R. Iravani. “Potential-function based control of a microgrid in islanded and grid-connected modes.” In: *IEEE Transactions on Power Systems* 25.4 (2010), pp. 1883–1891 (cit. on pp. 19, 20).
- [134] L. I. Minchala-Avila et al. “Optimal energy management for stable operation of an islanded microgrid.” In: *IEEE Transactions on Industrial Informatics* 12.4 (2016), pp. 1361–1370 (cit. on p. 35).
- [135] S. Mishra, G. Malleshham, and A. N. Jha. “Design of controller and communication for frequency regulation of a smart microgrid.” In: *IET Renewable Power Generation* 6.4 (2012), pp. 248–258 (cit. on p. 36).
- [136] S. Mishra, G. Malleshham, and P. C. Sekhar. “Biogeography based optimal state feedback controller for frequency regulation of a smart microgrid.” In: *IEEE Transactions on Smart Grid* 4.1 (2013), pp. 628–637 (cit. on p. 33).
- [137] S. Mishra, D. Ramasubramanian, and P. C. Sekhar. “A seamless control methodology for a grid connected and isolated PV-diesel microgrid.” In: *IEEE Transactions on Power Systems* 28.4 (2013), pp. 4393–4404 (cit. on p. 34).

- [138] Y. A. R. I. Mohamed and E. F. El-Saadany. “Adaptive decentralized droop controller to preserve power sharing stability of paralleled inverters in distributed generation microgrids.” In: *IEEE Transactions on Power Electronics* 23.6 (2008), pp. 2806–2816 (cit. on p. 39).
- [139] Y. A. R. I. Mohamed and E. F. El-Saadany. “Adaptive discrete-time grid-voltage sensorless interfacing scheme for grid-connected DG-inverters based on neural-network identification and deadbeat current regulation.” In: *IEEE Transactions on Power Electronics* 23.1 (2008), pp. 308–321 (cit. on p. 38).
- [140] Y. A. R. I. Mohamed and A. A. Radwan. “Hierarchical control system for robust microgrid operation and seamless mode transfer in active distribution systems.” In: *IEEE Transactions on Smart Grid* 2.2 (2011), pp. 352–362 (cit. on p. 29).
- [141] A. Mohanty et al. “Modelling, simulation and optimisation of robust PV based micro grid for mitigation of reactive power and voltage instability.” In: *International Journal of Electrical Power & Energy Systems* 81.Supplement C (2016), pp. 444–458 (cit. on pp. 44, 53).
- [142] J. Mongkoltanatas. “Participation d’un système de stockage à la stabilité des réseaux insulaires.” PhD thesis. Université de Grenoble, 2014 (cit. on pp. 3, 65, 68–70, 93, 183, 199).
- [143] J. Morroni, R. Zane, and D. Maksimović. “Design and implementation of an adaptive tuning system based on desired phase margin for digitally controlled DC-DC converters.” In: *IEEE Transactions on Power Electronics* 24.2 (2009), pp. 559–564 (cit. on p. 83).
- [144] V. Natarajan and G. Weiss. “Synchronverters with better stability due to virtual inductors, virtual capacitors, and anti-windup.” In: *IEEE Transactions on Industrial Electronics* 64.7 (2017), pp. 5994–6004 (cit. on p. 23).
- [145] H. Nikkhajoei and R. H. Lasseter. “Distributed generation interface to the CERTS microgrid.” In: *IEEE Transactions on Power Delivery* 24.3 (2009), pp. 1598–1608 (cit. on p. 19).
- [146] D. Niyato, L. Xiao, and P. Wang. “Machine-to-machine communications for home energy management system in smart grid.” In: *IEEE Communications Magazine* 49.4 (2011), pp. 53–59 (cit. on p. 15).
- [147] B. Nordman, K. Christensen, and A. Meier. “Think globally, distribute power locally: The promise of nanogrids.” In: *Computer* 45.9 (2012), pp. 89–91 (cit. on p. 13).
- [148] Bruce Nordman. *Local grid definitions*. Tech. rep. Smart Grid Interoperability Panel, Home Building and Industrial Working Group, 2016 (cit. on p. 13).
- [149] S. M. Nosratabadi, R.-A. Hooshmand, and E. Gholipour. “A comprehensive review on microgrid and virtual power plant concepts employed for distributed energy resources scheduling in power systems.” In: *Renewable and Sustainable Energy Reviews* 67 (2017), pp. 341–363 (cit. on p. 11).

- [150] W. Nwesaty. “LPV/ \mathcal{H}_∞ contrôle utilisé à conveoir des gestion énergetique à bord des véhicules électriques.” PhD thesis. Université de Grenoble, 2015 (cit. on pp. 3, 81, 199).
- [151] D. E. Olivares et al. “Trends in microgrid control.” In: *IEEE Transactions on Smart Grid* 5.4 (2014), pp. 1905–1919 (cit. on pp. 2, 17–20, 23, 32, 198).
- [152] A. Ovalle et al. “Decentralized control of voltage source converters in microgrids based on the application of instantaneous power theory.” In: *IEEE Transactions on Industrial Electronics* 62.2 (2015), pp. 1152–1162 (cit. on p. 31).
- [153] J. Pahasa and I. Ngamroo. “Coordinated control of wind turbine blade pitch angle and PHEVs using MPCs for load frequency control of microgrid.” In: *IEEE Systems Journal* 10.1 (2016), pp. 97–105 (cit. on p. 35).
- [154] J. Pahasa and I. Ngamroo. “PHEVs bidirectional charging/discharging and SoC control for microgrid frequency stabilization using multiple MPC.” In: *IEEE Transactions on Smart Grid* 6.2 (2015), pp. 526–533 (cit. on p. 35).
- [155] O. Palizban and K. Kauhaniemi. “Hierarchical control structure in microgrids with distributed generation: Island and grid-connected mode.” In: *Renewable and Sustainable Energy Reviews* 44 (2015), pp. 797–813 (cit. on pp. 27, 28).
- [156] O. Palizban, K. Kauhaniemi, and J. M. Guerrero. “Microgrids in active network management – Part I: Hierarchical control, energy storage, virtual power plants, and market participation.” In: *Renewable and Sustainable Energy Reviews* 36 (2014), pp. 428–439 (cit. on p. 28).
- [157] O. Palizban, K. Kauhaniemi, and J. M. Guerrero. “Microgrids in active network management – part II: System operation, power quality and protection.” In: *Renewable and Sustainable Energy Reviews* 36 (2014), pp. 440–451 (cit. on pp. 20, 21).
- [158] S. Parhizi et al. “State of the art in research on microgrids: A review.” In: *IEEE Access* 3 (2015), pp. 890–925 (cit. on p. 20).
- [159] G. Pepermans et al. “Distributed generation: definition, benefits and issues.” In: *Energy Policy* 33.6 (2005), pp. 787–798 (cit. on p. 10).
- [160] E. Planas et al. “General aspects, hierarchical controls and droop methods in microgrids: A review.” In: *Renewable and Sustainable Energy Reviews* 17 (2013), pp. 147–159 (cit. on p. 29).
- [161] D. Pudjianto, C. Ramsay, and G. Strbac. “Virtual power plant and system integration of distributed energy resources.” In: *IET Renewable Power Generation* 1.1 (2007), pp. 10–16 (cit. on p. 11).
- [162] Y. T. Quek, W. L. Woo, and T. Logenthiran. “Smart sensing of loads in an extra low voltage DC pico-grid using machine learning techniques.” In: *IEEE Sensors Journal* PP.99 (2017), pp. 1–1 (cit. on p. 13).
- [163] A. Raghani, M. T. Ameli, and M. Hamzeh. “Online droop tuning of a multi-DG microgrid using cuckoo search algorithm.” In: *Electric Power Components and Systems* 43.14 (2015), pp. 1583–1595 (cit. on p. 36).

- [164] M. M. Rezaei and J. Soltani. “Robust control of an islanded multi-bus microgrid based on input-output feedback linearisation and sliding mode control.” In: *IET Generation, Transmission Distribution* 9.15 (2015), pp. 2447–2454 (cit. on p. 34).
- [165] P. F. Ribeiro et al. “Energy storage systems for advanced power applications.” In: *Proceedings of the IEEE* 89.12 (2001), pp. 1744–1756 (cit. on p. 22).
- [166] J. Rocabert et al. “Control of power converters in AC microgrids.” In: *IEEE Transactions on Power Electronics* 27.11 (2012), pp. 4734–4749 (cit. on p. 27).
- [167] E. M. G. Rodrigues et al. “Grid code reinforcements for deeper renewable generation in insular energy systems.” In: *Renewable and Sustainable Energy Reviews* 53 (2016), pp. 163–177 (cit. on p. 109).
- [168] P. Rodriguez et al. “Control of grid-connected power converters based on a virtual admittance control loop.” In: *2013 15th European Conference on Power Electronics and Applications (EPE)*. 2013, pp. 1–10 (cit. on pp. 27, 30).
- [169] K. Rouzbehi et al. “DC voltage control and power sharing in multiterminal DC grids based on optimal DC power flow and voltage-droop strategy.” In: *IEEE Journal of Emerging and Selected Topics in Power Electronics* 2.4 (2014), pp. 1171–1180 (cit. on p. 29).
- [170] M. S. Sadabadi, Q. Shafiee, and A. Karimi. “Plug-and-play robust voltage control of DC microgrids.” In: *IEEE Transactions on Smart Grid* PP.99 (2017), pp. 1–1 (cit. on p. 44).
- [171] M. S. Sadabadi, Q. Shafiee, and A. Karimi. “Plug-and-play voltage stabilization in inverter-interfaced microgrids via a robust control strategy.” In: *IEEE Transactions on Control Systems Technology* 25.3 (2017), pp. 781–791 (cit. on p. 44).
- [172] M. J. Sanjari and G. B. Gharehpetian. “Game-theoretic approach to cooperative control of distributed energy resources in islanded microgrid considering voltage and frequency stability.” In: *Neural Computing and Applications* 25.2 (2014), pp. 343–351 (cit. on p. 36).
- [173] M. Sautreuil. “La robustesse: Une nouvelle approche pour l’intégration des systèmes de génération aéronautique.” PhD thesis. Université Joseph Fourier, 2009 (cit. on pp. 2, 49, 61, 62, 71, 199).
- [174] M. Savaghebi et al. “Secondary control for voltage quality enhancement in microgrids.” In: *IEEE Transactions on Smart Grid* 3.4 (2012), pp. 1893–1902 (cit. on p. 31).
- [175] F. Shahnia et al. “Primary control level of parallel distributed energy resources converters in system of multiple interconnected autonomous microgrids within self-healing networks.” In: *IET Generation, Transmission Distribution* 8.2 (2014), pp. 203–222 (cit. on p. 33).
- [176] X. She, A. Q. Huang, and R. Burgos. “Review of solid-state transformer technologies and their application in power distribution systems.” In: *IEEE Journal of Emerging and Selected Topics in Power Electronics* 1.3 (2013), pp. 186–198 (cit. on p. 29).

- [177] H. Shi et al. “A novel real-time voltage and frequency compensation strategy for photovoltaic-based microgrid.” In: *IEEE Transactions on Industrial Electronics* 62.6 (2015), pp. 3545–3556 (cit. on p. 31).
- [178] T. Shintai, Y. Miura, and T. Ise. “Oscillation damping of a distributed generator using a virtual synchronous generator.” In: *IEEE Transactions on Power Delivery* 29.2 (2014), pp. 668–676 (cit. on p. 23).
- [179] V. P. Singh et al. “Robust \mathcal{H}_∞ load frequency control in hybrid distributed generation system.” In: *International Journal of Electrical Power & Energy Systems* 46.Supplement C (2013), pp. 294–305 (cit. on p. 42).
- [180] S. Skogestad and I. Postlethwaite. *Multivariable feedback control: Analysis and design*. John Wiley & Sons, New York, 2005 (cit. on pp. 45, 46, 48–50, 52, 53, 55, 61, 85, 86, 88, 100, 101, 125, 138, 141, 142).
- [181] N. Soni, S. Doolla, and M. C. Chandorkar. “Improvement of transient response in microgrids using virtual inertia.” In: *IEEE Transactions on Power Delivery* 28.3 (2013), pp. 1830–1838 (cit. on p. 23).
- [182] X. Su et al. “Microgrid stability controller based on adaptive robust total SMC.” In: *Energies* 8.3 (2015), pp. 1784–1801 (cit. on p. 40).
- [183] S. A. Taher and M. Zolfaghari. “Designing robust controller to improve current-sharing for parallel-connected inverter-based DGs considering line impedance impact in microgrid networks.” In: *International Journal of Electrical Power & Energy Systems* 63.Supplement C (2014), pp. 625–644 (cit. on p. 44).
- [184] S. A. Taher et al. “A new approach for soft synchronization of microgrid using robust control theory.” In: *IEEE Transactions on Power Delivery* 32.3 (2017), pp. 1370–1381 (cit. on pp. 44, 53).
- [185] A. Tavakoli, M. Negnevitsky, and K. M. Muttaqi. “A decentralized model predictive control for operation of multiple distributed generators in an islanded mode.” In: *IEEE Transactions on Industry Applications* 53.2 (2017), pp. 1466–1475 (cit. on p. 35).
- [186] B. Tenenbaum et al. *From the bottom up: How small power producers and mini-grids can deliver electrification and renewable energy in Africa*. The World Bank, Washington, D.C., 2014 (cit. on p. 13).
- [187] P. Thounthong et al. “Energy management of fuel cell/solar cell/supercapacitor hybrid power source.” In: *Journal of Power Sources* 196.1 (2011), pp. 313–324 (cit. on p. 67).
- [188] K. Tsakalis. *Stability, controllability and observability*. 2013. URL: <http://tsakalis.faculty.asu.edu/notes/sco.pdf> (cit. on p. 85).
- [189] E. Unamuno and J. A. Barrena. “Hybrid AC/DC microgrids – Part II: Review and classification of control strategies.” In: *Renewable and Sustainable Energy Reviews* 52 (2015), pp. 1123–1134 (cit. on pp. 25–29).
- [190] T. L. Vandoorn et al. “Microgrids: Hierarchical control and an overview of the control and reserve management strategies.” In: *IEEE Industrial Electronics Magazine* 7.4 (2013), pp. 42–55 (cit. on pp. 27, 28).

- [191] T. L. Vandoorn et al. “Review of primary control strategies for islanded microgrids with power-electronic interfaces.” In: *Renewable and Sustainable Energy Reviews* 19 (2013), pp. 613–628 (cit. on pp. 28, 32).
- [192] D. B. Vannoy et al. “Roadmap for power-quality standards development.” In: *IEEE Transactions on Industry Applications* 43.2 (2007), pp. 412–421 (cit. on p. 21).
- [193] S. Vazquez et al. “Energy storage systems for transport and grid applications.” In: *IEEE Transactions on Industrial Electronics* 57.12 (2010), pp. 3881–3895 (cit. on pp. 21–23).
- [194] C. Wang et al. “Voltage control strategy for three/single phase hybrid multimicrogrid.” In: *IEEE Transactions on Energy Conversion* 31.4 (2016), pp. 1498–1509 (cit. on p. 44).
- [195] X. Wang and P. Yi. “Security framework for wireless communications in smart distribution grid.” In: *IEEE Transactions on Smart Grid* 2.4 (2011), pp. 809–818 (cit. on p. 13).
- [196] X. Wang et al. “Virtual-impedance-based control for voltage-source and current-source converters.” In: *IEEE Transactions on Power Electronics* 30.12 (2015), pp. 7019–7037 (cit. on p. 30).
- [197] Y. Wang et al. “An estimator-based distributed voltage-predictive control strategy for AC islanded microgrids.” In: *IEEE Transactions on Power Electronics* 30.7 (2015), pp. 3934–3951 (cit. on p. 35).
- [198] D. Wu et al. “A control architecture to coordinate renewable energy sources and energy storage systems in islanded microgrids.” In: *IEEE Transactions on Smart Grid* 6.3 (2015), pp. 1156–1166 (cit. on p. 29).
- [199] L. Xu and D. Chen. “Control and operation of a DC microgrid with variable generation and energy storage.” In: *IEEE Transactions on Power Delivery* 26.4 (2011), pp. 2513–2522 (cit. on p. 13).
- [200] Z. Xu et al. “Analysis on the organization and development of multi-microgrids.” In: *Renewable and Sustainable Energy Reviews* (2017) (cit. on p. 12).
- [201] A. Yazdani and R. Iravani. *Voltage-sourced converters in power systems*. John Wiley & Sons, 2010 (cit. on p. 63).
- [202] X. Yu et al. “Control of parallel-connected power converters for low-voltage microgrid – Part I: A hybrid control architecture.” In: *IEEE Transactions on Power Electronics* 25.12 (2010), pp. 2962–2970 (cit. on pp. 31, 32).
- [203] R. Zamora and A. K. Srivastava. “Controls for microgrids with storage: Review, challenges, and research needs.” In: *Renewable and Sustainable Energy Reviews* 14.7 (2010), pp. 2009–2018 (cit. on p. 29).
- [204] I. Zhang et al. “The steady state characteristics of an SSSC integrated with energy storage.” In: *2001 IEEE Power Engineering Society Winter Meeting. Conference Proceedings (Cat. No.01CH37194)*. Vol. 3. 2001, 1311–1316 vol.3 (cit. on p. 33).
- [205] M. Zhang et al. “Control strategy design and parameter selection for suppressing circulating current among SSTs in parallel.” In: *IEEE Transactions on Smart Grid* 6.4 (2015), pp. 1602–1609 (cit. on pp. 29, 31).

-
- [206] Q. C. Zhong and G. Weiss. “Synchronverters: Inverters that mimic synchronous generators.” In: *IEEE Transactions on Industrial Electronics* 58.4 (2011), pp. 1259–1267 (cit. on p. 23).
- [207] Q. C. Zhong et al. “Self-synchronized synchronverters: Inverters without a dedicated synchronization unit.” In: *IEEE Transactions on Power Electronics* 29.2 (2014), pp. 617–630 (cit. on p. 23).
- [208] K. Zhou, J. C. Doyle, and K. Glover. *Robust and Optimal Control*. Prentice Hall, New Jersey, 1995 (cit. on pp. 45, 46, 48, 49, 52, 53, 55, 100).
- [209] D. Zhu and G. Hug-Glanzmann. “Coordination of storage and generation in power system frequency control using an \mathcal{H}_∞ approach.” In: *IET Generation, Transmission Distribution* 7.11 (2013), pp. 1263–1271 (cit. on p. 42).

Contrôle avancé pour la stabilité des microréseaux d'énergie: co-conception robuste and validation temps réel

Résumé – Cette thèse porte sur les problèmes de stabilité en fréquence et en tension des microréseaux isolés avec forte pénétration d'énergies renouvelables en utilisant des dispositifs de stockage d'énergie, et se divise en deux parties principales.

Dans la première partie, nous proposons une conception systématique d'une structure de commande robuste multi-variable pour le réglage de fréquence dans un système de génération de puissance hybride diesel-photovoltaïque-supercondensateur fonctionnant en mode autonome. La structure de commande proposée repose sur une architecture à deux niveaux: les contrôleurs d'asservissement de courant basés sur commande PI classique sont placés sur le niveau de commande inférieur et reçoivent des références d'un niveau supérieur qui, lui, est basé sur commande \mathcal{H}_∞ . Une méthodologie compréhensive qui traduit les demandes d'ingénierie spécifiques de l'opération du microréseau dans le formalisme de commande \mathcal{H}_∞ est détaillée. Nous montrons également comment les spécifications de performance dynamiques en boucle fermée doivent à leur tour être prises en compte dans la configuration et le dimensionnement initiaux du microréseau, c'est-à-dire en choisissant de manière appropriée et en évaluant le système de stockage d'énergie. Ensuite, une analyse de performance robuste du contrôleur \mathcal{H}_∞ synthétisé en présence de diverses perturbations de charge, des variations de puissance active de la source photovoltaïque, et des incertitudes du modèle est effectuée afin de déterminer la plage de variation maximale des paramètres pour laquelle les performances imposées en boucle fermée sont respectées pour le point de fonctionnement considéré. Les simulations numériques réalisées avec MATLAB[®]/Simulink[®] montrent l'efficacité de la stratégie de commande robuste de fréquence proposée sur un microréseau d'ordre de quelques MVA. Un banc de test de prototypage rapide, qui est composé d'un système de stockage d'énergie réel à base de supercondensateurs et un réseau diesel-photovoltaïque-charge émulé, est développé afin de valider expérimentalement cette stratégie de commande.

La deuxième partie de cette thèse se concentre sur le calcul d'un contrôleur de tension multi-variable basé sur commande \mathcal{H}_∞ afin de forcer robustement l'amplitude de tension du point de couplage commun à satisfaire des spécifications dynamiques. La même idée de la structure de commande à deux niveaux en cascade – où ce contrôleur est placé sur un niveau de commande supérieur et fournit les références de courant aux contrôleurs de courant placés sur un niveau inférieur – est également adoptée. Ensuite, la performance et la robustesse du contrôleur \mathcal{H}_∞ proposé en présence de diverses perturbations de puissance réactive de la charge et des incertitudes du modèle sont étudiées en utilisant des simulations temporelles MATLAB[®]/Simulink[®].

Mots clés – Gestion énergétique, commande robuste, services systèmes, microréseau.

Advanced control of microgrids for frequency and voltage stability: robust control co-design and real-time validation

Abstract – This thesis addresses the frequency and voltage stability issues of stand-alone microgrids with high penetration of renewable energy by making use of energy storage devices, and is divided into two main parts.

In the first part, we propose a systematic design of a multi-variable robust control structure for frequency regulation in a diesel-photovoltaic-supercapacitor hybrid power generation system operating in stand-alone mode. The proposed control structure relies on a two-level architecture: classical PI-based current tracking controllers are placed on the low control level and receive references from an \mathcal{H}_∞ -control-based upper level. A comprehensive methodology that casts the specific engineering demands of microgrid operation into \mathcal{H}_∞ control formalism is detailed. It is also shown how closed-loop dynamic performance requirements must at their turn be taken into account in the initial microgrid setup and sizing, namely in appropriately choosing and rating the energy storage system. Then, a robust performance analysis of the synthesized \mathcal{H}_∞ controller in the presence of various load disturbances, photovoltaic output active power variations, and model uncertainties is carried out in order to determine the maximum parameter variation range for which the imposed closed-loop performances are respected for the considered operating point. Numerical simulations performed with MATLAB[®]/Simulink[®] show the effectiveness of the proposed frequency robust control strategy on a MVA-rated microgrid. A rapid-prototyping test bench, which is composed of a real supercapacitor-based energy storage system and an emulated diesel-photovoltaic-load grid, is developed in order to experimentally validate this control strategy.

The second part of this thesis focuses on computing an \mathcal{H}_∞ -based multi-variable voltage controller in order to robustly force the voltage magnitude of the point of common coupling to satisfy dynamic specifications. The same idea of cascaded two-level control structure – where this controller is placed on an upper control level and provides the references to current controllers placed on a lower level – is also adopted. Then, the performance and robustness of the proposed \mathcal{H}_∞ controller in the presence of various load reactive power disturbances and model uncertainties are studied based on MATLAB[®]/Simulink[®] time-domain simulations.

Keywords – Energy management, robust control, ancillary services, microgrid.

Grenoble Electrical Engineering laboratory (G2Elab)
Bâtiment GreEn-ER, 21 avenue des Martyrs, F-38031 Grenoble Cedex 1, France

Grenoble Images Speech Signal and Control laboratory (GIPSA-lab)
11 rue des Mathématiques, F-38402 Saint-Martin d'Hères Cedex, France